# Spectral analysis of the cerebral cortex complexity

Hamed Rabiei

## To cite this version:

Hamed Rabiei. Spectral analysis of the cerebral cortex complexity. Numerical Analysis [math.NA]. Aix-Marseille Universite, 2017. English. NNT : . tel-01881352

HAL Id: tel-01881352
https://hal.science/tel-01881352

Submitted on 25 Sep 2018

# Aix-Marseille University

## Doctoral School of Mathematics and Informatics of Marseille (ED184)

UFR Science

Institute of Neuroscience of la Timone (INT)
Institute of Mathematics of Marseille (I2M)
Laboratory of Information Science and Systems (LSIS)

Thesis presented to obtain the PhD degree of Mathematics and Informatics

Hamed Rabiei

# Spectral analysis of the cerebral cortex complexity

To be defended at 26/09/2017 in front of the jury :

| | | |
|---|---|---|
| Pierre Borgnat | ENS of Lyon | Rapporteur |
| Umberto Castellani | University of Verona | Rapporteur |
| Isabelle Bloch | LTCI, Telecom ParisTech | Examiner |
| Bruno Torresani | I2M, Aix-Marseille University | Examiner |
| Roberto Toro | Institut Pasteur, Paris | Examiner |
| Julien Lefèvre | LSIS, Aix-Marseille University | Supervisor |
| Frédéric Richard | I2M, Aix-Marseille University | Supervisor |
| Olivier Coulon | LSIS, Aix-Marseille University | Supervisor |

# Aix-Marseille Université

## École Doctorale en Mathématiques et Informatique de Marseille (ED184)

UFR Science

Institut de Neurosciences de la Timone (INT)
Institut de Mathématiques de Marseille (I2M)
Laboratoire des Sciences de l'Information et des Systèms (LSIS)

Thèse présentée pour obtenir le grade universitaire de docteur en Mathématiques et Informatique

Hamed Rabiei

# Analyse spectrale de la complexité du cortex cérébral

Soutenue le 26/09/2017 devant le jury :

| | | |
|---|---|---|
| Pierre BORGNAT | ENS de Lyon | Rapporteur |
| Umberto CASTELLANI | University of Verona | Rapporteur |
| Isabelle BLOCH | LTCI, Telecom ParisTech | Examinateur |
| Bruno TORRESANI | I2M, Aix-Marseille Université | Examinateur |
| Roberto TORO | Institut Pasteur, Paris | Examinateur |
| Julien LEFÈVRE | LSIS, Aix-Marseille Université | Directeur de thèse |
| Frédéric RICHARD | I2M, Aix-Marseille Université | Directeur de thèse |
| Olivier COULON | LSIS, Aix-Marseille Université | Directeur de thèse |

# Abstract

Surface shape complexity is a morphological characteristic of folded surfaces like the cerebral cortex. There is, however, no universal agreement on the notion of surface complexity and various measures in the literature evaluate different aspects of it. Most of these measures are not based on a clear definition of the surface complexity and are likely to be biased by other geometrical features of a surface e.g. depth of folds or size of surfaces. Moreover, it is not possible to justify what those methods really measure. Consequently, inconsistent results from different measures can be found in the literature.

To address this issue, by investigating advantages and disadvantages of existing measures in the literature, we propose some properties that a standard measure of surface complexity should possess. We then develop methods with two approaches to introduce surface complexity measures that satisfy the proposed properties. The proposed methods are based on the spectral analysis of surfaces which has been shown to be useful to capture relevant shape features.

In the first approach, we propose two clear definitions of the surface complexity based on surface bending properties. To quantify these definitions, the recently introduced graph windowed Fourier transform is extended to mesh model of surfaces. Through this local spectral method, we introduce two new local measures of complexity that satisfy most of the suggested standard properties. Especially, they quantify the surface complexity in multi-spatial scales and take into account the inter-subject size variability.

Through some experiments on synthetic surfaces, we show that surface area-based measures of surface complexity may not distinguish deep folds from oscillating ones with equal area. Furthermore, the proposed method is applied to a database of 124 healthy adult subjects. Our proposed measures appropriately assign low values to deep regular folds such as the insula and the central sulcus and high values to regions consisting of sharp or oscillating folds such as the prefrontal cortex. The effect of the brain volume on the global and local cortical complexity is also studied.

In the second approach, we define the surface complexity by the Hölder regularity of fractional Brownian motions defined on manifolds. Then, for the first time, we develop a spectral-regression algorithm to quantify the Hölder regularity of a given fractional Brownian surface by estimating its Hurst parameter $H$. Moreover, we discuss that the estimated $H$ has many properties of a standard measure of the surface complexity. Inspiring by the fractional Brownian motions in 1D, we give a conjecture on the relationship between $H$ and the fractal dimension.

The proposed method is evaluated on a set of simulated fractional Brownian spheres. Moreover, by assuming the cerebral cortex to be a fractional Brownian surface, the proposed algorithm is applied to estimate the Hurst parameters of a set of 14 fetal cerebral cortices. The results show consistently the progress of the brain gyrification process in fetal ages. Last but not least, regarding the proposed conjecture, the estimated Hurst parameters are in a good accordance with the fractal dimension of the cerebral cortex, given in the literature.

**Keywords :** Computational geometry, Shape analysis, Mesh processing, Surface shape complexity, Spectral analysis, Windowed Fourier transform, Gyrification index, Fractional Brownian surface, Hurst parameter, Cerebral cortex

# Table of contents

# List of figures

# List of tables

# Introduction

> The human brain has 100 billion neurons, each neuron connected to ten thousand other neurons. Sitting on your shoulders is the most complicated object in the known universe.
>
> – Michio Kaku

Michio Kaku's statement reflects the brain complexity in the microscopic scale which is also true in the macroscopic scale. Indeed, the human cerebral cortex in the macroscopic scale is very smooth in the middle of fetal stage. At this time, the primary folds appear on the cortex, they wrinkle more and develop side branches which form secondary and tertiary folds. The process of cortical folding, known as gyrification, proceeds until few months after the birth when the cortical surface is highly folded and resembles an adult one in terms of surface complexity.

Surface complexity is a morphological characteristic of any surface which describes its degree of folding. In the case of the cerebral cortex, the surface complexity changes a lot along the brain development. It looks highly variable across an individual cortex and also humans. This variety roots in genetic factors as well as mechanical factors and is also affected by environmental conditions. Quantification of this characteristic helps us to better understand the effect of these factors on the process of brain development and aging. It also provides valuable information to investigate the interplay between psychiatric or neurodegenerative disorders and the organization of cortical folds which may help for early diagnosis, prevention and treatment of such pathologies.

To quantify the surface complexity of the cortical surface, there are some methods in the literature. Almost all recent methods, falling within the context of computational anatomy and surface-based morphometry, rely on analyses of the magnetic resonance images (MRIs) of the brain. Once an MRI acquisition of the brain is performed, it is segmented by using image processing techniques to extract different tissues such as the white matter, gray matter and cerebro-spinal fluid etc. Then, the boundary between those tissues are reconstructed as surfaces modelled by triangular meshes. Finally, morphological analysis can proceed on those meshed surfaces and results of such analyses can be represented on those surfaces.

The existing methods of the surface complexity measurement can be categorized in 3 classes based on the geometrical features of the surface that they use for analysis :

- Surface area
- Surface curvature
- Surface fractal dimension

Most of these methods provide local measures of the surface complexity. In the literature, these measures are known as either the *gyrification index* (GI) in cases of surface area and curvature based methods or the *surface complexity* in the case of the fractal analysis. To avoid any ambiguity, in this thesis, we call all those measures "GI" and we refer to surface complexity as a characteristic of the cerebral cortex that is measured by a GI.

The variety of methods and their results imply that there are different implicit interpretations of the notion of surface complexity. Nevertheless, most of those methods have not been designed based on a clear definition of the surface complexity which may be misleading i.e. a proposed GI may be biased by other morphometric parameters such as the depth of folds and the brain size. Moreover, it is not possible to justify what the proposed GI really measure. Consequently, one may get inconsistent results by using different GIs.

Some inconsistent examples can be found in the literature e.g. most of the surface area-based methods (e.g. TORO et al. 2008 ; SCHAER et al. 2008) and even some curvature-based methods (e.g. LUDERS et al. 2006) show that the frontal cortex is not much folded whereas some other methods (e.g. surface area-based GI of LEBED et al. 2013 and curvature-based GI of KIM et al. 2016) put this region among highly folded regions. Another example appears in relation to pathologies : in patients with 22q11 Deletion Syndrome, SCHAER et al. 2008 and BAKKER et al. 2016, by using a surface area-based GI, reported only decreased cortical complexity of some regions while BEARDEN et al. 2009, by using a fractal dimension-based GI, found only increased complexity of occipital lobe. Other inconsistent examples can be found in relation to the surface complexity and brain volume (e.g. ROGERS et al. 2010 ; LI et al. 2014) and gender (e.g. LUDERS et al. 2006 ; LIU et al. 2003).

Regarding the properties of different GIs in the literature, this question arises :

> What are the properties that a GI should possess to consider it as a standard GI ?

This question may be answered through investigating drawbacks of the existing methods. For instance, as mentioned before, some proposed GIs are not based on an explicit definition of the surface complexity. Some GIs have limitations in locality such that they can assign only one value to a big portion of the brain while some others work only in very small spatial scales (e.g. KIM et al. 2016). Some methods do not take into account the inter-subject brain size variability thus result in inconsistent locality of analysis (e.g. GIs proposed by SCHAER et al. 2008 and TORO et al. 2008). Some GIs violate essential properties that is necessary in clinical studies e.g. they do not have geometry invariance properties thus depend on the embedding of brain surfaces and are hardly reproducible. For instance, YOTTER et al. 2011 have shown that the fractal dimension computed by the box-counting method is not invariant to surface rotation.

To address the above-mentioned question, we define explicitly the notion of the surface complexity and develop methods to introduce new GIs that overcome the mentioned issues of existing GIs in the literature by satisfying some standard properties. The main contributions of this thesis are given below.

## Contributions

In this thesis, by reviewing the advantages and disadvantages of the existing methods, we provide a list of properties that a standard GI should possess. Then, we develop spectral methods on meshed surfaces to measure the surface complexity in two directions :

1. Analysis of geometrical properties of surfaces
2. Identification of fractional Brownian surfaces

**In the first direction,** we propose two explicit definitions of the "*surface complexity*" notion in two intuitive ways that rely on the surface bending properties. Particularly, a surface has more local complexity in a neighbourhood of each point if 1) it is more bended (magnitude of bending), or 2) it consists of more bends (spatial variation of bends). To quantify these definitions, we take advantage of the mean curvature as a geometric tool to measure bending properties.

To avoid the issues of using the mean curvature in spatial domain e.g. too much locality and sensitivity to noise, it is transferred to a so-called spectral domain through a local spectral transformation. For this purpose, the recently introduced graph windowed Fourier transform (SHUMAN et al. 2016) is extended to the mesh setting by replacing graph Laplacian by finite element (FE) discretization of Laplace-Beltrami operator defined on a surface. Unlike the graph Laplacian that is constructed based on the connectivity of graph nodes, the FE Laplace-Beltrami operator is aware of mesh geometry by taking into account the local surface area and angles of mesh elements. Moreover, we replace the window function, used to define neighbourhoods, by an adaptive window function to overcome the inconsistency of analysis arising from the inter-subject brain size variability.

Through the proposed method, we introduce two new local GIs and show that they satisfy most of the suggested standard properties. Especially, they are constructed based on clear definitions of the surface complexity and we prove theoretically that they quantify exactly those definitions. Moreover, they are geometric invariant, taking into account the inter-subject brain size variability and computed directly on the cortical surface with neither of them requiring a non intrinsic reference surface nor a smoothing procedure. The locality of GIs can be tuned easily in a wide range of spatial neighbourhoods from a part of a gyrus or sulcus to a big portion of the cortical surface equivalent to a lobe. Indeed, it is done only by changing a parameter of the window function without any ceiling effect.

Through some experiments on designed synthetic wavy surfaces we show that the mostly used surface area-based methods cannot distinguish between a deep regular fold and a set of shallow oscillating folds with the same surface area. In other words, those measures are biased by the fold depth and tend to give higher values of GIs to deep folds where much surface area is found. In contrast, our proposed indices are able to disentangle the effect of depth on the surface complexity quantification.

**In the second direction,** we try to measure the surface complexity through identification of the recently introduced fractional Brownian surfaces. Indeed, GELBAUM 2014 has introduced a generative model of fractional Brownian motions (fBm's) defined on smooth manifolds. Through displacing the points of a smooth manifold by an fBm defined on it, in direction of normals to the manifold, a fractional Brownian surface (fBs) is constructed. An fBs is a kind of fractal surface which can be characterized by a so-called Hurst parameter (denoted by $H$) of the corresponding fBm. This parameter takes its values in the range of $(0, 1)$ and determines properties of the fBm e.g. the Hölder regularity : the lower the value of $H$ of an fBm, the more irregular the corresponding fBs.

Accordingly, we propose to define the surface complexity of a given fBs by the Hölder regularity of its corresponding fBm. Furthermore, for the first time, we propose an algorithm to estimate $H$ parameter of a given fBs to measure its complexity. The proposed algorithm relies mainly on the special structure of the underlying fBm which has been defined as a random series of Laplace-Beltrami eigenvalues and eigenvectors of the underlying smooth manifold (GELBAUM 2014). It encourages us to estimate $H$ by using a spectral analysis based on Laplace-Beltrami eigenpairs.

In the proposed algorithm, first, the underlying smooth manifold and fBm are approximated through surface smoothing and dilation procedures applied on a given fBs. Then, the Laplace-Beltrami eigenvalues and eigenvectors of the approximated smooth manifold are approximated by a linear FE method. By using the eigenvectors, the spectral powers of the approximated fBm are computed. Then, the spectral powers of fBm are modelled by a least square linear regression as a function of the Laplace-Beltrami eigenvalues. Finally, the estimation of $H$ is extracted from the slope of the regression line.

The smoothing procedure, involved in the proposed algorithm, might result in non convex smoothed surfaces. Consequently, dilation of a non convex surface may cause point crossing which corrupts the surface locally, especially when the amount of dilation is high. To overcome this issue, we propose an iterative dilation algorithm with *surface surgery*. Through this algorithm, dilation is broken into several iterations with lower amount of dilation. Moreover, in each iteration, the critical points that are going to cross each other are identified and fixed (not dilated). At the end of iterations, the fixed points are relocated by a weighted interpolation of their normal neighbour points.

By computing the Hurst parameter of a set of fetal cerebral cortices, we show that the human cerebral cortex can be considered as a fractional Brownian surface, at least in a range of its low frequencies. Moreover, we discuss that the $H$ have main properties of a standard GI. Especially, it is based on a clear definition of the surface complexity i.e. the Hölder regularity, it is geometric invariant and can be computed in a reasonable time.

The Hurst parameter, however, is a global measure of the surface complexity. To have a local measure, inspired by the idea of multi-fractional Brownian surfaces, we bring up the idea of using local spectral analysis (e.g. the windowed Fourier transform) to estimate the local Hurst parameter. In this manner, it is expected that other properties of a standard GI i.e. locality and consistency are also met due to the natural properties of the mesh windowed Fourier transform with adaptive window function established in the first direction of this thesis.

Since a fractional Brownian surface is a kind of fractal, we wonder if there is a relationship between its Hurst parameter and fractal dimension. Inspired by some relationships in case of fBm's defined on $\mathbb{R}$ or rectangular domains in $\mathbb{R}^2$, we give a conjecture on this relationship in case of fBm's defined on manifolds. If this conjecture comes to be true, it can be useful in two ways : 1) It provides a new estimation of the Hurst parameter by using the methods of estimating the fractal dimensions, 2) By using the generative model of fBm's, one can generate a fractal surface with a known FD from arbitrary manifolds.

## Organization

The materials of the thesis are organized as follows.

**In Chapter 1,** first, it is explained shortly what the cortical gyrification is, how it emerges and why it is useful to quantify it. The existing methods in the literature to quantify the gyrification are surveyed in Section 1.3. The advantages and disadvantages of those methods are listed in this section. At the end of this chapter, we propose a list of properties that a standard GI should possess (cf. Section 1.4).

**In Chapter 2,** we review the methods of spectral surface analysis with emphasis on the methods developed to analyse the cerebral cortex in Section 2.1. Specially, we explain the Fourier transform on meshed surfaces in Section 2.2. The windowed Fourier transform for 1D signals is illustrated through an example in Section 2.3. The recently introduced graph windowed Fourier transform is given here. Our extension of the framework to mesh setting is presented in Section 2.4. The proposed spectral gyrification indices and their properties are given in Section 2.5. A summary of contributions finalizes this chapter (cf. Section 2.6).

**In Chapter 3,** the proposed method in the previous chapter is applied to some synthetic and real surfaces. In Section 3.1, some synthetic wavy surfaces are designed to illustrate the features of the proposed GIs. For comparison, a surface area-based GI proposed by TORO et al. 2008 is also computed on these surfaces. Through these experiments, the effect of fold depth on surface area-based GIs is elucidated. Then, the method is applied to real adult brain surfaces in Section 3.2. The individual maps as well as group average maps of our GIs and Toro's GI are presented in Section 3.2.2. Some features of our GIs are also shown here through some examples on an individual brain surface. The relationship between our proposed GIs and the brain volume is investigated globally and locally in Section 3.2.3. Finally, a summary of results along with a discussion are given in the last section of this chapter (cf. Section 3.3).

**In Chapter 4**, our proposed estimator of the Hurst parameter of fractional Brownian surfaces is presented. First, the theory of fractional Brownian motion (fBm) in 1D is reviewed shortly in Section 4.1. The extension to manifolds together with the simulation on the sphere surface are also given in this section. Our proposed algorithm to estimate the Hurst parameter is presented in Section 4.2. Especially, the proposed technique of dilation of non convex surfaces with mesh surgery is also given in this section. The method is evaluated on simulated fractional Brownian spheres in Section 4.3.1. The method is then applied on a set of real cortical surfaces of fetuses in Section 4.3.2. This chapter is ended with some discussions on how the Hurst parameter can be considered as a global GI and the relationship between the Hurst parameter and the fractal dimension. The idea of local estimation of the Hurst parameter is also brought up in this section. Finally, we mention some limitations of our algorithm (cf. Section 4.4).

**In Appendix A**, the proof of a proposition about the precision of the proposed estimator of the Hurst parameter is given.

# 1. Gyrification process and measurements

The human brain changes enormously in size, shape, and complexity during its development from prenatal life to adulthood. In particular, during prenatal and early postnatal periods, cortical folds appear and the cortex becomes more and more convoluted, a process that is known as gyrification. The study and quantification of gyrification is of great interest to measure the changes occurring on the brain surface during development, aging and diseases. In this field, one usually tries to measure and characterize the geometric features of brain like its volume, surface area and fold properties (e.g. length, depth, complexity etc.). In this chapter, we review some studies that have attempted to answer these questions : What is the gyrification ? How does it happen ? What are the effects of various factors on it ? How can we quantify it and measure these effects ?

## 1.1. Theories of gyrification

The human brain, in the middle of fetal stage, has a smooth surface. Then it starts wrinkling and some primary folds appear on this surface as short isolated shallow grooves or triple junctions. These primary folds become progressively deeper, more elongated and more wrinkled and develop side branches which form secondary and tertiary folds. The process of fold appearing on the cerebral cortex is called gyrification ; see Fig. 1.1. It occurs mostly during the second half of fetal life but continues changing the shape of the folds during post-natal life (ARMSTRONG et al. 1995 ; WELKER 1990 ; YU et al. 2007 ; LEFÈVRE et al. 2015).

In spite of space limitations enforced by skull size, gyrification allows brain to increase its surface area, up to $2500$ cm$^2$ in average (JONES et al. 1986), with advantages for expansion of number of neurons (ROCKEL et al. 1980 ; RAKIC 1995). Moreover, the connections between different parts of the brain will be more packed i.e. the length of axons become shorter. In this way, brain networks are optimized in terms of time and energy consumption for information processing (CHERNIAK 1995 ; KAAS 2000 ; KARBOWSKI 2003 ; LAUGHLIN et al. 2003 ; ZILLES et al. 2013).

Brain folds consist of concave and convex parts that are called sulci and gyri,

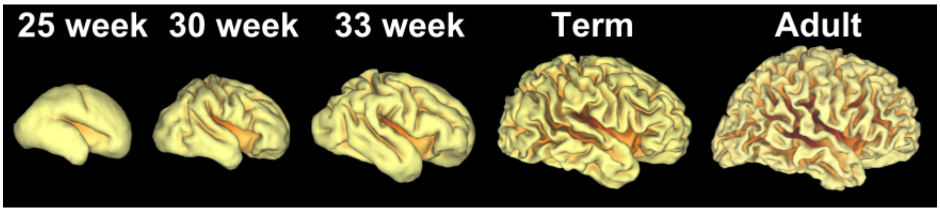

Figure 1.1.: Gyrification process from fetal to adult ages (adapted from Van Essen Lab, Washington University in St. Louis)

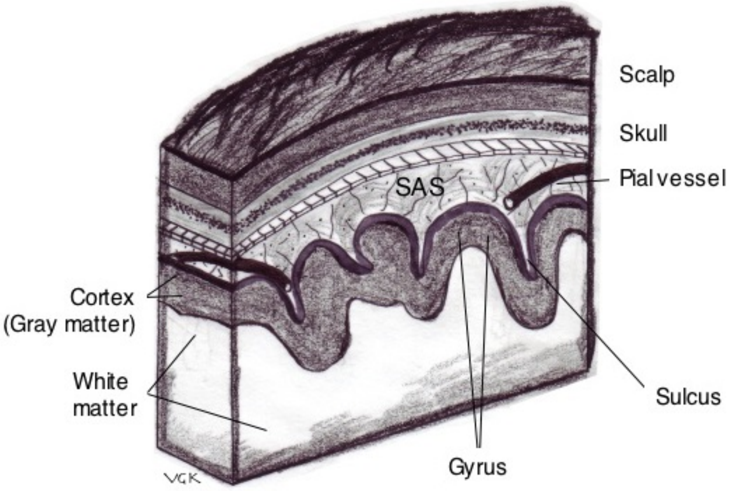

Figure 1.2.: A cross-section of the human head, from hairs to the white matter. A gyrus and sulcus are also indicated.

respectively ; see Fig. 1.2. Individual folding patterns show that the position and orientation of primary folds are not randomly determined and they are stable across individuals (WELKER 1990). In other words, although there is a high inter-individual variation in the shape of folds, all normal human brains include well-known primary folds in specific locations and orientations e.g. central sulcus, calcarine, superior temporal sulcus etc. This fact suggests that the gyrification is driven by specific mechanisms although it is not well understood yet. There are some studies that propose different scenarios behind gyrification process. Those studies have tried to unveil the underlying mechanisms of gyrification from different perspectives and scales : from genetic and molecular determinants to geometric patterns and mechanical forces. Here, we give a short review on some gyrification scenarios that are the most accepted in the brain development community.

VAN ESSEN 1997 proposed that axons in white matter pull the regions of the cortex which are strongly connected together and it forms gyri ; see Fig. 1.3. Accordingly, abnormal gyrification patterns stem from abnormal patterns of connectivity. In another hypothesis, RICHMAN et al. 1975 explained the gyrification process by the radial gradient of cortical tangential expansion. This suggests that the increasing expansion of upper layers of the cortex relative to the lower layers generates compressive stress leading to cortical folding ; see Fig. 1.3b. To test this hypothesis in practice, TALLINEN et al. 2016 have constructed a soft elastic tissue brain model based on a smooth fetal brain that mimics the gyrification process when immersed in solvents. Although the physical experiments, computational simulations and morphometric analysis show that the proposed mechanical approach can mimics the gyrification process at some extent, the folding pattern in this model is almost uniform in the whole cortex in contrast to that of a real brain (see e.g. Fig. 1d of TALLINEN et al. 2016). Recently, RONAN et al. 2014 proposed that differential tangential expansion causes folding. They supposed the non-uniform cytoarchitecture patterns cause different local growth rates of cortex. It, in turn, causes in-plane pressure that is mitigated through out-of-plane folding ; see Fig. 1.3c.

In the above-mentioned works, it is not answered why the position and orientation of the primary folds are reproduced across individuals. Through a joint analysis of experimental data and computational modelling, ZHANG et al. 2016 proposed that consistent folding patterns might have roots in heterogeneous regional growth in the cortex. They found that regions of cortex with faster growth rates form gyri consistently while more rigid regions form sulci.

## 1.2. Gyrification measurement : Applications

Morphological parameters of the cerebral cortex such as volume, surface area, sulcal shape features (like sulcal length, depth, width, position and asymmetry indices), cortical thickness, curvature and gyrification index (GI) are commonly used to quantify the gyrification process. Among these, GI is a direct measure that attempts to quantify the degree of folding of the cerebral cortex. It provides valuable information about structural changes occurring on a brain surface complexity during development, aging, and disease.

Detection of characteristic neuroanatomical patterns caused by abnormal brain development or neurodegenerative/psychiatric disorders may lead to early diagnosis, prevention and treatment of such pathologies. GI can be also employed to investigate differences in the brain surface structure between groups of individuals e.g. men vs. women, mediators vs. other people etc. The following paragraphs review some studies on how measurement of GI helps us to better understand the effect of various factors on the brain surface complexity. There are different definitions of GI that are given in the next section. Here, we refer to GI in its general sense as a descriptor of cortical complexity.

**(a)** Axonal Tension Hypothesis

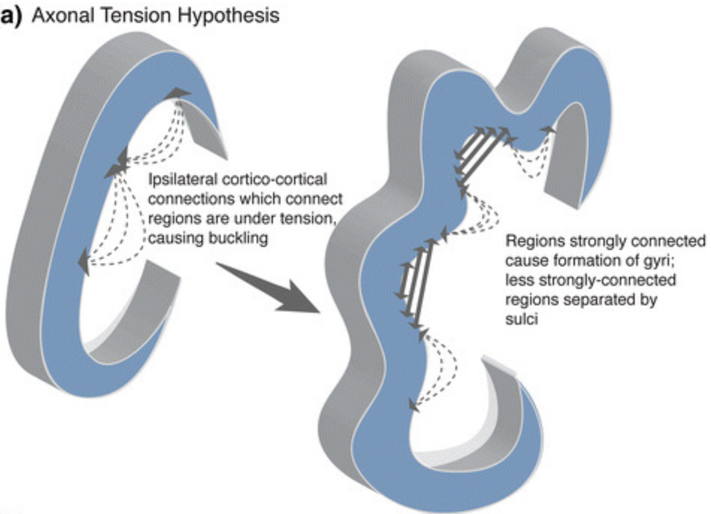

**(b)** Radial Expansion Hypothesis

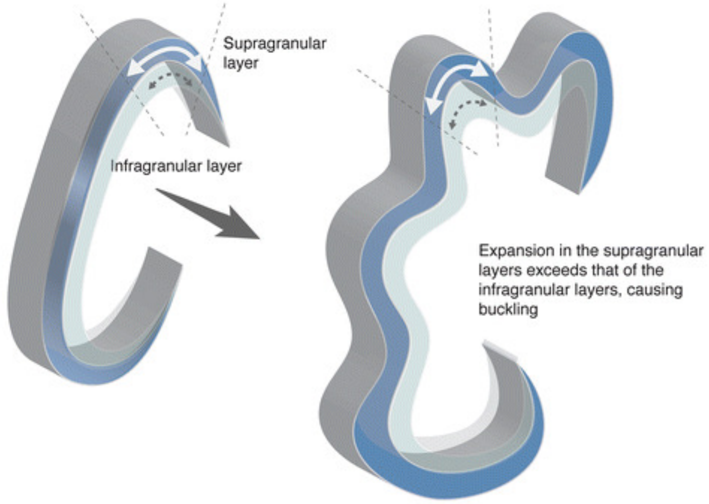

**(c)** Differential Tangential Expansion Hypothesis

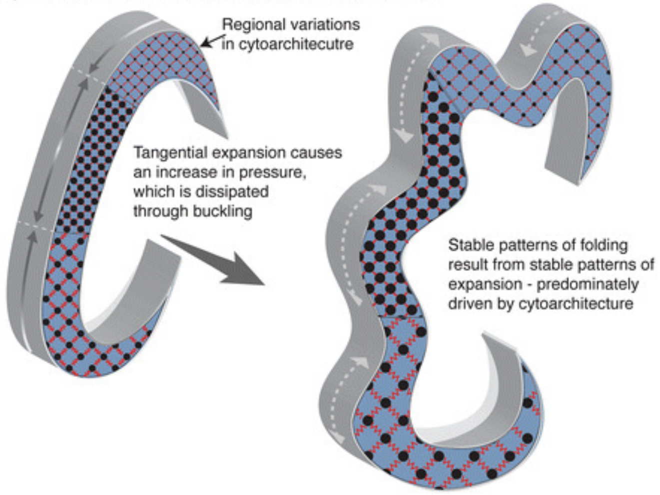

Figure 1.3.: Three major gyrification hypotheses (adapted from Ronan et al. 2014)

### 1.2.1. Development and aging

In many developmental studies, GI is one the most widely used indicators to identify normal and abnormal brain development from fetal to adult ages. In a cross-sectional study of gestational age-matched fetuses and preterm newborns, LEFÈVRE et al. 2015 showed that preterms have higher global GIs than fetuses. This finding reveals the increasing impact of early exposure to ex utero environment on the cortical complexity. In another comparison between term-born, healthy preterm and pathologic preterm infants, the power of gyrification index is highlighted where it is the only index among 22 indices that is able to distinguish those groups (SHIMONY et al. 2016).

KIM et al. 2016 studied the changes of cortical complexity occurring after birth from 6 to 24 months of age. They found that GI is positively correlated with age in this period of life. Moreover, they reported some sexual dimorphisms in the insula, middle cingulate, parieto-occipital sulcus and Broca's region. In another longitudinal study of infants from birth to 2 years of age, LI et al. 2014 found 16.1% and 6.6% of increase in global GI in the first and second year of life. Their results show heterogeneous developmental cortical changes with high-growth regions located in the association cortex, whereas the low-growth regions located in sensorimotor, auditory, and visual cortices. They showed that larger brains are more folded with a significant correlation between GI and the brain size in the prefrontal cortex. They also detected sexual dimorphisms such that males have larger GIs than females at 2 years of age.

In a lobar study on children and adults from 8 to 19 years of age, SU et al. 2013 found a gradual decrease in cortical complexity over time. The decreasing GI with age for adults of age $42.8 \pm 9.9$ has been also reported by BONNICI et al. 2007. Another comparison study between young ($27.7 \pm 4.4$ years of age) and old ($74.8 \pm 2.6$ years of age) subjects shows the decreasing effect of aging on brain surface complexity (ZHANG et al. 2007b). Moreover, the results of this study suggest that this decrease is not similar across genders and brain hemispheres, such that it significantly happens in the left hemisphere in old men but in the right hemisphere in old women.

In a study on adults between 20 and 86 years old, MADAN et al. 2016 found that the global cortical complexity of the gray matter decreases with age. Furthermore, the most decrease is observed on the prefrontal lobe followed by the parietal, occipital and temporal lobes. They also found that the cortical complexity is a more sensitive measure to aging than the whole brain mean cortical thickness.

In summary, GI measurement reveals that brain degree of folding increases with age in fetal period and few years after birth. Then it starts to decrease in school ages and continue to decrease in adulthood. These studies also show different evolutions of cortical complexity between male and female. Although, more research on cortical development, especially on longitudinal data, is still needed to give more precise inferences about evolution of cortical complexity.

### 1.2.2. Pathologies

Gyrification index has been also employed in many studies to identify the relationship between neurodegenerative pathologies/psychiatric disorders and cortical complexity. For instance, SCHAER et al. 2008 and BAKKER et al. 2016 recognized some cortical regions of patients with 22q11 Deletion Syndrome with decreased local cortical complexity while BEARDEN et al. 2009 identified an increase in GI of occipital lobe in those patients. In a study on patients with mental retardation, schizophrenia, comorbid mental retardation and Schizophrenia and controls, BONNICI et al. 2007 found that patients with mental retardation has the lowest GI in prefrontal cortex followed by comorbid, schizophrenia and controls. They also reported a significant age-related decline in GI for all four groups.

A decrease in cortical complexity has been also reported in patients with Schizophrenia (BULLMORE et al. 1994), dyslexia (CASANOVA et al. 2004), epilepsy (LIN et al. 2007), attention deficit hyperactivity disorder (WOLOSIN et al. 2009), mental retardation (ZHANG et al. 2010), neurofibromatosis type 1 (VIOLANTE et al. 2013), Parkinson (LEWIS et al. 2016) and amnestic mild cognitive impairment (WANG et al. 2016).

Some studies show an increase in GI in patients with manic-depressive disorder (BULLMORE et al. 1994) Williams syndrome (GASER et al. 2006), autism (JOU et al. 2010), Schizophrenia (SCHULTZ et al. 2013), dyslexia (PŁOŃSKI et al. 2016) major depressive disorder (HAN et al. 2016) and impulsivity (HIRJAK et al. 2016).

Some neurodegenerative pathologies like dementia (LEBED et al. 2013), Schizophrenia (PALANIYAPPAN et al. 2012 ; YOTTER et al. 2011) and bipolar disorder (NENADIC et al. 2017) increase the degree of gyrification in some cortical regions and decrease it in some other regions. Even some diseases that are not directly related to brain, like severe congenital heart disease, have been reported to reduce the degree of cortical folding in newborns (CLAESSENS et al. 2016).

In these studies, it has been argued that some neurological pathologies may affect the cortical complexity or they even may have roots in altered cortical complexity. Accordingly, altered cortical complexity may be considered as a sensitive marker for several neurodevelopmental disorders. The last mentioned study by CLAESSENS et al. 2016 raises this question that how pathologies of other organs affect the brain shape and folding. Consequently, quantification of changes in cortical complexity may open a way to investigate neurodegenerative pathologies and psychiatric disorders and even pathologies of other organs.

### 1.2.3. Miscellaneous factors

Besides development and diseases, some other events that happen in human life, may change the cortical complexity. For example, Kelly et al. 2013 have shown that children with maltreatment history have a less complex cortex in the lingual gyrus and the insula extending into pars opercularis in comparison to normal children. A study on people who had been involved in a motor vehicle accident in at least 6 month before the analysis revealed that post-traumatic stress disorder reduces the cortical complexity in the left lateral orbitofrontal cortex (Chu et al. 2016).

Recently, Riccelli et al. 2017 have shown that even personality is associated with variability in cortical anatomy, especially the degree of folding. They studied the famous five-factor model of human personality and found that 1) neuroticism is linked to smaller folding in prefrontal–temporal regions, 2) extraversion is linked to larger folding fusiform gyrus, 3) openness is linked to larger folding in prefrontal–parietal regions, 4) agreeableness is associated with larger inferior temporal cortex and 5) conscientiousness is linked to smaller area and folding in prefrontal regions. The correlation between dispositional anxiety and degree of folding has been studied by Miskovich et al. 2016. Their findings show a link between this personality trait and smaller folding in the left superior parietal region.

In a comparison study on gender differences, Luders et al. 2006 observed that the female brains are significantly more convoluted than male brains in all lobes while Zhang et al. 2007b got opposite results. In contrast, Liu et al. 2003 did not detect any difference in brain complexity between men and women.

Luders et al. 2008 studied the relation between intelligence quotients (IQ) and cortical complexity and found a significant positive correlation between IQ and GI in outermost section of the posterior cingulate gyrus. They also observed prominent gender differences within the right frontal cortex where "females showed uncorrected significant positive correlations and males showed a non-significant trend toward negative correlations." Im et al. 2006 have shown that people with higher intelligence quotient (IQ) have more complicated cortical structures and more interestingly, number of years of education has significant positive effect on the complexity of the cerebral cortex.

The effect of meditation on the brain gyrification has been also studied by Luders et al. 2012. They identified some regions, namely left precentral gyrus, right fusiform gyrus, right cuneus and left and right anterior dorsal insula with higher local GI in mediator subjects as well as a positive correlation between GI and the number of meditation years.

The relationships between the cortical complexity and other morphological properties of the cerebral cortex have been also investigated in several studies. Im et al. 2006 found a negative significant correlation between mean cortical thickness and complexity. They also found significant positive correlation between folding area[a] and complexity. They could not find any significant relationship between sulcal depth and complexity except in the left temporal lobe. In contrast, MADAN et al. 2016 found a strong positive correlation between mean cortical thickness and complexity.

Some studies reveal a positive correlation between cortical complexity and brain size, For instance TORO et al. 2008 have shown that the cortical complexity varies positively with total cortical surface area with the largest variation happens in the prefrontal region. IM et al. 2008, GERMANAUD et al. 2012 and GERMANAUD et al. 2014 found a positive correlation between brain volume and global cortical complexity. These results are in agreement with some mechanical models of gyrification process (TALLINEN et al. 2013 ; TALLINEN et al. 2016) and they support the hypothesis that larger brains are more folded.

## 1.3. Gyrification measurement : Methods

The extensive research mentioned in the previous section acknowledge the importance of gyrification measurement for which diverse methods have been suggested in the literature. A basic classification of these methods may be based on the level of GI assignment which varies from point-wise to global level. A method in point-wise level assigns a GI value to each point of the cerebral cortex that is usually computed in a pre-determined neighbourhood of each point. Some regional studies need to compute a GI for some regions of interest including sublobar regions, lobes and hemispheres. Finally, at the highest level, a single GI value is assigned to the whole brain surface. It is called a global GI and is a compact measure in which the information of total surface complexity is summarized. Although a global GI may be enough in some applications, describing the whole surface of a highly convoluted brain by only a single value is not sufficient to understand its local complexity. Especially in case of pathologies that deform cortical regions, a local GI is needed to localize this alteration.

A more sophisticated classification of gyrification measures may be presented based on the geometrical methodology : Some methods compute a ratio of surface area or contour perimeter of the brain(ZILLES et al. 1988 ; MOORHEAD et al. 2006 ; TORO et al. 2008 ; SCHAER et al. 2008 ; LEBED et al. 2013 ; SU et al. 2013 ; LI et al. 2014). Some other methods employ the surface curvature (VAN ESSEN et al. 1997 ; LUDERS et al. 2006 ; SHIMONY et al. 2016 ; KIM et al. 2016). There are also methods that mix the concepts and tools of the previous categories (SHISHEGAR et al. 2015) or are based on other geometrical features like fractal dimension (HOFMAN 1991 ; FREE et al. 1996 ; KISELEV et al. 2003 ; ZHANG et al. 2007b ; JIANG et al. 2008 ; YOTTER et al. 2011). In the following, we give a review of all these categories.

---

[a] Folding area is the ratio between the area occupied by sulci and total cortical surface area.

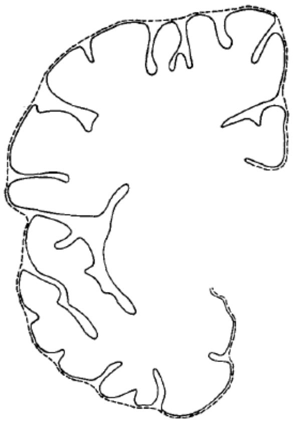

$$\mathrm{GI} = \frac{\text{Length of pial contour} \quad (\text{——})}{\text{Length of outer contour} \quad (\text{- - - -})}$$

Figure 1.4.: Left : A coronal section of a brain hemisphere. The pial contour is drawn by a solid line while the superficial outer contour is delineated by a dashed line. Right : Formula of Zilles' GI (Zilles et al. 1988).

It is noted that, in the literature, the gyrification measures that are based on surface area or curvature are usually called "*Gyrification Index*" (GI). On the other hand, the gyrification measures based on fractal dimension are called "*Cortical Complexity*". In this thesis, we call all of those measures as gyrification index and we refer to cortical complexity as a feature of the brain surface that is quantified by a gyrification index.

## 1.3.1. Surface area/perimeter-based GIs

An early attempt to measure the degree of human brain folding has been done by ZILLES et al. 1988 on post-mortem brains sliced on coronal plane. They defined the gyrification index of each coronal section of the brain as the ratio between the length of the pial contour and the length of a regular superficial outer contour as a reference contour ; see Fig. 1.4. The idea is that if a brain is more folded, this ratio will be larger. Despite of its easy interpretation, it raises some issues in implementation and results. For instance, in this method, the pial and outer contours have been delineated manually which is very time consuming in large scale studies and raises questions about reproducibility and reliability of results. Moreover, it has been discussed that due to complexity of folds in the 3D space, this measure by considering 2D coronal slices is prone to be biased and sensitive to slice orientation (ZILLES et al. 1989). Moreover, SCHAER et al. 2008 argued that the standard deviation of results obtained by Zilles' GI is too high to reveal group differences. In addition, while significant correlations between gyrification and brain volume (TORO et al. 2008 ; KAPELLOU et al. 2006 ; GERMANAUD et al. 2012) or gender (LUDERS et al. 2004 ; LUDERS et al. 2006) have been reported recently, Zilles' GI is not able to show this relation ZILLES et al.

1988.

Following the development of medical imaging technologies like MRI and advances in image processing algorithm in recent years, a 3D representation of brain can be reconstructed. Indeed, after anatomical MRI acquisition, the cerebrospinal fluid, gray and white matters are segmented in 3D volumes. Then, from the segmentation, the pial surface and white matter surface are reconstructed and modelled by triangular meshes.

By taking advantage of this representation, some attempts have been done to modify Zilles' GI. For instance, to deal with the manual delineation issue of Zilles' method, MOORHEAD et al. 2006 developed an algorithm to compute the pial and outer contours in the coronal sections of MR images automatically.

To take into account the 3D nature of the brain surface, SCHAER et al. 2008 extended Zilles' GI to 3D and proposed a local GI by the ratio between the area of a neighbourhood on a superficial outer surface and the area of the corresponding neighbourhood on the pial surface[b]. In this work, the outer surface is the hull surface that fills the sulci and covers the gyri. The outer neighbourhood around each point is then determined by the intersection of a sphere and the outer surface. Correspondence between the outer neighbourhood and the corresponding neighbourhood on the pial surface is computed by finding the points with the closest distance on both surfaces ; see Fig. 1.5a. This method assigns a GI value to every point of the outer surface. To compare GI values across cortices, an additional step has to be done to redistribute GI values from the outer surface to the pial surface through an averaging procedure.

To avoid this non intuitive step, LEBED et al. 2013 proposed to compute the outer surface by applying a surface-smoothing procedure. In this way, there exists a one-to-one vertex correspondence between the pial and the outer surfaces. LI et al. 2014 found the vertex correspondences between the cortex and the cerebral hull surface by solving the Laplace's equation and following the streamlines between the two surfaces.

Another method in the first category has been proposed by TORO et al. 2008. In this method, at each point of the pial surface, a sphere is centered and Toro's GI is defined as the ratio between the area of the pial surface contained in the sphere and the area of the great disc of the sphere[c] ; see Fig. 1.5b. The idea is that if the brain was not folded, the pial surface would be the great disc of the sphere. In this method, akin to Schaer's method, the neighborhood around each point is defined by a sphere of a certain radius $r$. By changing the radius of the sphere, it is possible to compute the GI in different spatial scales. According to GI maps shown in SCHAER et al. 2008, Fig. 4 and TORO et al. 2008, Fig. 5a-c, Toro's GI, is less sensitive to $r$ than Schaer's GI.

The locality of results of those methods depends on the radius of the spherical neighbourhood $r$. In order to deal with the brain size variability in a database,

---

[b] It is noteworthy that Schaer's method has been integrated in FreeSurfer software.

[c] The great disc is the largest disc that can be included inside a sphere.

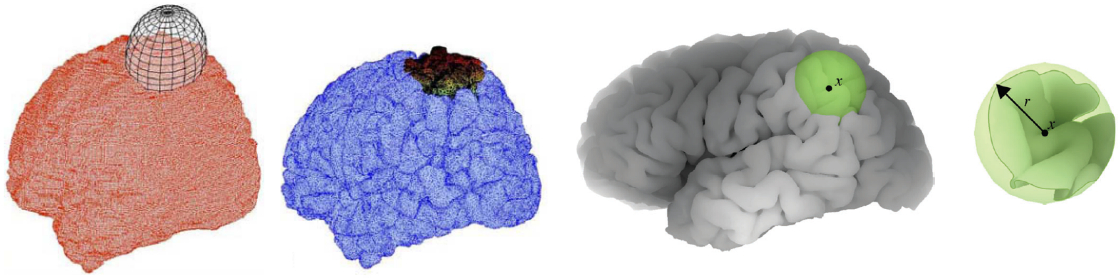

(a) (b)

Figure 1.5.: (a) Left : the pink surface is the brain hull surface. In Schaer's method, a neighbourhood around each point of the hull surface is determined by intersection of a sphere centred at that point and the hull surface. Right : the pial surface is shown on blue. The dark region is the projected neighbourhood from hull surface to pial surface. (b) Left : in Toro's method, a neighbourhood around each point of the pial surface is determined by intersection of a sphere centred at that point and the pial surface. Right : Such a neighbourhood is depicted. Figures are adapted from Schaer et al. 2008 and Toro et al. 2008.

the radius would have to be adapted for each subject. Otherwise the locality of analysis is not consistent between subjects. In other words, by using a fixed radius for a large and a small subject, the neighbourhood covers a greater portion of the surface area in small subject in comparison to large subject ; see Section 2.4.3 for more information. It will be more problematic when one is studying subjects with highly different sizes e.g. fetal brains.

Unfortunately, no intrinsic strategy exists to choose an adaptive neighbourhood in the above methods. To tackle this issue, Lefèvre et al. 2015 proposed to adapt the radius $r$ so that it equals a fraction of the brain length in the rostrocaudal direction. Li et al. 2014 also managed to deal with the size variability and to do a consistent analysis by resampling all cortical surfaces to the same standard mesh and taking $N$-ring neighbourhood around each vertex instead of geodesic neighbourhoods.

The main idea of the above methods is that if the brain was not folded, the local area of the pial surface and the reference surface would be the same. Accordingly, if the brain is more folded around a cortical point, the neighbourhood around that point contains a larger surface and the defined ratio will increase. This idea interprets the notion of cortical complexity based on the surface area. To our opinion, however, the main drawback of those methods stems from this interpretation. In fact, this interpretation is true when an unfolded region is to be compared with a folded region. Although, in case of two folded regions, this interpretation cannot distinguish between different kinds of folding. More precisely, those methods may not distinguish between deep folds and oscillating folds

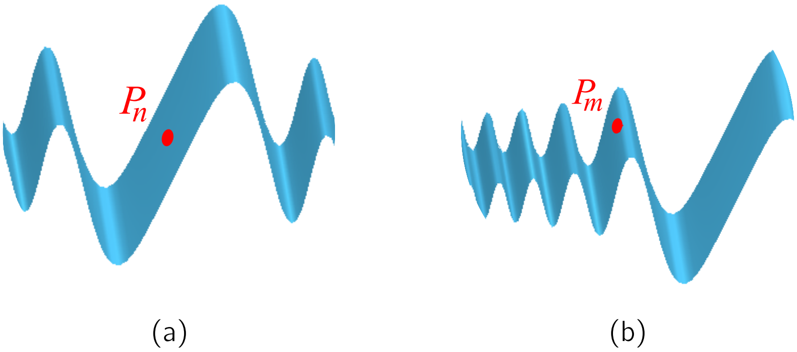

Figure 1.6.: (a) A folded region with few deep folds around $P_n$. (b) Another folded region with shallower but more oscillating folds around $P_m$. Toro's GI equals to 2.23 for both $P_m$ and $P_n$.

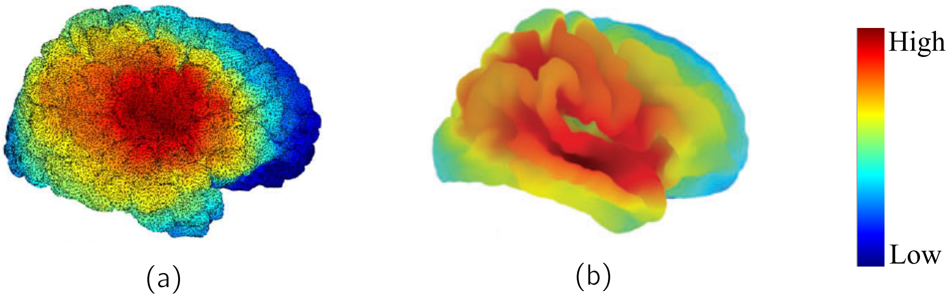

Figure 1.7.: GI maps resulted from (a) Schaer's method and (b) Toro's method. The blue and red colors indicate the extremes of low and high degree of folding respectively. It is seen that both methods tend to give larger GI values to deeper folds like the insula. Figures are adapted from Schaer et al. 2008 and Toro et al. 2008.

with equal surface areas.

For instance, in Fig. 1.6, two folded regions with equal surface areas are represented. The region around $P_n$ consists of few deep folds while the region around $P_m$ includes shallower but more oscillating folds. Due to equal surface areas around $P_m$ and $P_n$, the methods in this category give equal GI value to these points e.g. Toro's GI is about 2.23 for both $P_m$ and $P_n$. That is why Schaer's and Toro's methods both give high GI values to deep folds like the insula and the central sulcus. Indeed, in deep neighbourhoods, much surface area is found. In a more general way, both methods tend to produce similar GI maps ; see Fig. 1.7.

To address this issue, Su et al. 2013 proposed to weight the GI by the geodesic sulcal depth. In this method, the pial surface is wrapped by an outer hull surface. Then, for any ROI on the pial surface, the corresponding region on the hull surface is extracted by solving an differential equation of the negative gradient

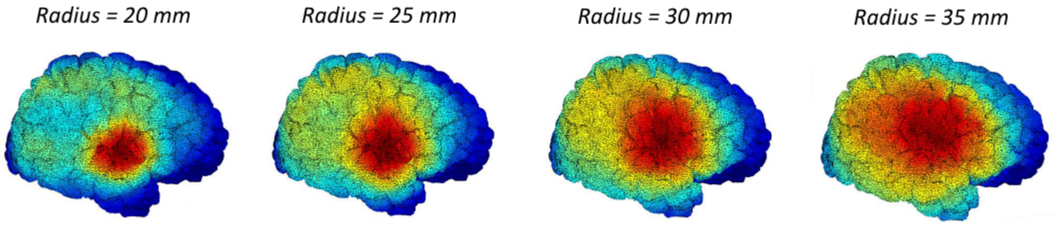

Figure 1.8.: Maps of Schaer's GI with different neighbourhood size : from $20mm$ to $35mm$. The blue and red colors indicate the extremes of low and high degree of folding respectively. The figure is adapted from Schaer et al. 2008.

of geodesic sulcal depth for points on the boundary of the pial ROI. Finally, the ratio between the weighted surface area of the considered ROI on the pial surface and the surface area of the corresponding region on the outer surface is computed where the weights are the geodesic sulcal depth. In this way, deep folds get higher weights than shallow ones.

The advantage of this method on the previous ones is two folded. First, there is no need for an extrinsic sphere to define a ROI/neighborhood on the cortex or the outer surface. Second, the weighted surface area ratio is able to discriminate deep and shallower folds with equal surface area. Nevertheless, we believe that this weighting strategy is in contradiction with the notion of surface complexity. In fact, if a cortical region with deep sulci and another region with shallow sulci have equal areas, the latter region should be more convoluted to keep the same area as the former one.

Moreover, the gyrification maps produced by these methods may be not localized enough for some applications. For example, in Fig. 1.8 adopted from Schaer's work, for a small spherical neighbourhood, the most folded region of the cortex is around the Sylvian Fissure and as the radius of the sphere increases, the same pattern propagates across the cortex. Therefore, it may fail to catch other folded parts of the brain and affect the reliability of findings.

### 1.3.2. Curvature-based GIs

Methods in the second category rely on the curvature and its derivatives e.g. the mean curvature. The mean curvature is a geometric tool that measures locally how a surface is deviated from being flat. It defines a function on the cerebral cortex and assigns positive values to points on gyri and negative values to points on sulci (see Meyer et al. 2003 and Section 2.5.1 for more information). The mean curvature map, however, is too local to deliver a helpful insight into the surface folding (Luders et al. 2006). Moreover, as Shimony et al. 2016 have recently shown, the curvature and its derivatives (e.g. the mean curvature, Gaussian curvature, shape index etc.) by themselves may not be able to discriminate between normal and aberrant cortical development.

Nevertheless, the curvature contains useful information about the surface bending. VAN ESSEN et al. 1997 defined a global folding index of each hemisphere by integrating a function of principal curvatures. To introduce a local measure of folding, LUDERS et al. 2006 defined a local GI by smoothing the magnitude of the mean curvature but the Luders' GI is not scale invariant. Indeed, if a cortical surface is just scaled while preserving its folding pattern, it is expected to keep its GI value as well but it is not the case for the Luders' GI[d].

KIM et al. 2016 has recently proposed a new GI by quantification of the shape index variance in a local region. In each neighbourhood, determined by a geodesic radius, the variability of some predefined shape types is computed, followed by a smoothing procedure. They introduced a two-phase adaptation of neighbourhood to deal with the size variability between subjects. In a longitudinal database of subjects from 6 to 24 month of age, first, for each 6-month-old subject, a fixed neighbourhood size is adapted globally by the ratio of the subject's hemisphere surface area to the average hemisphere surface area. Then, for older subjects, the normalized neighbourhood size is scaled by the changes of local surface area.

This analysis is done in very fine scales of at most $8mm$ with the advantage of differentiating between widening and deepening of cortical regions as well as to identify regions with developing secondary and tertiary sulci. The locality limitation leads to cortical complexity analysis within a sulcus or gyrus with neighbourhood size less than $8mm$; otherwise, a ceiling effect appears and less folded regions are not distinguishable from more folded ones (see Fig. 5a,b of KIM et al. 2016). The authors have also mentioned that the proposed GI changes by less than $0.1\%$ when the cortical surface is scaled from $80\%$ to $120\%$, thus not completely scale invariant. Moreover, due to the heat kernel smoothing procedure used in this method and Luders' method, they are likely to miss some folding features at fine scales.

In a recent work by SHISHEGAR et al. 2015, a new local GI has been proposed by computing the differential 1D signed curvature along the level sets of the first nontrivial Laplace-Beltrami eigenfunction weighted by the geodesic distance between each point and two closest gyral tops. In this way, the cortical curvature features are combined with sulcal depth which enable the method to discriminate between narrow sulci from wide sulci. This method focuses mainly on sulcal bending such that it assigns the lowest values to points on gyri and the largest values to deep narrow folds.

---

[d] Luders' method has been integrated in CAT toolbox of SPM12 software.

### 1.3.3. Fractal dimension-based GIs

In a different direction, the fractal dimension (FD) has been used to quantify the global degree of cortical folding. In fact, the human cerebral cortex has been approximately recognized as a fractal structure, at least in a limited range of spatial scales (HOFMAN 1991 ; FREE et al. 1996 ; KISELEV et al. 2003). Accordingly, FD as a measure of fractal irregularity, is applied as a global gyrification index. The more complex an object, the larger its FD value (MANDELBROT 1967). Fractal dimensions of different brain parts can also be computed and combined. For instance, ZHANG et al. 2007b proposed a hybrid FD consists of FD of white matter volume, white matter surface and the overall white matter structure (the sum of two former FDs).

The most widely used method to compute FD for human brain is the "box-counting method" introduced originally by RUSSELL et al. 1980 in a physics context (e.g. IM et al. 2006 ; THOMPSON et al. 1996). In this method, the surface of interest is mapped onto a rectangular grid or lattice. The grid consists of boxes with edges of equal length $r$. Then, the number of boxes occupied by one or more vertices of the mapped surface is counted. This procedure is done several times with different $r$'s and at each step, the number of occupied boxes is kept as $N(r)$. It has been shown that $N(r)$ is proportional to FD power of $r$ by $N(r) \propto (1/r)^{\mathrm{FD}}$. Now, the slope of the least-square regression line fitted to points $\{(1/r, N(r))\}$ in log-log scale gives FD (LIEBOVITCH et al. 1989 ; SARRAILLE et al. 1994 ; JIANG et al. 2008).

The human brain is not a pure fractal i.e. it does not have self-similarity in all scales. So, the range of box sizes $r$ in the box-counting method should be chosen carefully such that a linear relationship holds between $1/r$ and $N(r)$ in log-log scale (cf. NEZADAL et al. 2001 ; SILVA et al. 2006). Some limited attempts have been done to find upper and lower bounds for the box size (cf. CHEN et al. 1993 ; BISOI et al. 2001). Moreover, ASVESTAS et al. 1998 showed experimentally that the box-counting method is not numerically stable and underestimates the true value of FD.

Other methods have been also proposed to estimate FD and cover the limitations of box counting method e.g. differential box-counting method (CHAUDHURI et al. 1995), extended counting method (SANDAU et al. 1997) and frational Brownian motion methods (variogram by SOILLE et al. 1996 and power spectrum by PENTLAND 1984). To the best of our knowledge, none of them has been used to measure cortical complexity. A comprehensive review on above-mentioned methods for FD estimation along with their advantages and limitations are given by LOPES et al. 2009.

YOTTER et al. 2011 proposed recently a new way for estimating the FD through reconstruction of cortical surfaces by spherical harmonics (SPH). In this work, it is shown practically that the normalized surface area of reconstructed surfaces by SPH of degree at most $l$ varies linearly with $l$ in a certain range of $l$'s in log-

log scale. The slope of the fitted regression line is then considered as a global GI. A similar regression analysis in vertex level after a smoothing procedure gives a local GI. Moreover, they have shown that while this new GI is able to estimate the FD of fractal surfaces more accurately than the box counting method, the latter method is not invariant to rotation. As discussed at the end of this chapter, in practice, it is strongly expected from a well-defined GI to be invariant to isometric transformations like rotation [e].

## 1.4. Discussion

The aforementioned methods in all categories have different implicit interpretations of the concept of "*surface complexity*" that underlies GIs. AWATE et al. 2010 discussed the different meanings of surface complexity and categorized GIs based on their responses to different situations like surface scaling and variable spatial frequency of folds. It is also seen that sometimes different GIs give inconsistent or even conflicting results. For example, while most of the surface area-based methods and even Luders' GI show that the frontal cortex is not much folded, Kim's GI and Lebed's GI put this region among highly folded regions. Another evidence of the inconsistency appears in relation with the brain volume and the degree of cortical folding : ROGERS et al. 2010, by using an extension of Zilles' GI to 3D, showed that GI decreases with brain volume while an inverse correlation has been reported in some papers by using other surface-area based methods (see e.g. TORO et al. 2008 ; LI et al. 2014 ; GERMANAUD et al. 2014) and a curvature-based method (RABIEI et al. 2016).

This inconsistency also occurs when the effects of pathologies on cortical complexity are studied. For example, in patients with 22q11 Deletion Syndrome, SCHAER et al. 2008 and BAKKER et al. 2016 by using Schaer's GI reported only decreased cortical complexity of some regions while BEARDEN et al. 2009 by using a fractal dimension-based GI found only increased complexity of occipital lobe. Even in group comparison studies, inconsistent results have been reported. For instance, by using a curvature-based method, LUDERS et al. 2006 concluded that female brains are more complicated than men's while ZHANG et al. 2007b found that men show more complex brain surface than women and no difference was detected when the brain complexity is measured by fractal dimension (LIU et al. 2003).

Accordingly, the concept of the surface complexity needs to be defined explicitly. Moreover, a method should be developed to quantify this definition and satisfy some standard properties. We propose the following properties that a standard GI should possess :

1. **Clear basis :** A GI should be defined based on a definition of the "surface complexity" notion. It means that before developing a method to measure

---

[e] Yotter's method has been integrated in CAT toolbox of SPM12 software.

GI, a clear and reasonable definition of surface complexity should be given. Without having a clear definition of this notion, one may propose a new GI without knowing what the results are really meant. In this case, the effect of other geometric factors like the surface area or sulcal depth cannot be disentangled.

2. **Physicality :** A GI should have an interpretable physical meaning. In other words, it should be proven mathematically and practically that the proposed GI quantifies the assumed definition of the surface complexity.
3. **Locality :** A GI should be defined locally. Although depending on its application but in general, it is not adequate to describe a highly convoluted surface like the brain surface only with a single value. So, a good GI should be computed locally to measure the surface complexity in a reasonable neighbourhood around each point of the cortex. In this case, it is also possible to derive a single value as global cortical complexity.
4. **Multi–spatial scale :** It is an advantage if a method can propose GIs in a wide range of spatial scales. In other words, the locality of method around each point on the brain surface should be tuned easily from few millimeters (equivalent to $N$-ring neighbourhoods with small $N$'s) to larger areas ( e.g. areas of labor size). In this way, the method can be used for a wide range of applications by changing few parameters of locality.
5. **Consistency :** To have a consistent analysis across all subjects of a database, a GI should consider the inter-subject size variability. indeed, the size of neighbourhoods for each individual brain has to be adapted with the size of that individual brain surface. Otherwise, by using a fixed neighbourhood size for a small and a large brain, the neighbourhood covers relatively a larger proportion of the small brain than the large brain. In other words, there should exist a mechanism in the GI method to keep the relative spread of neighbourhoods constant across subjects.

   Beside the global size adaptation, for some applications e.g. developmental studies, it is an advantage for a GI method to have a mechanism of local size adaptation. It means that corresponding neighbourhoods across subjects should be adapted with respect to the local size of anatomical regions (see e.g. LI et al. 2014 and KIM et al. 2016).
6. **Geometric invariant :** Geometric transformations such as translation, rotation, reflection and scaling of a surface do not change its surface complexity. Consequently, it is reasonable to expect a good GI to preserve its value after such transformations. Otherwise, a kind of alignment is needed in preprocessing steps. However, as pointed out by YOTTER et al. 2011, "*alignment is a complicated endeavor that often requires manual delineation of areas that correspond geometrically across subjects, such as gyral landmarks or cortical sulci.*"

7. **Efficiency :** A GI should to be computed in a reasonable time and memory. In practice, efficiency is very important. There are some mathematical methods with interesting features that cannot be applied in this framework due to time and/or memory issues. For example, due to problems occurring sometimes in MR imaging of fetuses, segmentation algorithms fail which results in noisy surface triangulation. Consequently, one would like to apply meshless processing methods instead of mesh-based methods to get rid of noisy triangulation. But, due to non-sparsity of meshless methods and large number of vertices needed to model a complicated brain surface, it requires too much processing time and memory and makes it impractical.

# 2. Spectral gyrification indices

A spectral approach for solving a problem consists in transferring the problem from its own original space to a so called spectral space by using the eigenvalues and eigenfunctions of functional operators. The advantage of this transformation is that in the spectral space, data have a different structure that may be more suitable to solve a problem which is not easy or even impossible to solve in its original space (e.g. ZHANG et al. 2007a). In recent years, spectral methods have been proposed in the fields of graph theory, computer vision, machine learning, visualization, graph drawing, high performance computing, and computer graphics. Some important applications of these methods are describing and manipulating the geometry of a mesh. Such applications include mesh compression, correspondence, parameterization, segmentation, sequencing, smoothing, watermarking, surface reconstruction, remeshing and simulation ; see ZHANG et al. 2007a for a review on these applications and also TAUBIN 2000 ; ZHANG 2004 ; FLOATER et al. 2005 ; SORKINE 2005 among many others.

A growing application of spectral methods is in medical image analysis. They have been successfully exploited to analysis the volume and surface of organs reconstructed from magnetic resonance images (e.g. NIETHAMMER et al. 2007 ; WACHINGER et al. 2015). In neuroscience, the spectral methods have been used for brain segmentation, matching, surface and functional map smoothing, shape analysis of sulci and subcortical structures etc. (e.g. REUTER et al. 2007 ; SEO et al. 2011 ; GERMANAUD et al. 2012 ; LOMBAERT et al. 2015a).

In this chapter, first we survey spectral methods for surface analysis in sections 2.1 and 2.2. Particularly, in Section 2.3, we focus on a recently introduced spectral method on graphs, the graph windowed Fourier transform. We extend this method to 2D manifolds modelled by triangular meshes to analyse the surface complexity in Section 2.4. Moreover, an adaptive window function is introduced to deal with the inter-subject brain size variability. Then, we give two definitions of surface complexity and quantify these definitions by using the mesh windowed Fourier transform in Section 2.5. It results in definitions of our gyrification indices (GIs). Finally, in Section 2.6, a summary of contributions of this chapter is given.

Table 2.1.: A categorization of mesh operators

| Categories | Operators | References |
|---|---|---|
| Combinatorial | Graph Laplacian (Kirchoff) | Ohbuchi et al. 2001 |
| | Normalized graph Laplacian | Chung et al. 1997 |
| | Tutte Laplacian | Tutte 1963 |
| Geometric | Pinkall Laplacian | Pinkall et al. 1993 |
| | Meyer Laplacian | Meyer et al. 2003 |
| | FEM Laplacian | Dyer et al. 2005<br>Reuter et al. 2009a |
| Others | Discrete Schrödinger | Verdière 1990 |
| | Higher-order | Shi et al. 2000 ; Weiss 1999 |

## 2.1. Spectral surface analysis

In this section, we give an overview of spectral methods applied on meshes modelling surfaces. Spectral methods for mesh processing and analysis rely mainly on eigenpairs (eigenvalues and eigenvectors) of an operator defined on the surface. The eigenvalues, eigenvectors or eigenspace projections derived from such an operator are employed to analyse the mesh in the spatial domain or in a so-called spectral domain. The common framework of mesh spectral methods has usually 3 steps :

1. Definition of a discrete operator in a matrix form
2. Computing the eigenpairs of the involved matrix
3. Employing these eigenpairs to do the mesh processing or analysis task

Considering these steps, a great number of spectral methods have been proposed. Those methods vary depending on using different operators and different use of the eigenpairs to perform a specific task in different fields. According to these variations, Zhang et al. 2007a classified the spectral methods based on the operator used, the eigenstructure, and the dimensionality of the eigenstructure.

Depending on the problem at hand, there are different operators that can be defined on a mesh. A list of those operators, mostly adapted from Zhang et al. 2007a and Wardetzky et al. 2007, is given in Table 2.1. As it is seen in the table, different versions of discrete Laplacian operator are used in the literature. A general definition of discrete Laplacian operator is as follows (Zhang et al. 2007a).

**Definition 1.** *Let* $G = \{V, E\}$ *be a triangular mesh modelling the surface* $\mathcal{S}$ *where* $V$ *is the set of vertices,* $V = \{P_1, P_2, ..., P_N\}$, $|V| = N < \infty$ *and* $E$ *is the set of edges. If* $u = [u_1, u_2, \ldots, u_N]^T$ *is a function defined on vertices of the mesh, the*

*Laplacian $L$ of $u$ at vertex $P_i$ is defined by*

$$(Lu)_i := \frac{1}{m_i} \sum_{j=1}^{N} w_{ij}(u_i - u_j), \tag{2.1}$$

*where $w_{ij} \geq 0$ and $m_i > 0$ are arbitrary edge and vertex weights respectively.*

Given the notations of Definition 1, it is possible to define the Laplacian in a matrix form. To do so, let $W = [w_{ij}]$ be an $N \times N$ matrix of edge weights, then a diagonal matrix $D = [d_i]$ is defined by $d_i = \sum_{j \neq i} w_{ij}$. Moreover, let $M = [m_i]$ be a diagonal matrix of vertex weights and $A = D - W$. Now, the Laplacian operator is defined as $L := M^{-1}A$.

According to different ways of choosing weights $\{w_{i,j}\}$ and $\{m_i\}$ in definition of Laplacian, one can categorize this operator in two groups : combinatorial and geometric. The combinatorial Laplacian operators are defined by the graph associated with the mesh and the weights are chosen from connectivity of edges. In this manner, $W$ is called the weighted adjacency matrix and $d_i$ is the degree of vertex $P_i$ (Chung et al. 1997). For instance, when vertices $P_i$ and $P_j$ are connected by an edge, in graph Laplacian (Kirchoff) $m_i = w_{ij} = 1$ (known as umbrella weights) and in Tutte Laplacian $w_{ij} = 1/d_i$ and $m_i = d_i$ ; otherwise if $P_i$ and $P_j$ are not connected $w_{ij} = 0$.

In geometric Laplacians, the geometric information of the mesh is included in the weights. For example, $w_{ij}$'s contain information about area or angles of mesh elements. In this case, $A$ is called stiffness matrix and $M$ is called (lumped) mass matrix. Reuter et al. 2009a gives a quick review on geometric Laplacians. See also Section 2.4.1 for more information.

Each of these discrete Laplacians has some properties and as it is proved by Wardetzky et al. 2007, "*discrete Laplacians cannot satisfy all natural properties simultaneously ; retroactively, this explains the diversity of existing discrete Laplace operators.*" By natural properties, they mean the properties of the continuous Laplacian or Laplace-Beltrami operators[a] such as symmetry, locality, linearity, positivity, positive semi-definiteness and those that are useful in practice such as sparsity and convergence. The mentioned limitation means that there is no perfect discrete Laplacian. So, according to required properties for solving a problem, one may choose one of those operators.

Once an operator is chosen, its eigenpairs are computed. In the following, we survey some applications of the eigenvalues, eigenvectors and eigenspace projections of Laplacian operator in surface analysis with the main focus on the human brain surface.

---

[a] Laplace-Beltrami operator is the extension of Laplacian operator from Euclidean space to Riemannian manifolds e.g. 2D surfaces.

### 2.1.1. Laplacian eigenvalues

Laplacian eigenvalues of an object contain substantial geometrical and topological information of that object, including the volume, surface area, boundary length, Euler characteristic etc. (REUTER et al. 2006). For instance, WEYL 1911 and WEYL 1912 have proved an interesting result about the relationship between Laplacian eigenvalues of an object in $\mathbb{R}^d$ and its volume :

**Theorem 1.** *Given a bounded region $D$ of $\mathbb{R}^d$ with piecewise smooth boundary $B$ and its Laplacian eigenvalues $\{\lambda_k, k = 1, 2, \ldots\}$, then*

$$N(\lambda) \sim \frac{\omega_d \mathrm{vol}(D)\lambda^{d/2}}{(2\pi)^d}, \qquad \text{as} \quad \lambda \to \infty, \tag{2.2}$$

*where $N(\lambda)$ is the number of eigenvalues $\leq \lambda$, $\mathrm{vol}(D)$is the volume of $D$ and $\omega_d$ is the volume of the unit disc in $\mathbb{R}^d$.*

**Corollary 1.** *As a result of the Theorem 1, $\lambda_n$ grows in order of $\mathrm{O}(n^{d/2})$, i.e.*

$$\lambda_n \sim 4\pi^2\Big(\frac{n}{\omega_d \mathrm{vol}(D)}\Big)^{2/d}, \qquad \text{as} \quad n \to \infty. \tag{2.3}$$

*Especially, for $d = 2$*

$$\lambda_n \sim \frac{4\pi}{\mathrm{vol}(D)} n. \tag{2.4}$$

It should be noted that in this theorem, $\mathrm{vol}(D)$ is the Riemannian volume. So, for $d = 2$ it refers to surface area. Furthermore, Laplacian eigenvalues of an object are proportional to its squared spatial frequencies of vibration (e.g. GREBENKOV et al. 2013 ; GOLBABAI et al. 2012).

Due to mentioned properties of Laplacian eigenvalues, REUTER et al. 2006 introduced the "Shape-DNA" as a compact global shape descriptor of any 2D or 3D object. It consists of the first few (normalized) eigenvalues of the descritized Laplace-Beltrami operator computed via FEM on the mesh modelling the object. They have shown that the eigenvalues change continuously with topology-preserving deformations of the object's geometry. This property makes Shape-DNA suitable for shape comparison. It has a significant discriminatory power to identify and retrieve objects in a database such that in a contest with many other methods to do database retrieval, Shape-DNA performed very well and was among the 3 best methods (LIAN et al. 2013). Moreover, due to the isometry invariance of Laplace-Beltrami operator, it does not need vast mesh preprocessing like alignment, registration, mapping, or remeshing. It is invariant to pose and metric-preserving articulations.

The isospectral objects, i.e. the non isometric objects who share the same Laplace-Beltrami eigenvalues, however, are not distinguishable by this method. It should be noted that those objects are somewhat artificially constructed and appear to be exceptional. Nevertheless, those objects give negative answer to the famous question "*Can one hear the shape of a drum ?*" asked by KAC 1966 (see LIU et al. 2017 and references therein). REUTER et al. 2006, however, showed that by extracting the Shape-DNA of the 3D volumes together with the 2D boundary shells of 3D isospectral objects, it is possible to distinguish them.

Given this observation, WACHINGER et al. 2015 collected the complementary Shape-DNA of 3D volume and 2D boundary surface of brain cortical and subcortical structures in a matrix to introduce the "*BrainPrint*", a signature of the brain. Indeed, each row of the BrainPrint matrix includes the first $m$ Laplace-Beltrami eigenvalues of a considered cerebral segment. The power of the BrainPrint has been tested for subject identification, age and sex prediction, brain asymmetry analysis, and potential genetic influences on brain morphology.

In medical image analysis, NIETHAMMER et al. 2007, REUTER et al. 2007 and REUTER et al. 2009b also applied Shape-DNA to the classification of anatomical structures. They employed it as a volumetric global shape descriptor of the caudate nucleus and showed its discriminatory power to identify subjects with schizotypal personality disorder.

Laplacian eigenvalues of manifolds form digital spectral codes that contain geometrical and topological information of manifolds. By having appropriate properties such as isometry invariance, these codes have been successfully used as quantitative descriptors of manifolds, especially neuroanatomical surfaces. They have shown high discriminative power on neuroanatomical structures. The encrypted information in these spectral codes, however, include global features of surfaces, e.g. surface area, and it is not obvious how to extract local information of surfaces from them.

### 2.1.2. Laplacian eigenvectors

The Laplacian eigenvectors form a family of real-valued orthogonal vectors. Some of these eigenvectors are represented in Fig. 2.1. These vectors possess interesting topological properties that provide some tools to investigate geometrical features of structures. They show harmonic behavior which relates them to natural vibration modes of the object. In this sense, the eigenvectors related to smaller eigenvalues have simpler patterns and they carry information about the global geometry of the object. In contrast, as the corresponding eigenvalues increase, the eigenvectors show more complex patterns and more local geometric information are encoded in them. They are also isometry invariant and change smoothly with deformation of the object. Last but not least, the heat kernel embedding theorem demonstrates that Laplacian eigenvectors by themselves are able to determine the surface (BÉRARD et al. 1994 ; LAI et al. 2009).

Beside very interesting properties, eigenvectors are not suitable to serve directly as shape descriptors because they are incompatible across subjects. In other words, when the eigenvectors of two surfaces are ordered according to

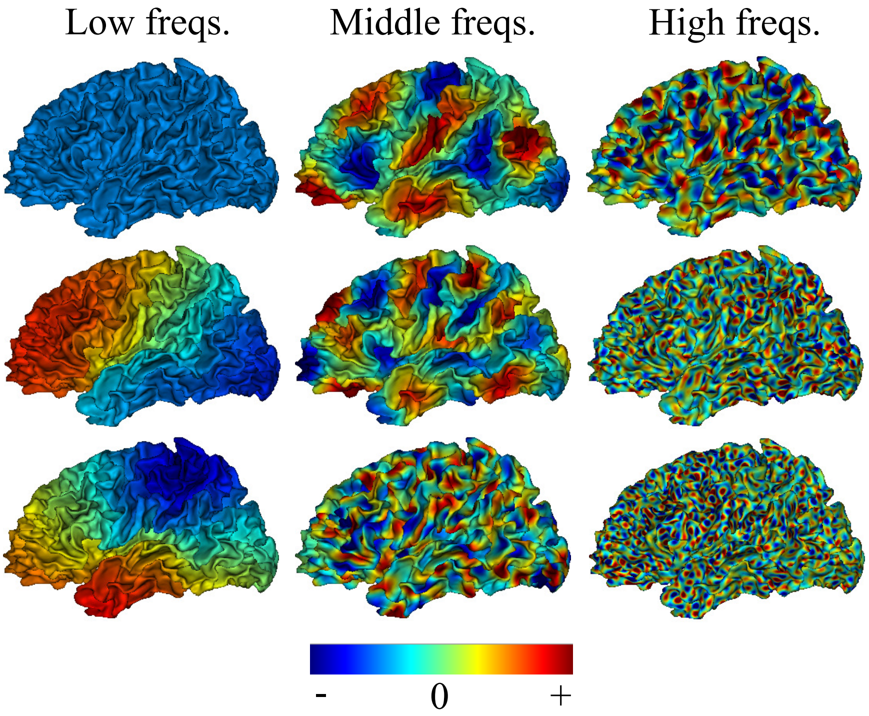

Figure 2.1.: Some examples of Laplacian eigenvectors of a brain surface. In the left column, some eigenvectors corresponding to small eigenvalues (low spatial frequencies) are shown. Eigenvectors in two other columns are corresponding to larger eigenvalues. The patterns of eigenvectors resemble a harmonic behavior and, as eigenvalue increases, the eigenvectors get more complex patterns.

the magnitude of their corresponding eigenvalues, they might switch order. This order switching includes sign or orientation changes and is due to multiplicities of eigenvalues, multiplicities in shape symmetry and numerical instabilities. These indeterminacies in the choice of signs and the particular ordering of eigenvectors makes it hard to consider a correspondence between eigenvectors of different surfaces.

To address this issue, BATES et al. 2011 proposed spectral shape descriptors that consist of symmetric functions of squared eigenfunctions weighted by exponentials of corresponding eigenvalues i.e. $f(e^{-\lambda_i t_i}\phi_i^2(x))$ for $i = 1, 2, \ldots$ at each point $x$ of the mesh and at each time $t$. In this work, the eigenpairs are computed from a graph Laplacian operator defined by Gaussian weights on edges. These descriptors have been successfully employed in a linear support vector machine (SVM) to identify subjects who are developing Alzheimer from normal controls.

REUTER et al. 2009a and REUTER 2010 used the nodal lines and nodal domains of eigenfunctions to segment surfaces into subregions. Nodal lines[b] of an

---

[b] Nodal lines are also called nodal sets in the literature.

eigenfunction $\phi$ are smooth closed contours where the eigenfunction value is zero i.e. $\phi^{-1}(0)$. Every connected component of complements of nodal lines i.e. $M \setminus \phi^{-1}(0)$ is called a nodal domain. Each nodal domain has a constant sign (positive or negative) that defines a subregion. The eigenfunctions corresponding to larger eigenvectors usually have more nodal domains. Accordingly, they segment a surface to more subregions. In this way, a set of eigenfunctions yield a series of segmentations with different number of subregions. Moreover, this method yields a symmetric segmentation such that the subregions are somewhat symmetric and are apparently meaningful parts of the surface. Due to properties of LBO, the segmentation is isometry invariant and robust to noise and surface sampling to some extent.

Lai et al. 2009 extracted a numerical sequence from eigenvectors as a shape descriptor. The proposed descriptor is a sequence of number of nodal domains. They have shown experimentally that this descriptor may have an advantage of differentiating between almost isospectral objects like caudate nucleus and putamen much better than Shape-DNA. Geometrical properties of the caudate nucleus have been also studied by Reuter et al. 2009b using the topological properties of selected eigenfunctions as shape descriptor. Specifically, the location of extrema, boundary length and surface area of nodal domains of some eigenvectors are used to localize shape features e.g. thickness and length.

The notion of nodal sets can be extended to level sets. A level set $\Gamma_\alpha$ of an eigenfunction $\phi$ is a smooth closed contour where the eigenfunction takes a specific values $\alpha$ i.e. $\Gamma_\alpha = \phi^{-1}(\alpha)$. Shishegar et al. 2015 analysed the brain surface complexity by using the level sets of the LB eigenvector corresponding to the first non-trivial eigenvalue. In this method, the differential 1D signed curvature along each level set is computed and weighted by the geodesic distance between each point and two next gyral tops. In this way, it assigns a gyrification index (GI) to each point of the brain surface.

By applying the K-means clustering algorithm on the first few non-trivial LB eigenvectors, Lefèvre et al. 2014 proposed an unsupervised segmentation of brain surface. The results of this segmentation is qualitatively similar to traditional lobar segmentation produced manually from anatomical landmarks such as the central and parieto-occipital sulci. The results reveal a link between anatomical landmarks and the structure of Laplacian eigenvectors that is worth to be explored more. Some evidences of this link can also be seen in the nodal domains-based segmentation (Reuter et al. 2009a ; Reuter 2010) in which the segments are meaningful parts of a surface.

Lombaert et al. 2013b and Lombaert et al. 2013a used the graph Laplacian eigenvectors for surface matching. With these eigenvectors, they employed the spectral correspondence as a regularization for direct matching of surface features. The method was then applied on shape analysis of subcortical structures (Shakeri et al. 2016 ; Shakeri et al. 2014) and longitudinal analysis of the preterm cortex (Orasanu et al. 2016b ; Orasanu et al. 2016a). Jain et al. 2006, MATEUS et al. 2008 and REUTER 2010 also used Laplacian eigenvectors to match articulated surfaces i.e. surfaces with similar shape but different poses e.g. consider two human hands with different bending of fingers.

The Laplacian eigenfunctions are Morse functions [c] and it motivated SHI et al. 2008b and SHI et al. 2008a to use the Reeb graph of Laplacian eigenfunctions to extract stable landmark features as boundary conditions to compute harmonic maps to the unit sphere. They applied this method on mapping three subcortical structures such as Hippocampus, Putamen and Caudate nucleus to unit sphere with a clinical application of deriving the map of local volume losses in the hippocampus of patients with secondary progressive multiple sclerosis.

Laplacian eigenvectors can be also used to introduce a new coordinate system for surfaces. In the literature, it is called "*spectral embedding*" through which a surface is embedded in the spectral domain of its eigenvectors. To do this, LEFÈVRE et al. 2015 has suggested a mapping by using the three first non trivial Laplacian eigenvectors $(\phi_1, \phi_2, \phi_3)$ such that every point $p$ of the surface with Euclidean coordinates $(x_p, y_p, z_p)$ is mapped to the space of these eigenvectors through

$$(x_p, y_p, z_p) \mapsto (\sqrt{\phi_1(p)^2 + \phi_2(p)^2 + \phi_3(p)^2})^{-1}(\phi_1(p), \phi_2(p), \phi_3(p)).$$

This mapping suggests a new representation of surfaces, has the advantage over Euclidean coordinates to be intrinsic to the surface, and accounts for the surface geometry. They also presented some applications of this mapping in simple and fast visualization of brain anatomy, registration of different surfaces and detection of abnormal cortical patterns.

By using an almost similar spectral representation in random decision forests algorithm, LOMBAERT et al. 2015b introduced the spectral forests which has been applied in cortical parcellation. Using the spectral representation instead of Euclidean coordinates, in one hand, enables the random decision forests algorithm to be performed directly on surfaces and improves its accuracy significantly (74% versus 28% Dice overlaps), specially on highly convoluted cortical regions like the medial occipital lobe. On the other hand, the spectral forest gives a parcellation as accurate as FreeSurfer parcellation but in a small fraction of FreeSurfer time (23 seconds vs. 3 to 4 hours).

Laplacian eigenvectors are successfully used in surface analysis for surface embedding, matching and segmentation. They, unlike the Laplacian eigenvalues, cannot be used directly as shape descriptor. Although, topological features of them such as nodal lines/domains introduce shape descriptors. Besides their own feature, they can be used to extract information from functions that are defined on surfaces. In fact, by using Laplacian eigenvectors of a surface, a function that is defined on the surface can be projected to a so-called spectral do-

---

[c] A smooth real-valued function on a manifold $\mathcal{M}$ is a Morse function if it has no degenerate critical points.

main. This projection is called "*eigenfunction projection*" or "*Fourier Transform on graph/mesh*". Our work is based on this projection and we explain it with more details in the following section.

## 2.2. Fourier transform on mesh

In the Euclidean domain, the set of complex exponential functions, $\{e^{-2\pi i\omega}, \omega \in \mathbb{R}\}$, serves as a basis for Fourier transform. These functions are the eigenfunctions of Laplacian operator in this setting. Accordingly, the eigenvectors of the discrete Laplacian can be considered as an extension of the Fourier basis to general manifolds represented by meshes (QIU et al. 2006). In this scenario, a smooth function $f$ which is defined on a surface $S$ can be represented as a linear combination of the surface Laplacian eigenvectors $\{\phi_1, \phi_2, \ldots, \phi_n, , \ldots\}$ :

$$f = w_1\phi_1 + w_2\phi_2 + \ldots + w_n\phi_n + \ldots. \tag{2.5}$$

In this equation, $w_k,\ k = 1, 2, \ldots$ are called *spectral (or Fourier) coefficients* and contain intrinsic geometrical properties of the function $f$ at different scales. The set of $\{|w_k|^2,\ k = 1, 2, \ldots\}$ is called *power (or Fourier) spectrum* and is a representation of function $f$ in the so-called spectral (or Fourier) domain and gives the frequency distribution of this function. An example is given in Fig. 2.2.

A famous example of such spectral basis functions is the spherical harmonics which are the Laplacian eigenfunctions of the unit sphere. In general, due to the fact that the basis of Fourier transform, the complex exponential functions, are the eigenfunctions of Laplacian in Euclidean domain, the Fourier transform on a meshed manifold is defined naturally based on the eigenvectors of the mesh discrete Laplacian. By analogy, the Laplacian eigenvalues and eigenvectors are interpreted as natural frequencies and vibration modes of the surface. This interpretation encourages us to benefit form the power of classical Fourier analysis in a mesh/graph setting.

The distinction between the discrete Laplacian based and classical Fourier transforms is that in the latter case, one uses a fixed family of basis functions while in discrete Laplacian based setting, the eigenvectors that are used as Fourier bases change depending on geometry of manifold (ZHANG et al. 2007a). For neuroanatomical surfaces with spherical topology, however, it is possible to fix the bases by using spherical harmonics after a spherical parametrization of the manifold. The ease of computation of spherical harmonics has motivated much research, especially for neuroanatomical surface representation and reconstruction ; see for example GU et al. 2004, CHUNG et al. 2007, YOTTER et al. 2010 and YOTTER et al. 2011.

Although, since the Laplace-Beltrami eigenfunctions reflect the intrinsic geometry of the manifold, using them as Fourier bases outperforms the conventio-

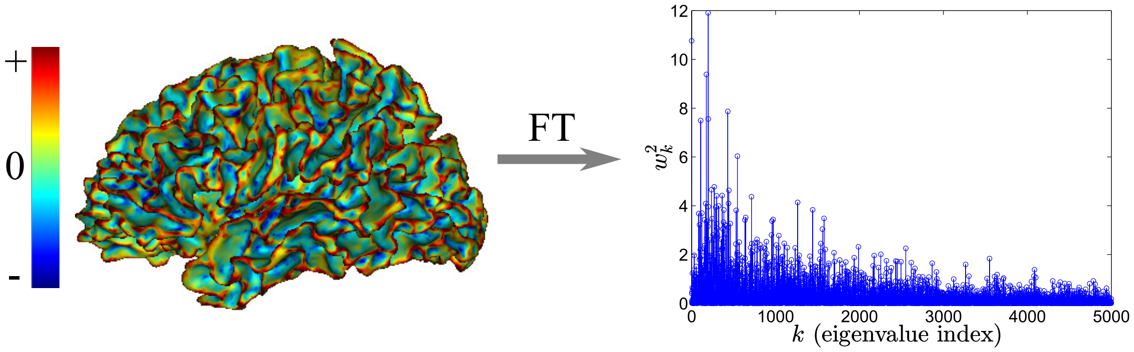

Figure 2.2.: Left : A function that is defined on a brain surface. Right : By applying the Fourier transform (FT) on this function, its power spectrum is computed. This is actually a representation of this function in the spectral domain. See Eq. (2.5) and the explanations after that.

nal spherical harmonics in terms of reconstruction accuracy and compactness ; at least for reconstruction of the cortical surface and amigdala (Seo et al. 2011). Moreover, in reconstruction of hippocampus surfaces, Shi et al. 2010 have shown that the Laplace-Beltrami eigenfunctions produce smooth, more detailed and more naturally looking surfaces than the spherical harmonics by not generating the artificial oscillation visible in the spherical harmonic results. Finally, as it is pointed out by Germanaud et al. 2012 "*this approach has the advantage of a direct processing of native data without non linear alignment and spherical parametrization steps.*"

The spectral decomposition of Eq. (2.5) can be used to reconstruct a function $f$ from spectral weights. In this case, the squared Fourier coefficient $|w_k|^2$, also known as *spectral power*, can be interpreted as the contribution of $k$-th Laplacian eigenvector $\phi_k$ on reconstructing $f$. A trivial application of this reconstruction is in smoothing (denoising) the function $f$ by truncating the composition (2.5) on a specific order while only the eigenfunctions corresponding to low frequencies are kept. In this way, by truncating the composition in different orders, different levels of smoothing can be achieved (Qiu et al. 2006 ; Lombaert et al. 2015a). As an interesting example, if the function $f$ is the coordinates of points of a surface, applying this method smooths the surface ; see Fig. 2.3 as an example of spectral smoothing of a brain surface and a functional map.

The weights of spectral decomposition (2.5) can be potentially used for surface comparison and matching but due to ambiguities of eigenfunction ordering across surfaces, it is not possible to use those weights directly. Lombaert et al. 2015a proposed an optimal spectral transformation of spectral weights between surfaces. Basically, the spectral decomposition weights of a surface are in a space that is spanned by the eigenvectors of this surface. This transformation defines a change of basis so that the decomposition weights of this surface can be transla-

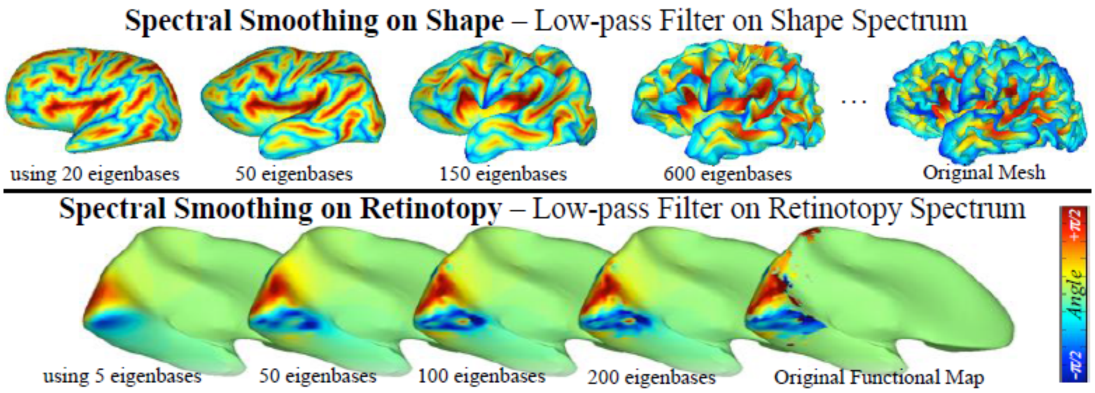

Figure 2.3.: (Top) Spectral smoothing of a brain surface by using 20 to 600 Laplacian eigenfunctions. As the number of eigenfunctions decreases, complex geometry of the surface disappear and the surface becomes smoother. The colormaps shows the sulcal depth. (Bottom) Spectral smoothing of fMRI map by using 20 to 600 Laplacian eigenfunctions. Here the function $f$ is a fMRI map of a visual task represented on the occipital lobe (Retinotopy). As the number of eigenfunctions decreases, the fMRI map becomes smoother. The figure is adopted from Lombaert et al. 2015a.

ted to another surface.

If an appropriate function $f$ is defined on a surface, the Fourier transform of $f$ provides tools to extract geometric information of the surface. In this direction, GERMANAUD et al. 2012 applied the Fourier transform to the mean curvature function of the brain surface to study the brain folding patterns. It transforms the mean curvature from a spatial domain of brain surface to the spectral domain of the first 5000 Laplace-Beltrami eigenvectors and generates a power spectrum. Then, the power spectrum is partitioned into seven spectral bands (B0-B6). A scheme of this method is shown in Fig. 2.4.

In the next step, the contribution of each band to synthesis of the mean curvature value at each vertex is computed. They observed that the contribution of the last 3 bands (i.e. B4, B5 and B6) to the total analysed spectral power is about 93% and they are associated with variations of fold patterns while the first bands reflect the global shape of the brain. Now, two synthesis strategies can be considered : non-cumulative or cumulative syntheses. In non-cumulative synthesis, that is equivalent to a band-pass filtering, each vertex is labelled by the number of the band that has the most contribution to synthesis of the mean curvature value. In cumulative synthesis, that is equivalent to low-pass filtering, each vertex is labelled by the number of the band that determines whether it belongs to the sulcal or gyral pattern. This determination is given by the differential contribution between two consecutive bands e.g. B6-B5 (Fig. 2.5).

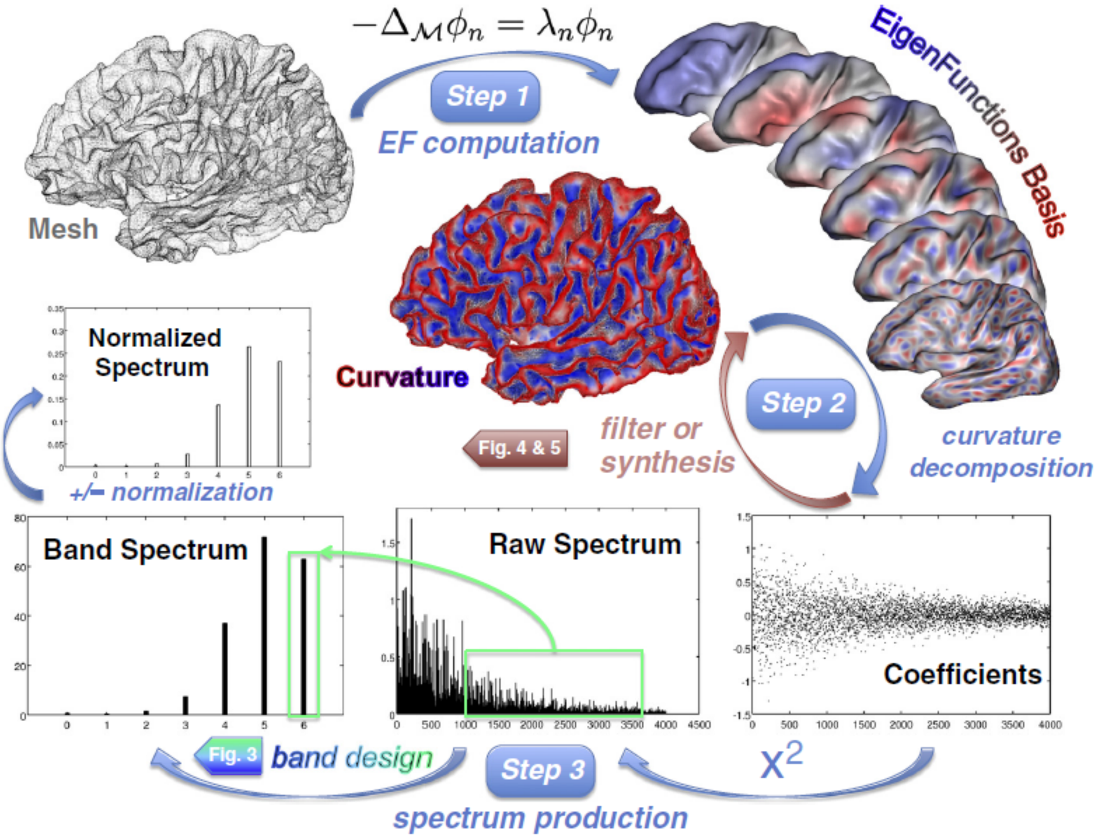

Figure 2.4.: A scheme of the SPANGY method suggested by Germanaud et al. 2012. From a mesh that represents the brain surface (in top left), the mean curvature function and Laplacian eigenvectors are computed (step 1). Then, the mean curvature function is decomposed by Laplacian eigenvectors as in Eq. 2.5 to produce the raw power spectrum (step 2). Finally, the raw power spectrum is binned into 7 bands that contain spectral information of mean curvature function and folding pattern. This figure is adopted from Germanaud et al. 2012.

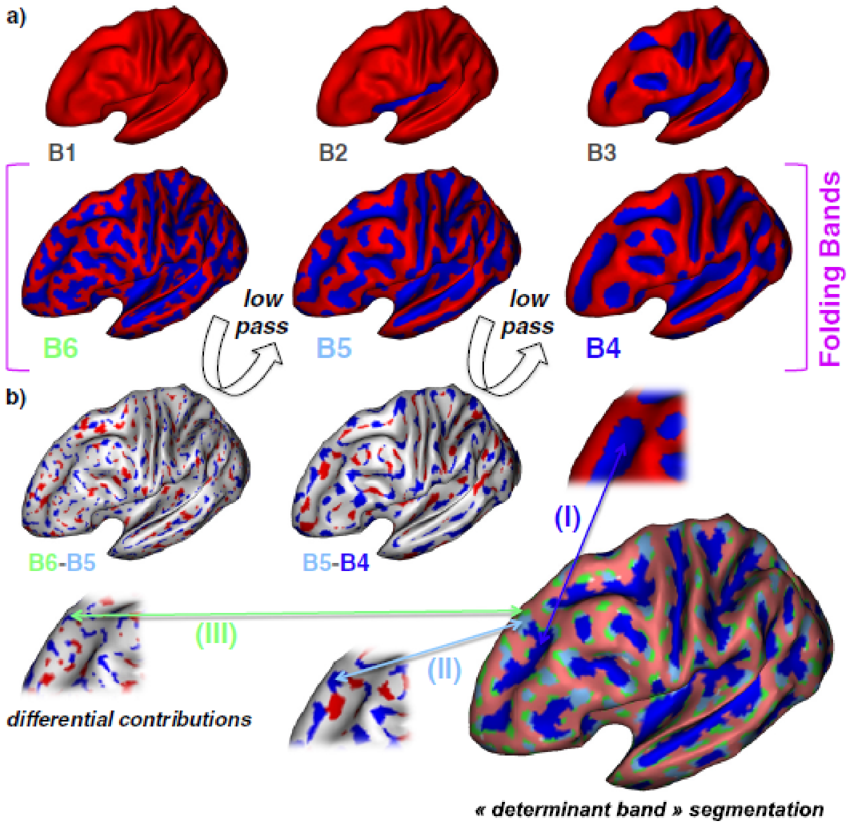

Figure 2.5.: Spectral parcellation of sulcal regions by determinant band strategy of SPANGY method. (a) Low-pass filtered mean curvature series, started from B6, with the 6 spectral bands (B1 to B6). The colormaps reflects the position of each point on gyri (red) or sulci (blue) resulted from low-pass filtering. (b) Differential contribution of two consecutive bands together with zoom on the vicinity of 3 points. The map on the right shows a cortical segmentation given by the dominant band color. The map is shown on a smoothed brain surface with a gyral mask (salmon red). This figure is adopted from Germanaud et al. 2012.

Both strategies give parcellations of brain surface into segments that are comparable to the developmentally-defined segmentation as the primary, secondary and tertiary folds. Indeed, in those maps, parcels with B4 labels overlap with primary folds like the central and superior temporal sulci while parcels with B5 and B6 labels coincide with remifications and kinks. The connection between the spectral bands and the primary, secondary and tertiary folds are supported by the results given by DUBOIS et al. 2016. Moreover, by using this method, they suggested 4 folding stages at the individual level during fetal to early post-natal ages. In case of pathologies, the analysed total spectral power, the power of B4, B5 and B6 bands and the count of primary, secondary and tertiary parcels resulted from cumulative strategy are successfully employed in allometric modellings to study the effect of microcephalies related to ASPM, PQBP1 and fetal alcohol syndrom (GERMANAUD et al. 2014).

Fourier analysis is local in the spectral domain but global in the spatial domain. In other words, it doesn't provide spectral information of functions in a spatial neighbourhood of a surface point. The spectral powers encode global information of the function and don't reflect its local behavior. Post-processing of spectral powers, however, might give some local information (GERMANAUD et al. 2012). Nevertheless, for functions that contain highly varying local information, it may be better to use a local analysis. Fortunately, some local spectral analyses have been developed in the literature in continuous and discrete domains. Among them, the windowed Fourier transform is a direct extension of the standard Fourier transform to local manner. In the next section, this method is explained completely and we will use it in our proposed surface complexity analysis.

## 2.3. Windowed Fourier Transform

Lef $f$ be a function defined on a surface $\mathcal{S}$. The mesh Fourier transform described in Section 2.2 gives a global frequency distribution of this function ; see Fig. 2.2 for an example. In order to find the local frequency distribution of a 1D function $f$ defined in $\mathbb{R}$, the windowed Fourier transform was introduced (GABOR 1946). In this method, $f$ is localized around a point $t$ in its domain by using a window function $g$. So the localized version of $f$ around point $t$ is : $f_t(u) = g(u-t)f(u)$. Now, the Fourier transform of $f_t$ is computed and gives Fourier coefficients as

$$\hat{f}(\omega, t) = \mathcal{F}(f_t(u)), \tag{2.6}$$

where $\mathcal{F}$ denotes the Fourier transform and $\omega$ is the frequency component. Accordingly, Fourier coefficients $\{\hat{f}(\omega, t)\}$ give local information about $f$ simultaneously in its original domain and frequency domain. We explain this method for a 1D continuous function $f(t)$ defined on the real line $\mathbb{R}$ adopted mostly from KAISER 2011.

**Example 1.** $f(u) = \sin(\pi u^2)$ is a chirp function defined on the real line $\mathbb{R}$ ; see Fig. 2.6a. This function has an instantaneous frequency $\omega_{\text{inst}}(u)$ which is given by the derivative of its phase :

$$2\pi\omega_{\text{inst}}(u) = \frac{d(\pi u^2)}{du} = 2\pi u. \tag{2.7}$$

Fourier coefficients of function $f$ is computed by

$$\hat{f}(\omega) := \mathcal{F}(f(t)) = \int_{-\infty}^{\infty} e^{-2\pi i\omega u} f(u)du. \tag{2.8}$$

The distribution of frequency powers $\{|\hat{f}(\omega)|^2,\ \omega \in \mathcal{R}^{\geq 0}\}$ of the chirp function is represented in Fig. 2.6b. The Fourier analysis computes the frequency components of function $f$ over the whole domain and accordingly, as it is clear in the figure, it hides the fact that $f$ has a well-defined instantaneous frequency.

To know the frequency distribution of $f$ around a specific point $t$, first we localize $f$ around this point by using a window function. Here, the Gaussian function $g(u) = (\frac{2}{a})^{1/4}\exp(-\pi a u^2)$ is considered as the window function. Originally, $g$ is centered at origin but when it is translated to the point $t$, its energy is concentrated around this point. For instance, Fig. 2.7a shows the translated window function with $a = 1$ to $t = 4$ i.e. $g(u - 4)$.

The localized version of $f$ around $t = 4$ is then given by $f_4(u) = g(u-4)f(u)$ ; see Fig. 2.7b. The Fourier transform of $f_4$ is now computed and its power spectrum is shown in Fig. 2.7c. It is seen that the energy of frequencies is concentrated around $\omega = 4$, consistent (although not exact) with instantaneous frequency of $f$ (i.e. $\omega_{\text{inst}}(4)$ which is equal to 4).

The spectrogram of chirp function that represents frequency distribution over spatial coordinate is shown in Fig. 2.8a. Now, from this spectrogram, it is clear that the local frequency of $f$ increases with $u$ while it was not detectable from global frequency distribution of Fourier transform ; compare Figs. 2.8a and 2.6b.

As it is seen in Fig. 2.7c, the obtained frequency components is not exactly equal to the true frequency $\omega_{\text{inst}}(4) = 4$ but the frequency distribution contains some other frequencies around $\omega_{\text{inst}}$. In fact, due to the Heisenberg's Uncertainty Principle, it is not possible to have sharp localizations in spatial domain and in frequency domain at the same time (Kaiser 2011). In other words, if $T$ is the spread of window function in spatial domain and $\Omega$ is that in frequency domain, $T$ is proportional to $\Omega^{-1}$. Mathematically speaking, there is a constant $c$ such that

$$T\Omega \geq c. \tag{2.9}$$

In the mentioned Gaussian window function $g$, parameter $a$ controls the spread of window function and is called "window size". So, a smaller window size gives a tighter localization in spatial domain which results in a wider frequency distribu-

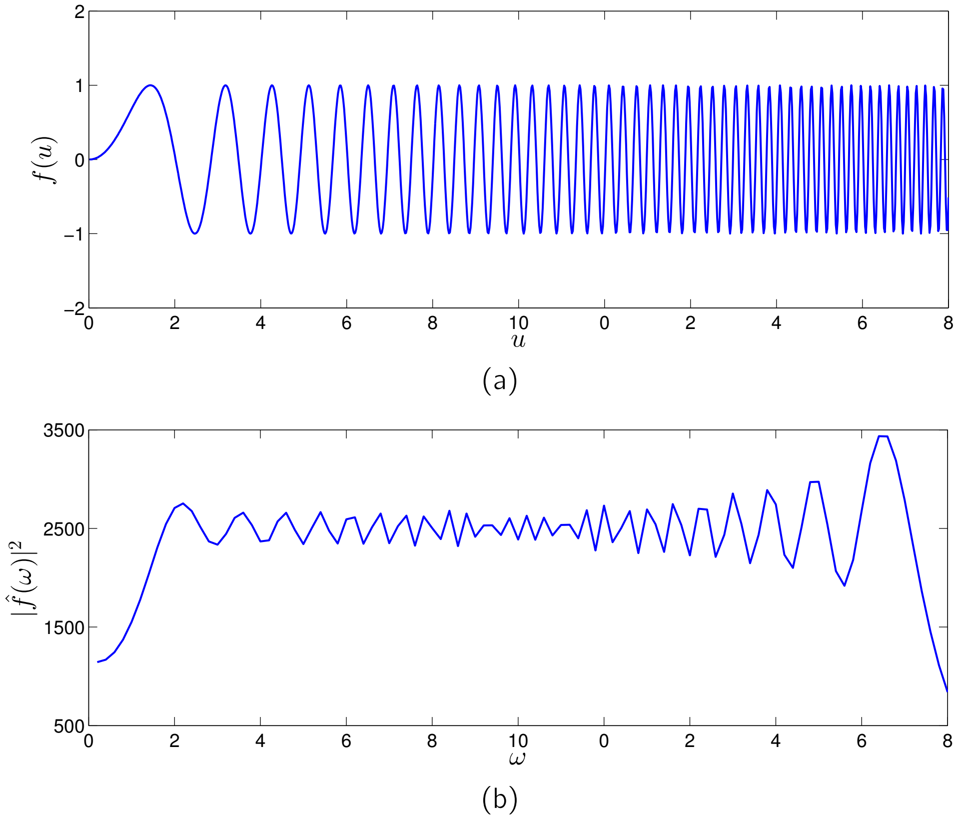

Figure 2.6.: (a) Chirp function : $f(u) = \sin(\pi u^2)$. It is seen that the local frequency of $f$ increases with $u$. (b) The power spectrum of $f$ is given by its Fourier coefficients and shows the *global* frequency distribution of $f$. From this distribution, however, it is not possible to detect the special frequency behaviour of $f$.

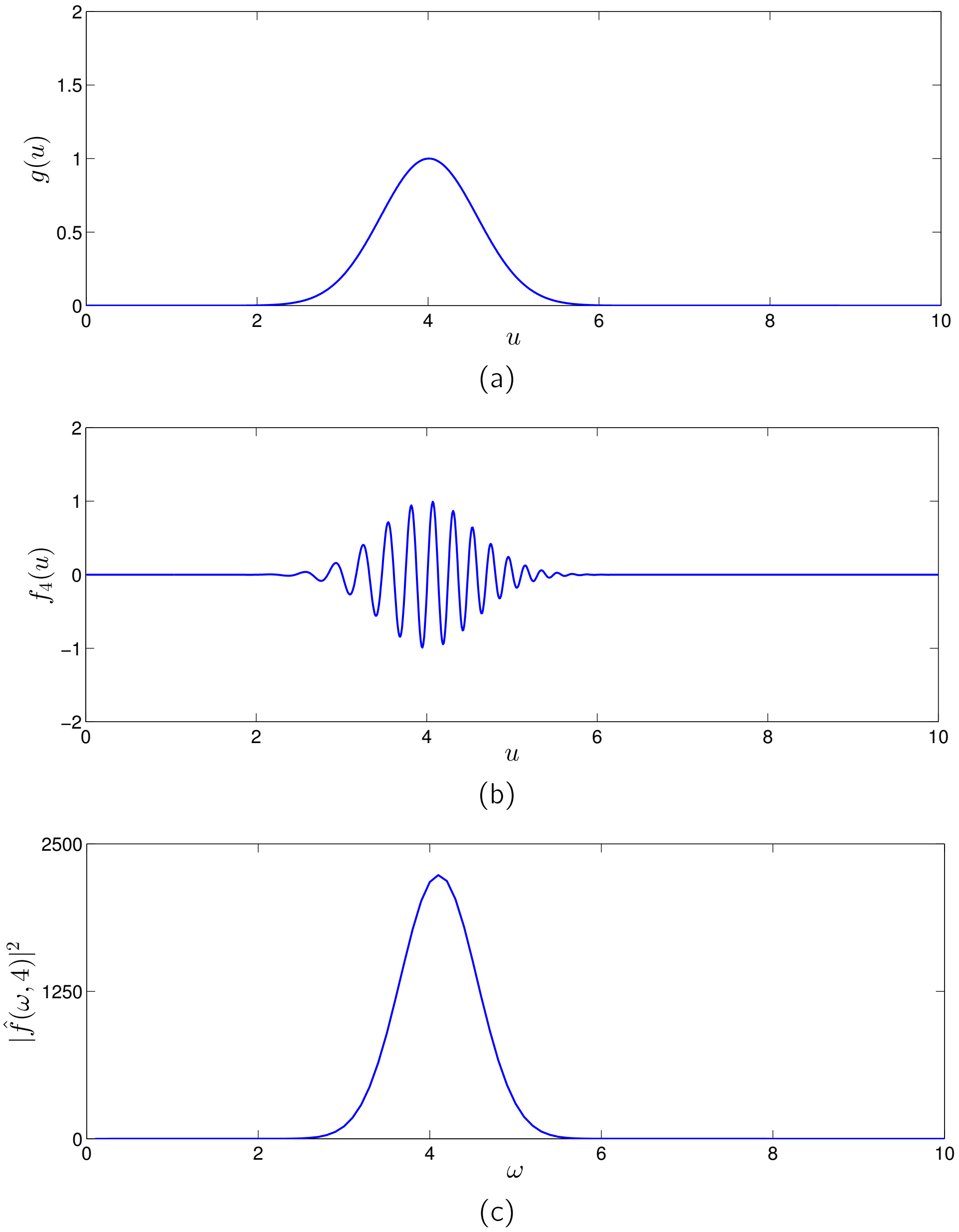

Figure 2.7.: (a) Translation of window function $g(u)$ to $u = 4$. (b) $f_4(u)$ : Localized version of the original function $f$ shown in Fig. 2.6a around $u = 4$. (c) $\hat{f}(\omega, 4)$ : Power spectrum of $f_4$. It is seen that the power of frequencies is concentrated around instantaneous frequency $\omega_{\text{inst}} = 4$.

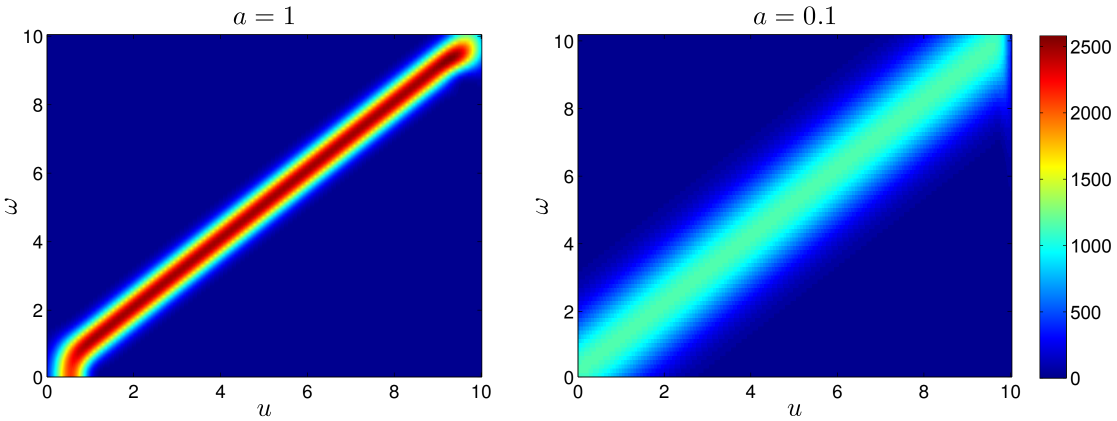

(a) (b)

Figure 2.8.: (a) spectrogram of $f$ with window size $a = 1$. Right : spectrogram of $f$ with a tighter window $a = 0.1$. See Fig. 2.9a to compare window spreads in spatial domain. It is seen that using a tighter window in spatial domain (i.e. smaller window size) results in a wider frequency distribution.

tion.

For instance, for the chirp function, if we set the window size as $a = 0.1$, a tighter window is achieved in spatial domain in comparison to a window with the size $a = 1$ (Fig. 2.9a), then the function is more localized around $t = 4$ (Fig. 2.9b) but a wider frequency distribution is obtained in spectral domain (Fig. 2.9c). The spectrograms derived from these two windows can be compared in Fig. 2.8. It is clear that using a tighter window in spatial domain gives a wider distribution of frequencies. It means that if we focus more in spatial domain, we get less accurate results in frequency domain. On the other hand, if we choose a very wide window, what we get is something like the ordinary Fourier transform.

There are a wide range of functions that can serve as a window. However, it has been shown that the Gaussian function is the unique window that optimizes the locality trade-off between spatial and frequency domains i.e. the inequality (2.9) becomes equality (MALLAT 2008, Theorem 2.5).

### 2.3.1. Extension to graphs

SHUMAN et al. 2016 have recently extended the windowed Fourier transform to graph setting which enables us to do a "*vertex-frequency analysis*" of a function that is defined on the vertices of a graph. Akin to continuous case, the general idea of this method is to localize the function around a vertex by a translated window function and then, compute the graph Fourier transform of this localized function.

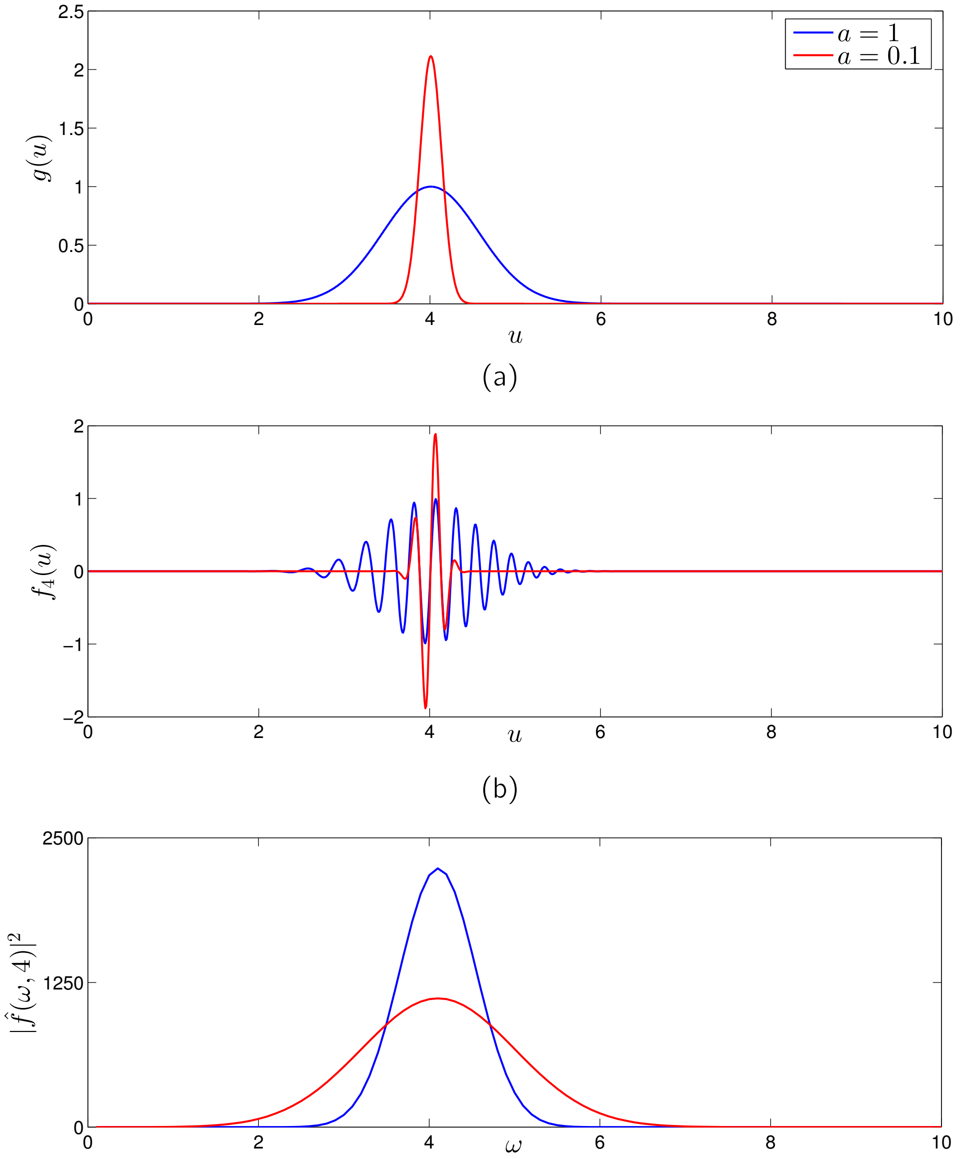

(a)

(b)

(c)

Figure 2.9.: The effect of window size on analysis. Blue and red curves are corresponding to window sizes $a = 1$ and $0.1$ respectively. (a) Translation of window function $g(u)$ to $u = 4$. For smaller $a$, the window is tighter. (b) $f_4(u)$ : Localized version of the original function $f$ shown in Fig. 2.6a around $u = 4$. It is seen that by using a tighter window, $f$ is more localized. (c) $\hat{f}(\omega, 4)$ : Power spectrum of $f_4$. It is seen that : 1) The power of frequencies is concentrated around instantaneous frequency $\omega_{\text{inst}} = 4$ ; 2) The frequency distribution is more spread for tighter window (red curve).

The main problem in graph setting, in comparison to continuous setting, is that the translation of a function on a graph is not trivial. In fact, the vertices are spread in space with no trivial origin and ordering direction. To define a translation operator in vertex domain, SHUMAN et al. 2016 took advantage of properties of convolution with Dirac delta.

Starting from continuous setting, for functions $f, g \in L^2(\mathcal{R})$, the classical convolution $h = f * g$ is defined as

$$h(u) = (f * g)(u) := \int_{\mathcal{R}} f(\tau) g(u - \tau) d\tau. \tag{2.10}$$

Two nice properties of convolution is that :

1. The Fourier transform of $h$ is the production of Fourier transforms of $f$ and $g$ i.e. $\hat{h} = \hat{f}\hat{g}$. As a result, from the definition of inverse Fourier transform, we get

$$h(u) = (f * g)(u) := \int_{\mathcal{R}} \hat{h}(\omega) e^{2\pi i \omega u} d\omega = \int_{\mathcal{R}} \hat{f}(\omega)\hat{g}(\omega) e^{2\pi i \omega u} d\omega. \tag{2.11}$$

2. Translation of any function $g \in L^2(\mathcal{R})$ can be computed by the convolution of $g$ with Dirac delta i.e.

$$(T_t g)(u) := g(u - t) = (g * \delta_t)(u). \tag{2.12}$$

From Eq. (2.11), we get

$$\begin{aligned} (T_t g)(u) := (g * \delta_t)(u) &= \int_{\mathcal{R}} \hat{g}(\omega)\hat{\delta}_t(\omega) e^{2\pi i \omega u} d\omega & (2.13)\\ &= \int_{\mathcal{R}} \hat{g}(\omega) e^{-2\pi i \omega t} e^{2\pi i \omega u} d\omega. & (2.14) \end{aligned}$$

By analogy[d], for any function $g$ defined on vertices $\{P_1, P_2, \ldots, P_N\}$ of a graph, a generalized translation of $g$ to an arbitrary vertex $P_i$ is defined by

$$(T_i g)(n) := \sqrt{N}(g * \delta_i)(n) = \sqrt{N} \sum_{l=1}^{N} \hat{g}(l)\phi_l(i)\phi_l(n), \tag{2.15}$$

where $\phi_l$'s are graph Laplacian eigenvectors. By using this operator, a window function $g$ can be translated to any vertex $P_i$. Now, the localized version of a function $f$ around vertex $P_i$ is computed by $f_i(n) = f(n) \times (T_i g)(n)$. Finally, the Fourier coefficients of $f_i$ can be computed as usual :

$$Sf(i, k) = \langle f_i, \phi_k \rangle, \qquad i, k = 1, 2, \ldots, N. \tag{2.16}$$

Theoretical aspects of the method together with some examples of signal pro-

---

[d] We remind that $e^{-2\pi i \omega u}$ is Fourier basis in continuous 1D setting.

cessing on graphs are given by SHUMAN et al. 2016. We use this method for surface complexity analysis where surfaces are modelled by triangular meshes. For this purpose, we extend the method to mesh setting through replacing the graph Laplacian by a geometric Laplacian which convey geometrical information of the underlying mesh, thus is more appropriate for surface analysis. The details are given in the next section.

## 2.4. Mesh windowed Fourier transform

In this thesis, we extend the graph windowed Fourier transform to mesh framework by using geometric Laplacian eigenvectors that account for the surface geometry. Since a mesh is a special kind of a graph, embedded in a surface, one may argue that the graph spectral theory tools can be applied on a mesh without any adaptation. In general, it is true but unlike the graph Laplacian in which only the connectivity of vertices are considered, the geometric Laplacian takes into account geometric properties of the surface. Moreover, as ZHANG et al. 2007a pointed, the geometric Laplacian approximates the continuous Laplace-Beltrami operator for Riemannian manifolds more accurately than the graph Laplacian. More discussions and comparisons between the graph Laplacian and the geometric Laplacian can be found in LEVY 2006 ; WARDETZKY et al. 2007 ; PEINECKE et al. 2007 ; REUTER et al. 2009a ; HAMMOND et al. 2011 ; TAN et al. 2015. In the following section, a geometric Laplacian is presented through the finite element discretization of Laplace-Beltrami operator.

### 2.4.1. Discretization of Laplace-Beltrami operator

For a compact Riemannian manifold $\mathcal{S}$ e.g. a 2D surface in $\mathbb{R}^3$, one can consider a set of square integrable functions defined on the surface : $\mathcal{L}^2(\mathcal{S}) = \{u : \mathcal{S} \to \mathbb{R} | \int_{\mathcal{S}} u^2 < \infty\}$. The Laplace-Beltrami operator $\Delta$, associated with the surface $\mathcal{S}$, is defined as a combination of the gradient and divergence operators, i.e. $\Delta = \mathrm{div} \circ \mathrm{grad}$ and is a generalization of the Laplacian operator in Euclidean space to Riemannian manifolds. The spectrum of this operator $\{(\lambda_k, u_k) \in \mathbb{R}^+ \times \mathcal{L}^2(\mathcal{S}), k = 1, 2, \dots\}$ is generated by solving the differential eigenvalue problem of $\Delta$ :

$$\Delta u_k = -\lambda_k u_k, \tag{2.17}$$

in which $\lambda_k$ and $u_k$ are called the $k$th-eigenvalue and eigenfunction of $\Delta$ (BERGER 2003). The spectral theory based on the Laplace-Beltrami spectrum can be used to obtain a new representation of the space $\mathcal{L}^2$ in the so called spectral domain. To solve the differential eigenvalue problem of $\Delta$ for a general surface, the surface is discretized followed by a discretization of Eq. (2.17).

**Finite element discretization.**

Here, we use the linear finite (FE) element method (Reuter et al. 2009a) to discretize the continuous differential eigenvalue equation (2.17). To do so, first the weak form of this equation is derived :

$$\langle \Delta u_i, \psi_j \rangle = -\lambda_i \langle u_i, \psi_j \rangle, \qquad \forall \psi_j \in \mathcal{L}^2(\mathcal{S}), \tag{2.18}$$

where $\langle ., . \rangle$ denotes the Euclidean inner product of $\mathcal{L}^2(\mathcal{S})$, i.e. $\forall u, v \in \mathcal{L}^2(\mathcal{S}) : \langle u, v \rangle = \int_{\mathcal{S}} uv$. Now, by using the Green Formula we obtain

$$\langle \nabla u_i, \nabla \psi_j \rangle = -\lambda_i \langle u_i, \psi_j \rangle, \qquad \forall \psi_j \in \mathcal{L}^2(\mathcal{S}). \tag{2.19}$$

To derive discretization, let $G = \{V, E\}$ be a triangular mesh modelling the surface $\mathcal{S}$ where $V$ is the set of vertices, $V = \{P_1, P_2, \ldots, P_N\}$, $|V| = N < \infty$ and $E$ is the set of edges. The linear discretized function $\psi_j$ is defined on the mesh vertices such that for every vertex $P_n$, $\psi_j(n) = \delta_{jn}$. In this way, the function $u_i$ can be interpolated by a linear combination of $\psi_j$'s :

$$u_i \simeq \phi_i = \sum_{k=1}^{N} \phi_{ki} \psi_k \qquad \text{where} \quad \phi_{ki} = u_i(k). \tag{2.20}$$

Now, by substituting the interpolant of Eq. (4.37) in the weak form (2.19), we get

$$\sum_{k=1}^{N} \phi_{ki} \langle \nabla \psi_k, \nabla \psi_i \rangle = -\lambda_i \sum_{k=1}^{N} \phi_{ki} \langle \psi_k, \psi_j \rangle, \tag{2.21}$$

where $\langle ., . \rangle$ denotes the Euclidean inner product of $l^2(G)$ :

$$l^2(G) = \{u : G \to \mathbb{R} | \sum_{i=1}^{N} u^2(i) < \infty\} \quad \text{and} \quad \forall u, v \in l^2(G) : \langle u, v \rangle = \sum_{i=1}^{N} u(i) v(i). \tag{2.22}$$

In matrix form, this is equivalent to the following algebraic generalized eigenvalue equation

$$A \phi_i = \lambda_i B \phi_i, \tag{2.23}$$

where $\phi_i = [\phi_{1i}, \phi_{2i}, \ldots, \phi_{Ni}]^T$ and $A$ and $B$ are $N \times N$ sparse matrices with the following elements :

$$A(i,j) = \begin{cases} \frac{\cot \alpha_{ij} + \cot \beta_{ij}}{2} & \text{if } (i,j) \in E, \\ -\sum_{k \in \mathcal{N}(i)} A(i,k) & \text{if } i = j, \\ 0 & \text{o.w.} \end{cases} \tag{2.24}$$

and

$$B(i,j) = \begin{cases} \frac{|t_1| + |t_2|}{2} & \text{if } (i,j) \in E, \\ \frac{\sum_{k \in \mathcal{N}(i)} |t_k|}{6} & \text{if } i = j, \\ 0 & \text{o.w.} \end{cases} \tag{2.25}$$

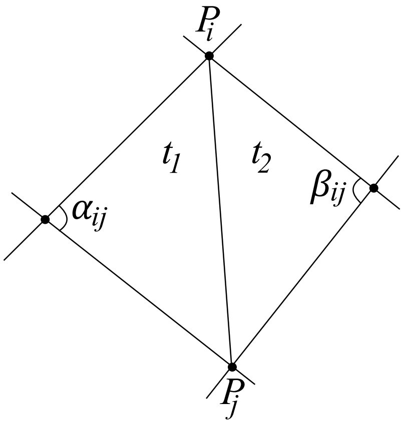

Figure 2.10.: A triangulation with two triangles $t_1$ and $t_2$ that share the edge $P_iP_j$. The angles $\alpha_{ij}$ and $\beta_{ij}$ are those that appear in discretization of Laplace-Beltrami operator by linear FEM ; see Eqs. (2.24) and (2.25).

where $\alpha_{ij}$ and $\beta_{ij}$ are the angles opposite to the edge $P_iP_j$ in two triangles $t_1$ and $t_2$ sharing this edge, $|t_k|$ indicates the area of the triangle $t_k$ and $\mathcal{N}(i)$ denotes the index set of all vertices of the 1-ring neighbourhood of $P_i$.

The matrix $B$ is positive definite and defines the so called $B$-inner product in $\mathbb{R}^N$ :

$$\forall f, g \in \mathbb{R}^N, \quad \langle f, g\rangle_B = f^t B g. \tag{2.26}$$

Solutions of the discrete eigenvalue problem (2.23) are nonnegative real eigenvalues $0 = \lambda_1 < \lambda_2 \leq \ldots \leq \lambda_N$ and a set of eigenvectors $\{\phi_j, j = 1, 2, \ldots, N\}$ in $\mathbb{R}^N$ which are orthonormal with respect to $B$-inner product i.e. $\langle \phi_i, \phi_j\rangle_B = \delta_{ij}$ where $\delta_{ij}$ is Kronecker delta.

**Advantages of FE Laplacian.**

An advantage of using FE Laplacian of a mesh surface is that it is convergent to the Laplace-Beltrami operator of the surface. Formally, Let $h$ be the mesh size i.e. the longest edge of the mesh. By decreasing $h$, the approximated eigenvalues and eigenvectors through linear FE scheme converge to their exact values i.e. those of the Laplace-Betrami operator with orders 2 and 1, respectively. Upper bounds of the approximation errors are given in the following theorem (STRANG et al. 1973) :

**Theorem 2.** *Let $(\tilde{\lambda}_i, \phi_i)$ be the approximation of $(\lambda_i, u_i)$ computed by linear FEM. Then*

$$\lambda_i \leq \tilde{\lambda}_i \leq \lambda_i + 2\gamma h^2 \lambda_i^2, \tag{2.27}$$

$$\|u_i - \phi_i\|_2 \leq C h^2 \lambda_i, \tag{2.28}$$

*where $\gamma$ and $C$ are constants.*

Another advantage of FE Laplacian of a mesh surface is that it accounts for the geometry of the mesh. In fact, the surface area and angles of mesh elements appeared in matrices $A$ (2.24) and $B$ (2.25) show how the geometry of neighbouring triangles on the mesh contributes to the definition of Laplacian operator.

**Mesh Fourier transform.**

Now, the FE Laplacian eigenvectors can be used to define the Fourier transform on a mesh. Given a function $f$ defined on the vertices of a mesh, Fourier transform coefficients of $f$ are given by the set

$$\hat{f}(l) := \langle f, \phi_l \rangle_B, \qquad l = 1, 2, \ldots, N \tag{2.29}$$

In this setting, the Parseval's identity is

$$\langle f, g \rangle_B = \langle \hat{f}, \hat{g} \rangle, \tag{2.30}$$

where $\langle ., . \rangle$ denotes the Euclidean inner product. It yields $\|f\|_B = \|\hat{f}\|_2$ where $\|.\|_B := \sqrt{\langle ., . \rangle_B}$ is the norm induced by the $B$-inner product.

In following, we prove a lemma explaining the interaction between the mesh Fourier transform and the FE Laplacian.

**Lemma 1.** *Let $f \in \mathbb{R}^N$ be a function defined on the vertices of a triangulation and $L \in \mathbb{R}^{N \times N}$ be the discrete Laplace-Beltrami operator i.e. $L = B^{-1}A$. Then, the Fourier coefficients of the function $y = Lf$ are $\hat{y}(l) = \lambda_l \hat{f}(l),\ l = 1, 2, \ldots, N$.*

*Proof.* The Fourier coefficients of $y$ are as

$$\begin{aligned}
\hat{y}(l) := \langle Lf, \phi_l \rangle_B &= f^t (B^{-1}A)^t B \phi_l \\
&= f^t \lambda_l B \phi_l \qquad (2.31) \\
&= \lambda_l \langle f, \phi_l \rangle_B \qquad (2.32) \\
&= \lambda_l \hat{f}(l),
\end{aligned}$$

where Eq. (2.31) is given by Eq. (2.23) and the symmetry of matrices $A$ and $B$, and the definition of $B$-inner product (2.26) gives (2.32). ☐

We will use the above lemma later to prove that our proposed gyrification indices quantify exactly the definitions of the surface complexity. It also enables us to compute the norm of the FE Laplacian $L$. To this end, we prove the following theorem.

**Theorem 3.** *For discrete Laplace-Beltrami operator $L \in \mathbb{R}^{N \times N}$, we have $\|L\|_B = \|L\|_2 = \lambda_N$.*

*Proof.* By definition of matrix norm we have

$$\begin{aligned}\|L\|_B &= \sup_{\|u\|_B=1} \|Lu\|_B \\ &= \sup_{\|\hat{u}\|_2=1} \|\widehat{Lu}\|_2 \qquad (2.33) \\ &= \sup_{\|\hat{u}\|_2=1} \left(\sum_{l=1}^{N} \lambda_l^2 \hat{u}_l^2\right)^{1/2}, \qquad (2.34)\end{aligned}$$

where (2.33) and (2.34) are derived from Parseval's identity and Lemma 1 respectively. Since the eigenvalues of $L$ are ordered increasingly, $0 = \lambda_1 \leq \lambda_2 \leq \ldots \leq \lambda_N$, one can write

$$\begin{aligned}\sup_{\|\hat{u}\|_2=1} \left(\sum_{l=1}^{N} \lambda_l^2 \hat{u}_l^2\right)^{1/2} &\leq \lambda_N \sup_{\|\hat{u}\|_2=1} \left(\sum_{l=1}^{N} \hat{u}_l^2\right)^{1/2} \\ &= \lambda_N. \qquad (2.35)\end{aligned}$$

On the other hand, we know that $\hat{\phi}_N = \delta_N$ where $\delta_N$ is Kronecker delta. So $\hat{\phi}_N = [0, 0, \ldots, 0, 1] \in \{u \in \mathbb{R}^N : \|\hat{u}\|_2 = 1\}$ and

$$\begin{aligned}\sup_{\|\hat{u}\|_2=1} \left(\sum_{l=1}^{N} \lambda_l^2 \hat{u}_l^2\right)^{1/2} &\geq \left(\sum_{l=1}^{N} \lambda_l^2 \hat{\phi}_N(l)^2\right)^{1/2} \\ &= \lambda_N. \qquad (2.36)\end{aligned}$$

Inequalities (2.35) and (2.36) together with (2.34) give $\|L\|_B = \lambda_N$. Since $L$ is symmetric, $\|L\|_2 = \lambda_N$ as well. ☐

### 2.4.2. Window function and translation operator

Now we extend the window Fourier transform from graph setting to mesh setting by exploiting the eigenvalues and eigenvectors of FEM Laplacian operator computed in the previous section. Let $f : V \to \mathbb{R}$ be a function defined on the vertices of a mesh. To localize this function around a specific vertex, we need a window function with local support and a translation operator to move the window function to that specific vertex. Following Shuman et al. 2016, we consider the window function

$$\hat{g}(l) = C \exp(-\tau \lambda_l), \qquad (2.37)$$

defined in the spectral domain. In this formula, $\tau$ is a parameter which determines the size of the window, $\lambda_l$ is the $l$-th Laplace-Beltrami eigenvalue and $C$ is chosen such that $\|\hat{g}\|_2 = 1$.

The window size parameter $\tau$ sets a locality trade-off between the frequency and spatial domains (SHUMAN et al. 2016 ; KAISER 2011). By increasing the window size, we will have a wider window in the spatial domain and the function $f$ will be localized in a larger neighbourhood around each vertex. On the other hand, we will obtain more local frequency distribution of the function in that neighbourhood. The spread of window function in spatial and frequency domains is measured by the area of the Heisenberg box (MALLAT 2008, Section 4.2, SHUMAN et al. 2016, Section 6.6). It is proved that the Gaussian function is the unique window that minimizes the area of the Heisenberg box (MALLAT 2008, Theorem 2.5). Since $\lambda_l$ is proportional to the square of the spatial frequency (GREBENKOV et al. 2013 ; GOLBABAI et al. 2012), i.e. $\lambda_l \propto \omega_l^2$, the window function (2.37) corresponds to a Gaussian function in the frequency domain $\hat{g}(l) \propto \exp(-\tau\omega_l^2)$.

Akin to graph setting, the fact that there is no canonical origin and direction on a triangulated mesh makes it non trivial to define a translation operator. Nevertheless, the translation operator of graphs, given by graph convolution operator Eq. (2.15), can be extended to mesh setting through some modifications to take into account the orthogonality of FE Laplacian eigenvectors (2.26).

In the following, we obtain the translation operator on mesh setting without using the convolution operator. In this way, the translation operator is constructed with inspiration from the properties of the generalized Fourier transform in continuous domain. More precisely, let $\{\phi_l, l = 1, 2, \ldots\}$ be the basis of the generalized Fourier transform in continuous domain and assume that those functions are orthonormal with respect to a function $\psi$ i.e. $\langle\phi_l, \phi_k\rangle = \int \phi_l \psi \phi_k = \delta_{kl}$. From the properties of the generalized Fourier transform, translation in spatial domain causes a modulation in the Fourier domain :

$$h(x) = g(x - x_0) \quad \Leftrightarrow \quad \hat{h}(k) = \phi_k(x_0)\psi(x_0)\hat{g}(k). \tag{2.38}$$

In other words, the translation of function $g$ to point $x_0$ is given by the inverse Fourier transform of the modulated Fourier coefficients $\hat{g}$ :

$$\begin{aligned}(T_{x_0}g)(x) \;&:=\; g(x - x_0) \\ &=\; \mathcal{F}^{-1}\{\phi_k(x_0)\psi(x_0)\hat{g}(k)\},\end{aligned} \tag{2.39}$$

where $\mathcal{F}^{-1}$ denotes the inverse Fourier transform.

In mesh setting, the Fourier basis is the set of Laplace-Beltrami eigenvectors $\{\phi_l, l = 1, 2, \ldots, N\}$ which are orthonormal with respect to the matrix $B$. If $g$ is a function defined on vertices of mesh, inspired by Eq. (2.39), the translation of $g$ to vertex $P_i$ is defined as

$$(T_i g)(n) \overset{(2.39)}{:=} \sqrt{N}\mathcal{F}^{-1}\{(B(i,:)\phi_l)(n)\hat{g}(l)\} \tag{2.40}$$

$$= \sqrt{N}\sum_{l=1}^{N}\sum_{m=1}^{N}\phi_l(n)\Big(B(i,m)\phi_l(m)\hat{g}(l)\Big), \tag{2.41}$$

where $B(i,:)$ denotes the $i$-th row of $B$.

Eventually, the translation operator on a triangular mesh is defined as,

$$\begin{aligned} T_i : \mathbb{R}^N &\to \mathbb{R}^N \quad i = 1, 2, \dots, N, \\ (T_i g)(n) &:= \sqrt{N} \sum_{l=1}^{N} \sum_{m=1}^{N} \left( \hat{g}(l) B(i,m) \phi_l(m) \phi_l(n) \right). \end{aligned} \tag{2.42}$$

The translation operator $T_i$ shifts the center of the window function $g$ to vertex $P_i$. In other words, $(T_i g)(n)$ is the value of $P_i$-centered window function at vertex $P_n$. We note again that the same translation operator on mesh setting can be constructed through the mechanism proposed by SHUMAN et al. 2016 along with some modifications for orthogonality of FE Laplacian eigenvectors.

**Experimental features.**

1. *Gaussian behavior* :

In continuous setting, the inverse Fourier transform of a modulated Gaussian function is still a Gaussian function in the spatial domain. In other words, Gaussian functions are the fixed points of the Fourier transform. In mesh setting, given a Gaussian window function $g$ in the spectral domain by Eq. (2.37), Eq. (2.40) says that $T_i g$ is the inverse Fourier transform of a modulation of $g$. Since the mesh Fourier transform is a good approximation of the Fourier transform in continuous setting (due to the convergent properties of FE Laplacian given in Theorem 2), inspired by the case in the continuous setting, one may expect $T_i g$ to be a Gaussian function. To the best of our knowledge, there is no theoretical proof for that but it can be observed experimentally. Particularly, the following properties are observed :

- $T_i g(n) > 0, \quad \forall i, n = 1, 2, \dots, N$
- The maximum value of $T_i g$ is obtained at vertex $P_i$, i.e.

$$(T_i g)(i) = \max_{1 \leq n \leq N} (T_i g)(n).$$

- The value of $(T_i g)(n)$ decreases with distance between $P_n$ and $P_i$.

2. *Window spread* :

A Gaussian window function $T_i g$, centered at a point $P_i$ in spatial domain, has a global support but its values decrease exponentially. Therefore, for points far from the center, the values of $T_i g$ almost vanish thus negligible in computations. Accordingly, we define the *windowed neighbourhood* of a point $P_i$ as a set of mesh points with nonnegligible $T_i g$ values. For this purpose, the values of $T_i g$ are thresholded.

Formally, consider a set of vertices around the central vertex $P_i$ where the value of $(T_i g)(n)$ is more than $0.001$ of $(T_i g)(i)$. We call the set as the *windowed*

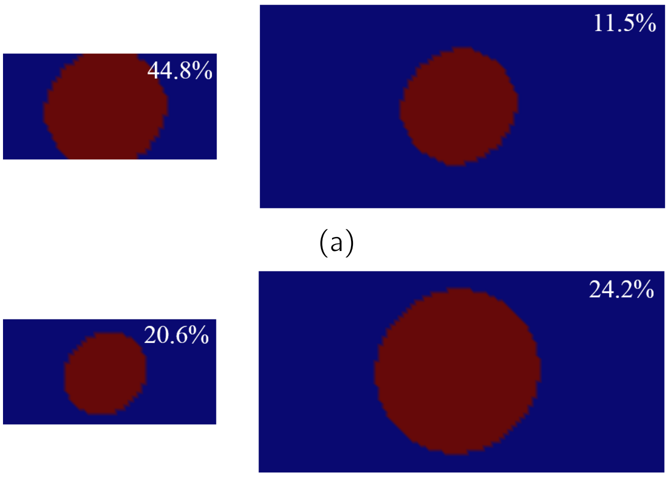

(a)

(b)

Figure 2.11.: (a) Classic window function Eq. (2.37) and (b) adaptive window function Eq. (2.44) with $\tau = 3e{-}3$ around the center point of a small and a large rectangle. The windowed neighbourhood (WN) of the center point is shown on red color and the relative spread of window has been written on each rectangle. It is clear that if the window size parameter $\tau$ is fixed, the relative spread of the classic window changes dramatically with the surface area while that of the adaptive window is almost stable.

*neighbourhood* (WN) of $P_i$ i.e.

$$\mathrm{WN}(P_i) = \{P_n \mid (T_i g)(n) \geq 0.001 \times (T_i g)(i)\}. \tag{2.43}$$

From this definition, one may compute the *spread of window function* around a vertex $P_i$ as the sum of area of triangles whose vertices are in $\mathrm{WN}(P_i)$. We use the definition of window spread later to compute the proportion of a brain surface that is covered by a window function with a specific size.

### 2.4.3. Adaptive window function

When a database of cortical surfaces with highly different sizes are to be analysed, choosing an appropriate window size is crucial. With the same window size, the relative spread of window (i.e. the ratio between the spread of window and the surface area) should be similar for all subjects. As we will show in following, it is not the case for the Gaussian window function given by Eq. (2.37). Consequently, using it leads to an inconsistent analysis across subjects. To treat this issue, we propose to modify the window function so that it is adapted automatically with respect to the surface size of each individual subject. The details

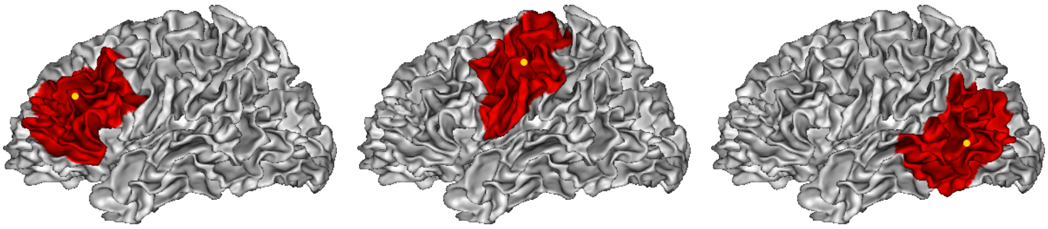

Figure 2.12.: Translation operator (2.42) moves the adaptive window function (2.44) with $\tau = 1e{-}3$ to three different vertices of the mesh. The red color highlights the window spread around the yellow central vertices.

of this strategy are given in the following.

It is easily seen from Eqs. (2.23)–(2.25) that if the surface area is scaled by a factor $q^2$, the eigenvalues are scaled by $1/q^2$. In this case, due to the definition of window function (2.37), the relative spread of window (i.e. the ratio between the spread of window and the surface area) is affected by the size of the surface. In other words, given a fixed window size $\tau$ for the original and the scaled surfaces, the window covers relatively larger space on the smaller surface and vice versa. This leads to an inconsistent large and small scale spectral analysis for small and large surfaces, respectively ; see Fig. 2.11a.

To keep the relative spread of window constant automatically across surfaces (see Fig. 2.11b), we introduce an adaptive window function in which the surface area is incorporated :

$$\hat{g}(l) = C \exp(-\tau |\mathcal{S}| \lambda_l), \tag{2.44}$$

where $|\mathcal{S}|$ denotes the surface area of surface $\mathcal{S}$. Note that by this definition, a dimensionless parameter is obtained inside the exponential function. As we will see in Section 2.5.3.1, the adaptive window function also plays an important role to derive scale invariant gyrification indices.

Translation of the adaptive window function (2.42) to different vertices is shown in Fig. 2.12. In Fig. 2.13, the spread of the adaptive window function (2.44) with 3 different window size parameters, $\tau = 2e - 4, 1e - 3$ and $5e - 3$ is plotted on a cortical surface around a specific vertex shown as a yellow point on the precentral gyrus. As $\tau$ increases, the spread of window in spatial domain increases as well. While the narrow window, $\tau = 2e - 4$, covers a part of a gyrus and/or sulcus, the medium window, $\tau = 1e - 3$, covers several folds and the wide window, $\tau = 5e - 3$, covers a big portion of the cortical surface equivalent to a lobe. Tuning the window size parameter $\tau$ changes the spatial scale of the analysis.

The adaptive window function with the same three sizes is shown in frequency

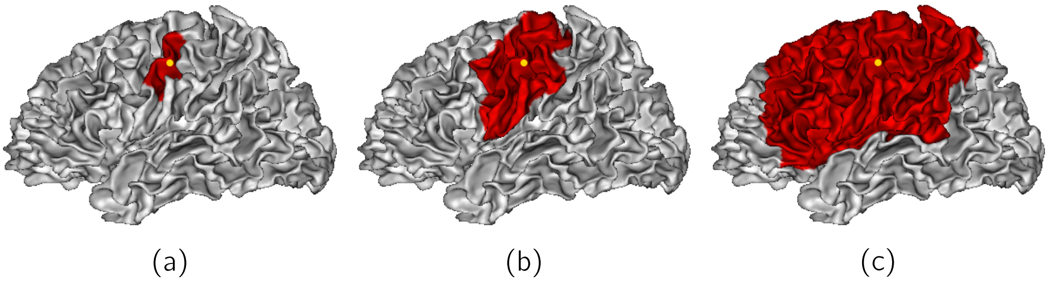
(a) (b) (c)

Figure 2.13.: The spread of the adaptive window function (2.44) with 3 different window sizes around the yellow vertex on a cortical surface. The red color highlights the window spread around the vertex. (a) A narrow window, with $\tau = 2e-4$, covers about 1.5% of the surface. (b) A medium window, with $\tau = 1e-3$, covers about 8% of the surface. (c) A wide window, with $\tau = 5e-3$, covers about 36% of the surface.

domain in Fig. 2.14. As expected, larger window sizes results in tighter windows in frequency domain. The window function with medium size $\tau = 1e-3$ is depicted in spatial and frequency domain in Fig. 2.15. It is clearly seen that the window function in spatial domain is localized around its center such that it has high values at points near the center and low values at points far from the center.

The goal of defining a window function and translation operator was to localize the function $f$ around each vertex of mesh. To this end, by multiplying the function $f$ by the translated window function $T_i g$, it is localized around vertex $P_i$ :

$$\tilde{f}_i(n) = (T_i g)(n) f(n). \tag{2.45}$$

The localization process is shown in Fig. 2.16.

### 2.4.4. Mesh windowed Fourier transform coefficients

The mesh windowed Fourier transform coefficients of a function $f \in \mathbb{R}^N$ are defined as the modulation of the localized function $\tilde{f}_i$ by Fourier atoms $\{\phi_k, k = 1, 2, \ldots, N\}$ :

$$Sf(i,k) := \langle \tilde{f}_i, \phi_k \rangle_B, \tag{2.46}$$

where $i = 1, 2, \ldots, N$ is the index of vertex and $k$ is the index of frequency. This gives us a frequency spectrum for every vertex $P_i$ of the mesh which consists of the so called "frequency powers" $|Sf(i,k)|^2,\ k = 1, 2, \ldots, N$ ; see Fig. 2.17. The frequency spectrum can be seen as frequency distribution of function $f$ in a local neighbourhood around the vertex $P_i$. The summation of the frequency powers is called the *total power* (TP) of the frequency spectrum (Mallat 2008).

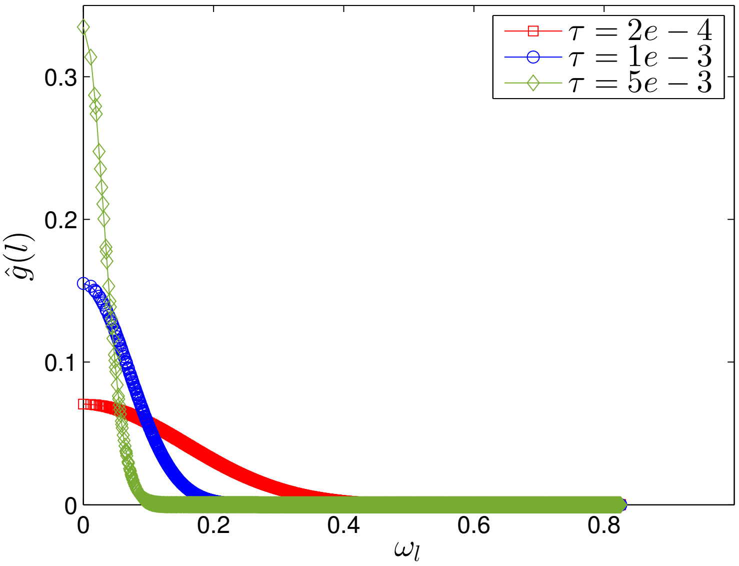

Figure 2.14.: Adaptive window function (2.44) with three different window sizes $\tau = 2e-4, 1e-3, 5e-3$ in frequency domain. As the window size increases, the window becomes tighter in this domain. $\omega_l$ denotes frequency component that equals to $\sqrt{\lambda_l}$. It is seen that the window function is a Gaussian function depicted in positive frequency domain.

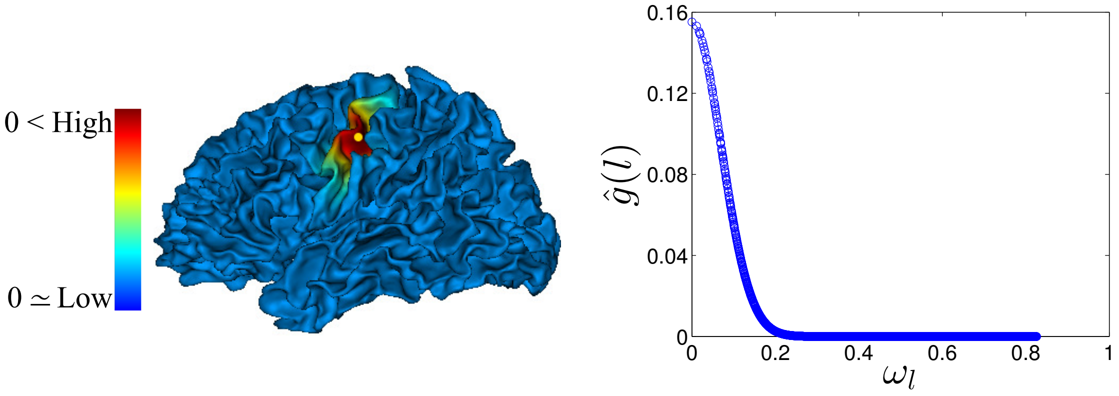

(a) (b)

Figure 2.15.: (a) Adaptive window function with size $\tau = 1e-3$ around the yellow point. It resembles a Gaussian function on the brain surface, with a peak on the center (yellow point) and lower values as we go far from the center. (b) The same window in frequency domain.

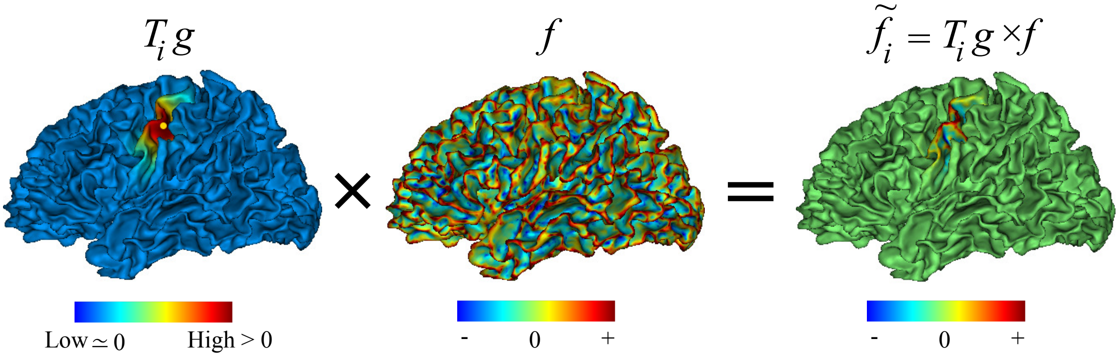

Figure 2.16.: This figure visualizes the localization of a function $f$ around the yellow point on the precentral gyrus ; see Eq. (2.45).

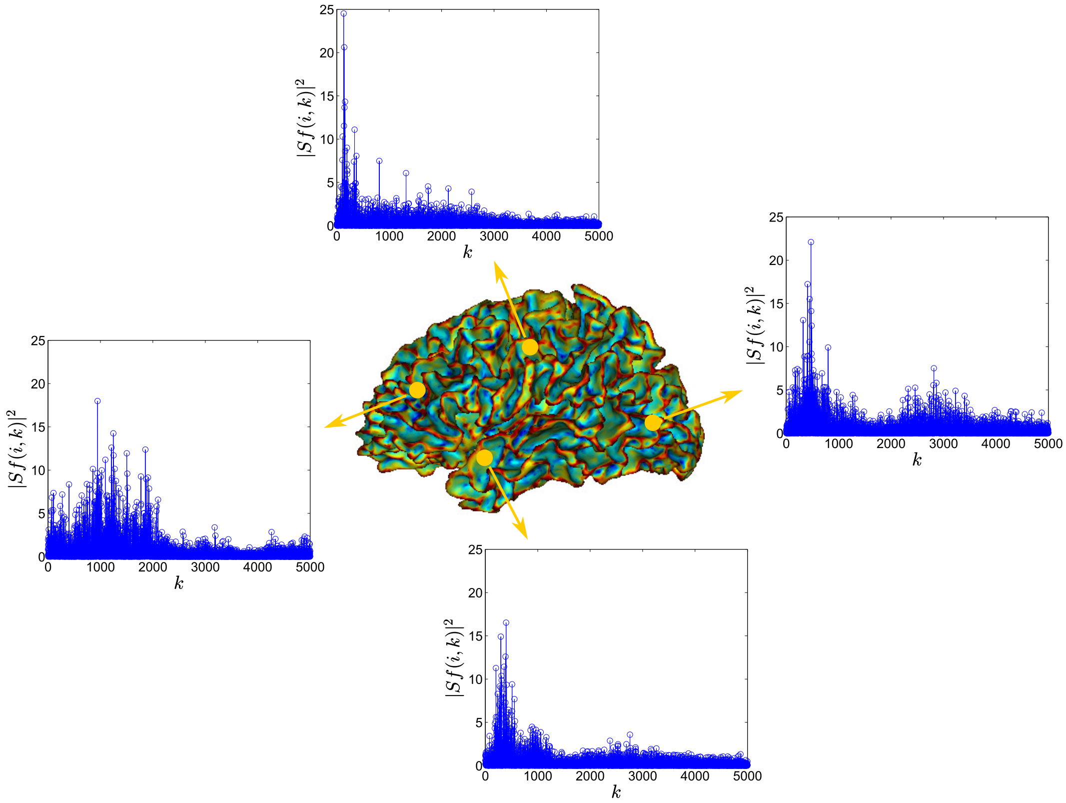

Figure 2.17.: Local frequency distributions of a function computed by the mesh windowed Fourier transform. In contrast, Fourier transform of this function gives a global frequency distribution as represented in Fig. 2.2.

## 2.5. The proposed gyrification indices

To define new gyrification indices (GIs), we apply the mesh windowed Fourier transform on the mean curvature of a brain surface. First, the notion of mean curvature is explained briefly. Then, the new GIs and their properties are introduced.

### 2.5.1. Mean curvature

Given any smooth curve $C$ and a point $P$ on it, the magnitude of curvature of the curve in that point is defined to be the reciprocal of the radius of its osculating circle ; see Fig. 2.18a. In this way, curvature measures locally how a curve is deviated from being a straight line. Mathematically speaking, if $\gamma(t) = (x(t), y(t), z(t))$ is a parametrization of $C$, then the curvature is defined by

$$\kappa(t) = \frac{|\gamma' \times \gamma''|}{|\gamma'|^3}. \tag{2.47}$$

For a smooth 2D surface $\mathcal{S}$ embedded in 3D space, at each point $P$, one can consider a normal outer vector $N_P$ and infinite number of tangent vectors $\{X_{iP}, i \in I \subset \mathbb{R}\}$ where $I$ is an indexing set. For each tangent vector $X_{iP}$, there is a unique plane $S_i$ that contains $X_{iP}$ and $N_P$. The intersection of this plane and the surface is a curve that passes through the point $P$. The curvature of this curve is called "*normal curvature*". Among infinite number of normal curvatures, the minimum and maximum ones are called "*principal curvatures*", $\kappa_{1P}$ and $\kappa_{2P}$ respectively that are corresponding to "*principal directions*" $X_{1P}$ and $X_{2P}$. These directions are proved to be orthogonal i.e. $X_{1P} \perp X_{2P}$ ; see Fig. 2.18b. Geometrically speaking, the mean curvature is an extrinsic parameter and is equal to half of the trace of the second fundamental form.

Principal curvatures are the maximal and minimal degrees of bending of the surface at point $P$. The average of $\kappa_1$ and $\kappa_2$ is called the "*mean curvature*" of the surface at point $P$. The mean curvature of point $P$ quantifies the degree of bending of the surface at this point. As examples, 1) the mean curvature of a sphere with radius $r$ at every point of the sphere surface is equal to $1/r$ ; 2) the mean curvature of a flat surface is 0.

To estimate the principal curvatures of a triangulation, we use the method proposed by TAUBIN 1995. In this method, first a tensor of curvatures is defined by a $3 \times 3$ matrix as a map that assigns normal curvatures to each point of the surface. Then, the principal curvatures and principal directions are computed by eigenvalues and eigenvectors of this matrix. The mean curvature of a brain surface is shown in Fig. 2.2. It has positive values in concave parts (gyri) and negative values in convex parts (sulci). In walls of gyri, where the surface is almost flat, the mean curvature is about 0. The readers are referred to KREYSZIG

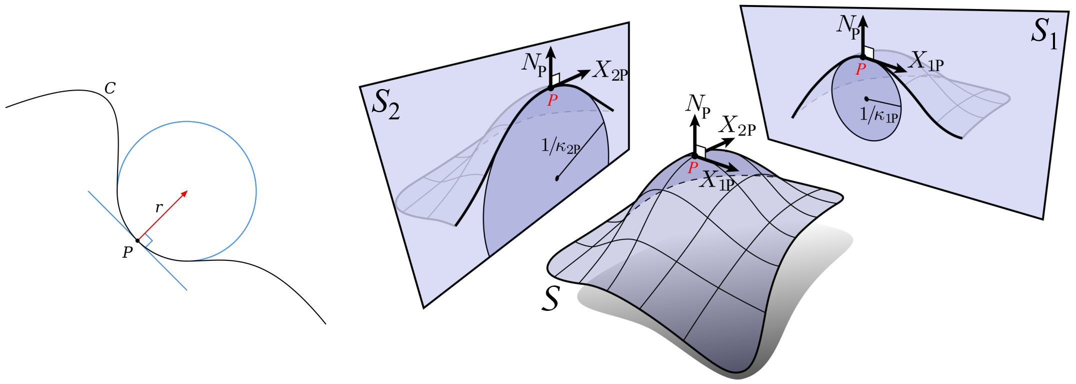

(a) (b)

Figure 2.18.: (a) Osculating circle of curve $C$ at point $P$. The curvature of the curve at point $P$ is inverse of the radius of this circle. (b) Principal curvatures $\kappa_{1P}$ and $\kappa_{2P}$ of surface $\mathcal{S}$ at point $P$ shows the maximal and minimal degree of bending of the surface at that point (Schröder et al. 2011)

1991 for more details.

## 2.5.2. New gyrification indices

In this section, we define two new GIs and we show that they satisfy all desirable properties mentioned in Section 1.4. To define a GI that measures "*surface complexity*", first we should have a clear interpretation of surface complexity. In this paper, we interpret this notion explicitly in two intuitive ways based on the features of the surface bending :

> *In a neighbourhood around each point of the cerebral cortex, the surface complexity is quantified by*
>
> *I. [MAG.] the magnitude of sulcal/gyral bending,*
>
> *II. [VAR.] the spatial variation of sulcal/gyral bends.*

Let $P_m$ and $P_n$ are two points of a surface $\mathcal{S}$. [MAG.] (resp. [VAR.]) means that the degree of surface complexity of point $P_m$ is less than that of $P_n$ if and only if in a neighbourhood around $P_m$ the surface is less bended than around $P_n$ (resp. if and only if in a neighbourhood around $P_m$ the variation of folds is less than that around $P_n$). The situation is depicted in Fig. 2.19a (Fig. 2.19b) where a cross-section of a surface is shown by green points and neighbourhoods around $P_m$ and $P_n$ are determined by red circles. [MAG.] ([VAR.]) implies that $\mathrm{GI}(P_m) < \mathrm{GI}(P_n)$.

Due to the natural link between the surface bending and the mean curvature, the [MAG.]/[VAR.] interpretations mean that in a highly folded region, [MAG.]

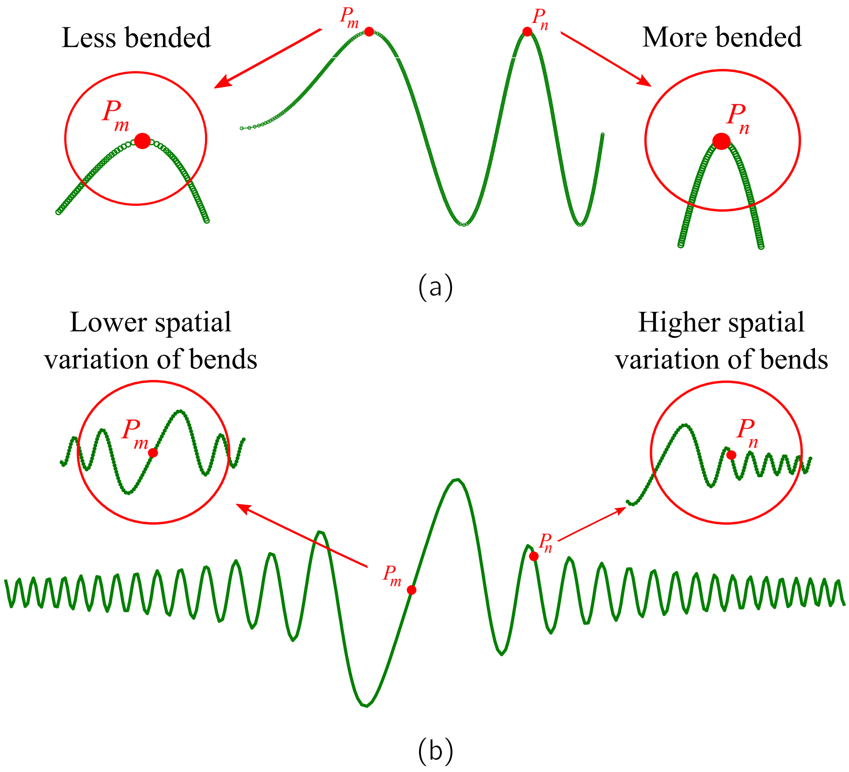

(a)

(b)

Figure 2.19.: This figure visualizes two features of surface bending that define the notion of surface complexity. (a) Surface is more complex where it is more bended. (b) Surface is more complex where the variation of bends is higher. They mean that we should define GIs such that $\mathrm{GI}(P_m) < \mathrm{GI}(P_n)$.

the magnitude / [VAR.] the variations of the mean curvature are higher in comparison to other regions.

To quantify those interpretations, we propose two novel local GIs, called spectral gyrification index (sGI) and weighted spectral gyrification index (wGI) based on a local spectral analysis of the mean curvature. They are scale invariant GIs computed directly on the cortical surface with neither requiring a reference surface nor a smoothing procedure.

While sGI gives information about the magnitude of the mean curvature in a neighbourhood around each point on the cortical surface ([MAG.]), wGI takes into account the spatial variation of folds in that neighbourhood ([VAR.]).

To define gyrification indices that fulfill our interpretations on the surface complexity, i.e. [MAG.] and [VAR.], we take the mean curvature as a function defined on the vertices of a meshed surface. By applying the mesh windowed Fourier transform to this function, we will have a local frequency spectrum at each vertex $P_i$ of the mesh. For the total power (TP) of a local frequency spectrum we have the following result.

**Proposition 1.** *The TP of the frequency spectrum of the localized mean curvature function at vertex $P_i$ is equal to the norm of this function i.e. $\sum_{k=1}^{N} |Sf(i,k)|^2 = \|\tilde{f}_i\|_B^2$, where $\tilde{f}_i$ is the localized version of the mean curvature around vertex $P_i$ and $Sf(i,k)$ is the mesh windowed Fourier transform coefficient of $\tilde{f}_i$ at frequency $k$.*

*Proof.* From the definition of window Fourier coefficient Eq. (2.46) we get

$$\sum_{k=1}^{N} |Sf(i,k)|^2 = \sum_{k=1}^{N} |\langle \tilde{f}_i \ , \phi_k \rangle_B|^2.$$

by Parseval's identity (2.30), we move to frequency domain

$$\sum_{k=1}^{N} |\langle \tilde{f}_i \ , \phi_k \rangle_B|^2 = \sum_{k=1}^{N} |\langle \hat{\tilde{f}}_i \ , \hat{\phi}_k \rangle|^2.$$

The Fourier transform of $\hat{\phi}_k$ is Kronecker delta $\delta_k$. It gives

$$\sum_{k=1}^{N} |\langle \hat{\tilde{f}}_i \ , \hat{\phi}_k \rangle|^2 = \sum_{k=1}^{N} |\hat{\tilde{f}}_i(k)|^2,$$

which by definition equals to $\|\hat{\tilde{f}}_i\|_2^2$. Finally, Parseval's identity gives

$$\|\hat{\tilde{f}}_i\|_2^2 = \|\tilde{f}_i\|_B^2,$$

and it delivers the desired equality :

$$\sum_{k=1}^{N} |Sf(i,k)|^2 = \|\tilde{f}_i\|_B^2. \tag{2.48}$$

□

Due to our first interpretation [MAG.], the degree of complexity of a region is determined by the magnitude of the localized mean curvature in that region which is encoded in its norm. On the other hand, Proposition 1 shows that the norm of the localized mean curvature at each vertex $P_i$ is equal to the total power of its local frequency spectrum. All in all, it is understood that the local degree of complexity can be computed from total frequency power of the localized mean curvature. Accordingly, it leads to the definition of our first degree of complexity :

*Spectral Gyrification Index* (sGI) *at vertex* $P_i$ :

$$\mathrm{sGI}(i,\mathcal{S}) = \sum_{k=1}^{N} |Sf(i,k)|^2. \tag{2.49}$$

In this equation, $\mathrm{sGI}(i, \mathcal{S})$ denotes the spectral gyrification index of vertex $P_i$ of surface $\mathcal{S}$ which equals to total frequency power of localized mean curvature around vertex $P_i$.

On the other hand, based on our second interpretation [VAR.], the variation of the mean curvature increases in more folded regions. Since the high variation of a function is encoded in the high frequency band of its frequency spectrum, we give larger weights to higher frequency powers to take into account this interpretation. Especially, if the weights are Laplacian eigenvalues, we will have the following result :

**Proposition 2.** *The weighted TP of the frequency spectrum of the localized mean curvature function at vertex $P_i$ is equal to norm of the Laplacian this function, i.e.*$\sum_{k=1}^{N}\left(\frac{\lambda_k}{\lambda_2}\right)^2|Sf(i,k)|^2 = \frac{1}{\lambda_2^2}\|L\tilde{f}_i\|_B^2$ *where $\tilde{f}_i$ is the localized version of the mean curvature around vertex $P_i$, $Sf(i,k)$ is the mesh windowed Fourier transform coefficient of $\tilde{f}_i$ at frequency $k$ and $L = B^{-1}A$ is the Laplacian operator.*

*Proof.* Since $Sf(i,k)$ is the Fourier coefficient of $\tilde{f}_i$, Lemma 1 gives

$$\lambda_k|Sf(i,k)| = (\widehat{L\tilde{f}_i})(k).$$

Summation over $k$ gives

$$\sum_{k=1}^{N}\left(\frac{\lambda_k}{\lambda_2}\right)^2|Sf(i,k)|^2 = \frac{1}{\lambda_2^2}\sum_{k=1}^{N}\left((\widehat{L\tilde{f}_i})(k)\right)^2. \tag{2.50}$$

Due to the definition of norm-2, the right-hand side of Eq. (2.50) is equal to $\frac{1}{\lambda_2^2}\|\widehat{L\tilde{f}_i}\|_2^2$. On the other hand, Parseval's identity gives $\|\widehat{L\tilde{f}_i}\|_2 = \|L\tilde{f}_i\|_B$, which proves the result. □

Since the Laplacian operator $L$ measures how much a function differs at a point from its average value at neighbour points, $(L\tilde{f}_i)(m)$ measures the variation of $\tilde{f}_i$ at vertex $P_m$ and then, $\|L\tilde{f}_i\|_B$ sums up all of these variations of localized $f$ around vertex $P_i$. Consequently, Proposition 2 shows that the weighted total power of frequency spectrum of the localized mean curvature at each vertex $P_i$ measures the variations of this function.

It brings us the second GI :

*Weighted Spectral Gyrification Index (*$\mathrm{wGI}$*)* :

$$\mathrm{wGI}(i, \mathcal{S}) = \sum_{k=1}^{N}\left(\frac{\lambda_k}{\lambda_2}\right)^2|Sf(i,k)|^2. \tag{2.51}$$

In this equation, the weights are the normalized eigenvalues of the Laplace-Beltrami operator that consist an increasing sequence and contain information about the shape of surface (REUTER et al. 2006 ; WACHINGER et al. 2015). The normalization by the first nonzero eigenvalue $\lambda_2$ removes the effect of the size of surface on weighting (LEFÈVRE et al. 2012). In this definition, both Laplace-Beltrami eigenvalues and eigenvectors are involved.

**Global Gyrification indices.**

For some medical purposes, we need to describe the cortical complexity with a global value for the entire cortex. To this end, a global GI can be computed from the proposed local $\mathrm{sGI}/\mathrm{wGI}$. Given a surface mesh with $M$ triangular faces $\mathcal{S} = \{t_1, t_2, \dots, t_M\}$, GI defines a function on the vertices of this mesh. We define the global GI of surface $\mathcal{S}$ as the mean value of this function :

$$\begin{aligned} \mathrm{GI}(\mathcal{S}) &:= \frac{1}{|\mathcal{S}|}\int_{\mathcal{S}} \mathrm{GI}(t,\mathcal{S})dt \\ &= \frac{1}{|\mathcal{S}|}\sum_{j=1}^{M}\frac{1}{3}\sum_{i=1}^{3}\mathrm{GI}_j(i,\mathcal{S})|t_j|, \end{aligned} \tag{2.52}$$

where $\mathrm{GI}(t,\mathcal{S})$ denotes the GI value ($\mathrm{sGI}$ or $\mathrm{wGI}$) of the surface element $t$, $|\mathcal{S}|$ is the surface area, $\mathrm{GI}_j(i,\mathcal{S})$ is the GI value of the $i$-th vertex of the face $t_j$ and $|t_j|$ is the area of $t_j$.

## 2.5.3. Properties of new gyrification indices

The intrinsic nature of the window Fourier transform enables us to compute the surface complexity at different spatial scales. Indeed, by changing the window size parameter, the mean curvature function is localized in different scales. Consequently, different amount of information is considered around each cortical point that results in complexity analysis at different spatial scales.

### 2.5.3.1. Geometric invariance

We now provide some important properties of the proposed GIs. The Laplace-Beltrami spectrum is invariant under isometric transformations. It makes $\mathrm{sGI}$ and $\mathrm{wGI}$ isometry invariant. Moreover, as demonstrated below, $\mathrm{sGI}$ and $\mathrm{wGI}$ are both scale invariant by their constructions.

**Proposition 3.** *The gyrification indices* sGI *and* wGI *are scale invariant.*

*Proof.* Assume that the surface $\mathcal{S}_2$ is the scaled version of the surface $\mathcal{S}_1$ by a factor $q^2$ i.e. $|\mathcal{S}_2| = q^2|\mathcal{S}_1|$. Since the matrix $B$ of Eq. (2.25) in discretization of $L$ is composed of area of triangles of the mesh, it is scaled by $q^2$. Accordingly, the Laplace-Beltrami eigenvalues are scaled by $1/q^2$ while the eigenvectors are scaled by $1/q$ to preserve the orthonormality. Mean curvature is also scaled by $1/q$.

Thanks to the adaptive window function (2.44), the translation operator and the mesh windowed Fourier coefficients $Sf(i,k)$ remain unchanged because

$$\begin{aligned} Sf(i,k)_{\mathcal{S}_2} &= \langle \tilde{f}_{i,\mathcal{S}_2}, \phi_{k,\mathcal{S}_2} \rangle_{B_{\mathcal{S}_2}} = q^2 \langle \frac{1}{q} \tilde{f}_{i,\mathcal{S}_1}, \frac{1}{q} \phi_{k,\mathcal{S}_1} \rangle_{B_{\mathcal{S}_1}} \\ &= Sf(i,k)_{\mathcal{S}_1}. \end{aligned}$$

Due to their definitions, it implies that sGI and wGI remain unchanged under scaling. ☐

It is noteworthy that based on its definition in Eq. (2.52), the global GI is scale invariant as the local ones.

### 2.5.3.2. Sensitivity to the number of mesh vertices

The proposed GIs, sGI and wGI, rely on a triangulation of the cortical surface. Hence, they may have interactions with the number of vertices of this triangulation. This possible interaction becomes more important when studying growing shapes/brains, due to the large variations of size and geometry across ages, that affect directly the number of necessary vertices to represent a cortical surface. The desired situation is that a GI should be robust to changes in number of vertices. In this section, we empirically show the dependency of our GIs on the number of vertices, using the unit sphere.

We consider a unit sphere surface triangulated by $N = 642$ vertices. The triangulation is refined 3 times such that at each time, each triangle is subdivided to 4 smaller triangles with approximately equal areas. Eventually, 4 triangulations of the unit sphere surface are available with $N = 642, 2562, 10242, 40962$ vertices.

The mean curvature and the first 500 eigenpairs of Laplace-Beltrami operator are computed for each surface. The global sGI and wGI of each surface are computed through Eq. (2.52) and the results are shown in Fig. 2.20. In this figure, the global values of sGI and wGI are plotted versus the natural logarithm of $N$. It is seen that while the number of vertices is multiplied approximately by 64, sGI and wGI are multiplied by 1.03 and 1.12, respectively which are very close to the desired value 1. Consequently, one may assume that sGI and wGI are almost robust to sampling and remeshing.

## 2.6. Summary

In this chapter, we gave two explicit definitions of the surface complexity that are close to our intuition of this notion. These definitions are based on bending properties : the magnitude of bending and the spatial variation of bends. To quantify the introduced definitions, we take advantage of the mean curvature function which is a geometric tool to measure bending properties of surfaces. To

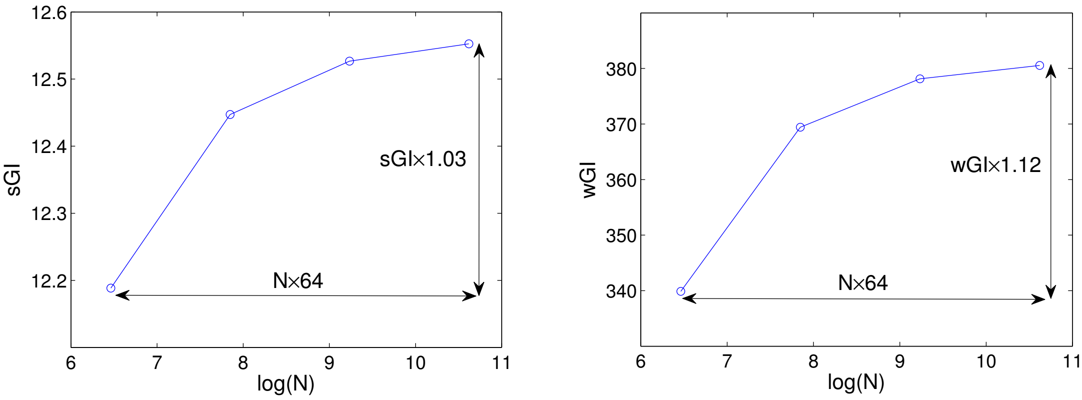

(a) (b)

Figure 2.20.: global (a) sGI and (b) wGI values of the unit sphere versus number of vertices $N$. It's seen that sGI and wGI are well robust to changes of $N$.

make the most out of this function, we decided to transfer it from its original spatial domain to a so-called spectral domain.

For this purpose, we extended the recently introduced windowed graph Fourier transform to mesh surface setting. In this extension, the graph Laplacian is replaced by the finite element (FE) discretization of Laplace-Beltrami operator. The latter operator takes into account the geometry of the mesh while the former one works only based on the connectivity of mesh vertices. Moreover, FE Laplacian converges to the Laplace-Beltrami operator (LBO) with advantages of preserving good properties of LBO.

This method is a local spectral analysis. The locality of the method is determined by a window function. Using a window function for a variety of surface with different sizes, e.g. cortical surfaces, leads to inconsistent analysis. To cope with this issue, we modified the window function to take into account the inter-subject surface size variability. By using the modified window function, the size of neighbourhoods are adapted with the size of surface.

By applying the mesh windowed Fourier transform on the mean curvature function, we proposed two local spectral measures to quantify our definitions of the surface complexity. These measures are known as spectral gyrification index (sGI) and weighted spectral gyrification index (wGI). By changing the size of the window function, it is possible to measure the surface complexity in different spatial scales. We proved that sGI and wGI are geometric invariant and moreover, they are almost stable to surface sampling.

From what presented in this chapter it is evidently seen that the proposed GIs have most of desirable properties of a standard GI given in Section 1.4 :

1. They are based on clear definitions of the surface complexity.

2. We proved theoretically that they have interpretable physical meanings. It will be also shown practically in the next chapter.
3. They measure the surface complexity locally.
4. They have flexible degree of locality which is tuned easily by the window size parameter.
5. The introduced adaptive window function makes the proposed GIs to analyse the surfaces consistently.
6. They are proved to be geometric invariant.
7. The efficiency of the method is explained in the next chapter, Section 3.2.2.

# 3. Results

In Chapter 2, we proposed two definitions for the "*surface complexity*" notion based on bending properties. The first definition interprets the surface complexity by the *magnitude of bending* while in the second definition, this notion is realized as the *variation of bends*. In accordance to these definitions, regions of a surface which are more bended or more oscillating have higher degree of complexity. We then introduced two gyrification indices, sGI and wGI to quantify these definitions through a local spectral analysis of the mean curvature of surfaces. We proved theoretically that sGI and wGI measure the magnitude of bending and the variation of bends respectively.

In this chapter, first, some synthetic wavy surfaces with different properties of fold depth and frequency are constructed in Section 3.1. Then, we use the proposed method to compute sGI and wGI of the synthetic surfaces. For comparison, a surface area-based GI proposed by Toro et al. 2008 is also computed for these surfaces. Through the experiments on synthetic surfaces, we investigate how sGI and wGI measure the surface complexity in practice. We also explain differences between our GIs and surface area-based GIs. Especially, the effect of fold depth on surface area-based GIs are investigated.

Furthermore, the method is applied to 124 real healthy adult brain surfaces reconstructed from MR images in Section 3.2. The local gyrification maps of sGI and wGI as well as Toro's GI of cortical surface of each subject are computed. The maps are then averaged to give cortical gyrification maps. These maps reveal the relative degree of complexity across cortical regions. Moreover, the relationship between our proposed GIs and the brain volume are investigated globally and locally. It interestingly helps us to understand how the increase of brain volume affects its global and local complexity.

Finally, a summary of results along with a discussion are given in the last section of this chapter.

## 3.1. Synthetic data

In order to illustrate the efficiency of sGI and wGI to quantify the proposed surface complexity definitions of a surface, and to show the effect of sulcal depth on surface area-based methods, we compute our GIs and Toro's GI on some synthetic surfaces for which we control the degree of folding. For this purpose, we construct 3 wavy surfaces with different properties. The first surface consists of folds with varying depth and spatial frequency. Then, we separate the source of variations so that in the second surface, the depth of folds is constant but the spatial frequency of folds are still varying along the surface. In contrast, the third surface is constructed in a way that the spatial frequency of folds are constant while folds have different depths.

It is noted that these surfaces are not designed to compare between sGI and wGI but rather to show the difference between our GIs and Toro's GI.

### 3.1.1. Wavy surface with varying fold frequency and depth

**Construction.**

A wavy rectangle in $\mathbb{R}^3$ is constructed by the equation

$$z = 2\sin(60\pi x^2)/(60\pi x), \qquad -0.7 \leq x \leq 0.7, \quad 0 \leq y \leq 1, \tag{3.1}$$

The constructed surface, shown in Fig. 3.1a, is a sinusoidal surface composed of folds with varying frequency and depth. The frequency and depth are dependent to $x$ coordinate such that when the absolute value of $x$ increases,

- the spatial frequency of folds, computed as $\omega := |d(60\pi x^2)/dx| = |120\pi x|$, increases,
- the depth of folds, controlled by the varying coefficient $|2/(60\pi x)|$, decreases.

To better visualize the situation, the intersection of the surface with the plane $y = 0.5$, indicated on the surface by green points, is plotted in Fig. 3.1b and is called the "*middle line*". It gives a 2D scheme of the wavy surface which shows the behavior of folds. It is seen that as one goes far from the center to the right/left border of this surface,

- the surface becomes more bended i.e. folds become sharper,
- the variation of folds increases.

Consequently, according to the proposed definitions of the surface complexity, given in Section 2.5.2, the center of the surface is less complex than the right/left border. So, one expects that values of the proposed gyrification indices, sGI and wGI, are lower in the center than those in the right/left border of the surface.

**sGI, wGI and Toro's GI.**

To compute the indices, sGI and wG, first, the surface is triangulated with $N = 40,000$ equidistant vertices. Then, the mean curvature of the triangulated surface is computed. In the next step, the first 3000 finite element Laplacian eigenvalues and eigenvectors of the triangulated surface are computed. Then, the adaptive window function, given by Eq. (2.44), with the window size $\tau = 2e - 3$ is considered and the translation operator (2.42) is computed. The windowed neighbourhood ($\mathrm{WN}$ given by Eq. 2.43) around two vertices, $P_m$ and $P_n$, of the

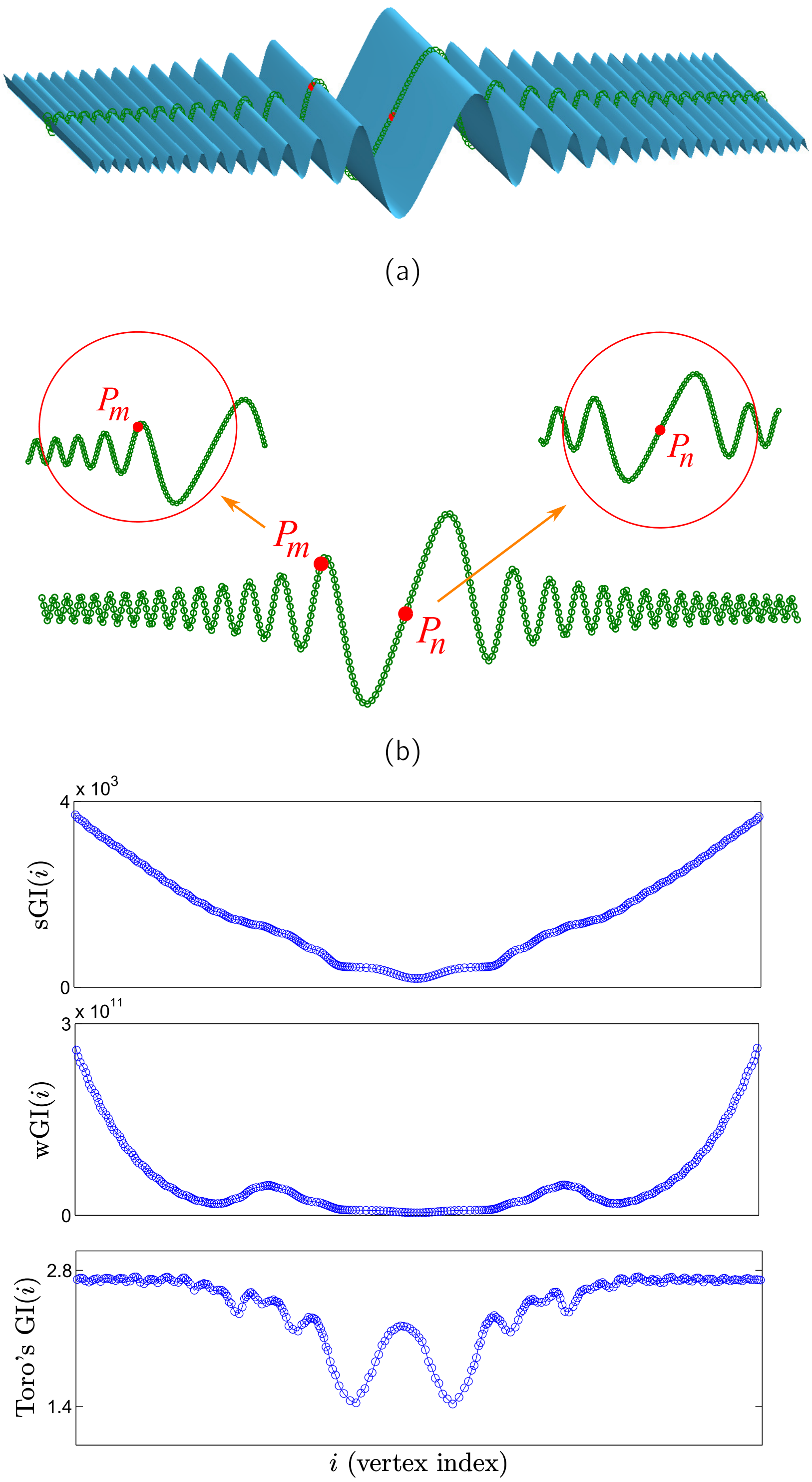

(c)

Figure 3.1.: (a) A wavy rectangle in $\mathbb{R}^3$. The "middle line" on the surface is formed by the vertices lie on the surface with the the same $y$-coordinate 0.5. (b) The middle line along with zoom on two neighbourhoods around vertices $P_m$ and $P_n$. (c) Plots of sGI, wGI and Toro's GI of the vertices located on the middle line.

middle line is shown in Fig. 3.1b. For both of these points, the relative spread of the translated adaptive window, i.e. (area of $\mathrm{WN}$)/(total surface area), is about $20\%$. Then, the mesh windowed Fourier coefficients of the surface mean curvature are computed by Eq. (2.46). Finally, the gyrification indices, sGI and wGI are computed by using the Eqs. (2.49) and (2.51) respectively.

To compare sGI and wGI with a surface area-based GI, Toro's GI (TORO et al. 2008) is computed for this surface. In this method, a neighbourhood around each surface point is determined by a sphere with radius $r$. Then the GI is defined as the ratio between the area of the surface surrounded by the sphere and the area of the great disc of the sphere ; see Section 1.3.1 for more explanations. For the wavy surface here, the spherical neighbourhood radius of Toro's GI is considered as $r = 0.22$ for which the relative neighbourhood spread is almost equal to that of our method.

sGI, wGI and Toro's GI values of the vertices along the green middle line of the wavy surface are plotted in Fig. 3.1c. As expected, minimum value of sGI is located at the center of the surface where the folds are smoother (less bended). In contrast, near the right/left border of the surface, where the folds are sharper, sGI increases. It is consistent with the role of sGI which is supposed to measure the magnitude of fold bending i.e. the definition [*MAG.*] of the surface complexity (see Section 2.5.2).

A similar situation is happening for wGI. As expected, minimum value of wGI is located at the center of the surface where the spatial frequency of folds are low. In contrast, near the right/left border of the surface, where the folds re more oscillating, wGI increases. It is consistent with the function of wGI which is supposed to measure the spatial variation of folds i.e. the definition [*VAR.*] of the surface complexity.

Toro's GI is high at the center of the surface where there are deep folds thus much surface area. By moving to the right/left border, it takes lower values to some extent. Again, near the right/left border where the folds are shallower but more oscillating, Toro's GI increases and may also converge to an asymptotic value. It is because the high oscillation of folds increases the surface area which causes Toro's GI to grow. It reveals that Toro's GI gives a positive response to any source of increasing surface area without considering that it may be due to deep smooth folds or oscillating complex ones. In other words, Toro's GI may not distinguish deep smooth folds from oscillating complex ones.

**Mechanisms of sGI and wGI.**

In order to explain how sGI and wGI work, the spectrogram of the mesh windowed Fourier transform of the mean curvature of the wavy surface, consists of the frequency powers $|Sf(i,k)|^2$ of the middle line, is shown in Fig. 3.2a. It is clearly seen that in the center, corresponding to deep and less oscillating folds, the spectral energy is concentrated around low frequencies while the higher variation of the mean curvature near left and right borders is demonstrated by the

Table 3.1.: Different GIs for vertices $P_m$ and $P_n$ of the wavy rectangle depicted in Fig. 3.1b

| vertex | sGI | wGI | Toro's GI |
|---|---|---|---|
| $P_m$ | 8.5561e2 | 2.8090e10 | 2.2268 |
| $P_n$ | 1.8487e2 | 3.8802e9 | 2.2271 |

concentration of energy in high frequencies.

Each column of the spectrogram shows the frequency distribution of the mean curvature in a neighbourhood of a mesh surface vertex. For instance, consider the surface neighbourhood around vertex $P_n$ of the middle line, shown in Fig. 3.1b. In this neighbourhood, there are deep but less oscillating folds. From the frequency distribution of $P_n$, plotted in Fig. 3.2c, it is seen that the spectral energy is low and almost concentrated in the low frequency band.

On the other hand, consider the surface neighbourhood around vertex $P_m$ of the middle line, shown in Fig. 3.1b. In this neighbourhood, folds are more oscillating. Consistently, in the corresponding frequency distribution, plotted in Fig. 3.2b, it is seen that the spectral powers are higher than those of $P_n$ and almost concentrated in the medium frequency band.

Since sGI is simply the summation of frequency powers (Eq. 2.49), evidently $\mathrm{sGI}(P_m) > \mathrm{sGI}(P_n)$. On the other hand, wGI gives higher weights to higher frequencies. Therefore, due to the shift of frequency energies from low to medium frequency bands, $\mathrm{wGI}(P_m) > \mathrm{wGI}(P_n)$.

The values of sGI, wGI and Toro's GI for the considered vertices $P_m$ and $P_n$ are given in Table 3.1 for comparison. While sGI and wGI give appropriately higher values to vertex $P_m$, Toro's GI gives equal values to both vertices. It shows that surface area-based GIs may not be able to discriminate between deep folds and complex folds with the same area.

**Conclusion.**

This example shows how higher local frequency powers increase in regions with high oscillating folds. It, in turn, explains the mechanisms of the proposed indices, sGI and wGI, based on a (weighted) summation of frequency powers to quantify the proposed definitions of the surface complexity.

Moreover, the observations clarify that sGI and wGI discriminate efficiently deep smooth folds from oscillating complex ones with a clear increase from the center of the wavy surface towards the left/right borders whereas Toro's GI shows high values on the center where there are deep folds as well as on the borders where there are high oscillating folds.

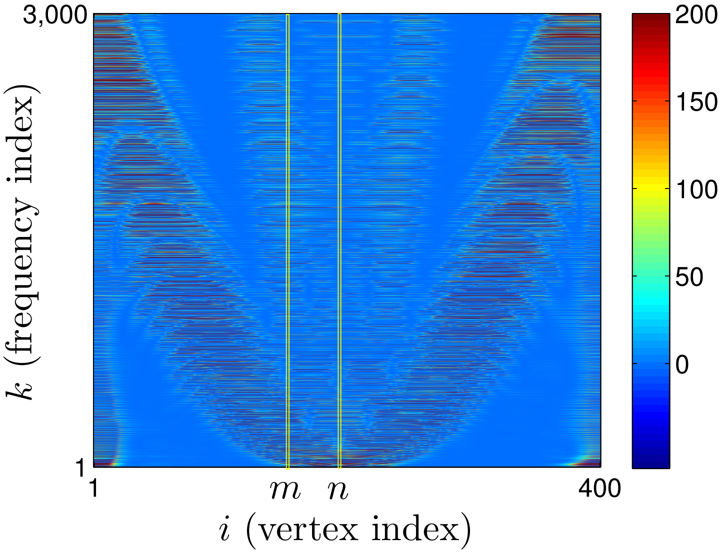

(a) Spectrogram

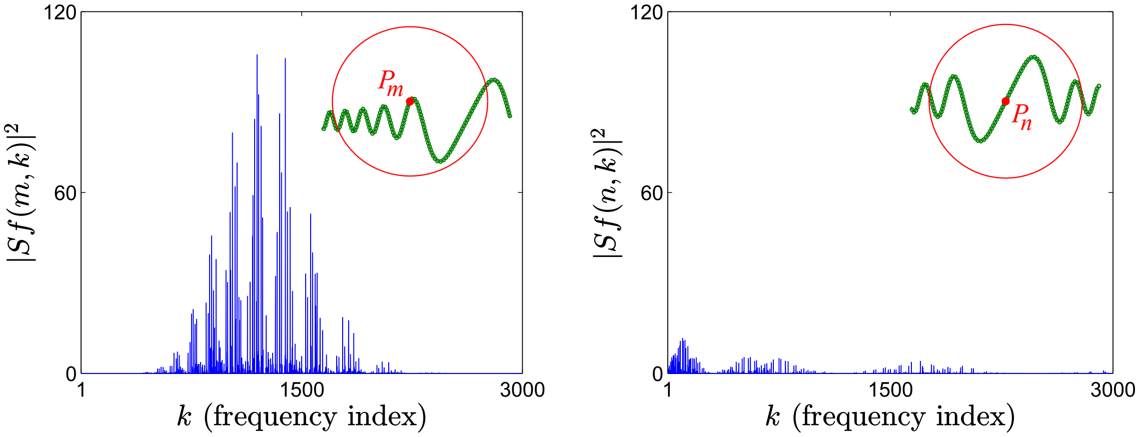

(b) The local frequency spectrum of the vertex $P_m$

(c) The local frequency spectrum of the vertex $P_n$

Figure 3.2.: (a) The spectrogram of the windowed Fourier transform applied on the mean curvature of the middle line of the wavy rectangle depicted in Fig. 3.1b. Two vertical yellow ribbons highlight the local spectrum of two vertices $P_m$ and $P_n$ depicted in Fig. 3.1b. The local spectrum of two vertices (b) $P_m$ and (c) $P_n$. It is clearly seen that for the vertex $P_m$ where there are more oscillating folds, the higher frequency powers increase in comparison to that of the vertex $P_n$ where there are less oscillating folds.

### 3.1.2. Wavy surfaces with one source of variation

To better elucidate the effect of the fold depth on the surface area-based GIs, two other surfaces are constructed. Each surface has one source of variation : spatial frequency of folds or fold depth. These surfaces are designed to study the effect of fold frequency and depth separately. sGI, wGI and Toro's GI are computed for these surfaces.

Note that, in comparison to the previous example, the following surfaces have deeper folds. Accordingly, the window size of our GIs and the spherical neighbourhood size of Toro's GI are increased so that each neighbourhood covers several folds.

**Varying frequency, fixed depth.**
The first surface is constructed through the following equation

$$z = \begin{cases} 0.1\sin(50\pi x^2), & 0 \le x \le 0.42, \\ -0.1\sin(50\pi(x-0.84)^2), & 0.42 < x \le 0.84, \end{cases} \tag{3.2}$$

and $0 \le y \le 1$. This is a sinusoidal surface with a quadratic phase which causes the frequency of folds increases as one moves from the left and right borders towards the center ($x = 0.42$). Moreover, the depth of folds are kept fixed. A cross-section of this surface is represented in Fig. 3.3a.

Toro's GI ($r = 0.39$) together with our GIs ($\tau = 0.02$) of the vertices located on the cross-section are shown in Figs. 3.3b-3.3d, respectively. As expected, all GIs give higher values to central vertices. From point of view of Toro's method, due to more compact folds around the center, there is much surface area in this region. That is why Toro's GI gives higher values to that region. On the other hand, the magnitude of mean curvature increases in the central region because the folds are sharper than those near borders. So, sGI assigns higher values to points in that region. Furthermore, due to the special design of the surface, the spatial variation of folds increases in the center and by its definition, wGI gives higher values to this part of the surface.

**Varying depth, fixed frequency.**
The second wavy surface is constructed by using the following equation

$$z = 0.3\exp(-x^2/0.16)\sin(20\pi x), \qquad -0.8 \le x \le 0.8, \quad 0 \le y \le 1. \tag{3.3}$$

In this surface, the depth of folds is controlled by the exponential function which increases in the center. The instantaneous frequency of folds that is determined by the phase of the sine function is constant (e.g. KAISER 2011). A cross-section of this surface is represented in Fig. 3.4a.

Toro's GI ($r = 0.75$) together with our GIs ($\tau = 0.01$) of the vertices located on the cross-section are shown in Figs. 3.4b-3.4d, respectively. In a neighbourhood

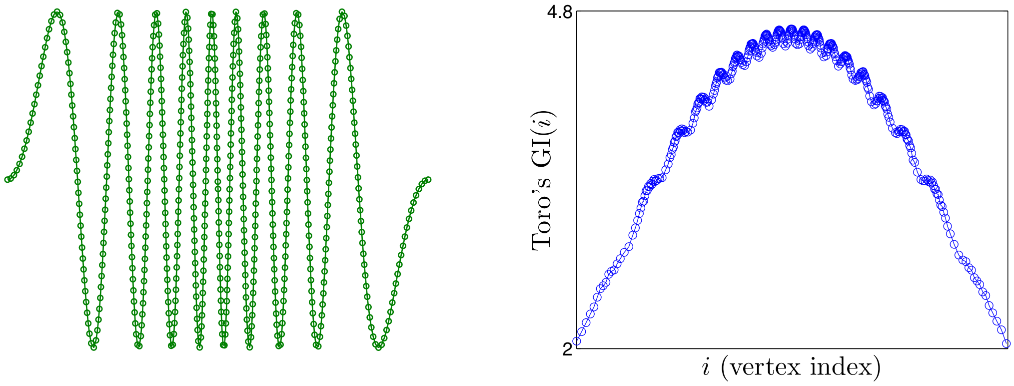

(a) Cross section of a wavy rectangle

(b) Toro's GI

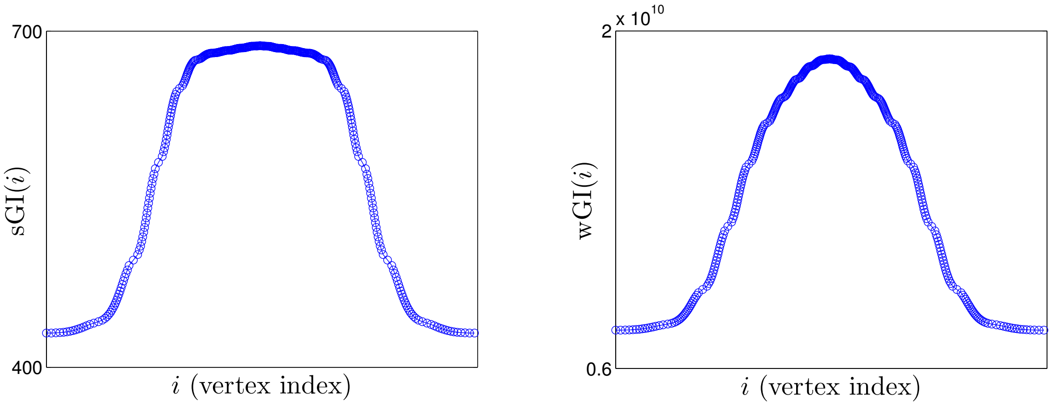

(c) sGI

(d) wGI

Figure 3.3.: (a) A cross section of a wavy surface with folds of varying frequency but equal depth. (b) Toro's GI, (c) sGI and (d) wGI of the vertices located on the cross section.

around a vertex in the center of the surface, due to deep folds, there is much surface area. It causes Toro's GI to give higher values to points located in this region. On the other hand, the variation of folds increases in borders. It means that a large enough neighbourhood around a vertex near the borders contains more oscillations of folds than a neighbourhood in the center of the surface (like the neighbourhood around vertex $P_m$ as shown in Fig. 3.1b). It causes wGI increases near the borders. In a neighbourhood near the borders, there are more peaks and valleys where the mean curvature has higher magnitude than the wall of folds. That is why sGI increases as we move from the center to the borders of the surface.

**Conclusion.**

These experiments elucidate how the depth of folds manipulates surface area-based Toro's GI as well as our GIs. In a surface consists of folds with equal depth,

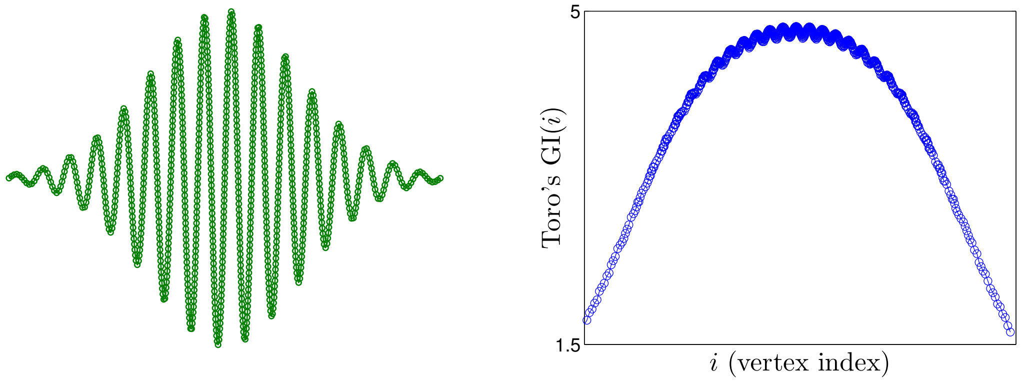

(a) Cross section of a wavy rectangle

(b) Toro's GI

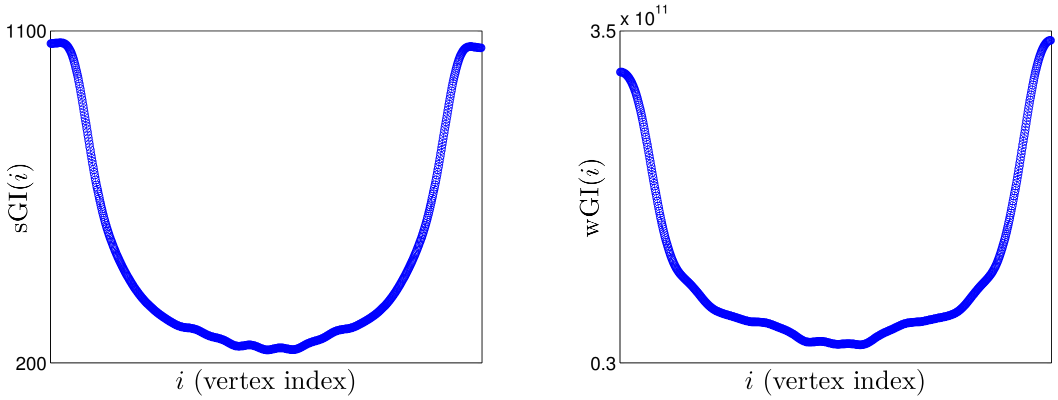

(c) sGI

(d) wGI

Figure 3.4.: (a) A cross section of a wavy surface with folds of varying depth but fixed oscillation. (b) Toro's GI, (c) sGI and (d) wGI of the vertices located on the cross section.

our GIs and Toro's GI give higher values to regions with more oscillating folds. In contrast, in a surface consists of folds with varying depths, Toro's GI gives higher values to deep folds whereas our GIs give higher values to shallower folds which are more oscillating.

As a consequence, Toro's GI as a representative of surface area-based GIs gives higher values to regions with larger surface area without taking into account the fact that large surface area may appear in different situation e.g. deep regular folds or high oscillating folds. In contrast, our GIs work based on measuring the local oscillations of folds thus is able to disentangle the effect of the depth of folds from their complexity.

It is noted that the above experiments were not designed to show how sGI and wGI quantify different aspects of folding. In the following section, however, it is shown on a real brain surface.

## 3.2. Real data

In this section, the proposed method is applied to a real database of cortical surfaces. The gyrification maps of an individual subject as well as group average maps across all subjects are presented. Moreover, it is shown how sGI and wGI catch different aspects of folds. Furthermore, the relation between the proposed GIs and the brain volume is studied in global and local scales.

### 3.2.1. Data and preprocessing

We applied the method to 124 adult subjects from the Open Access Series of Imaging Studies (OASIS) database [a], all healthy, right-handed with 18-34 years old. The OASIS cross-sectional database is a collection of 416 subjects aged from 18 to 96 years old, including some older adults with dementia. For each subject, three or four T1 anatomical Magnetic Resonance Images (MRIs) had been acquired at in-plane resolution of $1\text{mm} \times 1\text{mm}$, slice thickness = $1.25$ mm, TR = $9.7$ ms, TE = 4 ms, flip angle = 10u, TI = 20 ms, TD = 200 ms. Images of each subject were motion corrected and averaged to create a single image per subject with a high contrast-to-noise ratio.

The resulting anatomical MR images were segmented using BrainVISA [b]. The white matter surface of each hemisphere was then meshed using this software which resulted in triangular meshes with spherical topology and approximately 50,000 vertices depending on the subjects. The Hip-Hop algorithm (AUZIAS et al. 2013) implemented in BrainVISA was then applied to compute the spherical inter-individual correspondence between cortical surfaces.

### 3.2.2. Gyrification maps

To compute the proposed indices, sGI and wGI, of each hemisphere surface, the mean curvature is computed. Then, the first 5000 FE Laplacian eigenvalues and eigenvectors of each surface is computed. The adaptive window function, given by Eq. (2.44) with 3 different window sizes $\tau = 2e-4, 1e-3, 5e-3$, associated to very local, medium and wide windows respectively, is considered (see Fig. 2.13 for window sizes). To obtain the localized mean curvature in a neighbourhood around each surface vertex, the translated window function is computed and applied on the mean curvature function of the surface (Eq. 2.45). Now, the mesh windowed Fourier coefficients of the localized mean curvature are obtained through Eq. (2.46). Finally, the values of sGI and wGI of each vertex are given by Eqs. (2.49) and (2.51) respectively.

**Individual maps.**

---

a. http://www.oasis-brains.org/
b. http://brainvisa.info/

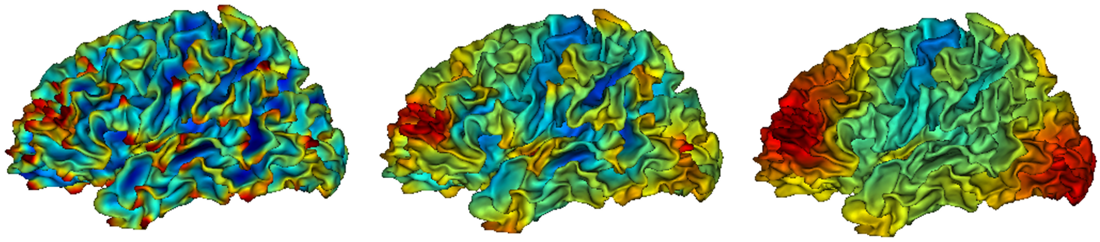

(a) sGI

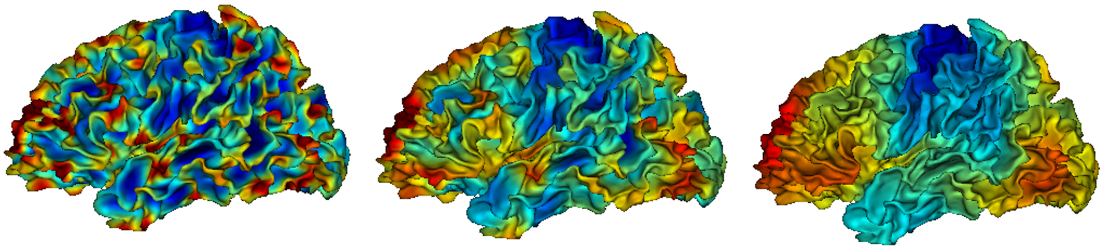

(b) wGI

Figure 3.5.: The map of gyrification indices (a) sGI and (b) wGI of the left hemisphere of an individual subject from our database in 3 different scales. In the first column $\tau = 2e - 4$, in the second column $\tau = 1e - 3$ and in the third column $\tau = 5e - 3$. The blue and red colors indicate the extremes of low and high degree of folding respectively.

The maps of sGI and wGI of the left hemisphere surface of a subject, called $\mathcal{S}^*$, in the database is shown in Fig. 3.5. In this figure, it is shown that the window size parameter $\tau$ can be used to control the scale of observations. At $\tau = 2e - 4$, the spatial scale is fine and high values are located mostly on the ridge of complex gyri, while low values are located on the walls of regular sulci. As the window size increases, a more regional effect becomes visible, with a very smooth and low variation map at value $\tau = 5e - 3$, which gives a coarse scale observation of the gyrification.

As an illustrative example to show how our method discriminates between deep and oscillating folds of a cortical surface, the left medial face of the subject $\mathcal{S}^*$ and its sGI and wGI maps ($\tau = 1e - 3$) are shown in Fig. 3.6a and 3.6b respectively (the lateral maps are shown in the middle column of Fig. 3.5). Two lines with equivalent geodesic length were drawn on the medial face : line 1 in the medial precentral region (blue line, geodesic length 34.63 mm) where both GIs have low values, and line 2 in the medial prefrontal region (red line, geodesic length 35.35 mm) where both GIs show high values (Fig. 3.6c).

Geodesic sulcal depth on the cortical surface was computed through the method described by Im et al. 2008 in order to get depth values at each point of both

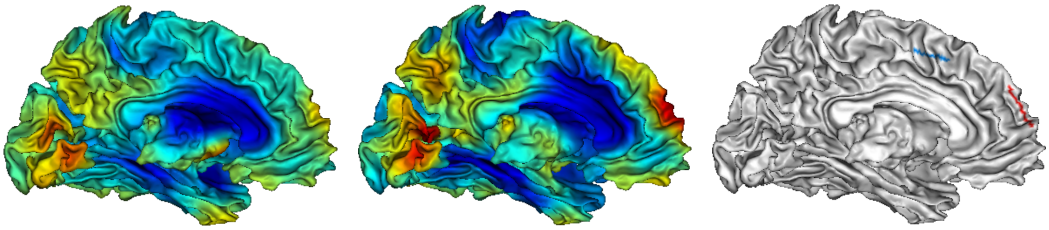

(a) sGI (b) wGI (c) Manual lines

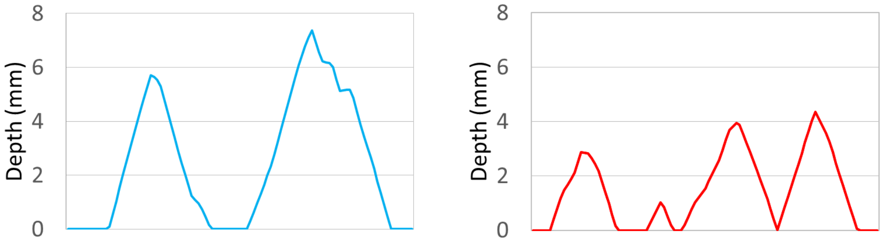

(d) Depth map of Line 1 (e) Depth map of Line 2

Figure 3.6.: Medical view of (a) sGI and (b) wGI maps of the subject $\mathcal{S}^*$. The blue and red colors indicate the extremes of low and high degree of folding respectively. (c) Two lines with almost equal geodesic length are drawn on the medial central region (Line 1, blue, geodesic length=34.63 mm) and the medial prefrontal region (Line 2, red, geodesic length=35.35 mm). The depth maps of (d) Line 1 and (e) Line 2 show that the frequency of folds in the medial prefrontal region is double of that in the medial precentral region while the depth of folds on the medial prefrontal region is almost half of that in the medial precentral region.

lines and produce depth curves along these lines. These depth curves, plotted in Fig. 3.6d and 3.6e, show that the frequency of folds in the medial prefrontal region (Line 2) is double of that in the medial precentral region (Line 1), while the depth of folds on the medial prefrontal region is almost half of that in the medial precentral region. This explains the high values of our gyrification index in the medial prefrontal region : despite an apparent smoothness due to the low sulcal depth, the folding frequency is higher.

As it has been discussed in Section 2.5.2, the indices sGI and wGI, based on their constructions, measure complementary properties of surface complexity : magnitude and oscillation of the mean curvature. This feature is shown in Fig. 3.7 where the mean curvature of the cortical surface $\mathcal{S}^*$ is depicted. Two regions on this surface, R1 and R2, have been chosen. R1 is a sharp spike located on the postcentral gyrus and R2 is a very shallow fold located on the superior parietal lobe. The mean curvature of the region R1 is very high whereas that of the region R2 varies a lot between positive and negative values. The maps of sGI and wGI of R1 and R2 are shown in this figure ($\tau = 2e-4$). Consistent with

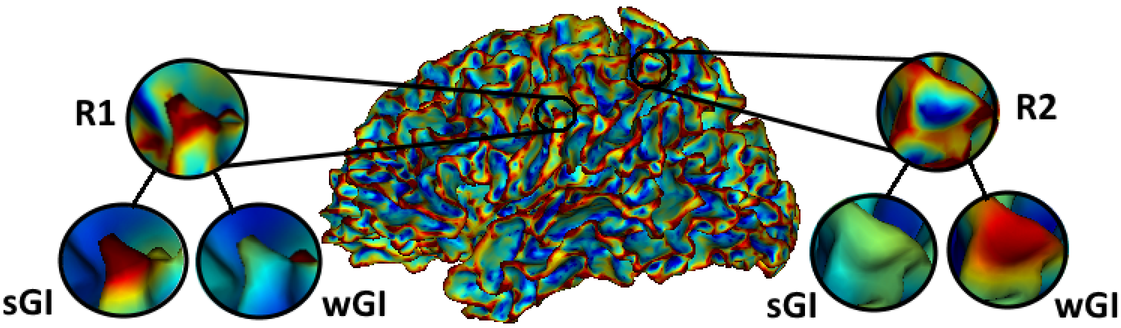

Figure 3.7.: Zoom on 2 regions, R1 and R2, of the cerebral cortex. The colormap of the cortex encodes its mean curvature (the blue and red colors indicate the extremes of negative and positive values respectively). sGI and wGI ($\tau = 2e - 4$) of the regions R1 and R2 are also represented (the blue and red colors indicate the extremes of low and high degree of folding respectively).

their definitions, sGI gives high value to R1 while wGI assigns high value to R2. It shows practically how sGI and wGI can discriminate different aspects of the surface complexity by measuring different bending properties i.e. magnitude and frequency of folds.

**Group maps.**
Individual maps of sGI and wGI in the medium scale ($\tau = 1e - 3$) are projected to the template cortical surface *hiphop138* [c] by using the cortical surface inter-subject matching method, *Hip-Hop* (AUZIAS et al. 2013). Then, individual values of sGI and wGI are averaged at each point of the template surface to obtain group average maps of sGI and wGI.

Results are depicted on the template cortical surface *hiphop138* in Fig. 3.8 for the left and right hemispheres respectively. The average patterns of sGI and wGI represented in Fig. 3.8 are similar to those observable on an individual subject (Fig. 3.5) which shows that the spatial patterns of the proposed GIs are reproducible across subjects.

As Figs. 3.8a and 3.8b shows, sGI gives higher values to vertices on the prefrontal and occipital lobes, inferior parietal lobe, inferior temporal sulcus and the medial area of the superior parietal cortex. wGI, as shown in Figs. 3.8c and 3.8d, assigns higher values to the prefrontal lobe, medial part of the occipital lobe and the posterior cingulate gyrus. Some folding is also captured by relatively high wGI values in the insula.

To compare with our results, the average maps of Toro's GI across all subjects in the database are presented in Figs. 3.8e and 3.8f for left and right hemispheres

---

[c] The *hiphop138* template is available at `http://www.meca-brain.org/softwares/hiphop138-cortical-surface-group-template/`

respectively. This method gives high GI values to deep folds like the central sulcus, the insula, the superior temporal sulcus and the parieto-occipital sulcus.

For all sGI, wGI and Toro's GI, by visual inspection, we observed no remarkable difference in gyrification patterns (in the medium neighbourhood size) between the left and right hemispheres.

**Efficiency.**

The proposed method has been performed by using MATLAB®R2014a on a node of a computation cluster with *Xeon X5675* processor[d] (6 cores, 3.06 GHz), 48 GB of RAM shared among 16 nodes. For the cortical mesh hemisphere with largest number of vertices in our database, $N = 71252$, all steps of the method took about 3.6 hours. A large portion of the runtime ($\sim 3$ hours) spent on computing the first 5000 Laplacian eigenpairs. Once the Laplacian eigenpairs are computed, they can be used to compute sGI and wGI in several spatial scales in a short time.

### 3.2.3. Scaling analysis

**Global scale.**

Recent studies show that larger brains are more folded than what is expected from an isometric scaling (e.g. TORO et al. 2008 ; GERMANAUD et al. 2012 ; GERMANAUD et al. 2014 ; IM et al. 2008). To investigate this phenomenon, the global sGI and wGI of each hemisphere are modelled by the following power law

$$\mathrm{GI} = kV^{\alpha}, \tag{3.4}$$

where $\mathrm{GI}$ denotes the global gyrification index (sGI or wGI) of a hemisphere computed through Eq. (2.52), $V$ is the hemispheric volume and $k$ and $\alpha$ are coefficients to be determined.

The power law has been widely used to model the interaction between the size (volume) and other geometrical features (e.g. length, surface area, shape) of a population of 3D objects (e.g. KAPELLOU et al. 2006 ; TORO et al. 2008 ; LEFÈVRE et al. 2015). For example, it is well-known that under the hypothesis of an isometric scaling, the volume ($V$) and surface area ($|\mathcal{S}|$) of simple objects such as sphere are theoretically related by the power law with $\alpha = 2/3$ i.e. $|\mathcal{S}| = kV^{(2/3)}$. In this case, if for an object, a different $\alpha$ than the theoretical one is observed, it is said that a volume-surface area *allometric relation* is held for that object. In other words, if the volume increases, the surface area will increase more (if $\alpha > 2/3$) or less (if $\alpha < 2/3$) than what expected from an isometric scaling. The case of $\alpha > 2/3$ is called *positive allometry* whereas the case of $\alpha < 2/3$ is called *negative allometry*.

---

[d] `http://ark.intel.com/products/52577/Intel-Xeon-Processor-X5675-12M-Cache-3_06-GHz-6_40-GTs-Intel-QPI`

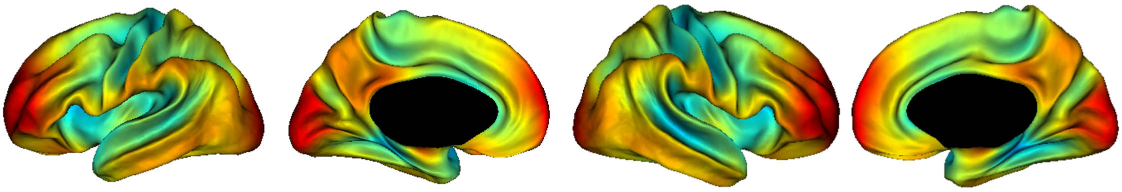

(a) sGI – left (b) sGI – right

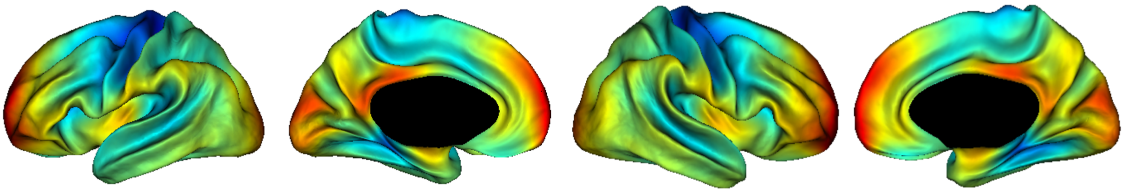

(c) wGI – left (d) wGI – right

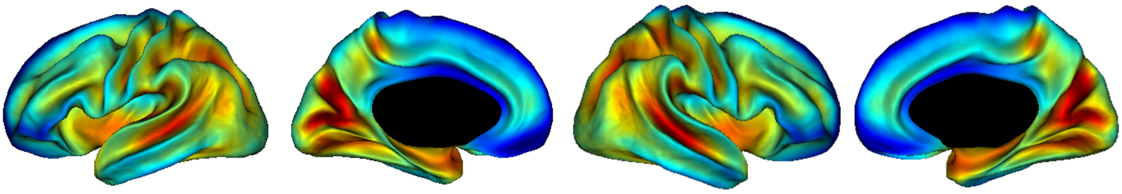

(e) Toro's GI – left (f) Toro's GI – right

Figure 3.8.: Average of gyrification indices : (a–b) sGI and (c–d) wGI derived from the medium window ($\tau = 1e - 3$), and (e–f) Toro's GI with spherical neighbourhood radius $r = 20$ across the left and right hemispheres of all 124 subjects on the *hiphop138* template surface. The blue and red colors indicate the extremes of low and high degree of folding respectively.

Since gyrification indices, sGI and wGI, are scale invariant (Proposition 3), the scaling exponent coefficient $\alpha$ of the power law (3.4), under the hypothesis of an isometric scaling of the brain volume, should equal 0. It means that if larger brains in our database were just scaled versions of smaller brains, they would have similar GIs thus $\alpha = 0$.

To investigate this relationship, the hemispheric data are considered in a log-log scale. In this scale, the power law (3.4) takes a linear form as

$$\log(\mathrm{GI}) = \alpha \log(V) + \log(k). \tag{3.5}$$

In this manner, the exponent coefficients $\alpha$ and $\log(k)$ can be computed from the slope and intercept of the linear least square regression analysis of the hemispheric data $\Big\{\Big(\log(\mathrm{GI}), \log(V)\Big)\Big\}$ respectively.

The hemispheric data along with the fitted power law model in logarithmic

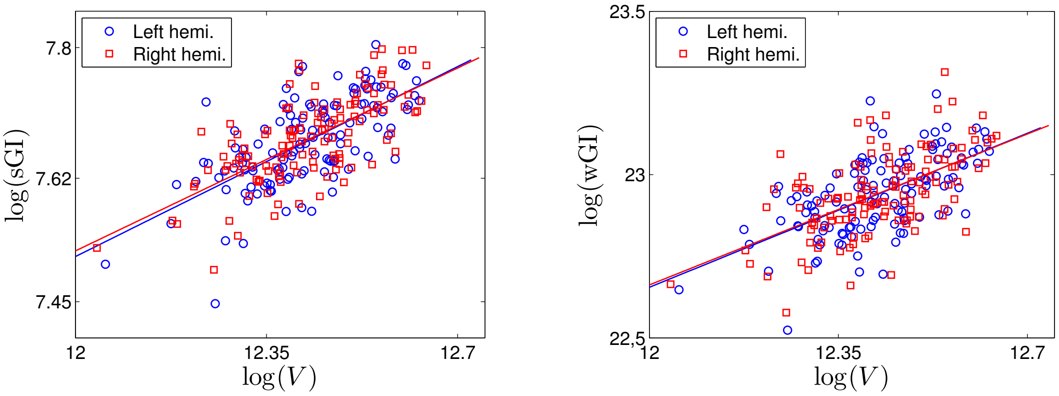

(a) sGI (b) wGI

Figure 3.9.: (a) Relationship between the volume (mL) of the left/right hemispheres and global sGI ($\tau = 1e - 3$). The fitted line for the left hemisphere is $y = 0.37x + 3.03$, $R^2 = 0.44$, $p < 0.001$. The fitted line for the right hemisphere is $y = 0.36x + 3.2$, $R^2 = 0.47$, $p < 0.001$. (b) Relationship between the volume (mL) of the left/right hemispheres and global wGI ($\tau = 1e - 3$). The fitted line for the left hemisphere is $y = 0.67x + 14.57$, $R^2 = 0.36$, $p < 0.001$. The fitted line for the right hemisphere is $y = 0.66x + 14.74$, $R^2 = 0.34$, $p < 0.001$.

scale are represented in Fig. 3.9. From the plots in this figure, one may draw the following conclusions :

- The significant positive exponent coefficients $\alpha$ ($p < 0.001$) reveal a positive allometric scaling of gyrification indices with volume.
- The positive allometric scaling confirms that the larger brains are more folded.
- The values of the exponent coefficient $\alpha$ of wGI is more than that of sGI ($0.67 > 0.37$ and $0.66 > 0.36$ for left and right hemispheres, respectively) while the proportion of the variance of sGI explained by the volume is higher than that of wGI ($0.44 > 0.36$ and $0.47 > 0.34$ for left and right hemispheres, respectively).
- The almost equal linear regression equations of the left and right hemispheres suggest that in the global hemispheric scale, the degree of folding of the left and right hemispheres increase with volume symmetrically.

**Local scale.**

The above-mentioned results support this hypothesis that the larger brains are more folded but they do not illustrate which cortical regions get more folded in larger brains. To address this question, we perform the scaling analysis at the vertex level. Thanks to the inter-subject matching by Hip-Hop method (AUZIAS et al. 2013), we are able to find the corresponding vertices across all subjects. More precisely, the sGI and wGI maps of each subject are projected to the template cortical surface *hiphop138* by Hip-Hop method. Then the power law model (3.4) is fitted to GI-$V$ data of corresponding vertices in a log-log scale where $\mathrm{GI}$ denotes the sGI or wGI value of a cortical vertex and $V$ is the original hemispheric volume (i.e. the volume of the hemisphere that the vertex belongs to). In this way, a pair of $(\alpha, \log(k))$ is obtained for each set of corresponding vertices.

The maps of the significant exponent coefficient $\alpha$ ($p < 0.05$, corrected for multiple comparisons using False Discovery Rate (FDR) BENJAMINI et al. 1995) for sGI and wGI of the left/right hemispheres derived from the medium window ($\tau = 1e - 3$) are represented in Fig. 3.10. In this figure, the vertices for which $\alpha$ is not significant are masked by the gray color. Fig. 3.10 shows that in the adult population, as brain size increases, deep folds with low gyrification (represented in blue in Figs. 3.8a–3.8d), such as the central sulcus, the insula, the superior temporal sulcus, and the parieto-occipital sulcus, show the largest increase in folding complexity.

We have not observed any vertex with significant negative exponent except in few vertices of the right hemisphere with the most local window ($\tau = 2e - 4$). In this case, for sGI map, we observed about 0.04% of vertices with significant negative $\alpha$ exponent located on the anterior cingulate and the superior parietal cortices. For wGI, there are only 0.02% of vertices with significant negative $\alpha$ exponent located on the isthmus cingulate cortex.

## 3.3. Summary and discussion

To quantify the surface complexity, the proposed GIs in Chapter 2, i.e. sGI and wGI, were computed for some synthetic surfaces as well as a database of 124 healthy adult brains. For comparison, a surface area-based GI, i.e. Toro's GI, is also computed for those surfaces. The experiments on synthetic surfaces elucidates the key feature of our method that surface area-based methods lack : differentiating deep smooth folds from high oscillating ones. The feature is also observed on individual and group gyrification maps of cortical surfaces.

Through some experiments on synthetic surfaces, we clarified that Toro's GI (TORO et al. 2008) may fail to discriminate between deep and oscillating folds. These experiments revealed that this method take the surface area ratio as GI without paying attention to the source of the surface area which may roots in deep smooth folds or high oscillating folds. Consequently, when computed on a cortical surface, it gives higher values to deep folds where there are more surface area than in oscillating shallow ones (Figs. 3.8e and 3.8f). We didn't repeat the experiments for other surface area-based methods such as Schaer's method but due to similar reasoning behind Toro's and Schaer's GI which results in almost similar GI maps (Fig. 1.7), we believe that a similar behavior can be observed in

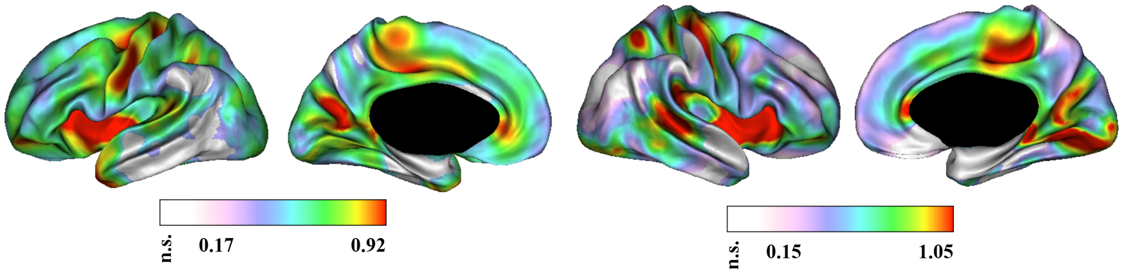

(a) sGI–left

(b) sGI–right

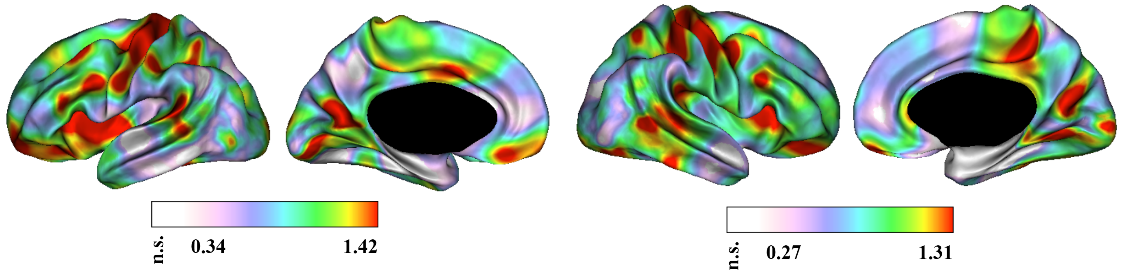

(c) wGI–left

(d) wGI–right

Figure 3.10.: The colormaps encode the significant exponent $\alpha$ ($p < 0.05$, corrected for multiple comparisons using FDR) of vertex-wise allometric analysis (3.4) of gyrification indices (a–b) sGI and (c–d) wGI of the left and right hemispheres derived from the medium window ($\tau = 1e - 3$). The magenta and red colors indicate the extremes of low and high values of $\alpha$. The regions where $\alpha$ is not significant (n.s.) are masked by gray color. The higher the value of $\alpha$, the higher the variation of folding with respect to volume.

the case of Schaer's GI.

In contrast, experiments on synthetic surfaces justify that our proposed GIs can distinguish deep folds from oscillating ones. They appropriately assign low values to walls of deep folds that are relatively smooth and high values to regions consisting of sharp or oscillating folds. The GIs when computed on cortical surfaces, demonstrate that the primary folds like the central sulcus and the insula are less folded than other regions. The central sulcus is a good example since it is a very deep fold but with a high regularity and straight shape where we expect a low measure of folding whereas surface area-based methods usually show high gyrification values (see Fig. 3.8). On an individual brain surface, we also showed how sGI and wGI distinguish different aspects of the surface complexity : magnitude of bending and frequency of bends.

Another difference between our method and surface area-based methods is that the latter may be not localized enough for some applications. For example, as depicted in Fig. 1.8, Schaer's GI shows that for a small spherical neighbourhood, the most folded region of the cortex is around the Sylvian Fissure and as the size of the neighbourhood increases, the same pattern propagates across the cortex. Therefore, it may fail to catch other folded parts of the brain, thus affecting the reliability of findings. In our method, by tuning the neighbourhood size, we get the results at different spatial scales, ranging from a very local scale (in order of a part of a sulcus/gyrus) to a more global scale (in order of a lobar cortex) ; see Figs. 2.13 and 3.5. Especially, distributions of sGI and wGI values in fine scales (e.g. the window size $\tau = 2e - 4$) justify that the proposed GIs are able to catch fine complexities of a cortical surface ; see the first column of Fig. 3.5.

To investigate the relationship between the volume and the degree of folding of the cerebral cortex, we considered a power law to model the GI as a response to the volume. The resulted positive exponent coefficient $\alpha$ indicates a positive allometric relation. It implies that if the brain volume is doubled, the GI is multiplied by factor $2^{\alpha}$. Moreover, it supports the well-known hypothesis in literature that larger brains are more folded than what expected by an isometric scaling. This result is predicted by some mechanical models of cortical folding process, introduced by Toro et al. 2005 and Tallinen et al. 2013, and deserves further investigations, in particular in longitudinal databases.

The relative low but still significant coefficient of determination of power law, $R^2$, clarifies that there is still enough room for other covariates, beyond the volume, to explain the degree of gyrification. One interesting direction for future studies is to take into account some biological factors like age, sex, genetic conditions etc. or cognitive factors like IQ and behavioural ones like sport skills, skill of playing musical instrument etc. in the scaling model. Similar studies by using different GIs have been documented in Section 1.2.

We also fitted the power law model to GIs at the vertex level to investigate how the degree of folding of adult brains changes locally with the hemispheric volume. The results illustrate that the less folded cortical regions, in terms of either the magnitude of the mean curvature or its variation, like the walls of the precentral and postcentral gyri and the insula, are more convoluted in larger brains. Regarding the allometric relation between the brain volume and the cortical surface area (Toro et al. 2008), one may conclude that the cerebral cortex of a larger brain is twisted in relatively flat walls of deep folds to accommodate the additional surface.

Finally, it is noteworthy that our method naturally allows us to monitor the changes of the degree of gyrification at different spatial scales simply by changing the window size $\tau$. Consequently, the local scaling analysis can be performed in arbitrary spatial scales. For example, tuning the window size up to a lobar window spread, makes it possible to see how the complexity of lobar regions change with the brain size.

# 4. Fractional Brownian gyrification index

Fractional Brownian surfaces have been introduced by GELBAUM 2014 through the definition of fractional Brownian motions (fBm's) indexed on manifolds. Such motions have the same properties as fBm's that are indexed on $\mathbb{R}$ i.e. self-similarity, Hölder continuous sample paths and stationary increments. An fBm indexed on a manifold $\mathcal{S}$ is defined as a random series of Laplace-Beltrami eigenfunctions corresponding to $\mathcal{S}$ :

$$R_H(x) = C \sum_{l=1}^{\infty} (\lambda_l)^{-(\frac{d}{4}+\frac{H}{2})} (\phi_l(x) - \phi_l(o)) \xi_l, \tag{4.1}$$

where $C > 0$ is an arbitrary coefficient, $x$ is a point of $\mathcal{S}$, $o$ is a fixed point of $\mathcal{S}$, $\lambda_l$ and $\phi_l$ denote the $l$-th Laplace-Beltrami eigenvalue and eigenfunction corresponding to $\mathcal{S}$, $d$ is the dimension of $\mathcal{S}$ and $\{\xi_l\}$ are i.i.d. standard normal random variables.

In this equation, $H \in (0, 1)$ is called the Hurst parameter, named after Harold Edwin Hurst (1880-1978), the British hydrologist who pioneered the field. It determines the characteristic of an fBm. Particularly, if $H < 1/2$, the increments of fBm are negatively correlated. In contrast, for $H > 1/2$, the increments of fBm are positively correlated. It means that in case of $H > 1/2$, if $R_H(x)$ deviates from its mean at point $x_0$, it has tendency to deviate more on other points around $x_0$ as well. In other words, observations of a motion, that are far from each other, are correlated strongly. This feature is called "*long-range dependency*" or "*long–term memory*" of fBm. $H$ also determines the Hölder regularity of an fBm : the smaller the $H$, the less regular the fBm.

Theoretically, the long-range dependency feature is characterized by the asymptotic behavior of the autocovariance function of fBm (e.g. COEURJOLLY 2000). Moreover, due to Weyl's theorem, we have $\lambda_n \sim O(n^{2/d})$ (see Corollary 1). Accordingly, as $H$ increases, the role of lower frequencies in constructing the field becomes more important which increases the regularity of the motion.

To identify an fBm, estimating its Hurst parameter is essential. To the best of our knowledge, however, there is no estimation of this parameter for fBm's indexed on manifolds. In this chapter, we develop an estimator of the Hurst parameter of a given fBs by using spectral analysis. We then interpret the Hurst parameter as a measure of surface complexity. In fact, large values of $H$ denote high regularity of the motion and are associated to less complex fractional Brownian surfaces. In contrast, low values of $H$ corresponds to more complex surfaces. Given this interpretation, we employ the Hurst parameter as a gyrification index of the cerebral cortex. In this analysis, we assume that the cortical surface may be recognized as a fractional Brownian surface.

In Section 4.1, we give a brief review on necessary definitions of standard and fractional Brownian motions indexed on $\mathbb{R}$. The generalization of fBm's to manifolds are also discussed in this section. Some methods for the estimation of Hurst parameter for fBm's defined on $\mathbb{R}$ are reviewed in Section 4.1.3. We present the proposed spectral estimator of Hurst parameter for fBm's indexed on manifolds in Section 4.2. Then, this estimator is evaluated on synthetic fractional Brownian spheres in Section 4.3. An application of this method to real fetal brains is also given in this section. Finally, some aspects of the proposed algorithm are discussed in Section 4.4.

## 4.1. Fractional Brownian motion

In this section, essentials of fBm's are reviewed briefly. First, the definitions and simulations of fBm's indexed on $\mathbb{R}$ are given. Then the extension of fBm's to manifolds is explained. Finally, existing estimation methods of Hurst parameter for fBm's indexed on $\mathbb{R}$ are briefly surveyed.

### 4.1.1. Fractional Brownian motion indexed on $\mathbb{R}$

Most of the following definitions are found in GELBAUM 2014.

**Definition 2.** *Let $(\Omega, \mathcal{F}, P)$ be a complete probability space where $\Omega$ is the sample set (i.e. the set of all possible outcomes), $\mathcal{F}$ is the set of events and $P$ is the probability function that assigns probabilities to events i.e. $P : \mathcal{F} \to [0, 1]$. Let $I$ be an index set that corresponds to points of $\mathbb{R}$. A set of random variables $\{X(t, \omega), t \in I, \omega \in \Omega\}$ is called a Gaussian random field (GRF) if for any finite subset $\{t_k, k = 1, 2, \ldots, n\} \subset I$, the random vector $\Big(X(t_k)\Big)_{k=1}^{n}$ has a joint normal distribution.*

**Definition 3.** *Let $\{X(t, \omega), t \in I, \omega \in \Omega\}$ be a GRF. For each $\omega \in \Omega$, $X(t, \omega)$ or briefly $X(t)$ defines a real valued function on $I$ that is called a sample path of that GRF.*

**Definition 4.** *A sample path $X(t)$ is said to be Hölder continuous (regular) of order $\alpha$ if there are nonnegative real constants $\mathcal{C}$ and $\alpha$ such that*

$$|X(t) - X(s)| \leq \mathcal{C}|t - s|^{\alpha}, \quad \forall t, s \in I. \tag{4.2}$$

**Definition 5.** *If* $\mathbb{E}[X(t)]$ *denotes the expectation value of* $X(t)$ *i.e.*

$$\mathbb{E}[X(t)] = \int_\Omega X(t,\omega)dP(\omega), \quad t \in I, \tag{4.3}$$

*then the covariance of the GRF* $\{X(t), t \in I\}$ *is defined by*

$$Cov\Big(X(s), X(t)\Big) := \mathbb{E}[X(s)X(t)] - \mathbb{E}[X(s)]\mathbb{E}[X(t)], \qquad s, t \in I. \tag{4.4}$$

An important feature of GFR's is that a GFR is uniquely determined by its covariance. For a centered GRF, i.e. $\mathbb{E}[X(t)] = 0,\ \forall t \in I$, which is the case here, the covariance of the field is reduced to $\mathbb{E}[X(s)X(t)],\ s,t \in I$.

The standard Brownian motion is an example of GRF on $[0, \infty)$ with a specific covariance function.

**Definition 6.** *The standard Brownian motion* $B(t)$ *on* $[0, \infty)$ *is the centered GRF with the covariance given by*

$$\mathbb{E}[B(s)B(t)] := min\{s,t\} = \frac{|s| + |t| - |t-s|}{2}. \tag{4.5}$$

*The generalization of this field to the fractional Brownian motion (fBm)* $R_H(t)$ *is obtained by the following covariance for* $H \in (0,1)$

$$\mathbb{E}[R_H(s)R_H(t)] := \frac{|s|^{2H} + |t|^{2H} - |t-s|^{2H}}{2}. \tag{4.6}$$

*In case of* $H = 0.5$*, fBm is simply a standard Brownian motion i.e.* $R_{0.5}(t) = B(t)$.

The fBm was first defined by MANDELBROT et al. 1968 as a fractional stochastic integral of a Gaussian pure white noise. It is known to be self-similar of order $H$ i.e. $R_H(ct) \overset{d}{=} c^H R_H(t),\ \forall c > 0$ where $\overset{d}{=}$ means to have the same statistical distribution. Moreover, it has stationary increments i.e. $R_H(t) - R_H(s) \overset{d}{=} R_H(t-s)$.

**Simulations.** In the literature, several methods have been suggested to simulate fBm's. The very first one, proposed by MANDELBROT et al. 1968, roots in an approximation of the integral definition of fBm. ABRY et al. 1996 suggested to decompose the Gaussian pure white noise by using wavelets and then do the integration. Another method is based on Choleski decomposition of the covariance matrix derived from Eq. (4.6) ; see e.g. ASMUSSEN 1999. Two other methods are based on the increment process of fBm's i.e. $X_H(t) = R_H(t+1) - R_H(t)$, known also as fractional Gaussian noise or fGn. In these methods, known as Levinson's (e.g. PELTIER 1998) and Wood-Chan's (DAVIES et al. 1987 and WOOD et al. 1994) methods, an increment process is generated. Then, an fBm is constructed by accumulated sums of fGn $R_t^H = \sum_{s=0}^{t} X_s^H$. A good review on those methods

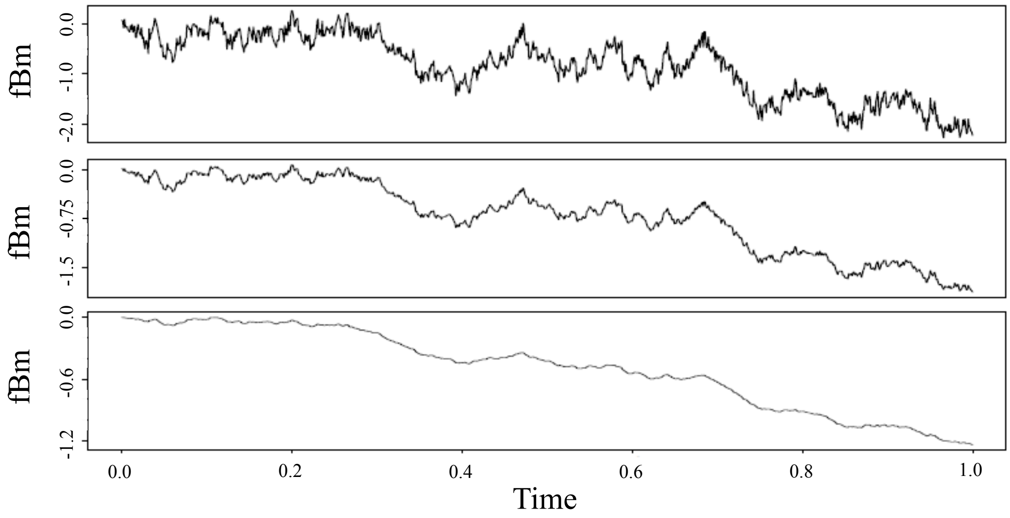

Figure 4.1.: An example of an fBm on $[0, 1]$, simulated by Wood-Chan's method. From top to bottom, $H = 0.3, 0.5, 0.8$. The figure is adapted from Coeurjolly 2000.

and a quantitative comparison between those methods are given by Coeurjolly 2000. Some other methods and references can also be found in Dieker 2004. An example of an fBm, simulated by Wood-Chan's method, is represented in Fig. 4.1 for different values of Hurst parameter.

### 4.1.2. Fractional Brownian surfaces

Some research has been done to replace $\mathbb{R}$ by other indexing sets e.g. manifolds. The first attempt has been done by Paul Lévy who extended the standard Brownian motion indexed on $\mathbb{R}$ to the one on $\mathbb{R}^d$ with the covariance function as

$$\mathbb{E}[B(s)B(t)] := \|s\| + \|t\| - \|t - s\|, \quad s, t \in \mathbb{R}^d, \tag{4.7}$$

where $\|.\|$ denotes the Euclidean norm of $\mathbb{R}^d$. A similar generalization can be done in the case of fBm where the norms get power of $H$. He, then, extended this field to the sphere $\mathbb{S}^d$ (Lévy 1965). He constructed a Brownian random field on $\mathbb{S}^d$ through the covariance function given by

$$d(x, o) + d(y, o) - d(x, y), \tag{4.8}$$

where $d(x, y)$ denotes the geodesic distance between $x$ and $y$ and $o$ is a fixed point on the sphere considered as the origin. Further extensions of Fractional Brownian motions to other manifolds have been done by Gangolli 1967 and Molchan 1988.

In the same direction, Istas 2005 extended the fractional Brownian motions to some specific manifolds (like spheres and hyperboloids) for a limited range of Hurst parameter $H \in (0, 0.5]$ with covariance

$$\frac{1}{2}(d(x,o)^{2H} + d(y,o)^{2H} - d(x,y)^{2H}), \tag{4.9}$$

where $d(.,.)$ is the metric of the manifold and $o$ is a fixed point on the manifold considered as the origin. He, however, showed that for a general manifold, function (4.9) can fail to define a covariance (see also VENET 2016).

Recently, GELBAUM 2014 has generalized the fractional Brownian motions to a variety of manifolds for the full range of Hurst parameter $H \in (0, 1)$. This variety includes any compact manifold and a wide range of non compact manifolds. In this work, instead of considering a covariance function in form of (4.9), a spectral characterization of the covariance has been chosen in terms of Laplacian operator on $\mathbb{R}^d$ which has a straightforward extension to manifolds by the Laplace-Beltrami operator $\Delta$.

Formally, for a Riemannian manifold $\mathcal{M}$ and its Laplace-Beltrami operator there is a corresponding heat kernel $K_t(x, y)$ which is the fundamental solution to the heat equation on $\mathcal{M} \times (0, \infty)$

$$\begin{cases} (\frac{\partial}{\partial t} - \Delta_x)K_t(x,y) = 0, \\ K_0(x,y) = \delta_x(y), \end{cases} \tag{4.10}$$

where the index $x$ of $\Delta$ underlines that this operator acts only on $x$ and $\delta$ is the Dirac delta. The heat kernel has an eigenfunction expansion based on the eigenvalues $\{\lambda_l, l = 1, 2, ...\}$ and eigenfunctions $\{\phi_l(x), l = 1, 2, ... x \in \mathcal{M}\}$ of Laplace-Beltrami operator :

$$K_t(x,y) = \sum_{l=1}^{\infty} e^{-\lambda_l t}\phi_l(x)\phi_l(y) \tag{4.11}$$

Now, from the spectral characterization of the covariance, the covariance of the fractional Brownian motion $R_H(x)$ over $M$ is defined by

$$\mathbb{E}[R_H(x)R_H(y)] := \frac{1}{\Gamma(\frac{d}{2}+H)}\int_0^{\infty} t^{\frac{d}{2}+H-1}(K_t(x,y) - K_t(x,o) - K_t(y,o) + K_t(o,o))dt, \tag{4.12}$$

where $o$ is a fixed origin on $\mathcal{M}$ and $\Gamma$ denotes the Gamma function. By replacing $K_t$ from Eq. (4.11) in the covariance (4.12) and taking the integral, a series expression of $R_H(x)$ is computed as below :

$$R_H(x) = C\sum_{l=2}^{\infty}(\lambda_l)^{-(\frac{d}{4}+\frac{H}{2})}(\phi_l(x) - \phi_l(o))\xi_l \tag{4.13}$$

where $C > 0$ is an arbitrary coefficient, $o$ is a fixed origin point on the manifold and $\{\xi_l\}$ are i.i.d. standard normal random variables.

It has been proved that this series is convergent, thus the motion exists over manifolds. Basic features of such motions, namely the self similarity, stationary of increments have been also proven. Especially, the Hölder regularity of $R_H$ is held (GELBAUM 2014, Theorem 3.14) :

**Theorem 4.** *If $\mathcal{M}$ is a compact Riemannian manifold, then the fractional Brownian motion defined on it is Hölder continuous of any order $\alpha \leq H$ i.e. there exist a constant $\mathcal{C}$ such that*

$$\forall \alpha \leq H, \forall x, y \in \mathcal{M}: \quad \mathbb{E}[|R_H(x) - R_H(y)|^2] \leq \mathcal{C} d(x,y)^{2\alpha}. \tag{4.14}$$

**Simulation.**

To simulate fractional Brownian surfaces, GELBAUM et al. 2014 applied a truncated series of Eq. (4.13) on triangulated smooth manifolds e.g. cylinder and sphere. For these manifolds, the analytic Laplace-Beltrami eigenvalues and eigenfunctions are known. In general, however, it is possible to use a discretization of Laplace-Beltrami operator on manifolds.

In this thesis, we use a linear finite element (FE) discretization of Laplace-Beltrami on a triangulated manifold to compute its eigenpairs ; see Section 2.4.1 for more information on the discretization. In this case, if a manifold is sampled by $N$ vertices, the FE discretization of Laplace-Beltrami operator gives a set of eigenvalues $\{\lambda_l, l = 1, 2, \dots, N\}$ and a set of eigenvectors $\{\psi_l, l = 1, 2, \dots, N\}$ which are orthonormal with respect to the $B$-inner product (2.26). Therefore, $\phi_l = B^{1/2}\psi_l$ are orthonormal with respect to Euclidean inner product i.e.

$$\langle \phi_k, \phi_l \rangle = \delta_{kl}.$$

If the triangulation is fine enough, due to Weyl's theorem, the contribution of $M$th term in Eq. (4.13) is of order $O(M^{-(d/4+H/2)})$ which becomes negligible for large $M$'s. It means that, in practice, only first $M < N$ eigenpairs are enough to generate the random field. Thus, for every vertex $P_n$, the fractional Brownian random field is approximated by

$$R_H(n) = C \sum_{l=2}^{M} (\lambda_l)^{-(\frac{d}{4}+\frac{H}{2})} (\phi_l(n) - \phi_l(o)) \xi_l, \tag{4.15}$$

where $o$ is a fixed vertex considered as origin. By displacing each vertex $P_n$ as much as $R_H(n)$ in direction of the normal vector to the surface at $P_n$, the fractional Brownian surface is constructed. For example, in Fig. 4.2, a fractional Brownian sphere is presented with different values of $H$. It is clear that as $H$ decreases, the irregularity of the surface increases.

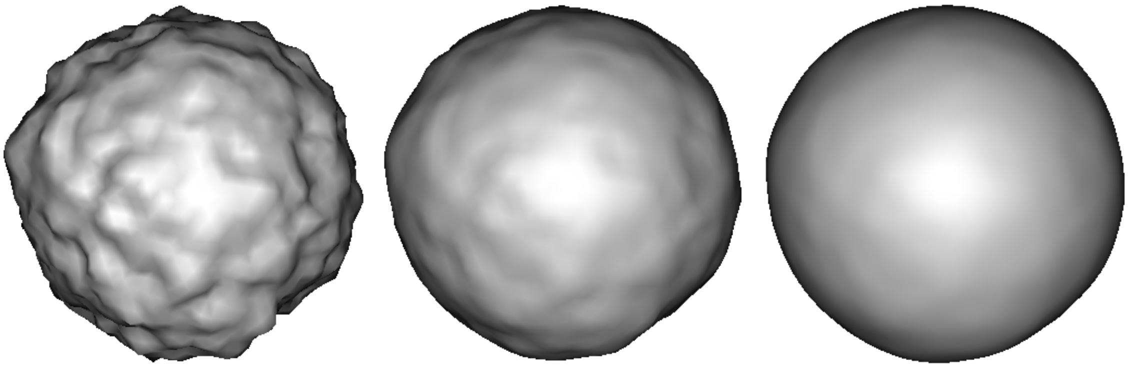

(a) $H = 0.1$ (b) $H = 0.5$ (c) $H = 0.9$

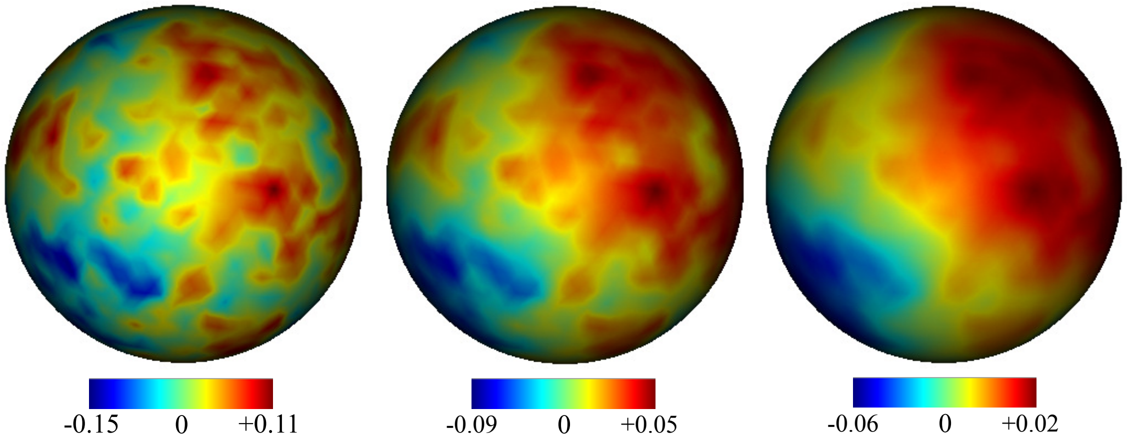

(d) $H = 0.1$ (e) $H = 0.5$ (f) $H = 0.9$

Figure 4.2.: Top row : fractional Brownian spheres with the same random variables $\{\xi_l\}$ but different $H$ values. Bottom row : Corresponding fractional Brownian motions.

### 4.1.3. Estimation of Hurst parameter for fBm's indexed on $\mathbb{R}$

Given an fBm realization, to analyse its properties and forecasting its behavior, one needs to estimate its Hurst parameter. Although, due to the non-stationary of fBm and its long–range dependency feature, estimation of $H$ is not an easy and straightforward task. It has been truly expressed in CLEGG 2006 :

> "*While the Hurst parameter is perfectly well-defined mathematically, it is, in fact, a very difficult property to measure in real life.*"

To do so, an extensive research has been done in past decades which results in several estimators. Here, we will review briefly some of them.

An early method is based on R/S statistic.
**R/S statistic.** (MANDELBROT et al. 1969)
If $R(n)$ is the range of the first $n$ data, i.e. the difference between the largest and smallest value of the sample, and $S(n)$ denotes the standard deviation of this sample, then

$$\mathbb{E}\left[\frac{R(n)}{S(n)}\right] = O(n^H), \qquad n \to \infty. \tag{4.16}$$

Now, the slope of linear regression of $\mathbb{E}\left[\frac{R(n)}{S(n)}\right]$ versus $n$ gives an estimation of $H$. This estimator is sensitive to outliers. Moreover, choosing a good range of $n$ is an issue in this method as well as for other methods described below.

An important set of methods are based on a spectral analysis.
**Log-periodogram.** (GEWEKE et al. 1983)
For any fBm $R_H(t)$, its fractional Gaussian noise (fGn) $X_H(t) := R_H(t+1) - R_H(t)$ admits a spectral density $f(\lambda)$ for which

$$f(\lambda) = O(|\lambda|^{1-2H}), \qquad \lambda \to 0. \tag{4.17}$$

On the other hand, the periodogram defined by

$$I_N(\lambda) = \frac{1}{2\pi N} |\sum_{t=0}^{N-1} X_H(t) e^{-it\lambda}|^2, \quad \lambda = \lambda_{k,N} = \frac{2\pi k}{N}, \tag{4.18}$$

is an asymptotic unbiased estimator of $f(\lambda)$. From Eqs. (4.17) and (4.18), it is deduced that

$$\log(\mathbb{E}[I_N(\lambda)]) \simeq \log(c) + (1 - 2H)\log(|\lambda|). \tag{4.19}$$

Accordingly, the slope of linear regression of $\log(\mathbb{E}(I_N(\lambda)))$ versus $\log(|\lambda|)$ near 0 gives an estimation of $H$.

**Variant of Lobato and Robinson.** (LOBATO et al. 1996)
Let $f$ still denote the spectral density of fGn and $F(\lambda) = \int_0^\lambda f(\theta)d\theta$. Then, for

$q \in (0,1)$,

$$\frac{F(q\lambda)}{F(\lambda)} = O(q^{2-2H}), \qquad \lambda \to 0. \tag{4.20}$$

Now, the logarithm of this equation for a range of values of $\lambda$ gives an estimation of $H$.

**Whittle's estimator.** (Beran 1994 ; Robinson 1995)
In this method, a functional of the periodogram $I_N(\lambda)$ is presumed. Then, by minimising the parameters of this functional through the maximum likelihood, $H$ is estimated. Choosing an appropriate functional is essential in this method. An example of such estimator is given by Beran 1994 :

$$\hat{H}_N = \arg\min_H \sum_{j=1}^{M} \frac{I_N(\lambda_{j,N})}{f(\lambda_{j,N},(1,H))}, \tag{4.21}$$

where $f(\lambda_{j,N},(1,H))$ is the spectral density with parameters $(1,H)$ of the fGn and $I_N(\lambda)$ denotes the periodogram.

**Wavelet decomposition.** (Abry et al. 1995) Let $\{\psi_{j,k}, j = 1,2,\ldots,J, k \in \mathbb{Z}\}$ be a family of wavelets and $\{\hat{R}_H(j)\}$ denotes the wavelet coefficients of an fBm $R_H(t)$. A linear relationship of the following form can be derived :

$$\log_2(\mathbb{E}[(\hat{R}_H(j))^2]) = (2H+1)j + C. \tag{4.22}$$

Accordingly, a linear regression of $\log_2(\mathbb{E}[(\hat{R}_H(j))^2])$ versus $j$ for a range of $j$ gives an estimation of $H$.

Some other methods including correlogram (e.g. Beran 1994) and temporal methods (Feuerverger et al. 1994 ; Coeurjolly 2001) can be found in literature. Some comparisons between these methods on synthetic and real data are found in Coeurjolly 2000 and Clegg 2006.

The above-mentioned methods propose some estimators of $H$ for fBm's indexed on $\mathbb{R}$. There is, however, no such $H$ estimator in the literature for fBm's indexed on manifolds. In the next section, we propose a method to deal with this situation.

## 4.2. The proposed spectral $H$ estimator for fractional Brownian surfaces

In this section, we develop an algorithm to estimate the Hurst parameter $H$ and $C$ of a given fractional Brownian surface. As explained in Section 4.1.2, a fractional Brownian motion $R_H$, defined on a smooth manifold, displaces the points of the manifold and produces a fractional Brownian surface. Accordingly,

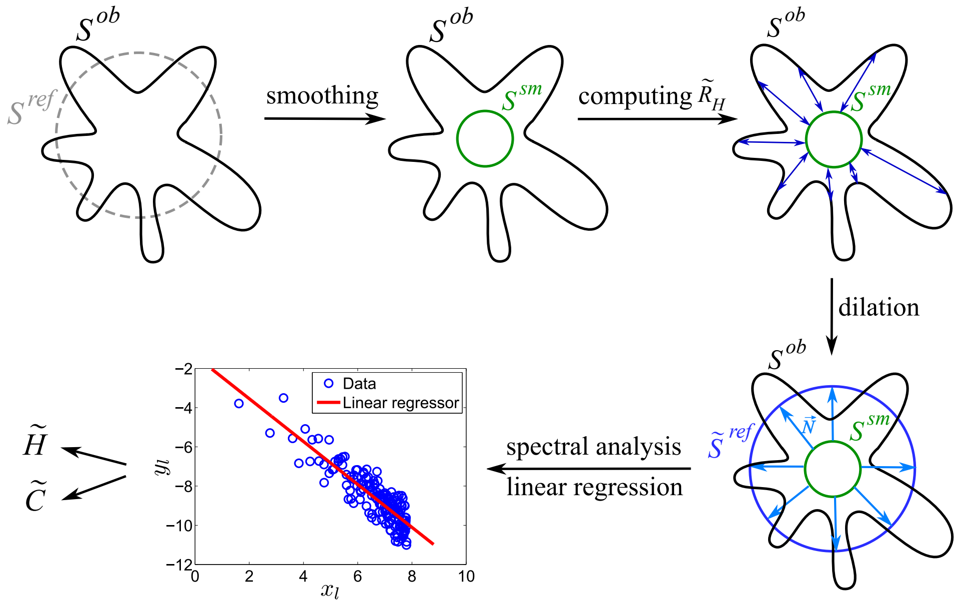

Figure 4.3.: A schematic representation of Algorithm 1. The input to the algorithm is an observed fractional Brownian surface ($\mathcal{S}^{ob}$) and outputs are estimation of the Hurst parameter $H$ and amplitude of the fractional Brownian motion $C$.

in this thesis, the original smooth manifold is called the *reference surface* and is denoted by $\mathcal{S}^{ref}$. Moreover, the given fractional Brownian surface is called the *observed surface* and is denoted by $\mathcal{S}^{ob}$.

In summary, the proposed algorithm is :

> Given a fractional Brownian surface $\mathcal{S}^{ob}$, we approximate the fractional Brownian motion $R_H$ and the reference surface $\mathcal{S}^{ref}$. Then, the spectral powers of approximated $R_H$ are modelled by a least square linear regression to estimate $H$ and $C$.

The proposed algorithm is given below in Algorithm 1 and is represented in Fig. 4.3. In following, we explain the details of this Algorithm.

**Algorithm 1** Estimation of Hurst parameter $H$

```
Require: Fractional Brownian surface $\mathcal{S}^{ob}$.
Smooth $\mathcal{S}^{ob}$ to get a smoothed surface $\mathcal{S}^{sm}$.
Compute $\tilde{R}_H$ as the centered Euclidean distance between $\mathcal{S}^{ob}$ and $\mathcal{S}^{sm}$.
Dilate $\mathcal{S}^{sm}$ to get an approximated reference surface $\tilde{\mathcal{S}}^{ref}$.
Compute the Fourier coefficients of $\tilde{R}_H$ on $\tilde{\mathcal{S}}^{ref}$ .
Apply the linear regression analysis in the spectral domain.
Return $\tilde{H}$ and $\tilde{C}$ derived from the slope and intercept of the linear regressor.
```

**1. Smoothing procedure.**

To get a smoothed surface from $\mathcal{S}^{ob}$, the mean curvature flow (MCF) is used. Generally speaking, MCF is based on solving the heat equation on a 2D manifold $\Omega_t$ with initial and boundary condition in a finite time (HUISKEN 1984) :

$$\begin{aligned} \frac{\partial f}{\partial t} &= -\Delta_t f, \qquad \text{on} \qquad \Omega_t \times (0,T] \\ f|_{t=0} &= f^0, \qquad \text{on} \qquad \Omega_t \end{aligned} \tag{4.23}$$

where $t$ is time variable, $\Omega_t$ is a spatial domain that may evolve with $t$, $f$ denotes a function of $t$ and spatial variables defined on $\Omega_t$ and $\Delta_t$ is the Laplace-Beltrami operator corresponding to the domain $\Omega_t$. If $\Omega_t$ is bounded, depending on situation, different boundary conditions can be applied e.g. Dirichlet or Neumann (see e.g. KREYSZIG 2010). Starting from an initial function $f = f^0$, as time progresses, the function $f$ becomes smoother.

To elucidate how the smoothing procedure works, let's consider an explicit discretization of the heat equation :

$$\frac{f^{m+1} - f^m}{dt} = -\Delta_m f^m \quad \Rightarrow \quad f^{m+1} = f^m - dt\Delta_m f^m \tag{4.24}$$

where $f^m$ denotes the value of $f$ at time $t_m$ and $dt$ is time step such that $t_m = m \times dt$. The Laplace-Beltrami operator $\Delta_m$ is related to the mean curvature $\kappa$ and normal vector $\overrightarrow{N}$ of $\Omega_m$ (MEYER et al. 2003) by

$$\Delta \equiv 2\kappa\overrightarrow{N}. \tag{4.25}$$

These equations together provide an interpretation of the mean curvature flow smoothing procedure :

$$f^{m+1} = f^m - 2dt\kappa\overrightarrow{N} f^m. \tag{4.26}$$

It means that in each time step, the value of $f$ at each spatial point is modified by a factor proportional to the mean curvature and inner normal vector of that point.

Let $f$ be the coordinate components of points of a surface $\Omega$. In this case, by applying Eq. (4.26) on $f$, the surface becomes smooth gradually. More precisely, given $f^0$ as the coordinate components of points of a domain $\Omega_0$, $f^m,\ m = 1, 2, \ldots$ will give the points of new domains $\Omega_m,\ m = 1, 2, \ldots$. Above equation explains that at every iteration of the mean curvature flow, each point moves in its corresponding inner normal direction by an amount proportional to the magnitude of the corresponding mean curvature. In this manner, convex points move inward whereas concave points move outward and the speed of movement is ruled by the magnitude of the mean curvature. Independent of the inward and outward movements, the surface always shrinks so that the total surface area will even-

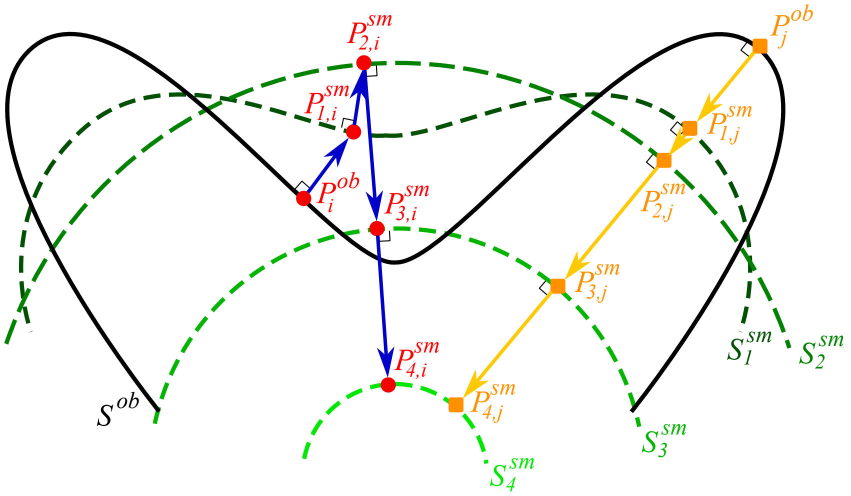

Figure 4.4.: A 2D drawing that explains the mean curvature flow smoothing procedure. Smoothing procedure applied on $\mathcal{S}^{ob}$ to get $\mathcal{S}^{sm}_m$, $m = 1, 2, 3, 4$ iteratively. Geodesic paths of two points $P^{ob}_i$ and $P^{ob}_j$ to their corresponding points on the final smoothed surface $\mathcal{S}^{sm}_4$ are shown in blue and yellow colors respectively.

tually go to zero in a finite time (e.g. COLDING et al. 2015).

A schematic representation of this procedure is given in Fig. 4.4. In this figure, the smoothing procedure is applied on $\Omega_0 = \mathcal{S}^{ob}$ to get surfaces $\Omega_m = \mathcal{S}^{sm}_m$, $m = 1, 2, 3, 4$ iteratively. Interestingly, the point correspondence between $\mathcal{S}^{ob}$ and $\mathcal{S}^{sm}_m$, $m = 1, 2, \ldots$ is preserved i.e. for each vertex $P^{ob}_n$ on $\mathcal{S}^{ob}$, there is a corresponding vertex $P^{sm}_{m,n}$ on $\mathcal{S}^{sm}_m$. The movement trajectories of two points $P^{ob}_i$ and $P^{ob}_j$ are depicted in Fig. 4.4. $P^{ob}_i$ and $P^{ob}_j$ are points of $\mathcal{S}^{ob}$ located on valley and top respectively. The blue and yellow lines show the smoothing trajectory of these points.

In practice, to solve Eq. (4.23) numerically, the time derivative is discretized by the first order backward finite difference method :

$$\frac{\partial f}{\partial t}\Big|_{t_{m+1}} \simeq \frac{f^{m+1} - f^m}{dt}, \tag{4.27}$$

The linear finite element method is used to discretize the Laplacian operator, as explained in Section 2.4.1. It results in two sparse matrices $A$ and $B$ corresponding to a mesh modelling the domain $\Omega$ ; see Eqs. (2.24) and (2.25). Therefore, an implicit discretization of the heat equation (4.23) is :

$$B\frac{f^{m+1} - f^m}{dt} = -Af^{m+1}, \tag{4.28}$$

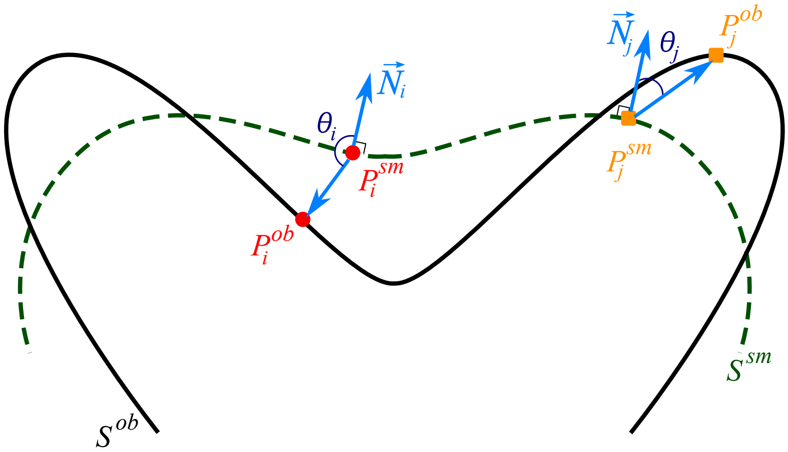

Figure 4.5.: A schematic representation of checking procedure of the relative positions of $\mathcal{S}^{ob}$ and $\mathcal{S}_m^{sm}$ by measuring angles. $P_i^{sm}$ is located out of $\mathcal{S}^{ob}$ thus $\theta_i > \pi/2$. In contrary, $P_j^{sm}$ is located inside the $\mathcal{S}^{ob}$, so $\theta_j < \pi/2$.

which is equivalent to

$$(B + dtA)f^{m+1} = Bf^m. \tag{4.29}$$

This approach is proven to be numerically stable even for large time steps and convergent, at least for convex surfaces (HUISKEN 1984).

It is noted that the mean curvature flow is originally a non-linear procedure. It is because the Laplacian operator is corresponding to the evolutionary domain and should be recomputed after each step of smoothing. To be efficient in computing time, however, we compute the Laplacian operator just once for the initial observed surface $\mathcal{S}^{ob}$. Moreover, we found that using the non-linear procedure leads to a smoothed surface with highly non-homogeneous mesh which will be troublesome for next steps of our algorithm, especially the dilation step.

In case of cortical surfaces, the smoothing iterations stop when the smoothed surface $\mathcal{S}_{\mathcal{N}}^{sm}$ is entirely inside the cortical surface $\mathcal{S}^{ob}$. This stopping criterion is checked automatically by using a heuristic method at each iteration : a vector from each point $P_n^{sm}$ on $\mathcal{S}^{sm}$ to its corresponding point $P_n^{ob}$ on $\mathcal{S}^{ob}$ is considered. The angle of this vector with the normal vector to $\mathcal{S}^{sm}$ at $P_n^{sm}$ is computed. If this angle is obtuse, it means that $\mathcal{S}^{sm}$ is still out of $\mathcal{S}^{ob}$. In Fig. 4.5, this checking procedure is shown.

Finally, it is noted that displacing the points of $\mathcal{S}^{ref}$ by $R_H$ moves its barycenter with a small value. The smoothing procedure also moves the barycenter of the surface after each iteration. Since the barycenter of $\mathcal{S}^{ref}$ is not known for us, we correct the barycenter of the smoothed surface after each iteration of smoothing to that of $\mathcal{S}^{ob}$. In this way, at the end of smoothing procedure, the barycenter of $\mathcal{S}_{\mathcal{N}}^{sm}$ is the same as that of $\mathcal{S}^{ob}$.

**2. Approximation of the fractional Brownian motion.**

After obtaining a smoothed surface $\mathcal{S}_{\mathcal{N}}^{sm}$ in the previous step, we continue with approximating $R_H$. In theory, $R_H(n)$ is the signed distance between a vertex $P_n^{ref}$ of the reference surface $\mathcal{S}^{ref}$ and the corresponding vertex $P_n^{ob}$ on the observed fBs $\mathcal{S}^{ob}$.

Since the reference surface is not known in practice, we approximate the distance by a distance between the observed surface and the smoothed surface. For this purpose, first, $R_H(n)$ is approximated by

$$R_H(n) \simeq d(n) - r(n), \tag{4.30}$$

where

- $d(n) = d(P_n^{ob}, P_{\mathcal{N},n}^{sm})$ is the distance between the vertex $P_n^{ob}$ and the corresponding vertex $P_{\mathcal{N},n}^{sm}$ of the smooth surface $\mathcal{S}_{\mathcal{N}}^{sm}$,
- $r(n) = d(P_{\mathcal{N},n}^{sm}, P_n^{ref})$ is the distance between $P_{\mathcal{N},n}^{sm}$ and the corresponding vertex $P_n^{ref}$ of the unknown reference surface.

Since the exact value of $r(n)$ is unknown, it is approximated by its average i.e. $\overline{r} = 1/N \sum_{n=1}^{N} r(n)$. So,

$$R_H(n) \simeq d(n) - \overline{r}, \quad \forall n = 1, 2, \ldots, N. \tag{4.31}$$

On the other hand, taking the average of each term in Eq. (4.30) gives

$$\begin{aligned} \frac{1}{N}\sum_{n=1}^{N} R_H(n) &= \frac{1}{N}\sum_{n=1}^{N} d(n) - \frac{1}{N}\sum_{n=1}^{N} r(n) && (4.32)\\ &= \overline{d} - \overline{r}, && (4.33) \end{aligned}$$

where $\overline{d}$ denotes the average of $d(n)$'s.

According to the model (4.15), the expectation of $R_H(n)$ is zero, hence $\overline{d} = \overline{r}$. Consequently, from Eq. (4.31), $\tilde{R}_H$, the approximation of $R_H$, is

$$\tilde{R}_H(n) = d(n) - \overline{d}, \tag{4.34}$$

and $\overline{d}$ is called *the characteristic radius*.

In our algorithm, the distance $d(n) = d(P_{\mathcal{N},n}^{sm}, P_n^{ob})$ is computed by the Euclidean distance between the corresponding points i.e.

$$d(n) = |P_{F,n}^{sm} - P_n^{ob}|. \tag{4.35}$$

Another choice to compute $d(n)$ could be the geodesic distance. Indeed, due to point trajectory between $P_{\mathcal{N},n}^{sm}$ and $P_n^{ob}$ i.e.

$$P_n^{ob} \equiv P_{0,n}^{sm} \rightarrow P_{1,n}^{sm} \rightarrow P_{2,n}^{sm} \rightarrow \cdots P_{\mathcal{N},n}^{sm},$$

given by the smoothing procedure, a way of computing $d(n)$ might be the geodesic distance between $P^{ob}_n$ and $P^{sm}_{F,n}$. It can be computed by a summation of the length of segments $P^{sm}_{i,n}P^{sm}_{i+1,n}$

$$d(n) = \sum_{i=0}^{F-1} |P^{sm}_{i+1,n} - P^{sm}_{i,n}|, \tag{4.36}$$

where $|a-b|$ denotes the Euclidean length between two points $a$ and $b$. Although the geodesic distance seems an intuitive choice, it overestimates the values of $R_H(n)$ for points $P_n$'s which are located on valleys. This overestimation is due to the behavior of the adapted smoothing procedure which moves points on valleys outward and then inward.

For example, as it is shown in Fig. 4.4, it is clearly seen that how $P^{ob}_i$ travels outward and inward to reach to the final point $P^{sm}_{4,i}$. This redundant outward and inward movements cause overestimation of $\tilde{R}_H(i)$. In contrast, $P^{ob}_j$ comes inward directly to its corresponding final point. Consequently, we choose the Euclidean distance which measures the shortest path between corresponding points thus causes no redundancy in the measurements.

In the mentioned approximation process of $R_H$, $r(n)$ is replaced by $\overline{r}$. Accordingly, the approximation quality depends on the difference between $r(n)$ and $\overline{r}$. So, if the variance of $r(n)$'s is low, then the approximation will be more precise.

In the following example, the motivation behind the proposed method of approximation of $R_H$ is explained in the case of a fractional Brownian sphere. For better understanding, a 2D drawing explains the situation in Fig. 4.6.

**Example 2.** *Let the reference surface $\mathcal{S}^{ref}$ be a sphere with radius $R$. Then, $R_H$ is applied on every point of the reference sphere in direction of the normal vector of the sphere to get the observed surface $\mathcal{S}^{ob}$.*

*Now, given the observed surface $\mathcal{S}^{ob}$, we want to approximate $R_H$. For this purpose, first, $\mathcal{S}^{ob}$ is smoothed by using the mean curvature flow. Let the smoothing procedure be iterated till we get the center of the sphere, $O$, as the smoothed surface $\mathcal{S}^{sm}_{\mathcal{N}}$*[a]*.*

*Consider a point $P^{ob}_i$ of $\mathcal{S}^{ob}$ for which $R_H(i) < 0$. The Euclidean path between $O$ and $P^{ob}_i$ overlaps with the radius $OP^{ref}_i$ of the sphere because the normal vector at $P^{ref}_i$ is in radial direction. So, two paths $OP^{ob}_i$ and $P^{ob}_iP^{ref}_i$ follow each other. Specially, $d(i) - R_H(i) = R$ where $d(i)$ is the length of $OP^{ob}_i$. The same situation is true for a point $P^{ob}_j$ for which $R_H(j) > 0$. In this case, two paths $OP^{ob}_j$ and $P^{ob}_jP^{ref}_j$ overlaps and $d(j) - R_H(j) = R$.*

*Similarly, for each $n$, the corresponding points $P^{ref}_n$ and $P^{ob}_n$ and the center of the sphere $O$ are colinear. Therefore, Eq. (4.30) holds exactly. Moreover, $\forall n : d(n) - R_H(n) = R$. It implies that $\forall n : r(n) = R$, and specially, $\overline{r} = \overline{d} = R$.*

---

[a] The MCF is not convergent to a point for any arbitrary non-convex surface but we observed it experimentally in the case of fBs's

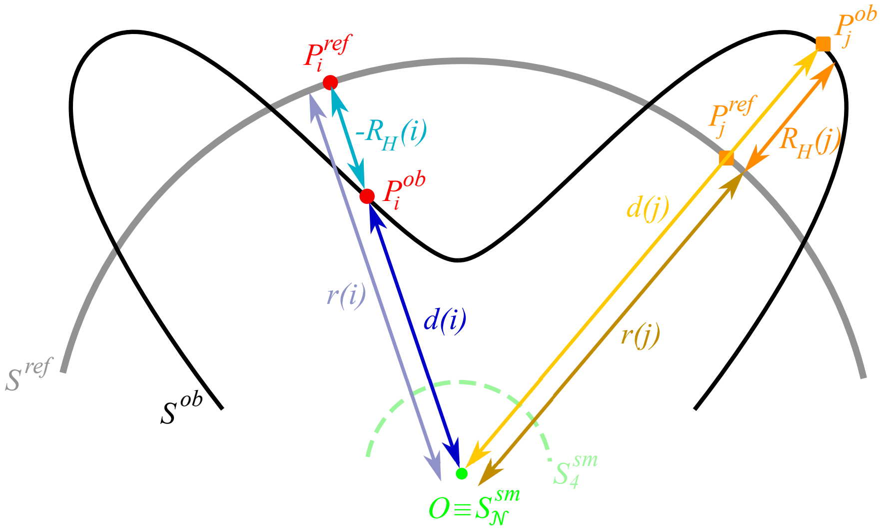

Figure 4.6.: The reference surface $\mathcal{S}^{ref}$ is assumed to be a sphere. Smoothing procedure is applied on $\mathcal{S}^{ob}$ to reach to the center of the reference sphere as the smoothed surface $\mathcal{S}_{\mathcal{N}}^{sm}$. The $R_H$, Euclidean distances $d$ and $r$ are shown for two points $P_i^{ob}$ and $P_j^{ob}$. It is seen that $r$ is equal to the radius of the reference sphere.

*That is why $\overline{d}$ is called the characteristic radius. Consequently, replacing $r(n)$ by $\overline{d}$ doesn't introduce error and the value of $R_H(n)$ can be computed exactly by $R_H(n) = d(n) - \overline{d}$.*

**3. Approximation of the reference surface.**

In this step, we approximate the reference surface from the small smoothed surface ($\mathcal{S}_{\mathcal{N}}^{sm}$). This surface is needed for the spectral analysis in the next step. To do this task, the $\mathcal{S}_{\mathcal{N}}^{sm}$ should be dilated to compensate the shrinkage induced by the mean curvature flow smoothing. In the case of the sphere as the reference surface and its center as the smoothed surface, mentioned in Example 2, if $\mathcal{S}_{\mathcal{N}}^{sm}$ is dilated as much as $\overline{d} \equiv R \equiv \overline{r}$ in radial directions (equivalent to normal directions in this case), then the reference surface is recovered ; see Fig. 4.6.

Inspired by the case of the fractional Brownian sphere, we adapt this dilation strategy in case of other fractional Brownian surfaces to compute an approximation of the reference surface $\tilde{\mathcal{S}}^{ref}$. Precisely, the smoothed surface $\mathcal{S}_{\mathcal{N}}^{sm}$ is dilated in direction of its normals as much as its characteristic radius $\overline{d}$.

If $\mathcal{S}^{sm}$ is not convex, the dilation may cause some mesh difficulties e.g. point crossing. Especially, it happens when the amount of dilation is high and vertices of very obtuse triangles are dilated in transverse directions. In this case, those triangles may pass through each other or make an excrescence, thus destroy the mesh locally. An example of this situation is presented in Fig. 4.7. In this example, a fetal brain hemisphere is smoothed and dilated by using the proce-

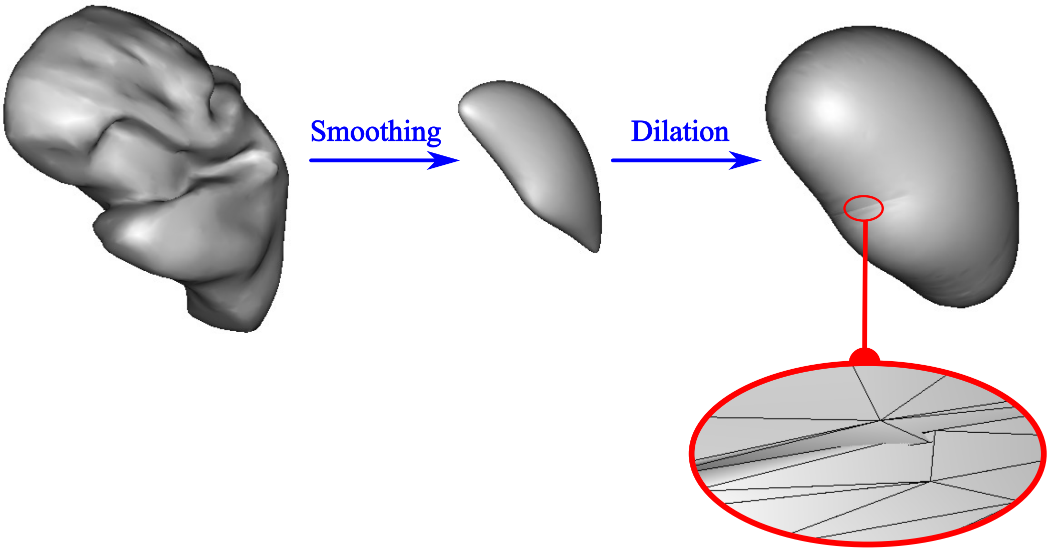

Figure 4.7.: This figure shows the results of smoothing and dilation processes on a fetal brain hemisphere. This is an example of dilating a non-convex smooth surface in one step. As the zoom on the dilated surface shows, it may corrupt the triangulation locally due to point crossing.

dures explained so far. The zoom on the location of the insular cortex shows how the triangles merge to each other and corrupt the mesh locally.

To avoid this situation, we introduce the idea of *iterative dilation with surgery*. The general concept of this idea is that instead of dilating the smoothed surface once by the amount of its characteristic radius $\overline{d}$, the dilation is done in $m$ iterations. At each iteration, problematic triangles are identified and kept fixed while other triangles are dilated by the amount of $\overline{d}/m$. So, by reducing the amount of dilation from $\overline{d}$ to $\overline{d}/m$, and by controlling problematic triangles, the issue of point crossing is treated.

The steps of this strategy is as follow :

(a) A number of iterations $m$ is chosen such that $\overline{d}/m$ is small enough.

(b) The *critical triangles* are identified by setting a threshold on their acute angles. We considered a triangle to be critical if it has an angle less than $\pi/30$. The vertices of such triangles are called *critical vertices*.

(c) Non-critical vertices are dilated as much as $\overline{d}/m$ in direction of their corresponding normal vectors while critical triangles are kept fixed (not dilated).

(d) Steps (b) and (c) are iterated $m$ times.

(e) After $m$ iterations, we have a smooth dilated surface with some holes in locations of critical vertices $P_{crit} = \{P_1, P_2, \ldots, P_K\}$. The holes are filled by a linear interpolation and faired by the mean curvature flow.

An example of this process is presented in Fig. 4.8 where the smoothed surface of Fig. 4.7 is dilated in $m = 5$ iterations. A zoom on the mesh of the insular cortex is shown at each iteration. The orange ellipse on each zoom highlights two specific triangles that are going to be critical after 2 dilation iterations. In this step, the vertices of these triangles are fixed which causes a hole on the surface in iteration 3. Two other holes, visible on the lateral surface, have been already appeared due to to fixing some other critical vertices in those regions. The zooms of iterations 3 to 5, that are shown in dashed frames, explain what would happen if the critical vertices were not fixed. It is seen that in this case, the critical triangles pass through each other in iteration 4 and make an excrescence in iteration 5.

To fill the holes after dilation iterations, one may use the algorithms existing in the literature (see e.g. ZHAO et al. 2007 ; BRUNTON et al. 2009). Those algorithms are really useful when there is no mesh structure in holes. In case of our problem, however, holes are structured. So, we use a simple weighted interpolation to fill the holes. To do so, the first ring neighbourhood of each critical vertex is identified. It may include some critical vertices as well as non critical ones. The critical vertex with maximum number of non critical neighbours is identified. Let us call it $P_i \in P_{crit}$. The non-critical neighbour vertices of $P_i$ are considered as $\{P_{i,1}, P_{i,2}, \ldots, P_{i,s_i}\} \subset V \setminus P_{crit}$. Then, the new location of $P_i$ is determined by a weighted interpolation of its non-critical neighbours :

$$\overline{P}_i = \sum_{j=1}^{s_i} w_j P_{i,j}. \tag{4.37}$$

The weights $w_j$'s are the inverse of distance between $P_i$ and $P_{i,j}$. As soon as the new location is designated to this critical vertex by Eq. (4.37), it is removed from the list of critical vertices i.e. $P_{crit} = P_{crit} \setminus P_i$. This procedure is iterated until no critical vertex remains in $P_{crit}$. The dilated surface after hole filling is shown in Fig. 4.9a.

Hole filling algorithms are often followed by a mesh fairing process (see e.g. the above-mentioned references). The aim of fairing process is to smooth the filled holes. To do so, the heat equation (4.29) with Dirichlet boundary condition is applied on holes :

$$\begin{aligned} \frac{\partial f}{\partial t} &= -\Delta f, \quad \text{in } \Omega \qquad (4.38)\\ f &= f_0, \quad \text{on } \partial\Omega, \qquad (4.39) \end{aligned}$$

where $f$ denotes a coordinate component of vertices i.e. $x$, $y$ or $z$, $\Omega$ is the union of regions of filled holes, $\partial\Omega$ is the boundary of $\Omega$ i.e. non-hole region and $f_0$ is the value of $f$ on non-hole region. Applying the heat equation on filled holes while other vertices (on non-hole region) are kept fixed by the Dirichlet boundary condition, makes the filled holes smoother and doesn't change the non-hole

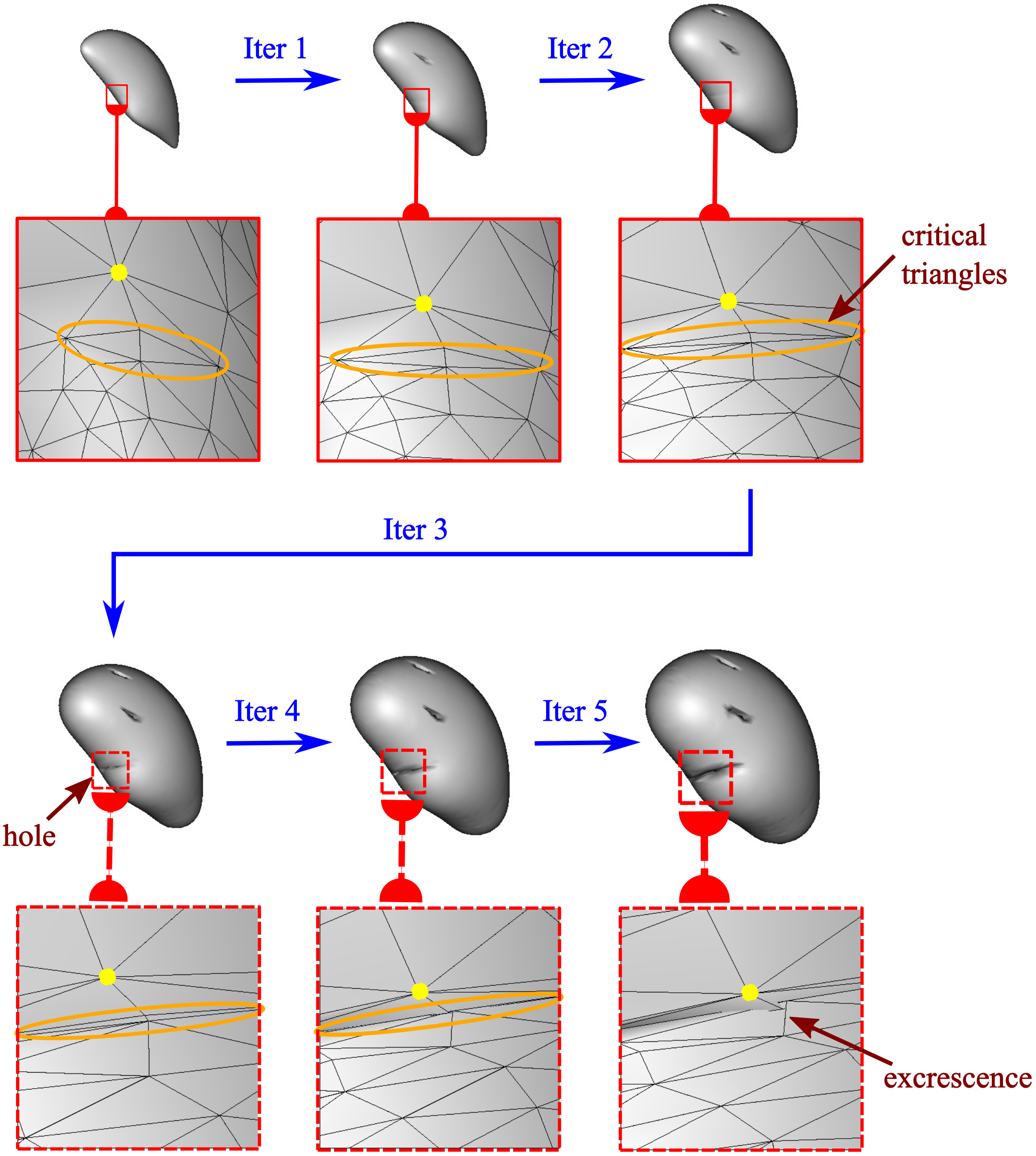

Figure 4.8.: Iterative dilation of a smoothed surface. A zoom on the mesh is presented for the smoothed surface and in iterations 1 and 2 (top row). The orange ellipse on these zooms highlights two triangles that become critical after 2 iterations. So, their vertices are kept fixed in iteration 3 which makes a hole on the surface (bottom row). Zooms in iterations 3 to 5 explain that if those two critical triangles were not fixed, they would collapse in iteration 4 and make an excrescence on the mesh in iteration 5, thus corrupting the mesh locally. The yellow vertex on zooms is represented as a reference to show the movements of vertices at each iteration.

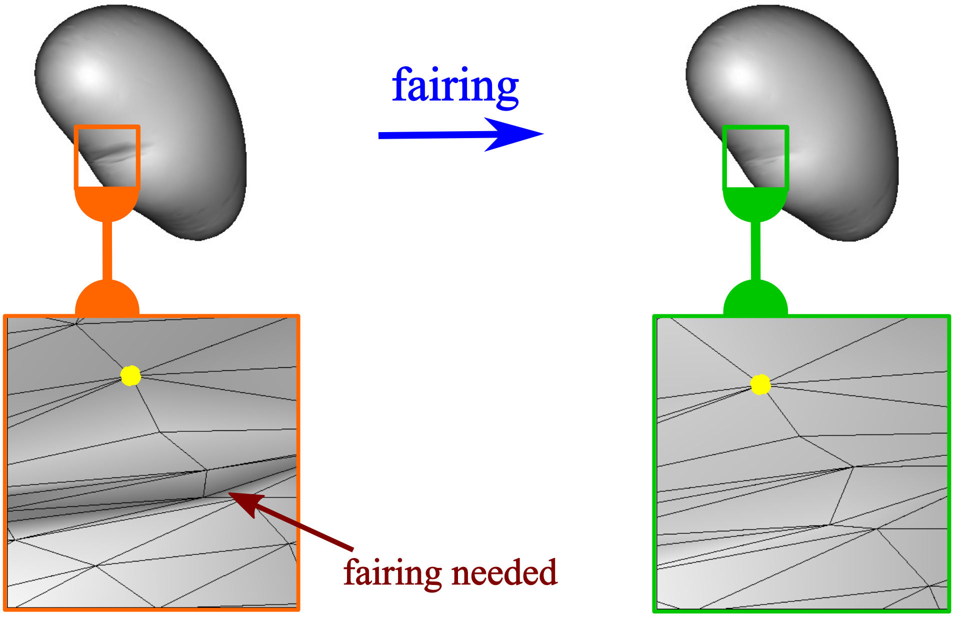

(a) (b)

Figure 4.9.: Mesh fairing process is applied on filled holes to make them smoother. A zoom on a filled hole (left panel) shows that although the hole is filled, it is not smooth. By applying the fairing process, the mesh on the filled hole region is smother as shown in the right zoom.

region. The result of fairing is shown in Fig. 4.9b.

**4, 5. Spectral analysis and linear regression.**
Given the fractional Brownian motion (4.15), the Fourier coefficients of this field is given through the inner product of $R_H$ and Laplacian eigenvectors of the reference surface :

$$\begin{aligned}\hat{R}_H(k) &= \langle R_H, \phi_k \rangle \\ &= C \sum_{n=1}^{N} \sum_{l=2}^{M} \lambda_l^{-(\frac{d}{4}+\frac{H}{2})} (\phi_l(n) - \phi_l(o)) \xi_l \phi_k(n) \\ &= C \lambda_k^{-(\frac{d}{4}+\frac{H}{2})} \xi_k - C \sum_{n=1}^{N} \phi_k(n) \sum_{l=2}^{M} \lambda_l^{-(\frac{d}{4}+\frac{H}{2})} \phi_l(o) \xi_l, \end{aligned} \tag{4.40}$$

for $k = 2, \ldots, M$. The first term of Eq. (4.40) is obtained due to orthogonality of eigenfunctions. It also requires $\sum_{n=1}^{N} \phi_k(n) = 0$ (because of the orthogonality of $\phi_k$ and $\phi_1$ which is a constant vector). So, the spectral powers are

$$\hat{R}_H(k)^2 = C^2 \lambda_k^{-2(\frac{d}{4}+\frac{H}{2})} \xi_k^2. \tag{4.41}$$

The expectation value of spectral powers is

$$\mathbb{E}[\hat{R}_H(k)^2] = C^2 \lambda_k^{-2(\frac{d}{4}+\frac{H}{2})} \mathbb{E}[\xi_k^2], \qquad k = 2, \dots, M. \tag{4.42}$$

Since $\{\xi_l\}$ comes from the standard normal distribution, $\mathbb{E}[\xi_l^2] = Var(\xi_l) = 1$. Now by taking the logarithm, we will have

$$\log \mathbb{E}[\hat{R}_H(k)^2] = -(\frac{d}{2} + H)\log(\lambda_k) + \log(C^2), \qquad k = 2, \dots, M. \tag{4.43}$$

This equation shows a linear relationship between $\log \mathbb{E}[\hat{R}_H(k)^2]$ and $\log(\lambda_k)$. Consequently, $H$ and $C$ can be estimated from the slope and intercept of a least square linear regression line computed on points $\{\lambda_k, \mathbb{E}[\hat{R}_H(k)^2]\}$ in log-log scale.

The expectation values in Eq. (4.42) could be approximated by using the law of large numbers if many realization of $R_H$'s with the same $H$ were available. Here, however, only one realization of $R_H$ is available. To address this situation, we start from Eq. (4.41). Taking the logarithm of this equation results in

$$\log(\hat{R}_H(k)^2) = -(\frac{d}{2} + H)\log(\lambda_k) + \log(C^2) + \log(\xi_k^2), \qquad k = 2, \dots, M. \tag{4.44}$$

In this equation, $\log(\xi_k^2)$ is a random variable with unknown distribution. So, applying the least square linear regression analysis is not possible as it was before.

To address this issue, we propose a binning strategy on the spectral index $k$. Formally, let $\{E_l, l = 1, 2, ..., L\}$ be a partition of spectral indices $\{2, 3, \dots, M\}$ i.e.

- $\bigcup_{l=1}^{L} E_l = \{2, 3, \dots, M\}$,
- $E_l \bigcap E_{l'} = \emptyset, \quad \forall l, l' \in \{1, 2, \dots, L\}, l \neq l'$,
- $|E_l| = N_l$

where $|E_l|$ denotes the cardinal number of $E_l$. Now, taking the averages in both sides of Eq. (4.44) in every bin $E_l$ gives

$$\frac{1}{N_l} \sum_{k \in E_l} \log(\hat{R}_H(k)^2) = \frac{-(\frac{d}{2} + H)}{N_l} \sum_{k \in E_l} \log(\lambda_k) + \frac{1}{N_l} \sum_{k \in E_l} \log(\xi_k^2) + \log(C^2). \tag{4.45}$$

If we denote

$$\begin{aligned} x_l &= \frac{1}{N_l}\sum_{k\in E_l}\log(\lambda_k), && (4.46)\\ y_l &= \frac{1}{N_l}\sum_{k\in E_l}\log(\hat{R}_H(k)^2), && (4.47)\\ \varepsilon_l &= \frac{1}{N_l}\sum_{k\in E_l}\log(\xi_k^2), &&\\ \alpha &= -2\Big(\frac{d}{4}+\frac{H}{2}\Big), && (4.48)\\ \gamma &= \log(C^2), && (4.49)\end{aligned}$$

then Eq. (4.45) can be rewritten as

$$y_l = \alpha x_l + \gamma + \varepsilon_l. \tag{4.50}$$

Due to the Central Limit Theorem, for large $N_l$, the distribution of $\varepsilon_l$ is approximated by a normal distribution of mean $\mu_0$ and variance $\sigma_0^2/N_l$ i.e.

$$\varepsilon_l \approx \mathcal{N}\Big(\mu_0, \frac{\sigma_0^2}{N_l}\Big), \qquad \text{such that} \tag{4.51}$$

$$\mu_0 = \mathbb{E}[\log(\xi_k^2)], \qquad \sigma_0^2 = \mathbb{V}[\log(\xi_k^2)], \tag{4.52}$$

where $\mathbb{E}$ and $\mathbb{V}$ denote expectation and variance values. Since $\{\xi_k\}$ comes from a standard normal distribution, $\{\xi_k^2\}$ has $\chi^2$ distribution and $\{\log(\xi_k^2)\}$ has the expectation value as

$$\mathbb{E}[\log(\xi_k^2)] = \log(2) + \psi\Big(\frac{1}{2}\Big), \tag{4.53}$$

where $\psi(.)$ is called the $\psi$-function and is actually the first derivative of the Gamma function (Pav 2015). According to the rule of large numbers, for large $N_l$, $\varepsilon_l$ tends to $\mu_0$. By replacing $\mu_0$ in Eq. (4.50) and defining

$$\beta = \gamma + \mu_0, \tag{4.54}$$

we get

$$y_l = \alpha x_l + \beta, \qquad l = 1, 2, \dots, L. \tag{4.55}$$

To find the coefficients $\alpha$ and $\beta$, a weighted least square linear regression analysis may now be used. More precisely, the coefficients are determined through minimization of the weighted mean square error :

$$J(\alpha,\beta) = \sum_{l=1}^{L}\frac{N_l}{\sigma_0^2}(y_l - \alpha x_l - \beta)^2. \tag{4.56}$$

It gives the following values for $\alpha$ and $\beta$ :

$$\begin{aligned}
\alpha &= \frac{\sum_{l=1}^{L}\frac{N_l}{N}x_l y_l - \left(\sum_{l=1}^{L}\frac{N_l}{N}x_l\right)\left(\sum_{l=1}^{L}\frac{N_l}{N}y_l\right)}{\sum_{l=1}^{L}\frac{N_l}{N}x_l^2 - \left(\sum_{l=1}^{L}\frac{N_l}{N}x_l\right)^2}, && (4.57)\\
\beta &= \sum_{l=1}^{L}\frac{N_l}{N}y_l - \alpha\sum_{l=1}^{L}\frac{N_l}{N}x_l. && (4.58)
\end{aligned}$$

Now, by following Eqs. (4.48), (4.49) and (4.54), estimations of $H$ and $C$ are extracted from $\alpha$ and $\beta$ respectively.

In this method, different binning strategies may be applied. The first intuitive strategy is a binning with equal number of elements in each bin i.e. $|E_1| = |E_2| = \ldots = |E_M|$. Number of elements should be large enough to apply the central limit theorem truly. It can be investigated by Chi-square goodness of fit hypothesis test (e.g. « Chi-square Goodness of Fit Test » 2008).

Of course, binning strategies may affect the quality of estimations. Especially, we found that the precision of $\alpha$ and $\beta$ is proportional to the inverse of the variance of $x_l$'s. More precisely, we have the following proposition.

**Proposition 4.** *The variances of $\alpha$ and $\beta$ computed by the weighted least square linear regression analysis, given in Eqs. (4.57) and (4.58), are equal to*

$$\begin{aligned}
\mathbb{V}(\alpha) &= \frac{\sigma_0^2}{N\sigma_x^2}, && (4.59)\\
\mathbb{V}(\beta) &= \frac{\sigma_0^2}{N}\left(1+\frac{\overline{x}^2}{\sigma_x^4}\right), && (4.60)
\end{aligned}$$

*where $\sigma_0$ comes from the variance of $\varepsilon_l$-distribution (4.51), and*

$$\begin{aligned}
\overline{x} &= \sum_{l=1}^{L}\frac{N_l}{N}x_l, && (4.61)\\
\sigma_x^2 &= \sum_{l=1}^{L}\frac{N_l}{N}x_l^2 - \overline{x}^2. && (4.62)
\end{aligned}$$

*Proof.* The proof is given in Appendix A. □

Once an approximation of the reference surface $\tilde{S}^{ref}$ is obtained in the previous step, its Laplacian eigenpairs $\{(\tilde{\lambda}_l, \tilde{\psi}_l), l = 1, 2, \ldots, N\}$ are computed by the linear FEM presented in Section 2.4.1. Then the spectral powers of $\tilde{R}_H$ are computed by

$$\hat{\tilde{R}}_H(l)^2 = |\langle \tilde{R}_H, \tilde{\phi}_l\rangle|^2. \qquad (4.63)$$

where $\phi_l = B^{1/2}\psi_l$. Now, by replacing $\tilde{\lambda}_l$ and $\hat{\tilde{R}}_H(l)^2$ in Eqs. (4.46) and (4.47) , estimations of $H$ and $C$ are computed from Eqs. (4.57) and (4.58) respectively.

In following, we prove an important property of the proposed estimators of $H$ and $C$.

### 4.2.1. Scale invariance

The Hurst parameter $H$ and $C$ of a fractional Brownian motion are independent parameters that do not change with scaling the corresponding fractional Brownian surface. Accordingly, it is expected that appropriate estimators of $H$ and $C$ preserve this property.

**Proposition 5.** *The proposed estimator of $H$ and $C$ are scale invariant.*

*Proof.* Let $\mathcal{S}_2^{ref}$ be a scaled version of a reference surface $\mathcal{S}_1^{ref}$ by a factor $q^2$ i.e. $|\mathcal{S}_2^{ref}| = q^2|\mathcal{S}_1^{ref}|$ where $|.|$ denotes the surface area. As discussed in Proposition 3 in Chapter 2, the Laplacian eigenvalues and eigenvectors of $\mathcal{S}_2^{ref}$ are those of $\mathcal{S}_1^{ref}$ scaled by $1/q^2$ and $1/q$ respectively. Moreover, the matrix $B$ of FE discretization of Laplace–Beltrami operator is scaled by $q^2$. Accordingly, the fractional Brownian random motion, generated by Eq. (4.15) is scaled as following

$$R_{H,2}(n) = q^{(\frac{d}{2}+H)} R_{H,1}(n), \quad n = 1, 2, \ldots, N, \tag{4.64}$$

where $R_{H,i}$ denotes the motion corresponding to $\mathcal{S}_i^{ref}$. Therefore, the spectral powers are scaled as

$$\hat{R}_{H,2}(l)^2 = q^{2(\frac{d}{2}+H)} \hat{R}_{H,1}(l)^2, \quad l = 1, 2, \ldots, M. \tag{4.65}$$

In logarithmic scale, it will be

$$\log(\hat{R}_{H,2}(l)^2) = 2(\frac{d}{2} + H)\log(q) + \log(\hat{R}_{H,1}(l)^2). \tag{4.66}$$

Moreover, for eigenvalues in logarithmic scale we have

$$\log(\lambda_{l,2}) = -2\log(q) + \log(\lambda_{l,1}). \tag{4.67}$$

By replacing Eqs. (4.67) and (4.66) in Eqs. (4.46) and (4.47), it is easily seen that

$$\begin{aligned} x_{l,2} &= -2\log(q) + x_{l,1}, \qquad (4.68)\\ y_{l,2} &= (d + 2H)\log(q) + y_{l,1}. \qquad (4.69) \end{aligned}$$

Finally, putting Eqs. (4.68) and (4.69) in Eq. (4.57) gives $\alpha_2 = \alpha_1$ that proves the proposition. With similar computations for $\beta$, it is easily seen that

$$\beta_2 = (d + 2H + 2\alpha_1)\log(q) + \beta_1. \tag{4.70}$$

Due to Eq. (4.48), it is proved that $\beta_2 = \beta_1$. □

## 4.3. Results

In this section, first, we show the efficiency of the method proposed in Section 4.2, by applying it on a set of synthetic data which includes fractional Brownian spheres. Then, the method is applied to real data which consists in a database of fetal cortical surfaces. Assuming that the cerebral cortex is a fractional Brownian surface, by using the proposed method, we try to find its Hurst parameter.

### 4.3.1. Synthetic data

To produce fractional Brownian spheres, a triangulated unit sphere with $N = 2562$ vertices is considered as the reference surface $\mathcal{S}^{ref}$. The first $M = 1600$ Laplacian eigenpairs of $\mathcal{S}^{ref}$ are computed by using the Linear FEM, presented in Section 2.4.1. Then, fractional Brownian motions $R_H$ on $\mathcal{S}^{ref}$ are generated via Eq. (4.15) with $C = 1$. By displacing the vertices of $\mathcal{S}^{ref}$ in direction of their corresponding normal vectors by amount of $R_H$, fractional Brownian spheres are constructed. Some examples of such surfaces are given in Fig. 4.2.

Here, we run two experiments. In Experiment 1, we apply the Algorithm 1 on one observed fractional Brownian sphere to illustrate and visualize the steps of the proposed algorithm. In Experiment 2, the algorithm is applied on 1000 observations with different $H$ parameters to show the quality of estimations.

**Experiment 1.**

We start with an example to illustrate and visualize the Algorithm 1. Given an observed fractional Brownian sphere $\mathcal{S}^{ob}$ e.g the one of Fig. 4.2a with $H = 0.1$, the mean curvature flow smoothing with parameter $dt = 0.1$ and $m = 10$ iterations is used to smooth the surface. Then the Euclidean distances between corresponding vertices of $\mathcal{S}^{ob}$ and $\mathcal{S}^{sm}$ are computed and centered to obtain the approximation of $R_H$ as given by Eq. (4.34). The $\tilde{R}_H$ mapped on the sphere surface is depicted in Fig. 4.10a. In comparison to $R_H$ in Fig. 4.2d, it is seen that both $\tilde{R}_H$ and $R_H$ share a very similar pattern, although their values are a bit different. The global error is

$$\frac{\|\tilde{R}_H - R_H\|_2}{\|R_H\|_2} \times 100 = 27\%,$$

and the map of local errors $\tilde{R}_H(n) - R_H(n)$ is given in Fig. 4.11a.

A part of this error is due to movement of barycenter of $\mathcal{S}^{ref}$ after displacing the points of $\mathcal{S}^{ref}$ by $R_H$. In this example, the distance between the barycenters of sphere and $\mathcal{S}^{ob}$ is about $8e-3$. If we knew the barycenter of $\mathcal{S}^{ref}$, the global approximation error of $R_H$ would be about $18\%$ and the local error would be as depicted in Fig. 4.11b.

Now, the reference surface is approximated by dilating the smoothed surface.

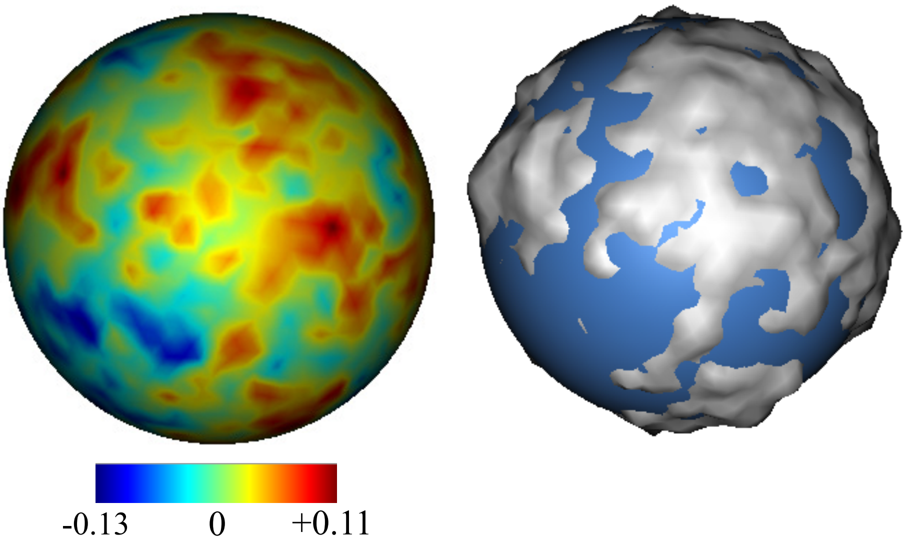

(a)

(b)

Figure 4.10.: (a) $\tilde{R}_H$ map : approximation of $R_H$ depicted in Fig. 4.2d. (b) Approximated reference surface $\tilde{\mathcal{S}}^{ref}$ (blue surface) of the observed surface $\mathcal{S}^{ob}$ (gray one) depicted in Fig. 4.2a. $\tilde{\mathcal{S}}^{ref}$ is computed from $\mathcal{S}^{ob}$ by smoothing and dilation processes.

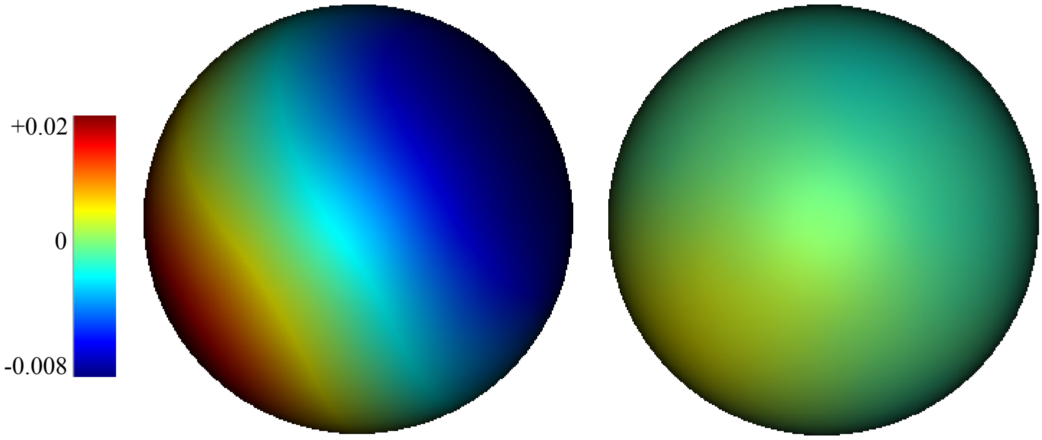

(a)

(b)

Figure 4.11.: Local approximation error of $R_H$ : $\tilde{R}_H(n) - R_H(n)$ when the barycenter of $\mathcal{S}^{ref}$ (a) is not known, (b) is known.

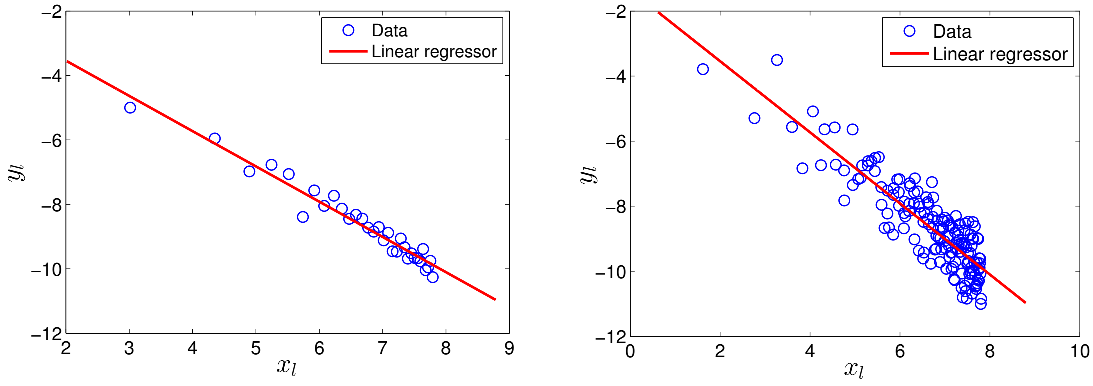

(a) (b)

Figure 4.12.: Linear regression analysis as proposed in Eq. (4.55) with (a) $n = 50$ and (b) $n = 10$ elements in each bin. $R^2$ coefficient of linear fitting is (a) 0.95 and (b) 0.77 respectively.

Since the smoothed surface is convex and the quality of mesh is good, the dilation is performed in 1 iteration with amount of $\bar{d} = 0.81$. It is reminded that $\bar{d}$ is the average of Euclidean distances $d(n)$ between corresponding vertices of $\mathcal{S}^{ob}$ and $\mathcal{S}^{sm}$. The approximated reference surface $\tilde{\mathcal{S}}^{ref}$ along with the observed surface are shown in Fig. 4.10b. As expected, it is seen that wherever the $\mathcal{S}^{ob}$ is out of $\tilde{\mathcal{S}}^{ref}$, the value of $\tilde{R}_H$ is positive and vice versa.

The Fourier coefficients of $\tilde{R}_H$ are computed through the Laplacian eigenpairs of $\tilde{\mathcal{S}}^{ref}$. Then the linear regression analysis with binning strategy is performed on spectral powers vs. Laplacian eigenvalues in a log-log scale. In Fig. 4.12 the regression analysis is shown when there are $n = 50$ and $n = 10$ elements in each bin. As predicted by Eq. (4.55), the linear behavior of $y_l$ versus $x_l$ is clearly evident in Fig. 4.12a. Finally, the estimation of $H$ and $C$ are extracted from the slope and intercept of the least-square regression line.

The results of estimations for this example are given in Table 4.1. The absolute errors of estimations of $H$ and $C$ show that, in the case of this example, the proposed method can approximate these parameters accurately. Moreover, changing the number of elements in bins ($n = 50, 10$) does not have significant effect of the approximation. In other words, the method is likely not sensitive to this parameter.

**Experiment 2.**

To see the quality of estimations for different values of $H$, we run an experiment with 1000 fractional Brownian spheres (fBs's) for which $H$'s are given by the uniform distribution in interval $(0.05, 0.95)$. For each fBs, $H$ is estimated through Algorithm 1 with the parameters used in Experiment 1. The global mean of biases (mBias) and the root mean square error (rMSE) of $\tilde{H}$ are computed by

Table 4.1.: Statistics of estimating $H$ and $C$ of the examplar case by linear regression analysis with a binning strategy (4.55). Bins have equal number of elements denoted by $n$.

| Statistics | Binned regression | |
|---|---|---|
| | $n = 50$ | $n = 10$ |
| $\lvert\tilde{H} - H\rvert$ | 0.0060 | 0.0067 |
| $\lvert\tilde{C} - C\rvert$ | 0.0403 | 0.0427 |
| $R^2$ coefficient | 0.95 | 0.77 |

Table 4.2.: Statistics of estimation of $H$ and $C$ by naive regression (4.43) and regression with a binning strategy (4.55). Bins have equal number of elements denoted by $n$.

| Statistics | Binned regression | | | | |
|---|---|---|---|---|---|
| | $n = 50$ | $n = 40$ | $n = 30$ | $n = 20$ | $n = 10$ |
| mBias of $\tilde{H}$ | -0.011 | -0.0089 | -0.0069 | -0.0041 | -0.00039 |
| rMSE of $\tilde{H}$ | 0.065 | 0.065 | 0.065 | 0.064 | 0.064 |
| mBias of $\tilde{C}$ | -0.035 | -0.029 | -0.022 | -0.013 | -0.0085 |
| rMSE of $\tilde{C}$ | 0.219 | 0.217 | 0.215 | 0.213 | 0.210 |
| $R^2$ coefficient | 0.87 | 0.86 | 0.85 | 0.83 | 0.83 |

the following formulas :

$$\text{mBias} = \frac{1}{N}\sum_{k=1}^{N}(\tilde{H}_k - H_k), \tag{4.71}$$

$$\text{rMSE} = \sqrt{\frac{1}{N}\sum_{k=1}^{N}(\tilde{H}_k - H_k)^2}. \tag{4.72}$$

The same statistics are computed for $\tilde{C}$. The results are presented in Table 4.2 for different $n = 50, 40, 30, 20, 10$ number of elements in each bin. Evidently, rMSE of $H$ and $C$ does not change significantly with $n$. Consequently, the quality of estimations is not heavily dependent to $n$. From now on, we will use $n = 10$ which ensures that there are enough data for regression analysis, especially in case of some experiments where due to numerical issues, a few number of data points can be computed.

To see the local error of estimations, the 1000 considered surfaces are clustered in 9 bins based on their $H$ values : group $i$ contains surfaces with $H \in [0.05 + (i-1) \times 0.1, 0.05 + i \times 0.1)$ for $i = 1, 2, \ldots, 9$. For each cluster, the mBias

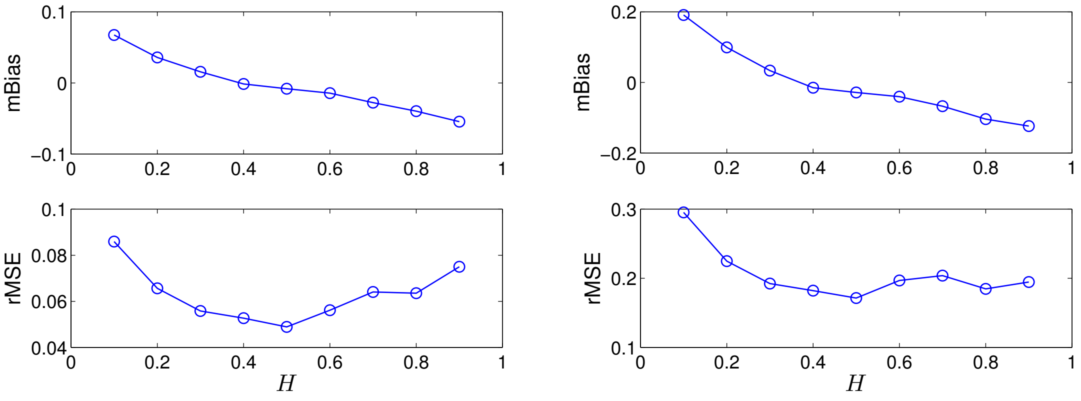

(a) (b)

Figure 4.13.: Mean of biases (mBias) and root mean square errors (rMSE) of estimation of (a) $H$ and (b) $C$ for 1000 fractional Brownian surfaces, shown in different clusters of $H$.

and rMSE of and are computed by using formula (4.71) and (4.72) while $N$ is replaced by $N_i$, the number of surfaces in cluster $i$.

mBias and rMSE of $H$ and $C$ of clusters are shown in Fig. 4.13. From positive values of bias for $H \leq 0.35$ it is understood that the proposed spectral estimator overestimates the exact values of $H$ in this range. In contrast, it underestimates $H$ for $0.35 < H < 0.95$. It means that $\tilde{H}$ remains in the appropriate interval between 0 and 1. Moreover, the most accurate result is achieved for surfaces with $H \in [0.45, 0.55)$ where the rMSE takes its minimum value : $0.049$ for $H$ and $0.017$ for $C$.

## 4.3.2. Fetal data

In this section, we show how the Hurst parameter can be considered as a global gyrification index. Indeed, the presumption is that each brain hemisphere is a fractional Brownian surface. So, we apply the proposed Algorithm 1 to estimate its Hurst parameter. We chose to work on fetal brain cortical surfaces since the increase of brain surface complexity with gestational age is clearly observable. Accordingly, we expect $H$ to decrease with age. This is presented in following.

**Subjects and preprocessing.**
We have a database of fetal subjects provided by the Department of Neuroradiology in La Timone Hospital (Marseille, France) between 1 January and 31 December 2011. The local ethical committee approved the acquisition protocol. The subjects have been either suspected of brain anomalies according to ultrasounds scans, requiring further examinations by MRI, or have personal-familial history of anomalies with a risk for fetal brain damage after 28 weeks GA even

when ultrasounds scans appeared normal (Girard et al. 2012). In utero acquisitions were performed on a 1.5-T MRI system (Symphony TIM, Siemens ; Erlangen, Germany). More details of MR acquisition are given by Lefèvre et al. 2015.

From this database, we selected 14 healthy subjects according to radiological criteria. The gestational age of subjects has been between 21 and 34 weeks at the time of MRI acquisition (mean age : $29.6 \pm 3.5$ weeks). For these subjects, at least 3 artifact-free volumes in different orientations (axial, coronal, sagittal) had been acquired and no disease was reported in the regular clinical follow-up. Image reconstruction is performed to get high-resolution volumes ($0.75 \times 0.75 \times 0.75 mm^3$). Then the interface between the developing cortex and the future white matter zone, also called inner cortical surface, was segmented and reconstructed in 3D. These preprocessing steps are explained in details in Lefèvre et al. 2015. Finally we have 28 triangulated hemispheric surfaces. Two surfaces (one left and one right hemisphere) are excluded due to low quality of triangulations.

**Application of the method.**
The proposed algorithm 1 is applied on each subject's hemisphere. First, each hemisphere ($\mathcal{S}^{ob}$) is smoothed by the mean curvature flow smoothing to get a smoothed surface $\mathcal{S}^{sm}$. The iteration of smoothing procedure is stopped when $\mathcal{S}^{sm}$ is completely inside the $\mathcal{S}^{ob}$. The stopping criterion is checked by the angular strategy explained in Section 4.2 (see Fig. 4.5).

A left hemisphere of a fetal subject ($\mathcal{S}^{ob}$) along with its smoothed surface ($\mathcal{S}^{sm}$) are shown on Fig. 4.14a. $\mathcal{S}^{ob}$ is made transparent so that $\mathcal{S}^{sm}$ become visible. The Euclidean distance between corresponding points on $\mathcal{S}^{sm}$ and $\mathcal{S}^{ob}$ are computed. Then, the Euclidean distance is centered to get $\tilde{R}_H$ and the characteristic distance $\overline{d}$ is computed. In next step, $\mathcal{S}^{sm}$ is dilated as much as $\overline{d}$ to get a reference surface $\tilde{\mathcal{S}}^{ref}$. This surface together with $\mathcal{S}^{ob}$ are represented in Fig. 4.14b. The map of $\tilde{R}_H$ depicted on $\tilde{\mathcal{S}}^{ref}$ is shown in Fig. 4.14c. By comparing the relative positions of these surfaces and the Euclidean $\tilde{R}_H$, a good consistency is seen between them i.e. in the regions where $\mathcal{S}^{ob}$ is inside $\tilde{\mathcal{S}}^{ref}$, the value of $\tilde{R}_H$ is negative and vice versa. For example, see the areas around the central sulcus and the insula.

If the geodesic distance between $\mathcal{S}^{sm}$ and $\mathcal{S}^{ob}$ was considered, we would get $\tilde{R}_H$ as depicted in Fig. 4.14d. It is seen that due to smoothing procedure, as shown in Fig. 4.4, the geodesic distance doesn't give an appropriate map of folds. For example, see the map around the central sulcus where it is wrongly shown that the precentral and postcentral gyri are deeper than the central sulcus !

The next step is to compute the spectral powers $\hat{\tilde{R}}_H(k)^2$ by using the Laplacian eigenvectors of $\tilde{\mathcal{S}}^{ref}$. A binning strategy with 10 elements in each bin is applied on Laplacian eigenvalues and spectral powers to obtain $x_l$'s and $y_l$'s given by Eqs. (4.46) and (4.47) respectively. They are shown in Fig. 4.15a. In this figure, it is seen that the decreasing behavior of $y_l$'s is not similar for low and high values of $x_l$'s. Moreover, if the regression analysis was performed on this data, from the

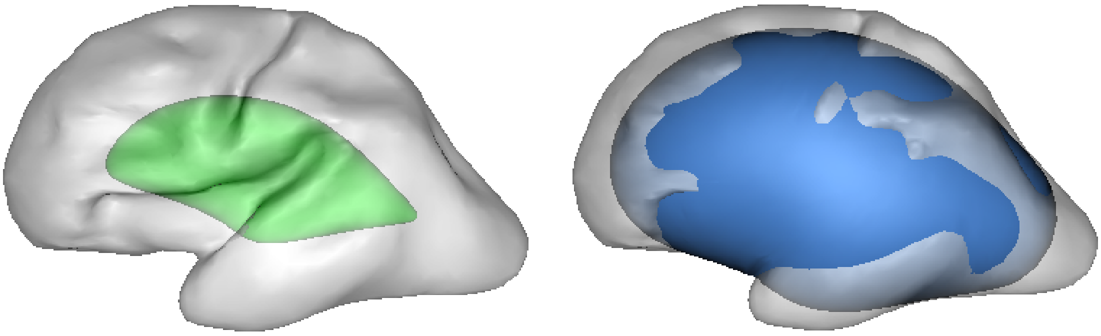

(a) $\mathcal{S}^{ob}$ (b) $\mathcal{S}^{ob}$ & $\tilde{\mathcal{S}}^{ref}$

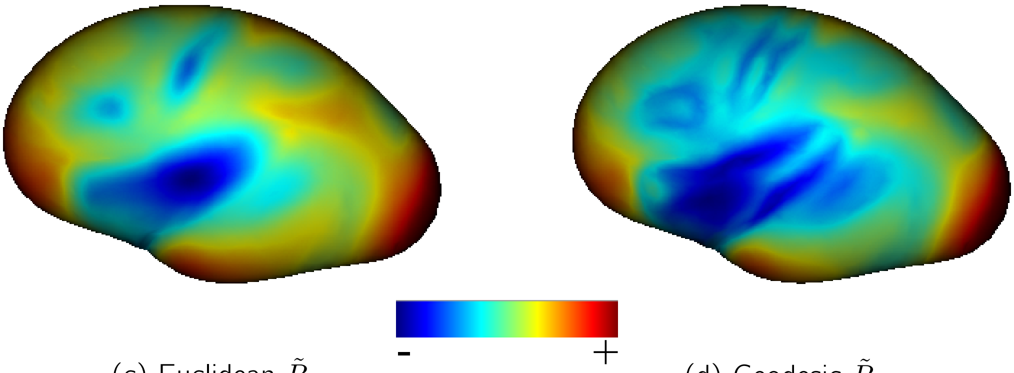

(c) Euclidean $\tilde{R}_H$ (d) Geodesic $\tilde{R}_H$

Figure 4.14.: (a) Left hemisphere of a subject $\mathcal{S}^{ob}$ together with its smoothed surface $\mathcal{S}^{sm}$ shown in green. (b) $\mathcal{S}^{ob}$ together with $\tilde{\mathcal{S}}^{ref}$. $\mathcal{S}^{ob}$ is transparent to show $\mathcal{S}^{sm}$ and also parts of $\tilde{\mathcal{S}}^{ref}$ which is inside the $\mathcal{S}^{ob}$. (e) $\tilde{R}_H$ as the centralized Euclidean distance between $\mathcal{S}^{ob}$ and $\mathcal{S}^{sm}$. (f) $\tilde{R}_H$ as the centralized geodesic distance between $\mathcal{S}^{ob}$ and $\mathcal{S}^{sm}$. It is noted that $\mathcal{S}^{sm}$ and $\tilde{\mathcal{S}}^{ref}$ are shown in their original sizes.

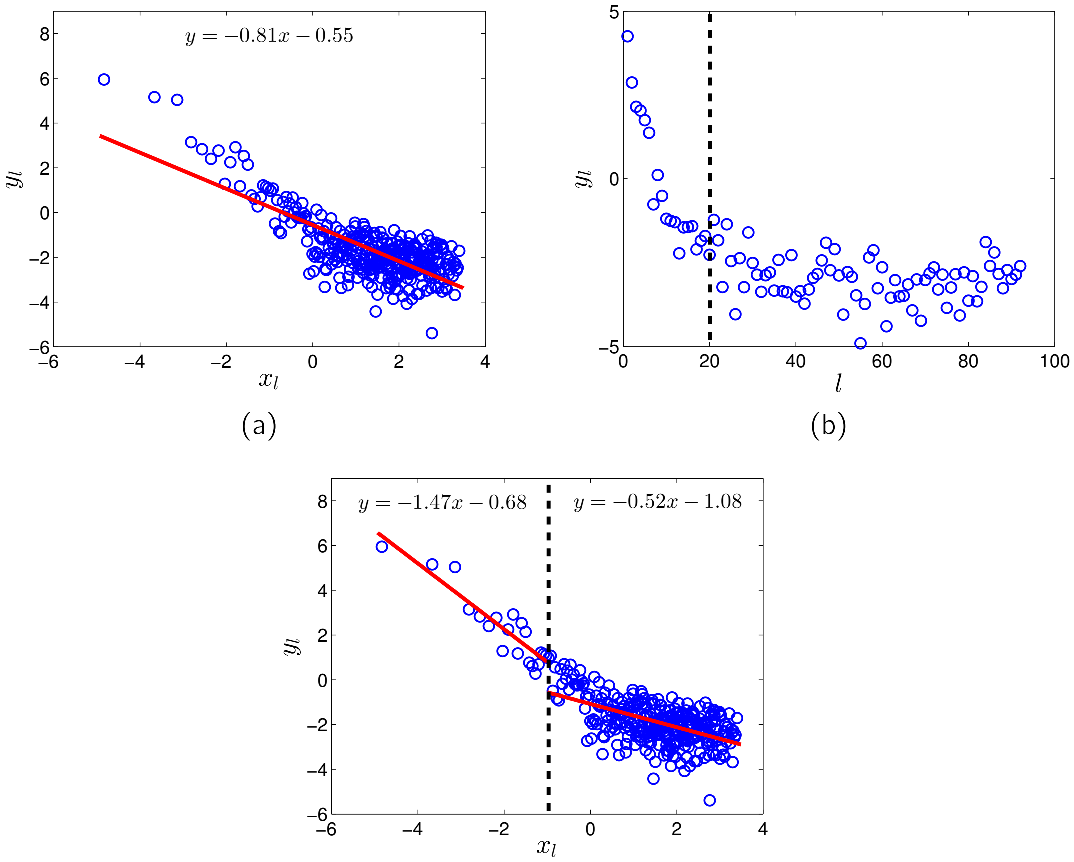

(a)

(b)

(c)

Figure 4.15.: (a) Linear regression analysis on $\{(y_l, x_l)\}$ of the surface in Fig. 4.14. The equation of the regression line is written on the plot. (b) $y_l$ versus $l$ of the smallest surface in our database. The breakpoint of segmented regression analysis is determined as the point where the decreasing behavior of $y_l$'s change (i.e. $l^* = 20$). (c) Segmented linear regression on $\{(y_l, x_l)\}$ of the surface in Fig. 4.14 with the breakpoint $l^* = 20$. The equation of the regression line of each segment is written on the plot.

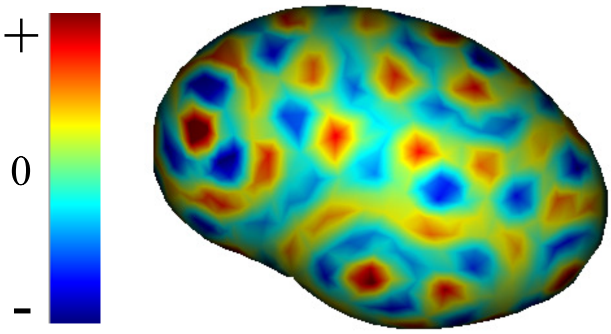

Figure 4.16.: The 200th Laplacian eigenvector of the smallest approximated reference surface in the database corresponding to the breakpoint $l^* = 20$.

slope of the regression line and Eq. (4.48), $H = -(1 - 0.81) = -0.19$ which is not in the expected range $(0, 1)$.

This issue may be due to mesh artefacts or numerical inaccuracy of approximating larger Laplacian eigenpairs. In fact, as indicated in Theorem 2, by using the linear finite element method, the absolute error of approximation of Laplacian eigenvalues is bounded by the square of eigenvalues. Moreover, the error of approximation of Laplacian eigenvectors is bounded by corresponding eigenvalues. In this manner, as eigenvalues increase, the error of approximation of them and their corresponding eigenvectors may increase as well. They increase inaccuracies in computing $x_l$ and $y_l$.

To deal with this situation, a segmented linear regression is performed. In this method, $x_l$'s are broken into two segments. The breakpoint (the border of low and high $x_l$'s) is determined from the data of the smallest surface in database. In Fig. 4.15b, $y_l$'s of the smallest surface are plotted versus $l$'s. It is seen that for $l \leq 20$, $y_l$'s are decreasing while after this limit, they are oscillating in a constant range. Consequently, $l^* = 20$ is adapted as the breakpoint. It corresponds to the 200th Laplacian eigenvector which is shown in Fig. 4.16. Due to inaccuracy in computation of large eigenvalues, we consider only the regression line on the low frequency segment (small eigenvalues).

It is noteworthy that the smallest surface in our database is modelled by a mesh with minimum number of vertices ($N = 930$) in comparison to other surfaces of the database. On the other hand, the maximum number of Laplacian eigenpairs of a meshed surface, computed by FEM, is equal to the number of its mesh vertices. Consequently, we chose the smallest surface for determination of the breakpoint $l^*$ to make sure that all surfaces in the database have enough data points. So, the determined breakpoint $l^*$ of the smallest subject is used for all other subjects.

It is also noted that the approximated reference surfaces of all subjects in the database have similar shapes but different sizes. So, their Laplacian eigenvalues

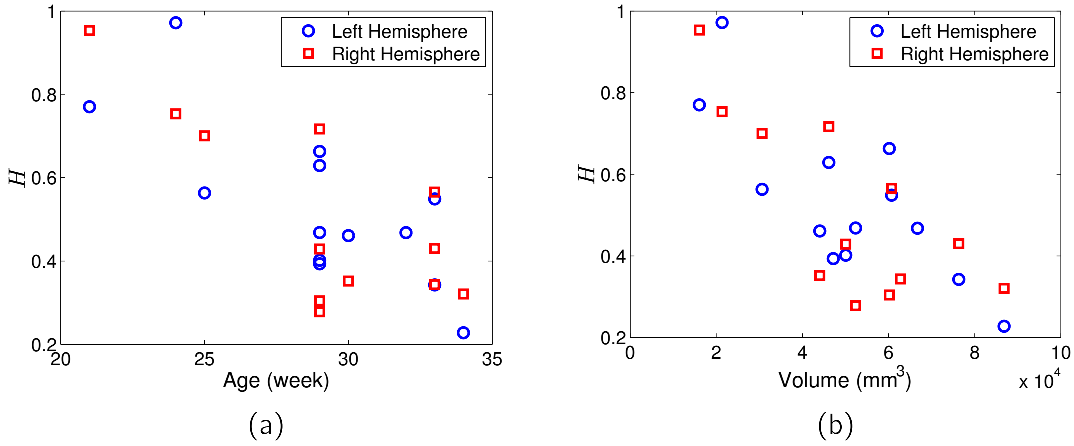

Figure 4.17.: (a) $H$ versus gestational age, and (b) $H$ versus hemispheric volume of fetal subjects.

are almost similar up to a scaling factor (Reuter et al. 2006) : larger surfaces have smaller eigenvalues. So, the $x_{l^*}$ value itself cannot be used as the breakpoint since it is scaled across subjects and results in regression analysis in different spectral bands across subjects. That is why the *index* $l^*$ of the $x_{l^*}$ is considered as the breakpoint.

By applying the breakpoint $l^* = 20$, the two segmented linear regression is performed on the data of Fig. 4.15a and the result is plotted in Fig. 4.15c. From the slopes in regions of low and high frequencies, $H$ will be $0.4$ and $-0.55$ respectively. As mentioned before, the regression analysis in low frequency is adapted here. Consequently, for this surface, $H = -(1 - 1.47) = 0.47$.

Now, the method is applied on all subjects of dataset. In Fig. 4.17a, the values of $H$ of left and right hemispheres are represented versus gestational age. It is seen that older subjects possess smaller values of $H$. The decreasing behavior of $H$ with age is expected since during fetal ages, folds appear on the brain surface and as age increases, the brain becomes more folded (Lefèvre et al. 2015).

It is already discussed in literature that larger fetal brains are more folded (Lefèvre et al. 2015). This is also verified by some mechanical models (Tallinen et al. 2013 ; Tallinen et al. 2016). In Fig. 4.17b, $H$ is plotted versus hemispheric volume. It is seen that as volume increases, $H$ decreases. It is consistent with the results in literature and may justify that $H$ can be considered as a global gyrification index.

## 4.4. Discussion and perspective

In this section, we discuss about the proposed method as well as the obtained results. It helps to better understand the method and also opens some perspectives of this work.

### 4.4.1. $H$ as a global GI

Based on the results presented in Section 4.3.2, the idea arises that the cerebral cortex might be a fractional Brownian surface, at least in a range of its low frequencies. In this manner, the Hurst parameter $H$, as a measure of regularity can be considered as a global gyrification index (GI). Here, we elucidate that $H$ can be potentially an appropriate GI according to the properties of a standard GI listed in Section 1.4.

**Clear definition of the surface complexity.**
To define a GI, first a clear definition of the notion of "*surface complexity*" is needed. Here, we assume that the cerebral cortex is a fractional Brownian surface. In this case, the Hölder regularity of the underlying fractional Brownian motion, mentioned in Theorem 4, defines the surface complexity.

**Physicality.**
The Hurst parameter $H \in (0, 1)$ determines the order of Hölder regularity of an fBm underlying an fBs. Therefore, by estimating the Hurst parameter of a given fBs, we can quantify its surface complexity. It is noted that the regularity is usually measured in a high frequency band. Nevertheless, since we assumed that the cerebral cortex is a fractional Brownian surface, it has the self similarity property. In other words, it is supposed to show similar behavior in low and high frequency bands. Due to inaccuracy of approximation of high frequencies, however, we measured $H$ in a low frequency band.

**Locality.**
Hurst parameter in the presented form is a global GI. Possible extensions to a local measure is discussed in Section 4.4.3.

**Geometric invariant.**
The Hurst parameter itself is defined independently. It does not change with isometric transformation (e.g. translation, rotation and reflection) nor with scaling. The proposed spectral estimator of $H$ has the same properties ; see Proposition 5.

**Efficiency.**
The proposed method has been performed by using MATLAB®R2014a on a node of a computation cluster with *Xeon X5675* processor [b] (6 cores, 3.06 GHz), 48 GB of RAM shared among 16 nodes. For the cortical mesh hemisphere with largest

---

[b] `http://ark.intel.com/products/52577/Intel-Xeon-Processor-X5675-12M-Cache-3_06-GHz-6_40-GTs-Intel-QPI`

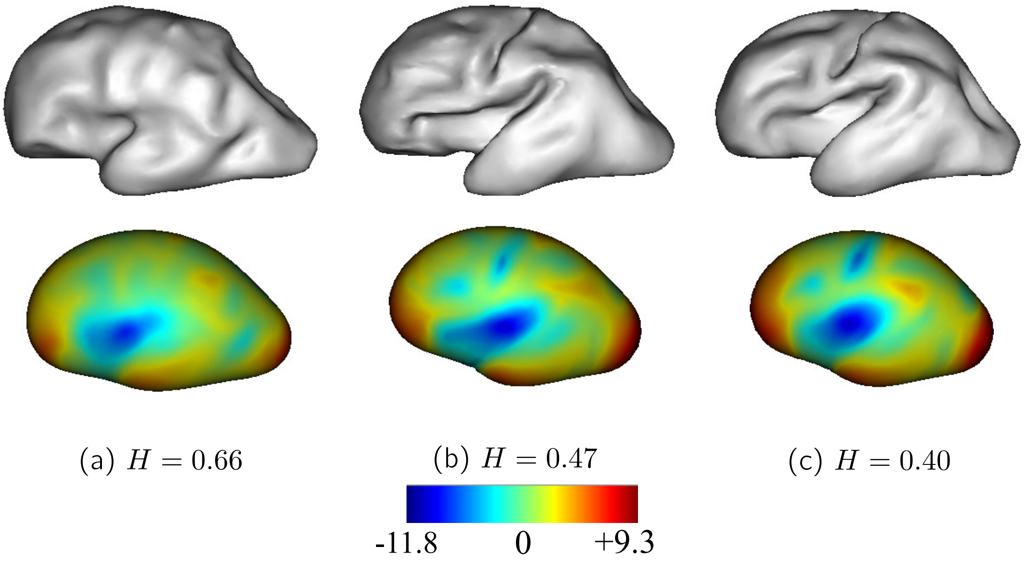
(a) $H = 0.66$ (b) $H = 0.47$ (c) $H = 0.40$

Figure 4.18.: Left hemisphere surfaces as $\mathcal{S}^{ob}$ along with their $\tilde{R}_H$ on corresponding approximated reference surfaces of 3 subjects in the database with the same gestational age 29 weeks. From left to right, more folds appear on surfaces and the value of $H$ decreases consistently.

number of vertices in our database, $N = 7910$, all steps of Algorithm 1 took about $45$ minutes to be performed.

**A comparative example.**
Here, we try to give a better intuitive picture of how $H$ can be considered as a global gyrification index. In Fig. 4.18, the left hemispheres of 3 subjects at the same age 29 are represented. The map of $\tilde{R}_H$ is also depicted on the corresponding approximated reference surface, $\tilde{\mathcal{S}}^{ref}$, of each subject. For these subjects, the value of $H$ varies between $0.40$ and $0.66$. Subjects 2 and 3 in Figs. 4.18b and 4.18c developed the central sulcus and the insula while the Subject 1 in Fig. 4.18a lacks the central sulcus but started to develop the insula. Apparently, the surface of Subject 1 is less folded than others. Consistently, it got the largest value of $H$ among others.

Moreover, due to almost similar distribution of folds on subjects 2 and 3, the patterns of $\tilde{R}_H$ for these subjects look almost similar. Although, the values of $R_H$ at anatomically corresponding regions are not the same. It is due to differences in the depth of corresponding folds. Among these subjects, Subject 3 with deeper folds (dark blue in color maps) have smaller $H$.

### 4.4.2. Comparison to fractal dimension

From the covariance function of fBm and the fact that fBm has stationary increments, it is proved that fBm is a self-similar process (e.g. CHOW 2011). More precisely, for an fBm $R_H$ indexed on $\mathbb{R}$

$$\forall c > 0,\ R_H(t_0 + ct) - R_H(t_0) \overset{d}{=} c^H(R_H(t_0 + t) - R_H(t_0)), \tag{4.73}$$

where the equality is understood in distribution. Especially, since $R_H(0) = 0$ almost surely, we have

$$\forall c > 0,\ R_H(ct) \overset{d}{=} c^H R_H(t). \tag{4.74}$$

This means that time scaling of fBm doesn't influence its distribution. In other words, fBm is a statistical fractal. That's why it is also called "*fractal Brownian motion*" (CHOW 2011). This property holds for fBm's indexed on manifolds as well (GELBAUM 2014). In this manner, the model described by Eq. (4.13) generates fractal surfaces from smooth manifolds. Being fBs a fractal, one may wish to compute its fractal dimension (FD). Here, we remind the definition of the fractal dimension adapted from CHOW 2011.

**Definition 7** (BARNSLEY 2014). *Let $A$ be a compact subset of a complete metric space. Given any $\varepsilon > 0$, let $N(A, \varepsilon)$ be the minimum amount of closed balls of $\varepsilon$ radius that cover $A$. If*

$$\mathrm{FD} = \lim_{\varepsilon \to 0} \frac{\log(N(A, \varepsilon))}{\log(\frac{1}{\varepsilon})} < \infty, \tag{4.75}$$

*then* FD *is called the fractal dimension of $A$.*

As discussed in Section 1.3, several methods have been suggested in literature to estimate the FD. Among them the box–counting method is frequently used. This method is directly based on Definition 7 ; see Section 1.3 or BARNSLEY 2014.

Estimating its FD is a way to characterize an fBm. Moreover, there is a simple relationship between $H$ and FD of fBm's :

**Theorem 5** (FALCONER 2004). *Let $R_H$ be a fBm indexed in $\mathbb{R}$ with Hurst parameter $H$. The fractal dimension of a $R_H$ is $2 - H$.*

A generalization of this theorem for fractional Brownian surfaces defined on the square $[0, 1] \times [0, 1]$ has been given by FALCONER 2004, (Chapter 16) :

**Theorem 6** (FALCONER 2004). *Let $R_H$ be a fBm indexed in $[0, 1] \times [0, 1]$ with Hurst parameter $H$. The fractal dimension of a $R_H$ is $3 - H$.*

Since this theorem is proved based on the Hölder continuity of $R_H$ which also holds in case of fBm's indexed on manifolds, we give the following conjecture :

Table 4.3.: FD of adult cortical surfaces reported in the literature and that of fetal cortex estimated from $H$. The unit of Age for our results is week whereas it is year for other results.

| Surface | FD (mean ± SD) | Age (mean ± SD) | Reference |
|---|---|---|---|
| inner | $2.45 \pm -$ | $28.31 \pm 8.24$ | COOK et al. 1995 |
| inner | $2.30 \pm 0.01$ | $27 \pm -$ | FREE et al. 1996 |
| inner | $2.57 \pm 0.01$ | $27.7 \pm 4.4$ | LIU et al. 2003 |
| GM volume | $2.80 \pm 0.05$ | range : $21 - 56$ | KISELEV et al. 2003 |
| outer | $2.42 \pm 0.02$ | $24.1 \pm 4.8$ | HA et al. 2005 |
| central | $2.58 \pm 0.0002$ | $32.1 \pm 10.0$ | YOTTER et al. 2010 |
| inner | $2.48 \pm 0.2$ | $29.04 \pm 3.8$ | our results |

**Conjecture 1.** *For an fBm indexed in an $n$-dimensional manifold, the fractal dimension is equal to $n + 1 - H$.*

So, in the case of fractional Brownian surfaces embedded in $\mathbb{R}^3$, the fractal dimension would be $3 - H$. This interesting relationship can be useful in two directions :

1. Given $H$ and a smooth manifold, one can generate a fractal surface with known FD. It can be used to evaluate the precision of FD estimators.
2. Given an fBs, one can approximate its FD by using well known methods such as box-counting method. It is a way to estimate the Hurst parameter of the given fBs.

In case of the brain surface, it has been considered as a fractal surface – at least in a limited range of spatial scales. Consequently, some research has been done to estimate its FD (e.g. HOFMAN 1991 ; FREE et al. 1996 ; KISELEV et al. 2003 ; YOTTER et al. 2011). To the best of our knowledge, however, none of these studies have been done on fetal brains. By using different estimators and considering different cortical surfaces (inner/outer/central[c]) or brain volume, different FD's have been reported. Some of those results are summarized in Table 4.3. A comprehensive review on fractal analysis of medical signals, including brain imaging, is given by LOPES et al. 2009.

For the fetal subjects in this study, the FD computed by $3 - H$ is in the range of $(2.03, 2.77)$ with mean±SD=$2.48 \pm 0.2$ ; see the last line of Table 4.3. In comparison to other FD's, presented in Table 4.3, the average values of FD computed from $H$ across fetal subjects (2.48) is close to the FD of adult subjects (2.30, 2.45 in and 2.57 reported in different studies on inner brain surface). Our results, however, show a higher standard deviation. It is, of course, because of vast changes

---

c. Inner : the white matter/gray matter interface. Outer : the pial surface i.e. gray matter/cerebrospinal fluid interface. Central : the mean of inner and outer surfaces.

of cortical complexity due to gyrification process in fetal ages. In contrast, other results in the table have been computed on subjects in adult ages when the cortical complexity doesn't change that much which results in FD values with less variability.

### 4.4.3. Multi-fractional Brownian surfaces and local Hurst parameter

Local measures of cortical complexity admit a heterogeneous complexity pattern of brain surface. With such a perspective, a more flexible model than a fractional Brownian motion as in Eq. (4.13) is needed to describe this surface. This model can be an extension of the fBs with locally variable Hurst parameter $H(x)$.

Such models have been defined on $\mathbb{R}$ as multifractional Brownian motions (mBm's). Two integral definitions of this model have been presented by PELTIER et al. 1995 and BENASSI et al. 1998. These definitions are proved to be identical in distribution (COHEN 1999). The covariance of this model is as following, looking a generalization of that of fBm (4.6) :

$$\mathbb{E}[R_{H(t)}(t)R_{H(s)}(s)] = g(H(t),H(s))\Big(|t|^{H(t)+H(s)} + |s|^{H(t)+H(s)} - |t-s|^{H(t)+H(s)}\Big), \tag{4.76}$$

where

$$g(H(t),H(s)) = K(H(t)+H(s))^{-1}\Big(K(2H(t))K(2H(s))\Big)^{1/2}, \tag{4.77}$$

and

$$K(\alpha) = \Gamma(\alpha+1)\frac{\sin(\alpha\pi/2)}{\pi}. \tag{4.78}$$

An example of such mBm is plotted in Fig. 4.19.

GELBAUM et al. 2014 proposed that the idea of mBm can be extended to manifolds. Although a theory of such extension has not been defined yet, still we can do some simulations with $H$ on a smooth indexing manifold. In this manner, a generalization of Eq. (4.13) with varying $H$ will be

$$R_{H(x)}(x) = C\sum_{l=2}^{\infty}(\lambda_l)^{-(\frac{d}{4}+\frac{H(x)}{2})}(\phi_l(x)-\phi_l(o))\xi_l. \tag{4.79}$$

In case of mBm, a spectral estimator of $H(x)$, akin to the one presented in Section 4.2 for fBm, can be proposed in a local manner. Indeed, instead of taking the Fourier transform of $R_H$, one may think of the windowed Fourier transform, presented in Chapter 2, that gives local distribution of spectral powers.

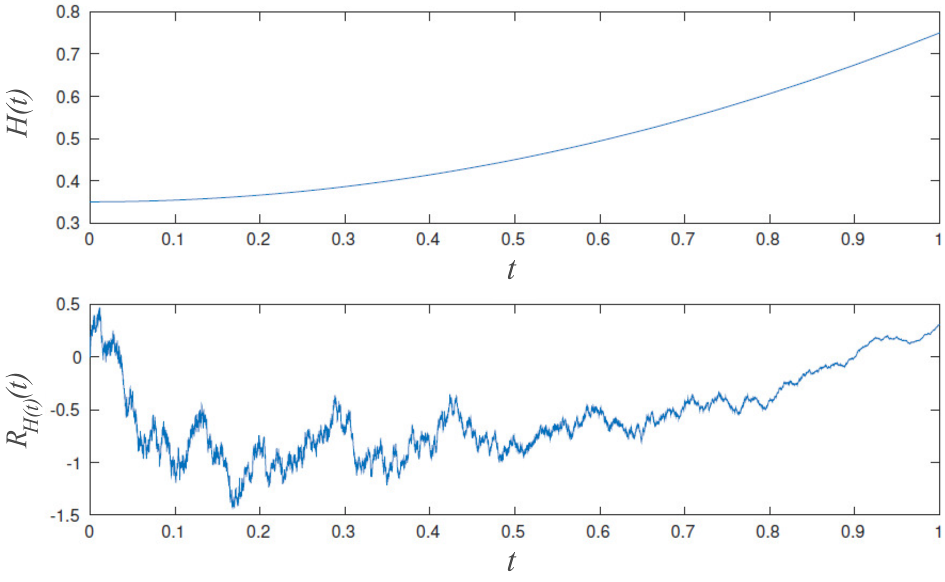

Figure 4.19.: Upper panel : a Hurst function $H_t = 0.35 + 0.4t^2,\ t \in (0,1)$. Lower panel : a corresponding mBm realization $R_{H(t)}(t)$ illustrating locally varying regularity. This figure is adapted from Edvinsson 2015.

Here, we explain this method through an example. A multifractional Brownian motion on sphere surface is given in Fig. 4.20a. The Hurst parameter $H(x)$ of this motion is ruled by

$$H(x) = -0.3 + \frac{1}{1 + x_1^2 + x_2^2}, \tag{4.80}$$

where $x = (x_1, x_2, x_3)$ denotes the Cartesian coordinates of $x$. This function is depicted on Fig. 4.20b. Starting from the equator of the sphere to its poles, $H$ increases and takes its maximum at the north and south poles of the sphere. Accordingly, the regions near the poles of the multifractional surface corresponding to this $H(x)$ are less complicated while the region around the equator is more complicated. The multifractional surface is shown in Fig. 4.20c. To apply the windowed Fourier transform, as explained in Chapter 2, we use the adaptive window function $g$, given by Eq. (2.44), and the translation operator $T$, given by Eq. (2.42) to move the window function across mesh vertices. Applying the translated window function $T_i g$ on $R_H$ gives a localized $R_H$ around each vertex $P_i$

$$R_{H,i}(n) = (T_i g)(n) R_H(n). \tag{4.81}$$

An example of such localized $R_{H,i}$ around an exemplar vertex is represented in Fig. 4.20d. It is seen that $R_{H,i}$ retains a similar pattern as $R_H$ near vertex $P_i$ but vanishes on vertices far from $P_i$. Now, by computing the windowed Fourier transform coefficients $\hat{R}_{H,i}$, given by Eq. (2.46), at this vertex, a localized distribution

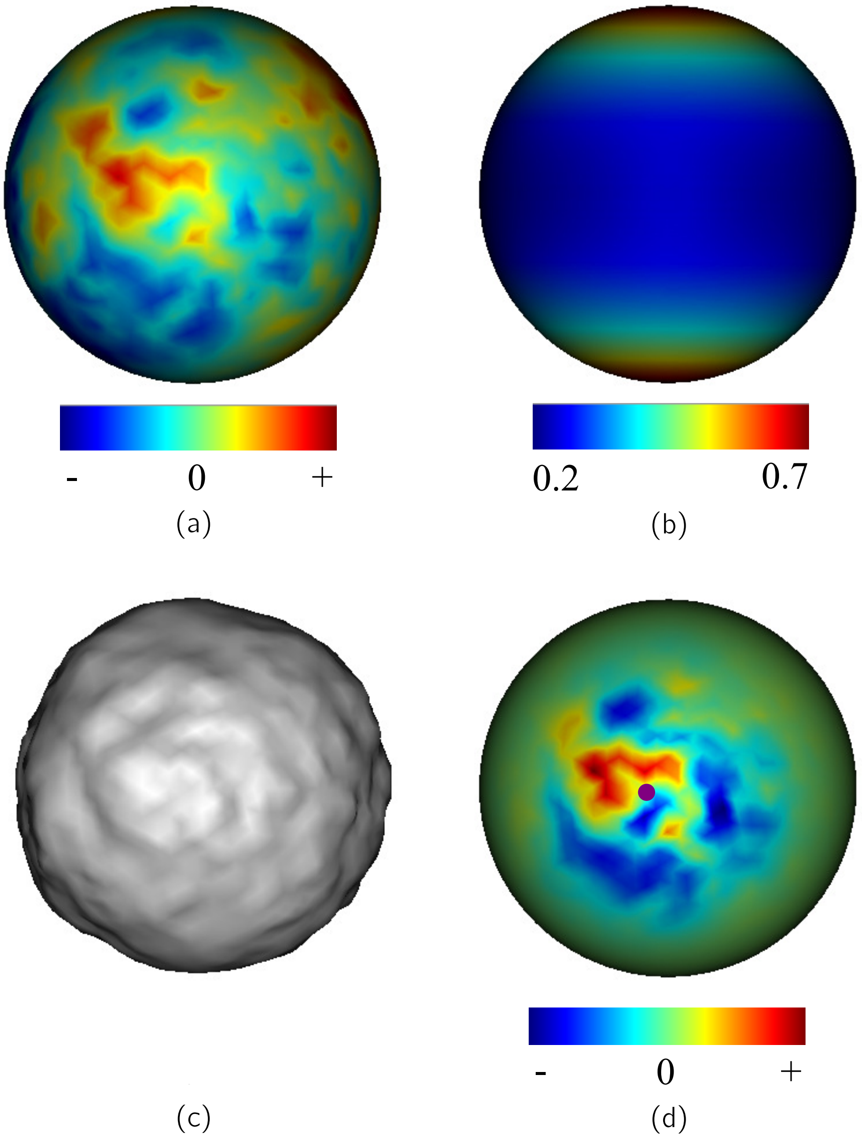

(a)

(b)

(c)

(d)

Figure 4.20.: (a) A multifractional Brownian motion on a sphere surface. (b) Map of $H(\mathbf{x})$ given by Eq. (4.80). (c) The multifractional surface. (d) An example of the localized $R_{H,i}$ around an exemplar vertex shown by the purple circle. (e) Map of absolute error $|\tilde{H}(i) - H(i)|$.

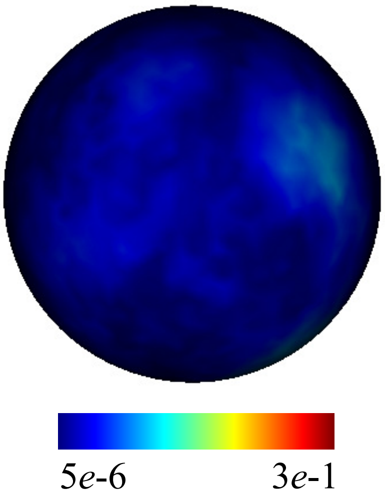

(e)

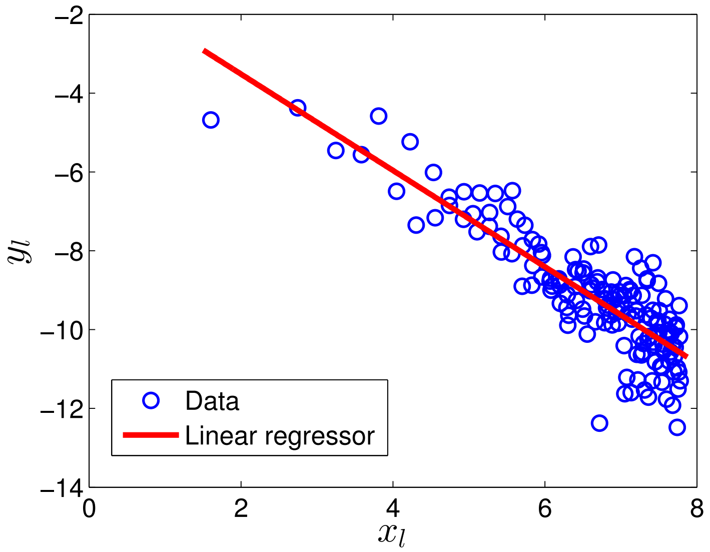

Figure 4.21.: Linear regression analysis on $\{(x_l, y_l)\}$ data of the exemplar vertex of the multifractional sphere shown in Fig. 4.20c

of spectral powers is obtained :

$$\hat{R}_{H,i}(k)^2 = C^2 \lambda_k^{-(\frac{d}{4}+\frac{H(i)}{2})} \xi_k^2.$$

Now, as in case of fBm, taking logarithm along with binning strategy gives

$$y_l = \alpha x_l + \beta, \tag{4.82}$$

where $x_l$ and $y_l$ are given by Eqs. (4.46) and (4.47) and $\alpha = -(d/2 + H(i))$. For the exemplar vertex, the distribution of $y_l$ vs. $x_l$ is shown in Fig. 4.21. Now, the slope of the regression line of this distribution gives an estimation of $H(i)$. For this example the mean and standard deviation of absolute errors across all vertices are

$$\begin{aligned} \text{mean}_{1\leq i\leq N}|\tilde{H}_i - H_i| &= 0.086, & (4.83)\\ \text{std}_{1\leq i\leq N}|\tilde{H}_i - H_i| &= 0.065. & (4.84)\end{aligned}$$

The map of absolute error of $H$ estimation is depicted in Fig. 4.21e. The same procedure may be applied on cortical surface to give a local gyrification index $H(x)$.

### 4.4.4. Limitations of the proposed method

The proposed algorithm gives an estimation of Hurst parameter of an observed fractional Brownian surface. In Section 4.3.1, it is seen that the mean square error of estimation of $H$ for 1000 trials of fractional Brownian spheres is about 0.064. This error roots in the approximation procedures existing in the proposed algorithm. These procedures are listed here :

1. Approximation of $R_H$
2. Approximation of the reference surface
3. Approximation of Laplacian eigenpairs of the reference surface by using linear FEM
4. Approximation of $H$ by regression analysis while only one observation is available

Dependency on several sources of error might be considered as a drawback of this algorithm. One may suggest more accurate methods for the above-mentioned approximations. It is worth to note that in the case of 1000 trials on sphere, if we had the real values of $R_H$ and the reference surface (i.e. the sphere itself), the first two roots of error would be eliminated but the mean square error of $H$ would be about 0.060. It shows that the procedures of approximating $R_H$ and the reference surface does not contribute mainly on the total error. So, to improve the results, one may consider more accurate approximating methods for Laplacian eigenpairs (e.g. REUTER et al. 2009a).

In our experiments on fractional Brownian spheres, we considered the coefficient of fBm as $C = 1$. Large amplitudes may spoil the estimation. It is mainly due to the approximation of the reference surface (i.e. sphere). More precisely, applying $R_H$ on a reference surface like sphere moves its barycenter. In fact, the larger the amplitude of $R_H$, the larger the barycenter movement of the reference surface. Besides, using the mean curvature flow smoothing for reconstruction of the reference surface from the fractional surface moves the barycenter at each step of smoothing. Since, we suppose that the reference surface is not available, we translate the barycenter of the smoothed surface to that of the observed surface. Consequently, if the barycenter of the observed surface is far from that of the reference surface because of a large amplitude, the approximated reference surface is not well superimposed on the real reference surface thus corrupt the estimation of $R_H$ and $H$.

The method is also sensitive to mesh quality. Especially, if the mesh quality is poor, the smoothing procedure, the inflation and approximation of Laplacian eigenvalues will be problematic thus corrupt the approximation of $R_H$, the reference surface and $H$. This might happen for brain surface data especially for fetal brains. Indeed the segmentation of white and gray matters of fetal brains are hard due to low contrast and head movement. So the preprocessing pipeline of MR images may fail to give a proper mesh surface.

# Conclusion

In this thesis, we dealt with the definition and quantification of the surface complexity as a morphological characteristic of folded surfaces. We defined the surface complexity notion and proposed methods to measure it. The proposed methods were then applied to measuring the degree of folding of the human cerebral cortex. The conclusions of this thesis are in two directions which are given below. Some directions for future research are outlined at the end of this section.

**In the first direction,** we defined the surface complexity in two ways, inspired by the intuitive perceptions of it which are based on the properties of the surface bending : 1) the magnitude of bending and 2) the spatial variation of bends. To quantify these definitions, we developed a local spectral analysis of surfaces modelled by triangular meshes. Indeed, we extended the graph windowed Fourier transform to mesh setting through 1) replacing the graph Laplacian operator by a linear finite element discretization of the Laplace-Beltrami operator of surfaces, 2) modifying the window function to be adapted by the size of surfaces.

We then applied the mesh windowed Fourier transform on the mean curvature of surfaces, as a local measure of bending, and proposed two local measures of surface complexity. The first one, called spectral gyrification index (sGI), is the total power of frequencies of the mean curvature in a neighbourhood around each mesh vertex. We proved that it measures the magnitude of bending. The second one, called weighted gyrification index (wGI), is a weighted sum of frequency powers of the mean curvature. Thanks to the special weights which are normalized Laplace-Beltrami eigenvalues, we proved that wGI measures the variation of bends in a neighbourhood around each mesh vertex. Integration of sGI or wGI on a surface gives a global measure of complexity of the surface. Finally, we discussed that sGI and wGI satisfy the most of properties of a standard GI.

The proposed method was then applied to some synthetic wavy surfaces as well as a database of 124 healthy adult human brain surfaces from OASIS database[d]. For comparison, a surface area-based GI, i.e. Toro's GI, is also computed for those surfaces.

Our experiments on synthetic wavy surfaces elucidated that Toro's GI may not

---

[d] Open Access Series of Imaging Studies (OASIS) is available at http://www.oasis-brains.org/

distinguish deep regular folds from oscillating ones. It reveals the main drawback of surface area-based GIs that compute a ratio of surface areas as a GI without paying attention to the configuration of folds thus they are biased by depth of folds. Consequently, when computed on a cortical surface, they give higher values to deep folds like the insula and the central sulcus where there is much surface area than in oscillating shallow ones.

In contrast, our proposed GIs appropriately assign low values to walls of deep folds that are relatively regular and high values to regions consisting of sharp or oscillating folds. The GIs, when computed on cortical surfaces, demonstrate that the primary folds like the central sulcus and the insula are less folded than other regions. They give highest values to the lateral prefrontal cortex and medial occipital cortex.

The proposed analysis can be done in different spatial scales which gives the complexity of the brain surface from gyrus/sulcus scale to a regional scale. The distribution of sGI and wGI values in fine spatial scales show that our GIs can catch the complexity of folds all over the brain. It is an advantage of our method over surface area-based methods which their GI maps in larger scales are a propagated version of those maps in fine scales. Therefore, they may fail to catch other folded parts of the brain, thus affecting the reliability of findings.

Our GIs, consistent with some experimental studies and a mechanical model of brain development, revealed a positive allometry relationship between the global cortical complexity and brain volume. In other words, the proposed GIs showed that larger brains are more folded than expected by an isometric scaling. This global analysis, however, cannot unveil the cortical regions that are more complex in larger brains. To address this question, a similar analysis has been performed in the vertex level. The results showed a heterogeneous increase of cortical complexity with brain volume. The most increasing complexity happens in the least complex regions like the walls of deep folds e.g. the insula and the central sulcus.

**In the second direction,** we worked on identification of the recently introduced fractional Brownian surfaces. Particularly, we proposed a spectral-regression algorithm to estimate the Hurst parameter ($H$) of those surfaces. The algorithm consists of mesh processing procedures such as smoothing and dilation together with a mesh Fourier transform and linear least-square regression analysis.

To test the efficiency of the proposed algorithm, we successfully used it to estimate the Hurst parameter of a set of simulated fractional Brownian spheres. Furthermore, by measuring the Hurst parameter of fetal cerebral cortices, we showed that the fetal cerebral cortex can be considered as a fractional Brownian surface, at least in a range of its low frequency band.

$H$ is a characteristic of fractional Brownian motions (fBm's) underlying fractional Brownian surfaces. It varies in the range of $(0, 1)$ and indicates the Hölder regularity of fBm's. For small $H$ of an fBm, the corresponding fBs is less regular. Following that, we defined the surface complexity by the Hölder regularity and we suggested $H$ as a global GI. We discussed that $H$ potentially has many properties of a standard GI such as a clear definition of the surface complexity, physicality, geometric invariance and efficiency. The main lack, however, is the locality of $H$. To address this issue, we brought up the idea of replacing the mesh Fourier transform in the proposed algorithm by the mesh windowed Fourier transform. In this way, the cerebral cortex is considered as a multi-fractional Brownian surface for which we can estimate local $H$ parameters.

Our results reflect the dynamical process of cortical folding during fetal ages. For example, the youngest fetus in our database has 21 weeks with a very smooth cortex without any fold. As expected, it has a high value of $H$ (>0.75). On the other hand, the oldest subject with 34 weeks developed with highly folded cortex gets the lowest $H$ value (<0.35). The similar interaction of $H$ to brain volume is also observed. The small brains have high $H$ values whereas large brains get low values of $H$.

Due to self-similarity property of an fBm, the corresponding fBs can be considered as a fractal. In this way, the fractal dimension (FD) which indicates the fractal regularity, can be also considered as a measure of surface complexity. For fBm's defined in 1D or on a 2D rectangle, there is a relationship between $H$ and the fractal dimension as $\mathrm{FD} = n + 1 - H$ where $n$ is the space dimension. We conjectured that the same relationship may be true in the case of fBm's defined on manifolds.

Accordingly, we compared our Hurst parameter GI ($H$) with fractal dimension GIs (FD) in the literature. Although, to the best of our knowledge, the fractal dimension of fetal subjects has not been reported yet. Nevertheless, the average values of FD computed from $H$ across fetal subjects (2.48) is close to the FD of adult subjects (2.30, 2.45 and 2.57 reported in different studies). The vast changes of the cortical complexity in fetal ages due to fast gyrification process, in comparison to less variability of that in adult ages, is manifested in high standard deviation (SD) of our results ($= 0.2 \simeq 20\times$SD of adult subjects).

# Future directions

While this thesis introduced new definitions of the surface complexity and developed methods to measure it, many theoretical and experimental opportunities for extending the scope of this thesis still remain. In this section, we present some of these directions.

- **Experimental : The relationship between our proposed GIs and other factors**

  In this thesis, we investigated the effect of brain size on the cortical complexity through a power law analysis of our proposed GI as a function of the brain volume. The relative low but still significant coefficient of determination of power law, $R^2$, clarifies that there is still enough room for other covariates, beyond the volume, to explain the cortical complexity. One interesting direction for future studies is to take into account some other factors in the power law model. Some potential factors are 1) biological ones like age, sex, genetic conditions, 2) cognitive ones e.g. IQ, 3) behavioural ones like special skills e.g. sport skills, skill of playing musical instrument, 4) geometric ones e.g. cortical thickness and fold depth. Some similar studies by using different GIs have been documented in Section 1.2.

- **Theoretical and experimental : comparing different GIs**

  We compared our spectral GIs with a surface area-based GI proposed by Toro et al. 2008. Although, the logic behind other surface area-based GIs is similar to Toro's GI, they differ on implementation. Accordingly, to have a better understanding of the function of those GIs as well as other GIs computed from the surface curvature and fractal dimensions, it is needed to organize an comprehensive comparison study. For this purpose, designing synthetic surfaces with special features and measuring their complexity with the existing GIs can be helpful.

- **Theoretical : the mesh windowed Fourier transform as a general analysis tool**

  We extended the windowed Fourier transform from graph setting to mesh models of surfaces. Then, we apply it on the mean curvature of surfaces to compute the surface complexity. Similarly, it is possible to apply the developed method on other geometrical parameters of surfaces e.g. curvedness, shape index (e.g. Awate et al. 2008 ; Lefèvre et al. 2015), sulcal depth (e.g. Im et al. 2008) etc. It potentially reveals other properties of surface structure.

- **Theoretical : non-linear mean curvature flow smoothing**

  We used the mean curvature flow to smooth the fractional Brownian surfaces. In theory, it is an iterative non-linear process due to updating the Laplace-Beltrami operator at each iteration. To ease the computations, we, however, used the Laplace-Beltrami operator of the initial surface in all iterations. Moreover, by using the non-linear process, the mesh of the final smoothed surface is highly heterogeneous. Consequently, to continue in the framework of our algorithm, the smoothed surface needs to be resampled otherwise the dilation procedure does not work properly. Nevertheless, using the non-linear process may reduce the error of smoothing steps and it is worth to try it.

- **Theoretical : local Hurst parameter as a local GI of the cerebral cortex**

  We brought up the idea of estimating the local Hurst parameter of a multifractional Brownian surface by using the mesh windowed Fourier transform. The evaluation of the idea on a simulated multifractional Brownian sphere shows a low error of estimation. On the other hand, the heterogeneity of the cerebral cortex complexity suggests that the brain surface may have a multifractional structure. So, by using the proposed idea, one can estimate the local Hurst parameter of the cerebral cortex as a local GI.

- **Theoretical : the relationship between FD and** $H$

  In Section 4.4.2, we presented a conjecture that the relationship between the fractal dimension (FD) and the Hurst parameter ($H$) for a fractional Brownian motion defined on a Euclidean space is true for a fBm defined on a manifold. If it comes true, it can be used in two directions :

  1. Given $H$ and a smooth manifold, one can generates a fractal surface with known FD. It can be used to evaluate the precision of FD estimators.
  2. Given an fBs, one can approximate its FD by using well known methods such as box-counting method. It is a way to estimate the Hurst parameter of the given fBs.

  By using this conjecture, we computed the FD of fetal brain surfaces and the results are comparable with those in the literature. It may be considered as an evidence for the conjecture to be true.

# A. Precision of the proposed Hurst parameter estimator

The proof of Proposition 4 is given in following :

*Proof.* We start with the variance of $\alpha$ :

$$\begin{aligned}
\mathbb{V}(\alpha) &= \mathrm{Cov}(\alpha, \alpha) \\
&= \frac{1}{\sigma_x^4}\mathrm{Cov}\left(\sum_{l=1}^{L}\frac{N_l}{N}x_l y_l - \overline{x}\ \overline{y}, \sum_{l=1}^{L}\frac{N_l}{N}x_l y_l - \overline{x}\ \overline{y}\right) \\
&= \frac{1}{\sigma_x^4}\left\{\mathrm{Cov}\left(\sum_{l=1}^{L}\frac{N_l}{N}x_l y_l, \sum_{l=1}^{L}\frac{N_l}{N}x_l y_l\right) - 2\mathrm{Cov}\left(\sum_{l=1}^{L}\frac{N_l}{N}x_l y_l, \overline{x}\ \overline{y}\right)\right. \\
&\qquad \left. + \mathrm{Cov}(\overline{x}\ \overline{y}, \overline{x}\ \overline{y})\right\}, \qquad \text{(A.1)}
\end{aligned}$$

where $\overline{y}$ is the weighted average of $y_l$'s

$$\overline{y} = \sum_{l=1}^{L}\frac{N_l}{N}y_l. \qquad \text{(A.2)}$$

Now, we compute each term of Eq. (A.1) separately :

$$\begin{aligned}
\mathrm{Cov}\left(\sum_{l=1}^{L}\frac{N_l}{N}x_l y_l, \sum_{l=1}^{L}\frac{N_l}{N}x_l y_l\right) &= \sum_{l=1}^{L}\frac{N_l^2}{N^2}x_l^2\mathbb{V}(y_l) \\
&= \sum_{l=1}^{L}\frac{N_l^2}{N^2}x_l^2\frac{\sigma_0^2}{N_l} \\
&= \frac{\sigma_0^2}{N}\sum_{l=1}^{L}\frac{N_l}{N}x_l^2. \qquad \text{(A.3)}
\end{aligned}$$

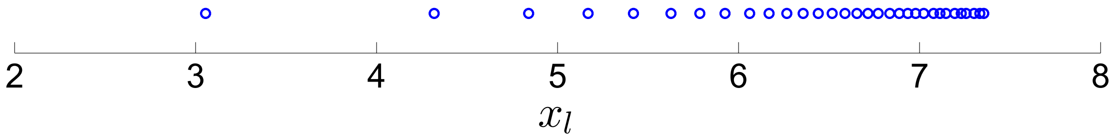

Figure A.1.: Distribution of $x_l$'s for the first 1600 Laplacian eigenvalues of sphere

$$\begin{aligned}
\mathrm{Cov}\left(\sum_{l=1}^{L}\frac{N_l}{N}x_l y_l, \overline{x}\ \overline{y}\right) &= \mathrm{Cov}\left(\sum_{l=1}^{L}\frac{N_l}{N}x_l y_l, \overline{x}\sum_{l=1}^{L}\frac{N_l}{N}y_l\right) \\
&= \overline{x}\sum_{l=1}^{L}\frac{N_l^2}{N^2}x_l\mathbb{V}(y_l) \\
&= \overline{x}\sum_{l=1}^{L}\frac{N_l^2}{N^2}x_l\frac{\sigma_0^2}{N_l} \\
&= \frac{\sigma_0^2\overline{x}^2}{N}. \qquad \text{(A.4)}
\end{aligned}$$

And the third term will be

$$\begin{aligned}
\mathrm{Cov}(\overline{x}\ \overline{y}, \overline{x}\ \overline{y}) &= \overline{x}^2\mathrm{Cov}(\overline{y}\ \overline{y}) \\
&= \overline{x}^2\mathrm{Cov}(\sum_{l=1}^{L}\frac{N_l}{N}y_l, \sum_{l=1}^{L}\frac{N_l}{N}y_l) \\
&= \overline{x}^2\sum_{l=1}^{L}\frac{N_l^2}{N^2}\curvearrowright\lessdot \\
&= \overline{x}^2\sum_{l=1}^{L}\frac{N_l^2}{N^2}\frac{\sigma_0^2}{N_l} \\
&= \frac{\sigma_0^2\overline{x}^2}{N}. \qquad \text{(A.5)}
\end{aligned}$$

Now, by substituting Eqs. (A.3)-(A.5) in Eq. (A.1), we get

$$\begin{aligned}
\mathbb{V}(\alpha) &= \frac{\sigma_0^2}{N\sigma_x^4}\left\{\sum_{l=1}^{L}\frac{N_l}{N}x_k^2 - \overline{x}^2\right\} \\
&= \frac{\sigma_0^2}{N\sigma_x^2}. \qquad \text{(A.6)}
\end{aligned}$$

Similar computations give the variance of $\beta$. ☐

This theorem suggests that if bins are chosen in a way that the points $x_l$'s are more spread, the precision of $H$ and $C$ estimations increases.

For instance, in case of the sphere, the Laplacian eigenvalues are

$$\lambda_{m,l} = l(l+1), \quad |m| \leq l, \;\; l = 0, 1, 2 \ldots$$

Consequently, the eigenvalues are not distributed homogeneously i.e. the density of eigenvalues is higher for large $l$'s. So, if The strategy of binning with equal number of elements in each bin is applied, the dispersion of $x_l$'s will be low, especially for large $l$'s ; see Fig. A.1 for the first 1600 eigenvalues. So, one may think of another binning strategy with higher variance of $x_l$'s.

# Bibliography

[1] P. ABRY et al. « Wavelets, spectrum analysis and 1/f processes ». *Wavelets and statistics*. Springer, 1995, p. 15–29 (cf. p. 97).

[2] P. ABRY et al. « The wavelet-based synthesis for fractional Brownian motion proposed by F. Sellan and Y. Meyer : Remarks and fast implementation ». *Appl. Comput. Harmon. A.* 3.4 (1996), p. 377–383 (cf. p. 91).

[3] E. ARMSTRONG et al. « The ontogeny of human gyrification ». *Cereb. Cortex* 5.1 (1995), p. 56–63. DOI : `10.1093/cercor/5.1.56` (cf. p. 11).

[4] S. ASMUSSEN. « Stochastic Simulation With a View Towards Stochastic Processes (MaPhySto Lecture Notes 2) ». *Centre Math. Phys. Stoch-Aarhus* (1999) (cf. p. 91).

[5] P. ASVESTAS et al. « A Power Differentiation Method of Fractal Dimension Estimation for 2-D Signals ». *J. Vis. Commun. Image R.* 9.4 (déc. 1998), p. 392–400. DOI : `10.1006/jvci.1998.0394` (cf. p. 25).

[6] G. AUZIAS et al. « Model-driven harmonic parameterization of the cortical surface : HIP-HOP ». *IEEE Trans. Med. Imag.* 32.5 (2013), p. 873–887. DOI : `10.1109/TMI.2013.2241651` (cf. p. 79, 82, 85).

[7] S. P. AWATE et al. « 3D Cerebral Cortical Morphometry in Autism : Increased Folding in Children and Adolescents in Frontal, Parietal, and Temporal Lobes ». *Medical Image Computing and Computer-Assisted Intervention – MICCAI 2008*. International Conference on Medical Image Computing and Computer-Assisted Intervention. Springer, Berlin, Heidelberg, 6 sept. 2008, p. 559–567. DOI : `10.1007/978-3-540-85988-8_67` (cf. p. 135).

[8] S. P. AWATE et al. « Cerebral cortical folding analysis with multivariate modeling and testing : Studies on gender differences and neonatal development ». *NeuroImage* 53.2 (2010), p. 450–459. DOI : `10.1016/j.neuroimage.2010.06.072` (cf. p. 26).

[9] G. BAKKER et al. « Cortical Morphology Differences in Subjects at Increased Vulnerability for Developing a Psychotic Disorder : A Comparison between Subjects with Ultra-High Risk and 22q11.2 Deletion Syndrome ». *PLOS ONE* 11.11 (9 nov. 2016), e0159928. DOI : `10.1371/journal.pone.0159928` (cf. p. 6, 16, 26).

[10] M. F. BARNSLEY. *Fractals everywhere*. Academic press, 2014 (cf. p. 125).

[11] J. BATES et al. « Spectral signatures of point clouds and applications to detection of Alzheimer's Disease through Neuroimaging ». *2011 IEEE International Symposium on Biomedical Imaging : From Nano to Macro*. 2011 IEEE International Symposium on Biomedical Imaging : From Nano to Macro. Mar. 2011, p. 1851–1854. DOI : `10.1109/ISBI.2011.5872768` (cf. p. 34).

[12] C. E. BEARDEN et al. « Alterations in Midline Cortical Thickness and Gyrification Patterns Mapped in Children with 22q11.2 Deletions ». *Cereb. Cortex* 19.1 (1<sup>er</sup> jan. 2009), p. 115–126. DOI : `10.1093/cercor/bhn064` (cf. p. 6, 16, 26).

[13] A. BENASSI et al. « Identifying the multifractional function of a Gaussian process ». *Stat. Probabil. Lett.* 39.4 (21 août 1998), p. 337–345. DOI : `10.1016/S0167-7152(98)00078-9` (cf. p. 127).

[14] Y. BENJAMINI et al. « Controlling the False Discovery Rate : A Practical and Powerful Approach to Multiple Testing ». *J. Roy. Stat. Soc. B Met.* 57.1 (1995), p. 289–300 (cf. p. 86).

[15] J. BERAN. *Statistics for long-memory processes*. T. 61. CRC press, 1994 (cf. p. 97).

[16] P. BÉRARD et al. « Embedding Riemannian manifolds by their heat kernel ». *Geom. Func. Anal.* 4.4 (1<sup>er</sup> juil. 1994), p. 373–398. DOI : `10.1007/BF01896401` (cf. p. 33).

[17] M. BERGER. *A Panoramic View of Riemannian Geometry*. en. Berlin, Heidelberg : Springer Berlin Heidelberg, 2003. ISBN : 978-3-540-65317-2 978-3-642-18245-7 (cf. p. 49).

[18] A. K. BISOI et al. « On calculation of fractal dimension of images ». *Pattern Recogn. Lett.* 22.6 (2001), p. 631–637 (cf. p. 25).

[19] H. M. BONNICI et al. « Pre-frontal lobe gyrification index in schizophrenia, mental retardation and comorbid groups : An automated study ». *NeuroImage* 35.2 (2007), p. 648 –654. DOI : `http://dx.doi.org/10.1016/j.neuroimage.2006.11.031` (cf. p. 15, 16).

[20] A. BRUNTON et al. « Filling holes in triangular meshes by curve unfolding ». *2009 IEEE International Conference on Shape Modeling and Applications*. 2009 IEEE International Conference on Shape Modeling and Applications. Juin 2009, p. 66–72. DOI : `10.1109/SMI.2009.5170165` (cf. p. 106).

[21] E. BULLMORE et al. « Fractal analysis of the boundary between white matter and cerebral cortex in magnetic resonance images : a controlled study of schizophrenic and manic-depressive patients ». *Psychol. Med.* 24.3 (août 1994), p. 771–781 (cf. p. 16).

[22] M. F. CASANOVA et al. « Reduced brain size and gyrification in the brains of dyslexic patients ». *J. Child Neurol.* 19.4 (avr. 2004), p. 275–281 (cf. p. 16).

[23] B. B. CHAUDHURI et al. « Texture segmentation using fractal dimension ». *IEEE T. Pattern Anal.* 17.1 (1995), p. 72–77 (cf. p. 25).

[24] S. S. CHEN et al. « On the calculation of fractal features from images ». *IEEE T. Pattern Anal.* 15.10 (1993), p. 1087–1090 (cf. p. 25).

[25] C. CHERNIAK. « Neural component placement ». *Trends Neurosci.* 18.12 (1995), p. 522–527 (cf. p. 11).

[26] « Chi-square Goodness of Fit Test ». *The Concise Encyclopedia of Statistics*. Springer New York, 2008, p. 72–76. ISBN : 978-0-387-31742-7 978-0-387-32833-1. DOI : `10.1007/978-0-387-32833-1\_55` (cf. p. 111).

[27] W. C. CHOW. « Fractal (fractional) Brownian motion ». *WIREs Comp. Stat.* 3.2 (1$^{er}$ mar. 2011), p. 149–162. DOI : `10.1002/wics.142` (cf. p. 125).

[28] C. CHU et al. « Cortical Folding in Post-traumatic Stress Disorder after Motor Vehicle Accidents : Regional Differences in Gyrification ». *Psychiatry Clin. Neurosci.* (1$^{er}$ nov. 2016), n/a–n/a. DOI : `10.1111/pcn.12485` (cf. p. 17).

[29] F.R.K. CHUNG et al. *Spectral graph theory*. CBMS-NSF regional conference series in mathematics, no. 92. Conference Board of the Mathematical Sciences, 1997. ISBN : 978-0-8218-0315-8. URL : `https://books.google.fr/books?id=5KYhjwEACAAJ` (cf. p. 30, 31).

[30] M. K. CHUNG et al. « Weighted Fourier Series Representation and Its Application to Quantifying the Amount of Gray Matter ». *IEEE Trans. Med. Imaging* 26.4 (avr. 2007), p. 566–581. DOI : `10.1109/TMI.2007.892519` (cf. p. 37).

[31] N. H. P. CLAESSENS et al. « Reduced cerebral cortical growth and folding in severe congenital heart disease ». *Pediatric Academic Societies Annual Meeting*. 2016 (cf. p. 16).

[32] R. G. CLEGG. « A practical guide to measuring the Hurst parameter ». *arXiv :math/0610756* (25 oct. 2006). arXiv :`math/0610756`. URL : `http://arxiv.org/abs/math/0610756` (cf. p. 96, 97).

[33] J.-F. COEURJOLLY. « Simulation and identification of the fractional Brownian motion : a bibliographical and comparative study ». *J. Stat. Softw.* 5.1 (2000), p. 1–53. DOI : `10.18637/jss.v005.i07` (cf. p. 89, 92, 97).

[34] J.-F. COEURJOLLY. « Estimating the parameters of a fractional Brownian motion by discrete variations of its sample paths ». *Stat. Infer. Stoch. Process.* 4.2 (2001), p. 199–227 (cf. p. 97).

[35] S. COHEN. « From Self-Similarity to Local Self-Similarity : the Estimation Problem ». *Fractals*. Springer, London, 1999, p. 3–16. DOI : `10.1007/978-1-4471-0873-3\_1` (cf. p. 127).

[36] T. COLDING et al. « Mean curvature flow ». *Bull. Amer. Math. Soc.* 52.2 (2015), p. 297–333. DOI : `10.1090/S0273-0979-2015-01468-0` (cf. p. 100).

[37] M. J. COOK et al. « Fractal Description of Cerebral Cortical Patterns in Frontal Lobe Epilepsy ». *ENE* 35.6 (1995), p. 327–335. DOI : `10.1159/000117155` (cf. p. 126).

[38] R. B. DAVIES et al. « Tests for Hurst effect ». *Biometrika* (1987), p. 95–101 (cf. p. 91).

[39] T. DIEKER. « Simulation of fractional Brownian motion ». *MSc theses, University of Twente, Amsterdam, The Netherlands* (2004) (cf. p. 92).

[40] J. DUBOIS et al. « Exploring the successive waves of cortical folding in the developing brain using MRI and spectral analysis of gyrification ». *2016 IEEE 13th International Symposium on Biomedical Imaging (ISBI)*. 2016 IEEE 13th International Symposium on Biomedical Imaging (ISBI). Avr. 2016, p. 261–264. DOI : `10.1109/ISBI.2016.7493259` (cf. p. 42).

[41] R. DYER et al. *An Investigation of the Spectral Robustness of Mesh Laplacians*. Simon Fraser University, 2005 (cf. p. 30).

[42] S. EDVINSSON. *Estimation of the local Hurst function of multifractional Brownian motion : A second difference increment ratio estimator*. 2015. URL : `http://www.diva-portal.org/smash/record.jsf?pid=diva2:828116` (cf. p. 128).

[43] K. FALCONER. *Fractal geometry : mathematical foundations and applications*. John Wiley & Sons, 2004 (cf. p. 125).

[44] A. FEUERVERGER et al. « Estimation of fractal index and fractal dimension of a Gaussian process by counting the number of level crossings ». *J. Time Ser. Anal.* 15.6 (1994), p. 587–606 (cf. p. 97).

[45] M. S. FLOATER et al. « Surface Parameterization : a Tutorial and Survey ». *Advances in Multiresolution for Geometric Modelling*. Springer, Berlin, Heidelberg, 2005, p. 157–186. DOI : `10.1007/3-540-26808-1\_9` (cf. p. 29).

[46] S. L. FREE et al. « Three-dimensional fractal analysis of the white matter surface from magnetic resonance images of the human brain ». *Cereb. Cortex* 6.6 (déc. 1996), p. 830–836 (cf. p. 18, 25, 126).

[47] D. GABOR. « Theory of communication ». *J. I. Elec. Eng.* 93 (1946), p. 429–457 (cf. p. 42).

[48] R. GANGOLLI. « Positive definite kernels on homogeneous spaces and certain stochastic processes related to Lévy's brownian motion of several parameters ». *Ann. I. H. POINCARE-PR.* 3.2 (1967), p. 121–226. URL : https://eudml.org/doc/76869 (cf. p. 92).

[49] C. GASER et al. « Increased local gyrification mapped in Williams syndrome ». *NeuroImage* 33.1 (2006), p. 46 –54. DOI : http://dx.doi.org/10.1016/j.neuroimage.2006.06.018 (cf. p. 16).

[50] Z. GELBAUM. « Fractional Brownian fields over manifolds ». *Trans. Amer. Math. Soc.* 366.9 (2014), p. 4781–4814. DOI : 10.1090/S0002-9947-2014-06106-0 (cf. p. 8, 89, 90, 93, 94, 125).

[51] Z. GELBAUM et al. « Simulation of Fractional Brownian Surfaces via Spectral Synthesis on Manifolds ». *IEEE T. Image Process.* 23.10 (oct. 2014), p. 4383–4388. DOI : 10.1109/TIP.2014.2348793 (cf. p. 94, 127).

[52] D. GERMANAUD et al. « Larger is twistier : spectral analysis of gyrification (SPANGY) applied to adult brain size polymorphism ». *NeuroImage* 63 (2012), p. 1257–72. DOI : 10.1016/j.neuroimage.2012.07.053 (cf. p. 18, 19, 29, 38–42, 83).

[53] D. GERMANAUD et al. « Simplified gyral pattern in severe developmental microcephalies ? New insights from allometric modeling for spatial and spectral analysis of gyrification ». *NeuroImage* 102, Part 2 (2014), p. 317–331. DOI : 10.1016/j.neuroimage.2014.07.057 (cf. p. 18, 26, 42, 83).

[54] J. GEWEKE et al. « The estimation and application of long memory time series models ». *J. Time Ser. Anal.* 4.4 (1983), p. 221–238 (cf. p. 96).

[55] N. J. GIRARD et al. « The brain in the belly : What and how of fetal neuroimaging ? » *J. Magn. Reson. Imaging* 36.4 (2012), p. 788–804 (cf. p. 118).

[56] A. GOLBABAI et al. « Hybrid shape parameter strategy for the RBF approximation of vibrating systems ». *Int. J. Comput. Math.* 89.17 (2012), p. 2410–2427. DOI : 10.1080/00207160.2012.710326 (cf. p. 32, 54).

[57] D. GREBENKOV et al. « Geometrical structure of Laplacian eigenfunctions ». *SIAM Rev.* 55.4 (2013), p. 601–667. DOI : 10.1137/120880173 (cf. p. 32, 54).

[58] X. GU et al. « Genus zero surface conformal mapping and its application to brain surface mapping ». *IEEE Trans. Med. Imaging* 23.8 (août 2004), p. 949–958. DOI : 10.1109/TMI.2004.831226 (cf. p. 37).

[59] T. H. HA et al. « Fractal dimension of cerebral cortical surface in schizophrenia and obsessive–compulsive disorder ». *Neurosci. Lett.* 384.1 (19 août 2005), p. 172–176. DOI : 10.1016/j.neulet.2005.04.078 (cf. p. 126).

[60] D. K. HAMMOND et al. « Wavelets on graphs via spectral graph theory ». *Appl. Comput. Harmon. Anal.* 30 (2011), p. 129 –150. DOI : 10.1016/j.acha.2010.04.005 (cf. p. 49).

[61] K.-M. HAN et al. « Local gyrification index in patients with major depressive disorder and its association with tryptophan hydroxylase-2 (TPH2) polymorphism ». *Hum. Brain Mapp.* (2016). DOI : 10.1002/hbm.23455 (cf. p. 16).

[62] D. HIRJAK et al. « Cortical folding patterns are associated with impulsivity in healthy young adults ». *Brain Imaging Behav.* (14 oct. 2016), p. 1–12. DOI : 10.1007/s11682-016-9618-2 (cf. p. 16).

[63] M. A. HOFMAN. « The fractal geometry of convoluted brains ». *J. Hirnforsch* 32.1 (1991), p. 103–111 (cf. p. 18, 25, 126).

[64] G. HUISKEN. *Flow by mean curvature of convex surfaces into spheres*. Australian National University, Centre for Mathematical Analysis, 1984 (cf. p. 99, 101).

[65] K. IM et al. « Fractal dimension in human cortical surface : Multiple regression analysis with cortical thickness, sulcal depth, and folding area ». *Hum. Brain Mapp.* 27.12 ($1^{\text{er}}$ déc. 2006), p. 994–1003. DOI : 10.1002/hbm.20238 (cf. p. 17, 25).

[66] K. IM et al. « Brain size and cortical structure in the adult human brain ». *Cereb. Cortex* 18.9 (2008), p. 2181–2191. DOI : 10.1093/cercor/bhm244 (cf. p. 18, 80, 83, 135).

[67] J. ISTAS. « Spherical and hyperbolic fractional Brownian motion. » *Electron. Commun. Prob.* 10 (2005), p. 254–262. URL : https://eudml.org/doc/127420 (cf. p. 92).

[68] V. JAIN et al. « Robust 3D Shape Correspondence in the Spectral Domain ». *Proceedings of the IEEE International Conference on Shape Modeling and Applications 2006*. SMI '06. Washington, DC, USA : IEEE Computer Society, 2006, p. 19–. DOI : 10.1109/SMI.2006.31 (cf. p. 35).

[69] J. JIANG et al. « A robust and accurate algorithm for estimating the complexity of the cortical surface ». *J. Neurosci. Meth.* 172.1 (15 juil. 2008), p. 122–130. DOI : 10.1016/j.jneumeth.2008.04.018 (cf. p. 18, 25).

[70] E. JONES et al. « Cerebral cortex series » (1986) (cf. p. 11).

[71] R. J. JOU et al. « Cortical Gyrification in Autistic and Asperger Disorders : A Preliminary Magnetic Resonance Imaging Study ». *J. Child Neurol.* 25.12 (déc. 2010), p. 1462–1467. DOI : 10.1177/0883073810368311 (cf. p. 16).

[72] J. H. KAAS. « Why is brain size so important : Design problems and solutions as neocortex gets biggeror smaller ». *Brain and Mind* 1.1 (2000), p. 7–23 (cf. p. 11).

[73] M. KAC. « Can One Hear the Shape of a Drum ? » *The American Mathematical Monthly* 73.4 (1966), p. 1–23. DOI : `10.2307/2313748` (cf. p. 33).

[74] G. KAISER. « Windowed Fourier Transforms ». English. *A Friendly Guide to Wavelets*. Modern Birkhäuser Classics. Birkhäuser Boston, 2011, p. 44–59. ISBN : 978-0-8176-8110-4 (cf. p. 42, 43, 54, 76).

[75] O. KAPELLOU et al. « Abnormal cortical development after premature birth shown by altered allometric scaling of brain growth ». *PLOS Med.* 3.8 (2006), e265. DOI : `10.1371/journal.pmed.0030265` (cf. p. 19, 83).

[76] J. KARBOWSKI. « How does connectivity between cortical areas depend on brain size ? Implications for efficient computation ». *J. Comput. Neurosci.* 15.3 (2003), p. 347–356 (cf. p. 11).

[77] P. A. KELLY et al. « Cortical Thickness, Surface Area, and Gyrification Abnormalities in Children Exposed to Maltreatment : Neural Markers of Vulnerability ? » *Biol. Psychiat.* Stress : Impact on Brain and Body 74.11 ($1^{er}$ déc. 2013), p. 845–852. DOI : `10.1016/j.biopsych.2013.06.020` (cf. p. 17).

[78] S. H. KIM et al. « Development of cortical shape in the human brain from 6 to 24 months of age via a novel measure of shape complexity ». *NeuroImage* 135 (2016), p. 163–176 (cf. p. 6, 15, 18, 24, 27).

[79] V. G. KISELEV et al. « Is the brain cortex a fractal ? » *NeuroImage* 20.3 (nov. 2003), p. 1765–1774. DOI : `10.1016/S1053-8119(03)00380-X` (cf. p. 18, 25, 126).

[80] E. KREYSZIG. *Differential Geometry*. New edition. New York : Dover Publications Inc., 4 nov. 1991. 384 p. ISBN : 978-0-486-66721-8 (cf. p. 61).

[81] E. KREYSZIG. *Advanced engineering mathematics*. John Wiley & Sons, 2010 (cf. p. 99).

[82] R. LAI et al. « Laplace-Beltrami nodal counts : A new signature for 3D shape analysis ». *2009 IEEE International Symposium on Biomedical Imaging : From Nano to Macro*. 2009 IEEE International Symposium on Biomedical Imaging : From Nano to Macro. Juin 2009, p. 694–697. DOI : `10.1109/ISBI.2009.5193142` (cf. p. 33, 35).

[83] S. B. LAUGHLIN et al. « Communication in neuronal networks ». *Science* 301.5641 (2003), p. 1870–1874 (cf. p. 11).

[84] E. LEBED et al. « Novel surface-smoothing based local gyrification index ». *IEEE Trans. Med. Imag.* 32.4 (2013), p. 660–669. DOI : `10.1109/TMI.2012.2230640` (cf. p. 6, 16, 18, 20).

[85] J. LEFÈVRE et al. « Fast surface-based measurements using first eigenfunction of the Laplace-Beltrami Operator : Interest for sulcal description ». *9th IEEE International Symposium on Biomedical Imaging (ISBI)*. 2012, p. 1527–1530 (cf. p. 66).

[86] J. LEFÈVRE et al. « Brain Lobes Revealed by Spectral Clustering ». *2014 22nd International Conference on Pattern Recognition*. 2014 22nd International Conference on Pattern Recognition. Août 2014, p. 562–567. DOI : 10.1109/ICPR.2014.107 (cf. p. 35).

[87] J. LEFÈVRE et al. « Are developmental trajectories of cortical folding comparable between cross-sectional datasets of fetuses and preterm newborns ? » *Cereb. Cortex* (2015), p. 1–13 (cf. p. 11, 15, 21, 83, 118, 122, 135).

[88] J. LEFÈVRE et al. « Can we hear the shape of a brain ? Spectral analysis of cortical anatomy. » The First International Conference on Mathematical NeuroScience (ICMNS). 8 juin 2015. URL : https://icmns2015.inria.fr/files/2015/03/Session2_icmns15_Lefevre.pdf (cf. p. 36).

[89] B. LEVY. « Laplace-Beltrami Eigenfunctions Towards an Algorithm That "Understands" Geometry ». *IEEE International Conference on Shape Modeling and Applications, 2006. SMI 2006*. Juin 2006, p. 13–13 (cf. p. 49).

[90] P. LÉVY. *Processus stochastiques et mouvement brownien*. Paris, 1965 (cf. p. 92).

[91] M. M. LEWIS et al. « The pattern of gray matter atrophy in Parkinson's disease differs in cortical and subcortical regions ». *J. Neurol.* 263.1 (jan. 2016), p. 68–75. DOI : 10.1007/s00415-015-7929-7 (cf. p. 16).

[92] G. LI et al. « Mapping Longitudinal Development of Local Cortical Gyrification in Infants from Birth to 2 Years of Age ». *J. Neurosci.* 34 (2014), p. 4228–4238 (cf. p. 6, 15, 18, 20, 21, 26, 27).

[93] Z. LIAN et al. « A comparison of methods for non-rigid 3D shape retrieval ». *Pattern Recogn.* 46 (2013), p. 449–461. DOI : http://dx.doi.org/10.1016/j.patcog.2012.07.014 (cf. p. 32).

[94] L. S. LIEBOVITCH et al. « A fast algorithm to determine fractal dimensions by box counting ». *Phys. Lett. A* 141.8 (1989), p. 386 –390. DOI : http://dx.doi.org/10.1016/0375-9601(89)90854-2 (cf. p. 25).

[95] J. J. LIN et al. « Reduced Neocortical Thickness and Complexity Mapped in Mesial Temporal Lobe Epilepsy with Hippocampal Sclerosis ». *Cereb. Cortex* 17.9 (1$^{er}$ sept. 2007), p. 2007–2018. DOI : 10.1093/cercor/bhl109 (cf. p. 16).

[96] J. Z. LIU et al. « Fractal Dimension in Human Cerebellum Measured by Magnetic Resonance Imaging ». *Biophys. J.* 85.6 (déc. 2003), p. 4041–4046. URL : http://www.ncbi.nlm.nih.gov/pmc/articles/PMC1303704/ (cf. p. 6, 17, 26, 126).

[97] X. H. LIU et al. « We can't hear the shape of drum : revisited in 3D case ». *arXiv :1701.05984 [math-ph]* (21 jan. 2017). arXiv :1701.05984. URL : http://arxiv.org/abs/1701.05984 (cf. p. 33).

[98] I. Lobato et al. « Averaged periodogram estimation of long memory ». *J. Econometrics* 73.1 (1996), p. 303–324 (cf. p. 96).

[99] H. Lombaert et al. « Diffeomorphic spectral matching of cortical surfaces. » *IPMI*. T. 7917. 2013, p. 376–389 (cf. p. 35).

[100] H. Lombaert et al. « FOCUSR : Feature Oriented Correspondence Using Spectral Regularization–A Method for Precise Surface Matching ». *IEEE T. Pattern Anal.* 35.9 (sept. 2013), p. 2143–2160. doi : `10.1109/TPAMI.2012.276` (cf. p. 35).

[101] H. Lombaert et al. « Brain Transfer : Spectral Analysis of Cortical Surfaces and Functional Maps ». *Information Processing in Medical Imaging*. International Conference on Information Processing in Medical Imaging. Sous la dir. de Sebastien Ourselin et al. Lecture Notes in Computer Science. Springer International Publishing, 28 juin 2015, p. 474–487. doi : `10.1007/978-3-319-19992-4\_37` (cf. p. 29, 38, 39).

[102] H. Lombaert et al. « Spectral Forests : Learning of Surface Data, Application to Cortical Parcellation ». *Medical Image Computing and Computer-Assisted Intervention – MICCAI 2015*. International Conference on Medical Image Computing and Computer-Assisted Intervention. Sous la dir. de Nassir Navab et al. Lecture Notes in Computer Science. Springer International Publishing, 5 oct. 2015, p. 547–555. doi : `10.1007/978-3-319-24553-9\_67` (cf. p. 36).

[103] R. Lopes et al. « Fractal and multifractal analysis : A review ». *Med. Image Anal.* 13.4 (août 2009), p. 634–649. doi : `10.1016/j.media.2009.05.003` (cf. p. 25, 126).

[104] E. Luders et al. « Gender differences in cortical complexity ». *Nat. Neurosci.* 7.8 (2004), p. 799–800. doi : `10.1038/nn1277` (cf. p. 19).

[105] E. Luders et al. « A curvature-based approach to estimate local gyrification on the cortical surface ». *NeuroImage* 29.4 (2006), p. 1224–1230. doi : `10.1016/j.neuroimage.2005.08.049` (cf. p. 6, 17–19, 23, 24, 26).

[106] E. Luders et al. « Mapping the Relationship between Cortical Convolution and Intelligence : Effects of Gender ». *Cereb. Cortex* 18.9 (1er sept. 2008), p. 2019–2026. doi : `10.1093/cercor/bhm227` (cf. p. 17).

[107] E. Luders et al. « The unique brain anatomy of meditation practitioners : alterations in cortical gyrification ». *Front. Hum. Neurosci.* 6 (2012), p. 34. doi : `10.3389/fnhum.2012.00034` (cf. p. 17).

[108] C. R. Madan et al. « Cortical complexity as a measure of age-related brain atrophy ». *NeuroImage* 134 (1er juil. 2016), p. 617–629. doi : `10.1016/j.neuroimage.2016.04.029` (cf. p. 15, 18).

[109] S. MALLAT. *A Wavelet Tour of Signal Processing, Third Edition : The Sparse Way*. 3rd. Academic Press, 2008. ISBN : 978-0-12-374370-1 (cf. p. 46, 54, 58).

[110] B. MANDELBROT. « How long is the coast of britain ? Statistical self-similarity and fractional dimension ». *Science* 156.3775 (5 mai 1967), p. 636–638. DOI : `10.1126/science.156.3775.636` (cf. p. 25).

[111] B. MANDELBROT et al. « Fractional Brownian Motions, Fractional Noises and Applications ». *SIAM Rev.* 10.4 ($1^{er}$ oct. 1968), p. 422–437. DOI : `10.1137/1010093` (cf. p. 91).

[112] B. B. MANDELBROT et al. « Computer experiments with fractional Gaussian noises : Part 2, rescaled ranges and spectra ». *Water Resour. Res.* 5.1 (1969), p. 242–259 (cf. p. 96).

[113] D. MATEUS et al. « Articulated shape matching using Laplacian eigenfunctions and unsupervised point registration ». *2008 IEEE Conference on Computer Vision and Pattern Recognition*. 2008 IEEE Conference on Computer Vision and Pattern Recognition. Juin 2008, p. 1–8. DOI : `10.1109/CVPR.2008.4587538` (cf. p. 36).

[114] M. MEYER et al. « Discrete differential-geometry operators for triangulated 2-manifolds ». *Visualization and mathematics III*. Springer, 2003, p. 35–57 (cf. p. 23, 30, 99).

[115] T. A. MISKOVICH et al. « Cortical Gyrification Patterns Associated with Trait Anxiety ». *PLoS ONE* 11.2 (12 fév. 2016), e0149434. DOI : `10.1371/journal.pone.0149434` (cf. p. 17).

[116] G. M. MOLCHAN. « Multiparameter Brownian motion ». *T. Prob. Math. Stat.* 36 (1988), p. 97–110 (cf. p. 92).

[117] T. W. J. MOORHEAD et al. « Automated computation of the gyrification index in prefrontal lobes : Methods and comparison with manual implementation ». *NeuroImage* 31.4 (2006), p. 1560–1566. DOI : `10.1016/j.neuroimage.2006.02.025` (cf. p. 18, 20).

[118] I. NENADIC et al. « Cortical complexity in bipolar disorder applying a spherical harmonics approach ». *Psychiat. Res-Neuroim.* 0.0 (21 fév. 2017). DOI : `10.1016/j.pscychresns.2017.02.007` (cf. p. 16).

[119] M. NEZADAL et al. « The box-counting : critical study ». *Proceedings of the fourth conference on prediction, synergetic and more*. 2001, p. 18 (cf. p. 25).

[120] M. NIETHAMMER et al. « Global Medical Shape Analysis Using the Laplace-Beltrami Spectrum ». *Med. Image Comput. Comput. Assist. Interv.* 10 (Pt 1 2007), p. 850–857. URL : `http://www.ncbi.nlm.nih.gov/pmc/articles/PMC2782516/` (cf. p. 29, 33).

[121] R. OHBUCHI et al. « Watermarking 3D Polygonal Meshes in the Mesh Spectral Domain ». *Proceedings of Graphics Interface 2001*. GI '01. Toronto, Ont., Canada, Canada : Canadian Information Processing Society, 2001, p. 9–17. ISBN : 978-0-9688808-0-7. URL : `http://dl.acm.org/citation.cfm?id=780986.780989` (cf. p. 30).

[122] E. ORASANU et al. « Cortical folding of the preterm brain : a longitudinal analysis of extremely preterm born neonates using spectral matching ». *Brain Behav.* 6.8 (2016). e00488, e00488–n/a. DOI : `10.1002/brb3.488` (cf. p. 35).

[123] E. ORASANU et al. « Longitudinal Analysis of the Preterm Cortex Using Multi-modal Spectral Matching ». *Medical Image Computing and Computer-Assisted Intervention – MICCAI 2016 : 19th International Conference, Athens, Greece, October 17-21, 2016, Proceedings, Part I*. Sous la dir. de Sebastien OURSELIN et al. Cham : Springer International Publishing, 2016, p. 255–263. ISBN : 978-3-319-46720-7. DOI : `10.1007/978-3-319-46720-7_30` (cf. p. 35).

[124] L. PALANIYAPPAN et al. « Aberrant cortical gyrification in schizophrenia : a surface-based morphometry study ». *J. Psychiatry Neurosci.* 37.6 (nov. 2012), p. 399–406. DOI : `10.1503/jpn.110119` (cf. p. 16).

[125] S. E. PAV. « Moments of the log non-central chi-square distribution ». *arXiv :1503.06266 [math, stat]* (21 mar. 2015). arXiv :`1503.06266`. URL : `http://arxiv.org/abs/1503.06266` (cf. p. 110).

[126] N. PEINECKE et al. « Laplace spectra as fingerprints for image recognition ». *Comput. Aided Design* 39.6 (2007), p. 460–476 (cf. p. 49).

[127] R. F. PELTIER. « Processus stochastiques fractals avec applications en finance ». Thèse de doct. 1998 (cf. p. 91).

[128] R.-F. PELTIER et al. *Multifractional Brownian Motion : Definition and Preliminary Results*. report. INRIA, 1995. URL : `https://hal.inria.fr/inria-00074045/document` (cf. p. 127).

[129] A. P. PENTLAND. « Fractal-Based Description of Natural Scenes ». *IEEE Trans. Pattern Anal.* PAMI-6.6 (nov. 1984), p. 661–674. DOI : `10.1109/TPAMI.1984.4767591` (cf. p. 25).

[130] U. PINKALL et al. « Computing Discrete Minimal Surfaces and Their Conjugates ». *Exp. Math.* 2.1 ($1^{er}$ jan. 1993), p. 15–36. DOI : `10.1080/10586458.1993.10504266` (cf. p. 30).

[131] P. PŁOŃSKI et al. « Multi-parameter machine learning approach to the neuroanatomical basis of developmental dyslexia ». *Hum. Brain Mapp.* ($1^{er}$ oct. 2016). DOI : `10.1002/hbm.23426` (cf. p. 16).

[132] A. QIU et al. « Smooth functional and structural maps on the neocortex via orthonormal bases of the Laplace-Beltrami operator ». *IEEE Trans. Med. Imaging* 25.10 (oct. 2006), p. 1296–1306 (cf. p. 37, 38).

[133] H. RABIEI et al. « Local Spectral Analysis of the Cerebral Cortex : New Gyrification Indices ». *IEEE Trans. Med. Imaging* (2016). DOI : `10.1109/TMI.2016.2633393` (cf. p. 26).

[134] P. RAKIC. « A small step for the cell, a giant leap for mankind : a hypothesis of neocortical expansion during evolution ». *Trends Neurosci.* 18.9 (sept. 1995), p. 383–388 (cf. p. 11).

[135] M. REUTER. « Hierarchical Shape Segmentation and Registration via Topological Features of Laplace-Beltrami Eigenfunctions ». *Int. J. Comput. Vis.* 89.2 (1er sept. 2010), p. 287–308. DOI : `10.1007/s11263-009-0278-1` (cf. p. 34–36).

[136] M. REUTER et al. « Laplace–Beltrami spectra as "Shape-DNA" of surfaces and solids ». *Comput. Aided Design*. Symposium on Solid and Physical Modeling 2005 38.4 (avr. 2006), p. 342–366. DOI : `10.1016/j.cad.2005.10.011` (cf. p. 32, 33, 65, 122).

[137] M. REUTER et al. « Global Medical Shape Analysis Using the Volumetric Laplace Spectrum ». *International Conference on Cyberworlds, 2007. CW '07*. International Conference on Cyberworlds, 2007. CW '07. Oct. 2007, p. 417–426. DOI : `10.1109/CW.2007.42` (cf. p. 29, 33).

[138] M. REUTER et al. « Discrete Laplace-Beltrami operators for shape analysis and segmentation ». English. *Comput. & Graph.* 33 (2009), p. 381–390. DOI : `DOI10.1016/j.cag.2009.03.005` (cf. p. 30, 31, 34, 35, 49, 50, 131).

[139] M. REUTER et al. « Laplace–Beltrami eigenvalues and topological features of eigenfunctions for statistical shape analysis ». *Comput. Aided Design*. Selected Papers from the 2007 New Advances in Shape Analysis and Geometric Modeling Workshop 41.10 (oct. 2009), p. 739–755. DOI : `10.1016/j.cad.2009.02.007` (cf. p. 33, 35).

[140] R. RICCELLI et al. « Surface-based morphometry reveals the neuroanatomical basis of the five-factor model of personality ». *Soc. Cogn. Affect. Neur.* 1 (2017), p. 14 (cf. p. 17).

[141] D. P. RICHMAN et al. « Mechanical model of brain convolutional development ». *Science* 189.4196 (4 juil. 1975), p. 18–21 (cf. p. 12).

[142] P. M. ROBINSON. « Gaussian semiparametric estimation of long range dependence ». *The Annals Stat.* (1995), p. 1630–1661 (cf. p. 97).

[143] A. J. ROCKEL et al. « The basic uniformity in structure of the neocortex ». *Brain* 103.2 (juin 1980), p. 221–244 (cf. p. 11).

[144] J. ROGERS et al. « On the genetic architecture of cortical folding and brain volume in primates ». *NeuroImage*. Imaging Genetics 53.3 (15 nov. 2010), p. 1103–1108. DOI : `10.1016/j.neuroimage.2010.02.020` (cf. p. 6, 26).

[145] L. RONAN et al. « Differential tangential expansion as a mechanism for cortical gyrification ». *Cereb. Cortex* 24.8 (août 2014), p. 2219–2228. DOI : `10.1093/cercor/bht082` (cf. p. 13, 14).

[146] D. A. RUSSELL et al. « Dimension of Strange Attractors ». *Phys. Rev. Lett.* 45.14 (6 oct. 1980), p. 1175–1178. DOI : `10.1103/PhysRevLett.45.1175` (cf. p. 25).

[147] K. SANDAU et al. « Measuring fractal dimension and complexity—an alternative approach with an application ». *J Micros-Oxford* 186.2 (1997), p. 164–176 (cf. p. 25).

[148] J. J. SARRAILLE et al. « FD3 : A Program for Measuring Fractal Dimension ». *Educ. Psychol. Meas.* 54.1 ($1^{er}$ mar. 1994), p. 94–97. DOI : `10.1177/0013164494054001010` (cf. p. 25).

[149] M. SCHAER et al. « A surface-based approach to quantify local cortical gyrification ». *IEEE Trans. Med. Imag.* 27 (2008), p. 161–170. DOI : `10.1109/TMI.2007.903576` (cf. p. 6, 16, 18–23, 26).

[150] P. SCHRÖDER et al. *A Quick and Dirty Introduction to the Curvature of Surfaces*. Course of Discrete Differential Geometry, presented in California Institute of Technology. 2011. URL : `http://brickisland.net/cs177/?p=144` (cf. p. 62).

[151] C. C. SCHULTZ et al. « The visual cortex in schizophrenia : alterations of gyrification rather than cortical thickness–a combined cortical shape analysis ». *Brain Struct. Funct.* 218.1 (jan. 2013), p. 51–58. DOI : `10.1007/s00429-011-0374-1` (cf. p. 16).

[152] S. SEO et al. « Laplace-Beltrami eigenfunction expansion of cortical manifolds ». *2011 IEEE International Symposium on Biomedical Imaging : From Nano to Macro*. 2011 IEEE International Symposium on Biomedical Imaging : From Nano to Macro. Mar. 2011, p. 372–375. DOI : `10.1109/ISBI.2011.5872426` (cf. p. 29, 38).

[153] M. SHAKERI et al. *Groupwise shape analysis of the hippocampus using spectral matching*. 2014. DOI : `10.1117/12.2043615` (cf. p. 35).

[154] M. SHAKERI et al. « Statistical shape analysis of subcortical structures using spectral matching ». *Comput. Med. Imag. Grap.* 52 (2016), p. 58 –71. DOI : `http://dx.doi.org/10.1016/j.compmedimag.2016.03.001` (cf. p. 35).

[155] J. SHI et al. « Normalized Cuts and Image Segmentation ». *IEEE Trans. Pattern Anal. Mach. Intell.* 22.8 (août 2000), p. 888–905. DOI : `10.1109/34.868688` (cf. p. 30).

[156] Y. SHI et al. « Anisotropic Laplace-Beltrami eigenmaps : Bridging Reeb graphs and skeletons ». *2008 IEEE Computer Society Conference on Computer Vision and Pattern Recognition Workshops*. 2008 IEEE Computer Society Conference on Computer Vision and Pattern Recognition Workshops. Juin 2008, p. 1–7. DOI : `10.1109/CVPRW.2008.4563018` (cf. p. 36).

[157] Y. SHI et al. « Harmonic Surface Mapping with Laplace-Beltrami Eigenmaps ». *Medical Image Computing and Computer-Assisted Intervention – MICCAI 2008*. International Conference on Medical Image Computing and Computer-Assisted Intervention. DOI : 10.1007/978-3-540-85990-1_18. Springer, Berlin, Heidelberg, 6 sept. 2008, p. 147–154. URL : `http://link.springer.com/chapter/10.1007/978-3-540-85990-1_18` (cf. p. 36).

[158] Y. SHI et al. « Robust Surface Reconstruction via Laplace-Beltrami Eigen-Projection and Boundary Deformation ». *IEEE Trans Med Imaging* 29.12 (déc. 2010), p. 2009–2022. DOI : `10.1109/TMI.2010.2057441` (cf. p. 38).

[159] J. S. SHIMONY et al. « Comparison of cortical folding measures for evaluation of developing human brain ». *NeuroImage* 125 (2016), p. 780–790. DOI : `10.1016/j.neuroimage.2015.11.001` (cf. p. 15, 18, 23).

[160] R. SHISHEGAR et al. « Quantifying gyrification using Laplace Beltrami eigenfunction level-sets ». *2015 IEEE 12th International Symposium on Biomedical Imaging (ISBI)*. 2015 IEEE 12th International Symposium on Biomedical Imaging (ISBI). Avr. 2015, p. 1272–1275. DOI : `10.1109/ISBI.2015.7164106` (cf. p. 18, 24, 35).

[161] D. I. SHUMAN et al. « Vertex-frequency analysis on graphs ». *Appl. Comput. Harmon. Anal.* 40.2 (2016), p. 260–291. DOI : `10.1016/j.acha.2015.02.005` (cf. p. 7, 46, 48, 49, 53–55).

[162] D. D. SILVA et al. « A Critical Appraisal of the Box Counting Method to Assess the Fractal Dimension of Tree Crowns ». *Advances in Visual Computing*. International Symposium on Visual Computing. DOI : 10.1007/11919476_75. Springer, Berlin, Heidelberg, 6 nov. 2006, p. 751–760. URL : `http://link.springer.com/chapter/10.1007/11919476_75` (cf. p. 25).

[163] P. SOILLE et al. « On the validity of fractal dimension measurements in image analysis ». *J. Vis. Commun. Image R.* 7.3 (1996), p. 217–229 (cf. p. 25).

[164] O. SORKINE. « Laplacian Mesh Processing » (2005). DOI : `10.2312/egst.20051044` (cf. p. 29).

[165] G. STRANG et al. *An analysis of the finite element method*. T. 212. Prentice-hall Englewood Cliffs, NJ, 1973 (cf. p. 51).

[166] S. SU et al. « Geometric computation of human gyrification indexes from magnetic resonance images ». *Hum. Brain Mapp.* 34.5 (2013), p. 1230–1244. DOI : `10.1002/hbm.21510` (cf. p. 15, 18, 22).

[167] T. TALLINEN et al. « Surface Sulci in Squeezed Soft Solids ». *Phys. Rev. Lett.* 110.2 (8 jan. 2013), p. 024302. DOI : `10.1103/PhysRevLett.110.024302` (cf. p. 18, 88, 122).

[168] T. TALLINEN et al. « On the growth and form of cortical convolutions ». *Nat. Phys.* advance online publication (1er fév. 2016). DOI : `10.1038/nphys3632` (cf. p. 13, 18, 122).

[169] M. TAN et al. « Spectral Laplace-Beltrami wavelets with applications in medical images ». *IEEE Trans. Med. Imag.* 34.5 (2015), p. 1005–1017 (cf. p. 49).

[170] G. TAUBIN. « Estimating the tensor of curvature of a surface from a polyhedral approximation ». *Proceedings of IEEE International Conference on Computer Vision*. Proceedings of IEEE International Conference on Computer Vision. Juin 1995, p. 902–907. DOI : `10.1109/ICCV.1995.466840` (cf. p. 61).

[171] G. TAUBIN. « Geometric Signal Processing on Polygonal Meshes » (2000). URL : `https://diglib.eg.org:443/handle/10.2312/egst20001029` (cf. p. 29).

[172] P. M. THOMPSON et al. « Three-Dimensional Statistical Analysis of Sulcal Variability in the Human Brain ». *J. Neurosci.* 16.13 (1er juil. 1996), p. 4261–4274. URL : `http://www.jneurosci.org/content/16/13/4261` (cf. p. 25).

[173] R. TORO et al. « Brain size and folding of the human cerebral cortex ». *Cereb. Cortex* 18.10 (2008), p. 2352–2357. DOI : `10.1093/cercor/bhm261` (cf. p. 6, 10, 18–22, 26, 70, 73, 83, 86, 88, 135).

[174] Roberto TORO et al. « A Morphogenetic Model for the Development of Cortical Convolutions ». *Cereb. Cortex* 15.12 (1er déc. 2005), p. 1900–1913. DOI : `10.1093/cercor/bhi068` (cf. p. 88).

[175] W. TUTTE. « How to draw a graph ». *Proc. Lond. Math. Soc.* 13 (1963), p. 743–767. URL : `http://www.ams.org/mathscinet-getitem?mr=28:1610` (visité le 08/11/2016) (cf. p. 30).

[176] D. C. VAN ESSEN. « A tension-based theory of morphogenesis and compact wiring in the central nervous system ». *Nature* 385.6614 (23 jan. 1997), p. 313–318. DOI : `10.1038/385313a0` (cf. p. 12).

[177] D. C. VAN ESSEN et al. « Structural and functional analyses of human cerebral cortex using a surface-based atlas ». *J. Neurosci.* 17.18 (15 sept. 1997), p. 7079–7102 (cf. p. 18, 24).

[178] N. VENET. « Nonexistence of fractional Brownian fields indexed by cylinders ». *arXiv :1612.05983 [math]* (18 déc. 2016). arXiv :`1612.05983`. URL : `http://arxiv.org/abs/1612.05983` (cf. p. 93).

[179] Y. C. de VERDIÈRE. « Sur un nouvel invariant des graphes et un critère de planarité ». *J. Comb Theory B.* 50.1 ($1^{\text{er}}$ oct. 1990), p. 11–21. DOI : `10.1016/0095-8956(90)90093-F` (cf. p. 30).

[180] I. R. VIOLANTE et al. « Gyrification, cortical and subcortical morphometry in neurofibromatosis type 1 : an uneven profile of developmental abnormalities ». *J. Neurodev. Disord.* 5.1 (2013), p. 3. DOI : `10.1186/1866-1955-5-3` (cf. p. 16).

[181] C. WACHINGER et al. « BrainPrint : A discriminative characterization of brain morphology ». *NeuroImage* 109 (avr. 2015), p. 232–248 (cf. p. 29, 33, 65).

[182] T. WANG et al. « Abnormal Changes of Brain Cortical Anatomy and the Association with Plasma MicroRNA107 Level in Amnestic Mild Cognitive Impairment ». *Front. Aging Neurosci.* (2016), p. 112. DOI : `10.3389/fnagi.2016.00112` (cf. p. 16).

[183] M. WARDETZKY et al. « Discrete Laplace Operators : No Free Lunch ». *Proceedings of the Fifth Eurographics Symposium on Geometry Processing*. SGP '07. Aire-la-Ville, Switzerland, Switzerland : Eurographics Association, 2007, p. 33–37. URL : `http://dl.acm.org/citation.cfm?id=1281991.1281995` (cf. p. 30, 31, 49).

[184] Y. WEISS. « Segmentation using eigenvectors : a unifying view ». *The Proceedings of the Seventh IEEE International Conference on Computer Vision, 1999*. The Proceedings of the Seventh IEEE International Conference on Computer Vision, 1999. T. 2. 1999, 975–982 vol.2. DOI : `10.1109/ICCV.1999.790354` (cf. p. 30).

[185] W. WELKER. « Why does cerebral cortex fissure and fold ? » en. *Cerebral Cortex*. Sous la dir. d'Edward G. JONES et al. Cerebral Cortex 8B. Springer US, 1990, p. 3–136. ISBN : 978-1-4613-6706-2 978-1-4615-3824-0 (cf. p. 11, 12).

[186] H. WEYL. « Ueber die asymptotische Verteilung der Eigenwerte ». *Nachrichten von der Gesellschaft der Wissenschaften zu Göttingen, Mathematisch-Physikalische Klasse* 1911 (1911), p. 110–117. URL : `https://eudml.org/doc/58792` (cf. p. 32).

[187] H. WEYL. « Das asymptotische Veteilungsgesetz der Eigenwerte linearer partieller Diffentialgleichungen ». *Math. ann.* 71 (1912), p. 441–479 (cf. p. 32).

[188] S. M. WOLOSIN et al. « Abnormal cerebral cortex structure in children with ADHD ». *Hum. Brain Mapp.* 30.1 (2009), p. 175–184. DOI : `10.1002/hbm.20496` (cf. p. 16).

[189] A. T. WOOD et al. « Simulation of stationary Gaussian processes in [0, 1] d ». *J. Comput. Graph. Stat.* 3.4 (1994), p. 409–432 (cf. p. 91).

[190] R. A. YOTTER et al. « Estimating local surface complexity maps using spherical harmonic reconstructions ». *Med. Image Comput. Comput. Assist. Interv.* 13 (Pt 2 2010), p. 169–176 (cf. p. 37, 126).

[191] R. A. YOTTER et al. « Local cortical surface complexity maps from spherical harmonic reconstructions ». *NeuroImage* 56.3 (1er juin 2011), p. 961–973. DOI : `10.1016/j.neuroimage.2011.02.007` (cf. p. 7, 16, 18, 25, 27, 37, 126).

[192] P. YU et al. « Cortical surface shape analysis based on spherical wavelets ». *IEEE Trans. Med. Imag.* 26.4 (2007), p. 582–597. DOI : `10.1109/TMI.2007.892499` (cf. p. 11).

[193] H. ZHANG. « Discrete combinatorial Laplacian operators for digital geometry processing ». in SIAM Conference on Geometric Design, 2004. 2004. URL : `http://citeseerx.ist.psu.edu/viewdoc/citations;jsessionid=C3D064457EBC995938DB7FFFC7563F60?doi=10.1.1.85.5068` (cf. p. 29).

[194] H. ZHANG et al. « Spectral methods for mesh processing and analysis ». *Proceedings of Eurographics State-of-the-art Report*. 2007, p. 1–22 (cf. p. 29, 30, 37, 49).

[195] L. ZHANG et al. « Quantifying degeneration of white matter in normal aging using fractal dimension ». *Neurobiol. Aging* 28.10 (oct. 2007), p. 1543–1555. DOI : `10.1016/j.neurobiolaging.2006.06.020` (cf. p. 15, 17, 18, 25, 26).

[196] T. ZHANG et al. « Mechanism of Consistent Gyrus Formation : an Experimental and Computational Study ». *Sci. Rep.-UK* 6 (17 nov. 2016), p. 37272. DOI : `10.1038/srep37272` (cf. p. 13).

[197] Y. ZHANG et al. « Reduced Cortical Folding in Mental Retardation ». *Am. J. Neuroradiol.* 31.6 (2010), p. 1063–1067. DOI : `10.3174/ajnr.A1984` (cf. p. 16).

[198] W. ZHAO et al. « A robust hole-filling algorithm for triangular mesh ». *Visual Comput.* 23.12 (1er déc. 2007), p. 987–997. DOI : `10.1007/s00371-007-0167-y` (cf. p. 106).

[199] K. Zilles et al. « The human pattern of gyrification in the cerebral cortex ». *Anat. Embryol.* 179 (1988), p. 173–9 (cf. p. 18, 19).

[200] K. Zilles et al. « Gyrification in the cerebral cortex of primates ». *Brain Behav. Evol.* 34.3 (1989), p. 143–150 (cf. p. 19).

[201] K. Zilles et al. « Development of cortical folding during evolution and ontogeny ». *Trends Neurosci.* 36.5 (mai 2013), p. 275–284. doi : `10.1016/j.tins.2013.01.006` (cf. p. 11).